

8-2021

## Design, Development, and Testing of Research Payloads on Various Suborbital Flight-Test Platforms

Vijay Vishal Duraisamy

Follow this and additional works at: <https://commons.erau.edu/edt>

 Part of the [Mechanical Engineering Commons](#)

---

This Dissertation - Open Access is brought to you for free and open access by Scholarly Commons. It has been accepted for inclusion in PhD Dissertations and Master's Theses by an authorized administrator of Scholarly Commons. For more information, please contact [commons@erau.edu](mailto:commons@erau.edu).

DESIGN, DEVELOPMENT, AND TESTING OF RESEARCH PAYLOADS ON  
VARIOUS SUBORBITAL FLIGHT-TEST PLATFORMS

by

Vijay Vishal Duraisamy

A Dissertation Submitted to the College of Engineering Department of Mechanical  
Engineering in Partial Fulfillment of the Requirements for the Degree of  
Doctor of Philosophy in Mechanical Engineering

Embry-Riddle Aeronautical University  
Daytona Beach, Florida  
August 2021

DESIGN, DEVELOPMENT, AND TESTING OF RESEARCH PAYLOADS ON  
VARIOUS SUBORBITAL FLIGHT-TEST PLATFORMS

by

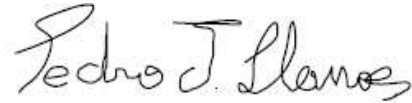
Vijay Vishal Duraisamy

This dissertation was prepared under the direction of the candidate's Dissertation Committee Chair, Dr. Birce Dikici, Associate Professor, Daytona Beach Campus, and Dissertation Committee Co-Chair Dr. Pedro Llanos, Associate Professor, Daytona Beach Campus, and Dissertation Committee Members Dr. Sathya Gangadharan, Professor, Daytona Beach Campus, Dr. Fardin Khalili, Visiting Assistant Professor, Daytona Beach Campus, Dr. Victor Huayamave, Assistant Professor, Daytona Beach Campus, and Dr. Mandar Kulkarni, Assistant Professor, Daytona Beach Campus and has been approved by the Dissertation Committee. It was submitted to the Department of Mechanical Engineering in partial fulfillment of the requirements for the degree of Doctor of Philosophy in Mechanical Engineering.

Dissertation Review Committee:

**Birce Dikici** Digitally signed by Birce Dikici  
Date: 2021.08.05 12:25:21  
-04'00'

Birce Dikici, Ph.D.  
Committee Chair



Pedro Llanos, Ph.D.  
Committee Co-chair

**Sathya Gangadharan** Digitally signed by Sathya  
Gangadharan  
Date: 2021.08.05 12:34:00 -04'00'

Sathya Gangadharan, Ph.D., P.E.  
Committee Member

**Fardin Khalili** Digitally signed by Fardin Khalili  
Date: 2021.08.05 12:45:42  
-04'00'

Fardin Khalili, Ph.D.  
Committee Member

**Victor Huayamave** Digitally signed by Victor  
Huayamave  
Date: 2021.08.05 12:57:08 -04'00'

Victor Huayamave, Ph.D.  
Committee Member

**Mandar D. Kulkarni** Digitally signed by Mandar D.  
Kulkarni  
Date: 2021.08.05 13:53:35 -04'00'

Mandar Kulkarni, Ph.D.  
Committee Member

**Eric Coyle** Digitally signed by Eric Coyle  
Date: 2021.08.05 14:25:19  
-04'00'

Eric Coyle, Ph.D.  
Ph.D. Program Chair,  
Mechanical Engineering

**Eduardo Divo** Digitally signed by Eduardo Divo  
Date: 2021.08.05 14:28:30  
-04'00'

Eduardo Divo, Ph.D.  
Department Chair,  
Mechanical Engineering

**Maj Mirmirani** Digitally signed by Maj Mirmirani  
Date: 2021.08.05 14:51:25 -04'00'

Maj Mirmirani, Ph.D.  
Dean, College of Engineering

**Lon Moeller** Digitally signed by Lon Moeller  
Date: 2021.08.05 15:08:29  
-04'00'

Lon Moeller, J.D.  
Senior Vice President for Academic  
Affairs and Provost

*In loving memory of my dear father, Duraisamy, who went through immense sacrifices for our family and always believed in my abilities in academics; and my best friend, Syed, who has inspired me to enjoy every moment and face everything in life with a smile.*

## **Acknowledgments**

I want to dedicate this research work to my parents, Umaa Saivignesh and Saivignesh, who have always supported me and encouraged me. Special thanks to Prabashini, my awesome wife, who encouraged and supported me in pursuing my Ph.D.

I would like to express my deepest gratitude to my advisor, Dr. Birce Dikici, for her extensive support, encouragement, and her willingness to assist me in every way she could throughout this research. I would like to thank you for your patience and your advice on navigating through my Ph.D. research and defense.

I would like to mention my special thanks to Dr. Pedro Llanos for mentoring me and providing me opportunities that have brought immense value to my professional portfolio. I would like to express my sincere gratitude to Dr. Sathya Gangadharan for his support and guidance. You have been a guardian and a mentor for me since I joined Embry-Riddle, for which I am forever grateful.

I take this opportunity to thank my committee members: Dr. Fardin Khalili, Dr. Victor Huaymave, and Dr. Mandar Kulkarni, for their valuable feedback and insights on my dissertation. I would like to acknowledge the Department of Mechanical Engineering and the Department of Applied Aviation Sciences for supporting my research. I would like to thank Bill Russo, Alvey Gary, and Mike Potash for their fabrication help.

I would like to express my special gratitude to Leander Paul, Manikandan Vairamani, Nikita Amberkar, Justin Nafziger, Cynthia Stockton, Topolski Collin, and Morgan Shilling for their help with my research. Finally, and most importantly, I would like to thank my friends, Christable, Shruthi, Faizal, Lokesh, Deepak, and all my roommates for their moral support and the great times we have had together.

## Abstract

Researcher: Vijay Vishal Duraisamy  
Title: Design, Development, and Testing of Research Payloads on Various Suborbital Flight-Test Platforms  
Institution: Embry-Riddle Aeronautical University  
Degree: Doctor of Philosophy in Mechanical Engineering  
Year: 2021

With recent advances in the commercial space industry, suborbital payload launches have become more common and accessible to researchers actively seeking solutions for problems involving prolonged space travel and future missions to Moon and Mars. Suborbital payload missions compared to orbital launches are less expensive and offer faster turnaround times; however, the novelty of this domain provides unique challenges. This multidisciplinary research effort aims to tackle some of these challenges by detailing the design, development, and testing techniques followed in the successful launch and recovery of payload experiments in currently active and upcoming suborbital launch vehicles. The research methodology involves collecting payload requirements, CAD design, computational analysis, mass optimization, 3D printing, vibration, and load testing, model rocketry development, simulation, and launch operations. Structural analysis using FEA and vibration testing on a shaker table shows the compliance of the payload prototypes in the maximum predicted flight environments. Multiphase CFD analysis is used as benchmarking technique to characterize the behavior of payloads containing liquids in microgravity. Hands-on model rocketry has proven as a valuable research platform for subsequent payload deliveries.

# Table of Contents

	Page
Dissertation Review Committee .....	ii
Acknowledgments.....	iv
Abstract.....	v
Table of Contents .....	vi
List of Tables .....	xi
List of Figures .....	xii
1. Introduction.....	1
1.1. Significance of Study.....	4
1.2. Problem Statement.....	5
1.3. Research Facilities .....	9
1.4. Limitations and Assumptions .....	11
2. Review of Relevant Literature .....	17
2.1. Suborbital Reusable Vehicles .....	17
2.2. Suborbital Space Vehicles as a Platform for Microgravity Research.....	18
2.3. Payload User Guides.....	18
2.4. NASA’s Flight Experiment Onboard Blue Origin’s New Shepard Vehicle .....	19
2.5. CubeSat Approach .....	19
2.6. Propellant Gauging in Microgravity .....	20

2.7. Investigation of MAPMD using Floating Membranes .....	21
2.8. Vibration Testing of Small Satellites.....	21
2.9. Model Rocket Projects.....	22
2.10. Summary .....	22
2.11. Research Contribution .....	23
3. CRExIM Payload .....	26
3.1. Payload Design .....	27
3.2. FEA with Acceleration Loads.....	30
3.3. Random Vibration Analysis.....	33
3.4. Mass Optimization.....	34
3.5. Cell Vials Slosh Testing Using CFD .....	36
3.6. 3D Printing.....	39
3.7. Results.....	41
3.7.1 Structural Analysis with Acceleration Loads.....	41
3.7.2 Modal and Random Vibration Analysis.....	44
3.7.3 Structural Design Optimization .....	46
3.7.4 Cell Vials Slosh Analysis.....	50
3.7.5 Prototyping using 3D Printer and Final Assembly .....	52
3.8. Flight Operations and Post-flight Analysis.....	55



3.8.1 Deliverables and Payload Review.....	56
3.8.2 Pre-flight and Post-flight Operations .....	58
3.8.3 Flight Data Analysis .....	60
4. MESSI McXIMUS Payload.....	64
4.1. Payload Requirements .....	66
4.2. Payload Design .....	68
4.3. Payload Electronics.....	73
4.3.1 Custom Data Logger with Flight Data Interface.....	73
4.4. Suborbital Flight Test .....	77
5. PLD Payloads.....	79
5.1. PLD ERAU Payload Design.....	80
5.1.1 Scope of Study .....	84
5.2. Avionics Payload Development.....	85
5.2.1 Payload Design .....	87
5.2.2 Payload Electronics.....	88
5.3. MAPMD CFD Analysis.....	92
5.3.1 Payload Background .....	92
5.3.2 Fluid Domain .....	97
5.3.3 Fluid Mesh .....	98

5.3.4	Overset Mesh .....	101
5.3.5	Simulation Physics, Governing Equations, and Boundary Conditions.....	103
5.3.6	Simulation Cases.....	106
5.3.7	DFBI Motion.....	107
5.3.8	Simulation Execution.....	112
5.3.9	Post Processing .....	113
5.4.	MAPMD CFD Results.....	116
5.5.	PLD Payloads Vibration Test Campaign.....	122
5.5.1	Test Objectives.....	122
5.5.2	Test Equipment .....	123
5.5.3	Test Fixture .....	126
5.5.4	Test Plan and Test criteria.....	127
5.5.5	Test Setup Procedures .....	134
5.5.6	Vibration Test Results.....	137
6.	Suborbital Payload Rocket Research Platforms .....	148
6.1.	Level 1 Rocket.....	149
6.1.1	Rocket and Payload Development .....	149
6.1.2	Level 1 Rocket Launch and Flight Analysis .....	153
6.2.	Level 3 Rocket.....	156

6.2.1 Preliminary Rocket Design and Fabrication .....	156
6.2.2 Level 3 Rocket Simulations .....	161
6.2.3 Analysis of Custom Payload Bay .....	163
6.3. Vacuum Chamber Test Capability.....	165
7. Conclusions and Future Recommendations.....	167
References.....	172
Appendix A.....	180
Appendix B.....	193

## List of Tables

Table	Page
1: Comparison of microgravity research opportunities and their capabilities .....	17
2: Payload requirements and launch profile characteristics.....	28
3: Material properties .....	32
4: Mass optimization variables .....	35
5: FEA results of the NanoLab structure .....	43
6: Modal analysis of the NanoLab structure .....	44
7: Random vibration analysis results of the NanoLab structure .....	46
8: Optimization results.....	49
9: Payload deliverables timeline .....	56
10: MESSI/McXIMUS Payload mass .....	72
11: Custom Datalogger components and power requirements .....	75
12: Calculated payload physical parameters for the PLD ERAU payload assembly .....	84
13: List of electronic components in each avionics/telemetry payload .....	91
14: Mesh independence study.....	101
15. DFBI setup parameters .....	110
16: Low-level sine sweep test parameters .....	130
17: Random vibration profile breakpoints .....	132
18: Sine-burst test specifications .....	133
19: Accelerometer placement locations .....	135
20: Vibration test campaign results.....	147

## List of Figures

Figure	Page
1: Suborbital payload development process .....	4
2: TRL measurement system .....	5
3: Research objectives.....	9
4: PATO lab .....	10
5: VEGA supercomputer.....	10
6: Electrodynamic shaker at Micaplex.....	11
7: NASA's SFEM-2 payload flown onboard New Shepard's P8 flight mission .....	19
8: CAD of the payload housing structure (Initial model) .....	29
9: CAD of the payload housing structure (Updated model) .....	30
10: Structural mesh of CRExIM NanoLab .....	31
11: Boundary conditions .....	32
12: Simulated random vibration profile.....	33
13: CFD setup .....	38
14: 3D printing the NanoLab structure .....	41
15: Equivalent stress distribution with acceleration load applied in the positive Z direction. ....	43
16: Equivalent stress results with random vibration spectrum applied in the Y direction .....	45
17: Optimization parameter tradeoff charts .....	47
18: Parameter sensitivities .....	47
19: Recorded optimization parameter histories .....	48

20: Wall $y^+$ values .....	50
21: Scalar scenes showing the time history of liquid slosh inside 5.0 mL Eppendorf tube with lateral actuation and gravity acting vertical direction.....	51
22: Tube actuation and corresponding slosh response observed in the Eppendorf tube .	52
23: 3D Printed NanoLab structures. ABS with initial design holder (left) ABS with improved device holder (middle) and CFRP ABS (right) .....	54
24: CRExIM payload final assembly .....	55
25: Safety load test.....	58
26: CRExIM operational timeline.....	59
27: Acceleration data recorded by EDL-XYZ during the suborbital flight. X-axis (dark blue), Y-axis (light blue) and Z-axis (purple) .....	61
28: Flight profile showing acceleration experienced at different altitudes .....	62
29: Temperature and relative humidity measured inside the NanoLab .....	63
30: Bio organisms used in MESS/McXIMUS payload experiments.....	65
31: Initial MESSI/McXIMUS NanoLab CAD model .....	68
32: MESSI/McXIMUS updated CAD model .....	70
33: MESSI/McXIMUS updated CAD model design components .....	71
34: Updated NanoLab lid design .....	73
35: Electronics test dry run .....	76
36: Fully assembled MESSI/McXIMUs payload preflight .....	77
37: MESSI/McXIMUS flight acceleration profile.....	78
38: PLD Space’s MIURA 1 launch vehicle and flight parameters .....	79
39: MIURA 1 payload specifications . All units are in mm .....	80

40: PLD ERAU payload experiments – Initial CAD model.....	81
41: MAPMD design modification .....	82
42: Updated CAD model of the PLD ERAU payload assembly .....	83
43: PLD Space MIURA 1 vehicle coordinate system .....	83
44: PLD ERAU Avionics payload design .....	88
45: Assembled avionics payload NanoLabs .....	90
46: Liquid slosh in a cylindrical tank.....	92
47: Slosh mitigation using PMD. Passive damping (left). Hybrid Damping (right) .....	93
48: MAPMD Zero-G flight experiment rig .....	95
49: Modified avionics payload flown onboard parabolic Zero-G flight.....	95
50: Zero-G parabolic flight aircraft .....	96
51: Acceleration profile. Zero-G parabolic flight conducted on November 19, 2020.....	96
52: MAPMD CFD domain showing distinct background (Tank) and overset regions ...	97
53: Volume Mesh. 3D Mesh view (left). Mesh cross-section (right) .....	98
54: Mesh Details. Prism layer cells around the flow boundaries (left). Overset mesh on the floating membrane (right) .....	99
55: Free slosh comparison .....	100
56: Overset cell status on the overset region .....	103
57: Overset cell status on the background (Tank) region .....	103
58: Parabolic acceleration profiles used in CFD simulation cases .....	106
59: Time taken by the Star-CCM+ solver for each time step .....	112
60: Acceleration profile for each simulation case.....	116
61: Average Courant number on the water surface .....	117

62: Maximum water level; Passive damping cases.....	118
63: Maximum water level; Active damping cases.....	118
64: Liquid forces on tank walls.....	119
65: Membrane spatial parameters .....	120
66: Passive damping case visualized at various time steps.....	121
67: Electrodynamic shaker used in the vibration test campaign.....	124
68: Acceleration sensor mounting scheme .....	126
69: Test fixture design .....	127
70: Crosstalk test setup .....	129
71: Sine sweep profile setup on the DVC-8 sine controller software.....	131
72: Random vibration profile setup on the DVC-8 sine controller software.....	132
73: Sine burst profile setup on the DVC-8 sine controller software.....	133
74: Acceleration sensor locations on the sub payloads.....	135
75: PLD ERAU payloads mounted in the vertical configuration (old design).....	136
76: Lateral testing configuration on the horizontal slip table .....	136
77: Crosstalk test in vertical configuration (X-axis excitation).....	137
78: Preliminary MAPMD hardware FRF .....	138
79: Modified and final flight hardware version mounted on the shaker table.....	139
80: Random vibration test ASD response of the Lateral Y test.....	139
81: Lateral test of high-level sine burst with 3 G quasi-static load condition .....	140
82: FRF comparison: Vertical test configuration, MAPMD sub payload .....	141
83: FRF comparison: Lateral test configuration (Y direction), MAPMD sub payload .	142
84: FRF comparison: Lateral test configuration (Z direction), MAPMD sub payload .	143



85: FRF comparison: Vertical test configuration (X direction), Shunt sub payload .....	144
86: FRF comparison: Vertical test configuration, Vertical avionics sub payload .....	145
87: FRF comparison: Vertical test configuration, Horizontal avionics sub payload.....	146
88: Level 1 rocket data logger .....	150
89: RockSim level 1 rocket simulation.....	152
90. Simulated flight profile and flight parameters using RockSim .....	152
91: Marea Roja level 1 rocket flight phases.....	154
92: Actual flight profile of the level 1 rocket .....	154
93: Level 1 rocket data logger payload data .....	155
94: STEVE level 3 rocket design.....	157
95: STEVE design exploded view with all rocket parts labeled.....	158
96: Motor tube assembly.....	159
97: Fabricated motor tube after completion of the sanding and grinding processes .....	160
98: Fin alignment box .....	160
99: OpenRocket Level 3 rocket simulation results .....	161
100: Cambridge rocketry Monte Carlo run results .....	161
101: Simulated level 3 rocket motion parameters.....	162
102: Simulated level 3 rocket stability parameters .....	163
103: Custom payload bay.....	164
104: Custom payload bay structural analysis.....	164
105: Vacuum chamber design considerations.....	165
106: Assembled vacuum chamber testbed.....	166

## 1. Introduction

Space research has enabled humans to reach new frontiers and look for answers to critical questions such as the origin of the Universe and life on Earth. These fundamental questions have been the basis of human evolution for millions of years, and now we have the unique opportunity to find the answers with advancements in technology in the last few decades. NASA is planning to revisit the Moon and, this time to create a habitat and conduct research on the lunar surface through its Artemis program [1]. The Moon missions are planned for the mid of 2020s, and there are also plans to go to Mars in the 2030s. The prospect of making humans an interplanetary civilization ensures the prolonged survival of the human species while helping the advancement of technology back on Earth. Such has been the case throughout the evolution of technology since the dawn of the space age, where essential inventions that we use today on Earth are byproducts of space research conducted in the development of Saturn V, space shuttle, and the International Space Station (ISS).

NASA has released taxonomies in the year 2020 [2] to highlight key research areas and technologies that require development to realize the goal of the Moon and Mars missions. One of the critical areas is the study of long-duration space travel on human physiology. Even though NASA has invested significant efforts in researching this area, more analysis is required to understand the effects of the harsh space environment for prolonged periods on humans [3]. The other areas highlighted in the taxonomies are new propulsion, landing, robotic, guidance, and navigation systems.

Before delivering and deploying in space, any new space technology requires extensive planning and testing in the intended mission environment. Ground testing

offers a venue to test these payloads and systems; however, the space environment involving microgravity and other factors is difficult to simulate on the ground. ISS has been the most widely used test platform for new technology and experiments involving flight support systems. ISS is also a valuable research support platform to provide valuable crew time and continuous operations throughout the year. However, NASA is already in the process of retiring the ISS in the next few years. Even though the cost of launching payloads to Low Earth Orbit (LEO) has reduced in recent years [4], it is still a significant expense, and there are other costs involved with a launch to the ISS, integration, and crew time usage. Also, the development of payloads to the ISS requires stringent protocols to be followed and may require space-rated hardware, which is immensely expensive. The overall effort needed to prepare and fly payloads to orbit also very high.

Recently, a new space research platform has emerged through commercial reusable suborbital space launch vehicles [5]. Suborbital launches offer many advantages over LEO missions considering their faster turnaround times, lower development timelines, less stringent test requirements, and significantly lower cost margins. The suborbital launch capability can conduct science experiments and new technology demonstration missions at a fraction of the cost and effort. Therefore, payloads could be validated using these platforms before launching on more expensive deployment missions.

Commercial suborbital launches are recent ventures, with vehicle development started in the early 2000s. The first commercial spaceflight was Virgin Galactic's SpaceShipOne on 21<sup>st</sup> June 2004. The first commercial payload mission was conducted in Blue Origin's New Shepard vehicle on 12<sup>th</sup> December 2017. Other international ventures involve PLD

Space in Spain and Copenhagen Suborbitals in Denmark. According to NASA [6], currently, several commercial companies such as Blue Origin, Masten Space Systems, UP Aerospace, Virgin Galactic, and Exos Aerospace have been identified as suborbital flight providers. Some of these companies targeted space tourism while developing this capability and have been actively involved in getting their launch vehicles human-rated. Although the main goal was to tap the space tourism market, the ability to launch payloads on the same platform has greatly invigorated the science community. According to the market survey carried out by The Tauri Group [6], the second-largest source of demand after “Space Tourism” is “Basic and Applied Research,” accounting for about 10% of forecasted demand.

Suborbital spaceflight is the trajectory where the space vehicle does not complete a full orbit but reaches space demarcated by the Karman line (100km above Earth). The velocities required are about 15-20% of an orbital flight, and therefore, the suborbital launch vehicle development is much simpler and less expensive. Suborbital launches were performed by almost every space organization before testing orbital systems. However, the new era of commercial operators in this area has brought in reusability, making the launches accessible to educational institutions, researchers, and aerospace industries. The competition between these companies expects to grow in the coming decades, greatly benefiting the payload research community. The payload development process is much more flexible than an orbital launch. However, the small mass and capacity constraints and the availability of only a few minutes of microgravity time should be considered. A typical suborbital payload development process workflow is

shown in Figure 1. The processes shown will be explained in detail in this research through various suborbital payload research projects.



Figure 1: Suborbital payload development process

### 1.1. Significance of Study

This research will provide new insights into the processes involved in developing and testing suborbital research payloads. The experiences gained through successful flight missions conducted on Blue Origin’s New Shepard vehicle and a prospective flight on PLD Space’s MIURA I rocket.

The novel nature of the suborbital launch market offers challenges to new payload researchers both in academics and the aerospace industry. The techniques presented in this study will simplify the future efforts on the engineering development of payloads specifically focused on biological experiments and liquids.

This research aims to support NASA’s technology roadmaps towards developing interplanetary missions and long-distance space travel. Finally, the progress done in developing payload research platforms at Embry-Riddle Aeronautical University (ERAU) will enable future students and researchers to gain hands-on payload launch experience.

NASA recommends a Technology Readiness Level (TRL) measurement system to develop and deliver new space hardware or technology. New technology inventors follow this suggested development sequence (Figure 2), and the project is assigned a TRL rating based on the progress. It can be noted that TRL7 requires testing of the new system in a space environment. Commercial suborbital reusable flights offer a unique advantage in cost and simplicity compared to orbital missions, enabling this TRL's achievement. The Suborbital Reusable Vehicle (SRV) utilization to perform a technology demonstration in space is discussed in this research.

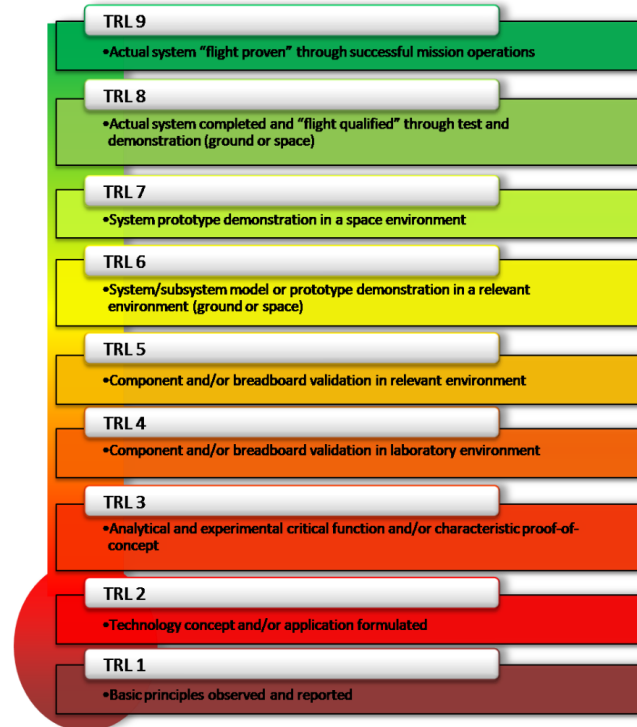


Figure 2: TRL measurement system [7]

## 1.2. Problem Statement

A streamlined method and approach are required for the commercial suborbital market's industrial and academic science research application. Hence, a detailed design,

development, and testing methodology are necessary to mature novel suborbital payload technology.

This study entails the development of processes to support multiple suborbital payload experiments. Each payload has a unique set of research hypotheses, requirements, and outcomes. For instance, bioscience experiments have distinctive requirements to ensure the survival of biological components and unique science goals. On the other hand, the technology demonstration experiments have a different set of requirements and objectives. The approach carried out in this work is modified and tailored to meet the demands of each suborbital payload. The science and engineering hypotheses of each payload experiment are explained under corresponding sections.

The primary objective of the research is to benchmark the design and development of experimental payloads on multiple suborbital platforms. The space environment is very challenging and filled with risks for mission success. To ensure safety and reliability, testing and verification of space payloads per the launch provider's requirement. The novelty of the commercial suborbital payload launch opportunities offers a unique payload development environment. In this research, this field is navigated using innovative design, 3D printing fabrication, FEA. CFD, vibration analysis and testing, optimization, model rocket payload platforms.

Section 1 will provide a background of the suborbital launch market and the various platforms available to researchers. This chapter will state the preconditions and the essentiality of this research in supporting the opportunities available in relatively young commercial suborbital space. The research facilities and tools used in performing this effort are listed, and the list of abbreviations and nomenclature are listed.

Section 2 will summarize the review of relevant literature. The multidisciplinary effort carried out in this research involves the design, structural and fluid analysis, mass optimization, vibration testing, and model rocketry. Previous work completed on similar fields of study is gathered and reviewed. The significance and the impact of conducting this research on future and current payload development communities are explained.

The development and testing of three different payloads are elaborated in the following sections. Section 3 explains the engineering development process carried out on ERAU's first suborbital payload termed CRExIM. The biology payload experiment was designed and fabricated using 3D printing technology to test the effects of microgravity and the space environment on T cells. An FEA analysis was performed on the payload housing structure to simulate flight loads and parameters. A CFD analysis was performed on the cell tubes containing liquid medium to estimate the slosh forces on the vial walls. Payload mass is an essential constraint for small suborbital payload platforms. A mass optimization is performed to reduce the mass of the structure, thereby increasing payload capacity. CRExIM was successfully launched and recovered on Blue Origin's New Shepard vehicle, and post-flight analysis of data is explained.

Section 4 covers the engineering development of the MESSI/McXIMUS payload, which contained two different biological experiments. The objective of the MESSI mission was to study the growth rates of Spirulina algae in space which is being increasingly considered a food source for astronauts in the future. McXIMUS payload contained live zebrafish embryos and studied the effect of space stressors on muscle growth. The payload design and development processes were derived from the CRExIM mission and builds on the experiences gathered in the previous mission. The development



of the MESSI/McXIMUS payloads had unique challenges as the mission involving two in-vivo experiments, and novel payload electronics were also required. The conceptualization and the operation of the payload electronics architecture are detailed in Section 4.

Section 5 details the vibration testing and analysis of a proposed payload stated to be launched with PLD Space on their upcoming space flight debut. The payload package consists of multiple sub-payloads with various mission requirements and objectives. An avionics/telemetry payload is proposed as a pathfinder mission to evaluate and record the flight environment inside the first launch of the MIURA 1 rocket. The goal is to utilize the flight opportunity and the available electronics interfaces to develop a sophisticated data logging payload. The electronics system development and fabrication are detailed. MAPMD is another sub payload and a technology demonstration mission that will fly along with the other sub payloads measuring and recording the effectiveness of new technology in mitigating liquid slosh in microgravity. A CFD analysis technique is benchmarked by analyzing the fluid dynamics of this payload. This analysis aims to characterize fluid behavior in microgravity and develop a method to support future payloads that primarily contain liquids. A vibration test campaign of all the flight hardware is performed to verify the performance and survivability of all the experiments involved in this suborbital mission. This acceptance test was required to clear the safety requirements set by PLD Space. The test setup and the results of the test and analysis are discussed in Section 5.

Section 6 introduces the capabilities that were devised to support and improve suborbital payload research. Model rocketry was used as a tool to develop in-house

launch options to test and prepare future suborbital payloads. A level 1 rocket was fabricated and successfully flown with a payload onboard. The hands-on experience in fabricating model rockets enabled a better understanding of operations and preparations behind rocket development and launches. A level 3 rocket with higher performance characteristics was conceptualized and designed using CAD tools. Rocket simulations were performed to predict the flight profiles, and the results were applied in optimizing the rocket design.

Section 7 provides a summary and recommendations for future payload researchers, followed by references and appendices. The objectives of this research are summarized in Figure 3.

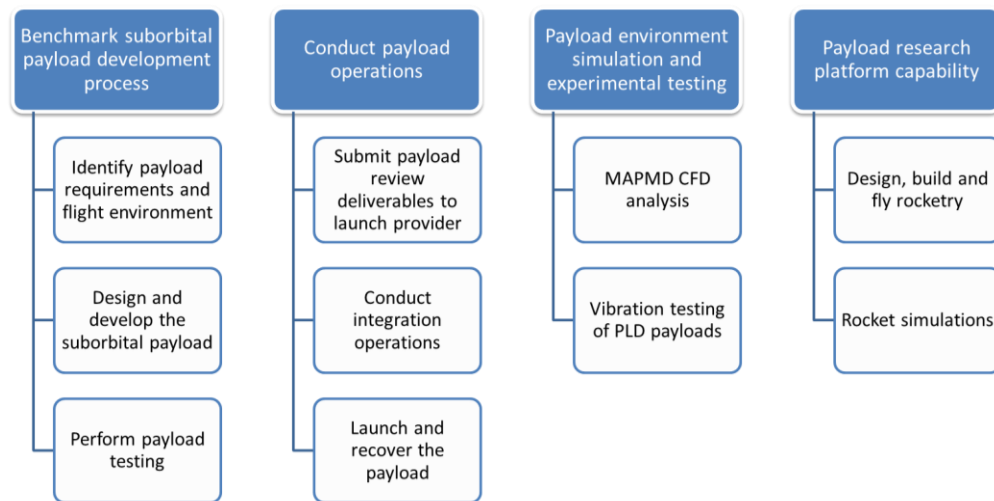


Figure 3: Research objectives

### 1.3. Research Facilities

Payload Applied Technology and Operations (PATO) lab shown in Figure 4 is currently located in the Advanced Flight Simulation Center building. The lab space (floorplan shown in Appendix B) was primarily used for the development of payloads and rocket components. The same lab was previously located on the roof in the College

of Aviation building, and the new lab was established with new capabilities to support payload and model rocketry fabrication. The lab has essential engineering tools and hardware along with electronics stations. A Raise3D 3D printer is available for prototyping and a computer software suite such as CATIA, ANSYS, Arduino IDE, and rocketry simulation software.



Figure 4: PATO lab

CFD analysis was performed using star-CCM+ software at the offices in the M building. The Vega supercomputer's (Figure 5) high-performance computing capabilities were utilized to batch run simulations with multiple processors. Vega is a Cray supercomputer with 84 nodes and 2x18 cores for each processing node. A maximum of 360 cores is allowed per student user.

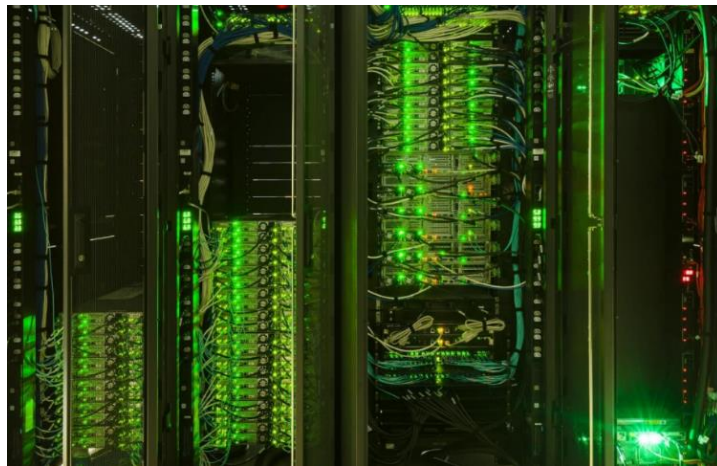


Figure 5: VEGA supercomputer

The electrodynamic shaker system at Micaplex Structures lab was utilized to conduct the vibration test campaign. The shaker table is capable of vibration testing all three axes. Further details on the equipment are provided in the PLD payload vibration test campaign.



Figure 6: Electrodynamic shaker at Micaplex

#### **1.4. Limitations and Assumptions**

The NanoLab payloads were 3D printed using ABS, and the expected loads and vibrations were analyzed using Finite Element Analysis (FEA) tools. 3D printed structures have nonuniform internal geometries not modeled in the Finite Element Model (FEM) to reduce complexity. This analysis aims to increase the confidence level of the payload design before fabrication and to identify critical areas in the model susceptible to flight loads. A physical load test was performed per the payload integrator's specifications and finally reviewed by the payload integrator team before the flight.

Random vibration analysis in ANSYS does not simulate the actual vibration excitation on the structure. Instead, it uses a statistical method to estimate structural responses using data from the modal analysis. Similarly, in the CFD analysis of cell vial slosh, the random vibration excitation is not applied to the tubes. A complex synthesis of the PSD breakpoints is required to replicate the random acceleration waveform.

Numerous assumptions and limitations were used and encountered in the preliminary benchmarking CFD study of MAPMD. A zero-gap interface between the interset mesh and the background region is used to resolve close membrane encounters with the tank walls. The zero-gap interface turns OFF cells when the membrane reaches a certain distance from the tank boundaries. The membrane motion is a 6 DOF problem, and the analysis is performed with only 4 degrees of freedom. The membrane translation motion in the X and Y lateral direction was fixed to avoid continuous impacts between the membrane and tank walls. The electromagnetic forces were not modeled in the active cases, and the membrane was assumed to be rigidly fixed at the initial water surface. This assumption was used to expedite the solution process as the solver time for resolving impacts or contact couplings was three times the magnitude of a regular DFBI motion solution.

The classical shock module of the DVC-8 controller used in the vibration test campaign had limitations on input shock profiles. The Shock Response Spectrum (SRS) specified by PLD Space could not be used in the vibration controller software. The software could produce shock signals only in a time-dependent acceleration waveform and not as an SRS in the frequency domain.

**Definition of Terms**

$G$	Acceleration due to gravity
$U$	Unit
$a_i$	Volume fraction of phase $i$
$V_i$	Volume occupied by phase $i$ inside a cell
$V$	Total volume of the cell
$\rho$	Density
$\mu$	Dynamic viscosity
$C_p$	Specific heat
$S_{a_i}$	Source or sink of phase $i$
$v$	Fluid velocity
$S$	Mass source term
$p$	Pressure
$I$	Unity tensor
$T$	Stress Tensor
$f_b$	Vector of body sources
$E$	Total energy
$H$	Total enthalpy
$\dot{q}''$	Heat flux vector
$S_E$	User-defined energy source term
$p_f$	Pressure acting on face $f$
$a_f$	Area vector of face $f$

$r_f$	Distance vector from body center of mass to center of face f
$\tau_f$	Shear stress acting on face f

### List of Acronyms

ABS	Acrylonitrile Butadiene Styrene
ASD	Acceleration Spectral Density
CAD	Computer Aided Design
CD & H	Command Data and Handling
CFRP	Carbon Fiber Reinforced Plastic
CFD	Computational Fluid Dynamics
CG	Center of Gravity
COTS	Commercial-off-the-shelf
CRExIM	Cell Research Experiment In Microgravity
DFBI	Dynamic Fluid Body Interaction
DOF	Degree of freedom
ERAU	Embry-Riddle Aeronautical University
ERAU	Embry-Riddle Aeronautical University
FEA	Finite Element Analysis
FEM	Finite Element Model
FFF	Fused Filament Fabrication
FRF	Frequency response function
HPC	High Performance Computing
IDE	Integrated Development Environment
IL	Interleukin

ISS	International Space Station
LEO	Low Earth Orbit
LSIP	Launch Site Integration Package
MAPMD	Magneto Active Propellant Management Device
McXIMUS	Muscle characterization eXperiment In Microgravity Universal Spacelab
MDS	Material Data Sheet
MESSI	Microgravity Experiment Spirulina Superfood In-vitro
MPE	Maximum Predicted Environment
MUSC	Medical University of South Carolina
NASA	National Aeronautical and Space Administration
NFF	NanoRacks Feather Frame
PATO	Payload Applied Technology Operations,
PDP	Payload Data Package
PLA	Polylactic Acid
PMD	Propellant Management Device
PPF	Payload Processing Facility
PSD	Power Spectral Density
PSP	Payload Safety Package
PUG	Payload User Guide
RANS	Reynolds-Averaged Navier-Stokes
REM	Research and Education Mission
SFEM	Suborbital Flight Experiment Monitor



SHM	Simple Harmonic Motion
SRV	Suborbital Reusable Vehicle
STEVE	Suborbital Technology Experimental Vehicle for Exploration
TRL	Technology Readiness Level
TVOC	Total Volatile Organic Compounds
U	Unit
USB	Universal Serial Bus
UTHSCSA	University of Texas Health Science Center at San Antonio
VOF	Volume of Fluid
WTLS	West Texas Launch Site

## 2. Review of Relevant Literature

### 2.1. Suborbital Reusable Vehicles

The study performed by the Tauri Group [6] highlights the developments that happened during the infancy of the commercial suborbital spaceflight industry. The researchers identify the various contenders in the suborbital market and forecast the evolution of the sector. The Suborbital Reusable Vehicle (SRV) demand in eight different markets is characterized and estimated: commercial human spaceflight, basic and applied research, aerospace technology and demonstration, media and public relations, education, satellite deployment, remote sensing, and point to point to transportation. The targeted applications are being served by the launch providers successfully today. Overall, the literature gives a good comparison of various flight providers and applications of commercial suborbital flight. Today, in 2021, two space companies Blue Origin and Virgin Galactic, have gone through the human flight rating of their vehicles. Virgin Galactic successfully completed its first astronaut mission (Unity 22) while this dissertation was being produced, and Blue Origin's first human flight mission was completed on July 20<sup>th</sup>, 2021. Different microgravity test platforms are compared, and their capabilities are listed in Table 1.

Table 1: Comparison of microgravity research opportunities and their capabilities [6]

Platform	Maximum microgravity time	Maximum Altitude (km)	Typical payload mass	Cost
SRV	5 min	110	200 kg	\$500/kg
Sounding rocket	20 min	1600	Few hundred kg	\$1M-\$3.5M
Drop Tower	10 s	N/A	Grams to 500 kg	\$1-\$10/kg per drop
Orbital testing	Days or Years	400 and above	Thousands of kg	\$10k/kg and more

## **2.2. Suborbital Space Vehicles as a Platform for Microgravity Research**

Although commercial suborbital space vehicles were conceived to cater to the space tourism market, the other potential users of this platform are applied science and microgravity research. Most of the suborbital launches that have been completed in recent times are focused on human spaceflight. The researchers [8] provide a comparison between suborbital flight capabilities and other microgravity testing venues such as parabolic aircraft, drop towers, sounding rockets, and orbital launch vehicles.

## **2.3. Payload User Guides**

Every suborbital launch vehicle provider goes through the flight hardware development process and performs many flight tests and simulations. The launch provider characterizes the flight environment of the space vehicle through these simulations, ground tests, and actual flight tests. The launch providers share some relevant results with the payload customers to aid the design and development of the payload experiments. All the general information of the flight vehicle and the payload requirements are shared in a Payload User Guide (PUG). PUG also details the development timeline, test requirements, launch operations, and payload review guidelines. The payload customer must fully understand the scope of the document and all the pertaining information related to their specific payload. The Maximum Predicted Environment (MPE) of flight, acceleration levels, vibration levels, temperatures, mechanical and electrical interfaces are detailed in this document. The payload customer must conduct the tests recommended in the PUG as per the test standards specified. The Blue Origin PUG [9], [10] provides information on the New Shepard space vehicle and pertains to standard payload locker. NanoRacks is the flight integrator offering the

specialized Feather Frame payload locker, and their PUG is tailored to support NanoLab payloads [11]. Finally, the PLD Space's PUG [12] is used to acquire information on the MIURA 1 rocket, and interface details on the single payload bay compartment are used.

#### 2.4. NASA's Flight Experiment Onboard Blue Origin's New Shepard Vehicle

NASA Johnson Space center launched a pathfinder experiment on multiple New Shepard flight missions. The SFEM-2 was flown onboard Blue Origin's New Shepard vehicle's single payload locker. The SFEM-2 was designed to characterize the test environment in suborbital vehicles. The integrated package provided acceleration data, cabin temperature, pressure, carbon dioxide (CO<sub>2</sub>), and sound level measurements. The flight data revealed microgravity levels of  $\pm 0.02$  G for a duration of 2.5 minutes [13]. The cabin thermal control system was active in the final mission, and the temperature sensors recorded a significant difference in the temperature levels between previous and the last flights.

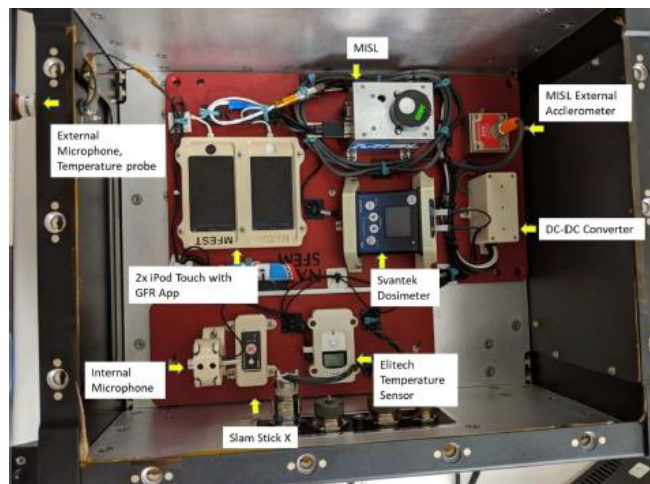


Figure 7: NASA's SFEM-2 payload flown onboard New Shepard's P8 flight mission [13]

#### 2.5. CubeSat Approach

Initially, the CubeSat Program was conceptualized as a tool to help teach students about the process involved in developing, launching, and operating a spacecraft [14].

CubeSat was conceptualized in 1999 by California Polytechnic State University to improve space access to students and university teams. The recent advances in small-scale technologies and commercial off-the-shelf systems along with low-cost rideshare programs developed by NASA enabled these low-cost and rapid development platforms. The new program involved the development of new standards and satellite deployment systems. The mass and volume constraints are analogous to the suborbital payloads, and the technologies developed in the CubeSat architecture have been extensively employed in smaller suborbital payloads. The processes currently utilized by the CubeSat Program evolved by balancing the desires of the CubeSat developers and launch providers with what was realistically possible in an academic environment [14].

## **2.6. Propellant Gauging in Microgravity**

Since 2008, a multidisciplinary undergraduate team from Carthage college has designed and flight-tested a propellant gauging system. The proposed system has been tested in a parabolic flight and subsequently in a suborbital flight. The majority of a spacecraft's mass is propellant, and reducing launch mass is an essential design specification for low-gravity fuel [15]. The payload flown on Blue Origin is documented, and the design considerations for liquid containment are discussed. The research highlights the inadequacies of parabolic flight testing in terms of microgravity duration and quality. The liquid propellant gauging technique uses the modal frequency of liquids in equilibrium, and preliminary CFD analysis shows that the liquids reach equilibrium most of the time in microgravity.

## **2.7. Investigation of MAPMD using Floating Membranes**

Liquid slosh is a common issue observed in applications involving liquids experiencing motion in microgravity. This phenomenon is an essential concern in spacecraft and launches vehicle design. Propellant Management Device (PMDs) are utilized to mitigate slosh in propellant tanks and ensure the positive flow of propellants to the engines. In this research, an active PMD floating membrane device is demonstrated on a slosh testbed. Active membranes limit the rapid motion of the fluid under the influence of external stimuli as they float on top of the liquid surface [16]. Ground testing shows better damping characteristics with the active membrane compared to free slosh cases.

## **2.8. Vibration Testing of Small Satellites**

In a series of papers from 2014 to 2017 [17], Instar engineering has detailed and documented the guidelines and recommendations for vibration testing of small satellites. The guidelines cover the preparation of test objectives and criteria, fixture design and test configurations, low-level sine sweep testing, random vibration testing, and sine-burst testing. The primary test criteria are the comparison of the FRF responses between each major vibration test. Such criteria should apply only to the modes showing the highest response acceleration in a given test, using the accelerometer channels that show the highest response for those modes [17]. Small changes between pre- and post-test sine-sweep data, such as from localized yielding in fastened joints or slight loss of fastener preload, are unavoidable in many structures and usually are not detrimental [17]. The guidelines are based on commonly used test standards utilized by the spaceflight industry in-flight hardware testing.

## **2.9. Model Rocket Projects**

Model rocketry is a scaled-down hands-on approach to understanding the development and operational difficulties encountered during a launch vehicle development. In 2015, students from the Catholic University of America conducted research [18] to develop and launch a model rocket as part of their “Aerospace Design” course. Flight trajectories were derived from simulations and experimental testing. Equations of motion and drag equation were used to estimate the launch angle to optimize the landing location of the rocket body. The wind velocity profile model was incorporated into the calculations to estimate launch angles and supplemented by wind speed measurements.

## **2.10. Summary**

Suborbital rocket launches have been prevalent during the early 1960s and are usually carried out by every space organization while developing new launch systems. However, these launches have become more accessible to the aerospace industry and university students through commercial SRV launch opportunities. The current focus on utilizing this capability is conducting human spaceflight, microgravity research, technology demonstrations, and pathfinder missions. Throughout the history of payload development, the aim has been to miniaturize space systems to save launch mass and cost. This goal has been achieved with developments in technology and the utilization of commercial-off-the-shelf hardware that is readily available nowadays. The development of suborbital payloads requires the assimilation of the payload environment and the launch provider's compliance requirements. Previous research has proven the successful implementation of suborbital payloads containing liquids. A technology demonstration of

a new slosh mitigation device called MAPMD was performed in parabolic flights, increasing the TRL to 5. Ground tests and preliminary CFD models of a propellant gauging system were performed, showing that the short parabolic flight time was insufficient for the liquid to reach equilibrium. The current trend in model rocketry conducted by University teams focuses on improving the performance of the rockets to compete in rocket launch competitions.

### **2.11. Research Contribution**

The commercial suborbital reusable vehicle is a niche market offering access to space for microgravity research and technology demonstrations. Current suborbital payloads launched by universities and the aerospace industry strive to utilize this opportunity; however, the development process and the lessons are not adequately communicated. The available literature focuses only on the payload experiment's hypotheses and its outcomes. The development process and the procedures performed to validate the compliance of these payloads to launch provider's requirements are not documented clearly. The research aims at bridging this gap through a streamlined approach, integrating all the aspects of suborbital payload design, development, and testing.

Biomedical space research, studying the effects of long-duration exposure to the space environment, has been investigated since the dawn of human spaceflight (12<sup>th</sup> April 1961) [19]. Further understanding of this field is required to support upcoming long-duration missions to Mars and the Moon. Commercial suborbital platforms offer a unique opportunity to conduct such biomedical space experiments. This type of payload requires special considerations on harsh vibration, thermal, acceleration, and stressors related to a rocket launch to ensure the survival of live organisms. The flight hardware was designed



and developed using multidisciplinary engineering tools to carry the biomedical experiments in small containments called NanoLabs. These NanoLabs served as the life support system and provided a safe environment for these biological systems through launch, flight, and recovery. The payload design techniques focused on improving the payload volume utilization, and mass optimization tools were used to reduce the overall mass of the payload housing, increasing payload capacity. A single payload containing T-cells and a dual payload containing Zebrafish and Spirulina was launched onboard Blue Origin's New Shepard vehicle.

An upcoming suborbital mission onboard PLD Space's MIURA 1 rocket will carry four payloads: slosh mitigation through technology demonstration of MAPMD, In-vitro cancer experiment, Cerebrospinal fluid shunt experiment, and avionics/telemetry system. This research will contribute towards the improvement of TRL progress for a slosh mitigation device that has been developed at ERAU. A CFD approach and a novel methodology have been developed to simulate the behavior of liquids and a floating membrane in microgravity conditions using multiphase fluid modeling, overset mesh, and DFBI motion. A general vibration test methodology for ensuring the compliance of suborbital payloads has been developed. The test campaign helped highlight essential modifications that were required to payload structures. The vibration test plans will aid future payload researchers in conducting payload testing on the shaker table.

The flight-proven hardware could be used as a commercial product and used as a COTS kit. Future payload customers could use this hardware to fly their payloads on commercial suborbital missions. The approach created in this paper could save time, money, and effort for future payload researchers and members of the aerospace industry.

Model rocketry has been used to develop in-house rockets to carry specially prepared payloads, enabling future students to get hands-on experience fabricating and launching payloads. This capability is used to test future suborbital payloads before the main launch, thereby offering opportunities to modify the design and identify issues before the actual flight. A payload research facility was established at ERAU to support current and future research on payloads. This research builds ERAU's suborbital payload heritage and acts as a precursor to possible future orbital missions.

The novelty of this research effort is a) The design, development, and the achievement of mission goals of sophisticated bioscience experiments with unique requirements involving T-cells, zebrafish, and Spirulina which is a first on suborbital payloads, b) Characterization of the flight environment in the first commercial missions of Blue Origin's New Shepard vehicle and PLD Space's MIURA 1 rocket, c) Creation of a streamlined suborbital payload development process, and a flight-proven sensor and NanoLab hardware kit which will save time, effort and money for future payload researchers and users in the aerospace industry, d) A CFD approach capturing the motion of a DFBI body suspended in a multiphase fluid in microgravity using overset mesh, e) Documentation of test procedures and test criteria for vibration testing suborbital payloads suitable for MIURA 1 rocket and other suborbital launch systems, and f) Usage of model rocketry to launch student payloads and primarily function as a payload research and testing platform for future suborbital payloads.

### 3. CRExIM Payload

The Arete STEM project provided researchers at Embry-Riddle Aeronautical University (ERAU) with the opportunity to launch a science research experiment onboard Blue Origin's New Shepard launch vehicle. Cell Research Experiment In Microgravity (CRExIM) payload will be flown to an expected altitude of approximately 328,000 feet (100 km) and experience continuous microgravity for roughly 3 to 4 minutes during its suborbital flight. After completing the suborbital flight, the capsule containing the payload flies back to the landing zone and performs a rocket-powered vertical landing. Parachutes and retro thrusters are used to assist reentry and reduce landing loads. The whole mission is expected to last for 11 minutes. Depending on the landing area location and environmental conditions, the payload could be recovered within a few hours of landing.

*Scientific Objective:* Suborbital flights offer a convenient microgravity research platform. There is experimental evidence suggesting that microgravity alters the cellular processes of immune cells. Previous studies [20] investigating micro-gravity effects on the immune system demonstrated various alterations in Murine and human cells, such as apoptosis, changes in proliferation, and cytokine production. Although our understanding of the micro-gravity effect on the immune system is expanding, the molecular pathways mediating this effect have not been completely understood [21]. The scientific goal of this study is to investigate the effect of microgravity on Murine immune cells during the suborbital flight. We used three experimental conditions: 1) cells primed with the cytokine IL-2; 2) cells primed with the cytokine IL-12, and 3) control cells not primed with any cytokines. These cytokines play a critical role in cell immunity and enhance

immune cells' behavior in a very short period. Therefore, it is hypothesized that the difference in cellular processes could be evident during the short suborbital flight.

Furthermore, the shorter duration of the flight would permit a quick assessment of payloads before and after the flight. The biological science experiment is developed and investigated by the University of Texas Health Science Center at San Antonio (UTHSCSA) and the Medical University of South Carolina (MUSC). The payload development is carried out as a collaboration between UTHSCSA, MUSC, and ERAU. Researchers at ERAU carried out the engineering development and payload operations, and the science payload involving murine T cells was processed pre and post-flight at UTHSCA's medical laboratories.

Novel payload design, computational analysis, and experimental testing is necessary to fulfill the mission requirements of the payload while adhering to the technical requirements of the flight system. Computational methods are powerful tools that can be used to test and develop engineering solutions that aid in achieving the design objectives quickly and efficiently. CAD, FEA, and CFD applications simulate the conditions experienced by the payload in flight and accordingly help with the payload design. Detailed specifications of the flight envelopes and cabin environments are available in the Payload User Guide (PUG) provided by the launch provider [9]. The data in the PUG is used to simulate the flight environment using computational simulations.

### **3.1. Payload Design**

CRExIM consists of eight Eppendorf 5.0 mL tubes containing immune T cells primed with different cytokines in each tube suspended in a nutrient-rich medium. The weight of each Eppendorf tube is approximately 7.7 g. The payload also consists of an EDL-XYZ

data logger device that records accelerations in X, Y, and Z directions, temperature, and relative humidity. The data logger records vital parameters of the payload environment and is used to track the various phases of the mission. The role of the payload containment structure is to safely house and secure the Eppendorf tubes and the data logger while conforming to both the launch provider's requirements and the flight environment.

The first requirement of the NanoLab structure is to geometrically conform to the dimensions of a NanoRacks's payload locker [11]. NanoRacks provides the lockers to integrate REM payloads in the Blue Origin's New Shepard launch vehicle. This payload locker is capable of housing a NanoLab of a 2 Unit (2U) form factor. The NanoLab is designed following the above dimensions with allowable tolerances, as shown in Table 2. Initially, the design plan was directed towards reducing the mass of the housing structure to increase the available payload mass. The preliminary NanoLab design incorporated holes, similar to a frame-only structure. However, this design feature had to be changed due to constraints set by the flight provider. All the high-level payload requirements are derived from Table 2 based on the information in PUG [9].

Table 2: Payload requirements and launch profile characteristics

Requirement	Value
Size (mm)	2U: 100 (L) x100 (W) x 200 (H)
Mass (kg)	0.499
Power supply (V)	5.0 (USB)
Microgravity time (minutes)	3 - 4
Maximum acceleration loads (G)	15
T-cells Eppendorf tubes	6-12
Liquid containment	Two levels

One of the primary requirements of the flight provider is the containment of the contents inside the payload. In the event of a fluid leak, the containment ensures that other payloads in the vehicle are not affected. With this requisite, the first NanoLab design was developed with an encapsulated structure to provide a high level of liquid containment. However, the outer skin structure comes with an added mass, and the outer skin should be as thin as possible. The thin outer skin is reinforced with trusses that help strengthen the NanoLab by evenly distributing the loads on the structure. The NanoLab design developed in the first iteration with the above considerations is denoted as the Initial model. The Initial model is shown in Figure 8. A push and lock lid mechanism is designed for payload experiment access from the top of the NanoLab. The lid is secured to the housing section of the NanoLab using underwater tape to ensure liquid containment.

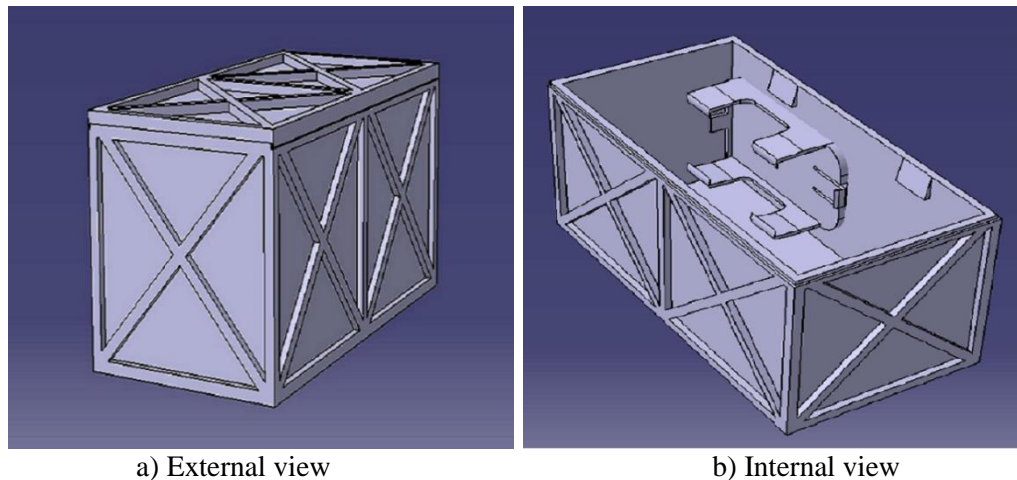


Figure 8: CAD of the payload housing structure (Initial model)

The initial design was further revised to accommodate polycarbonate standoffs which are part of the payload installation into the payload lockers. The standoffs are small rectangular pads glued over the payload housing before integration into the launch

vehicle. These standoffs provide the necessary damping for the payloads in contact and ensure a tight fit inside the payload locker. The initial model consisted of trusses on the outside, which provided a minimum surface area for installing the polycarbonate standoffs. Therefore, the following design was developed with the skin section on the outside and the truss section inside the NanoLab. This design will be denoted as the “Updated model” henceforth. The Updated model is shown in Figure 9.

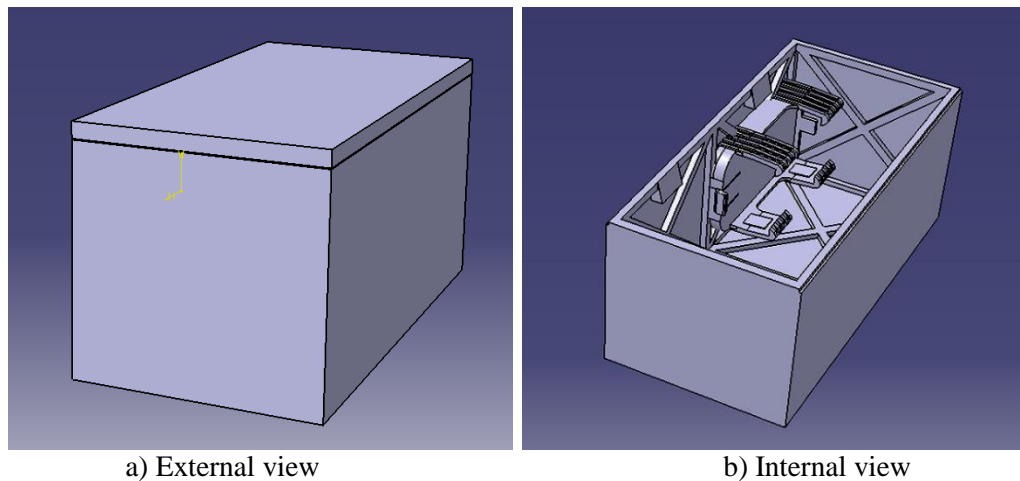


Figure 9: CAD of the payload housing structure (Updated model)

The CAD models are developed using CATIA V5. The NanoLab designs are developed after performing various analyses, which will be discussed in the following sections. The CAD model of the holder for the EDL-XYZ device is developed following the instrument’s dimensions. The lid, bottom section, and the device holder are assembled into the final CAD model.

### 3.2. FEA with Acceleration Loads

A structural analysis is performed on the NanoLab using ANSYS “Static structural” module [22]. The acceleration loads (G loads) experienced by the NanoLab in flight are simulated on the payload structure.

The CAD design of the NanoLab is imported into the ANSYS “Design Modeler” and is converted to a Finite Element Model (FEM) by creating a mesh on the model. A “Hex dominant mesh” method is used to develop a structured mesh on the model. A “zero displacement” boundary condition is applied on all the outer faces of the NanoLab, which constrains the NanoLab as though it were placed inside a payload locker. Three separate cases are analyzed where a 15 G acceleration load is applied on the whole body in three different directions. 15 G load is used to simulate an off-nominal case of a single parachute failure landing. The load applied is approximately twice that of the maximum G-load experienced in a nominal mission. The results from this analysis are used to identify the deformations and the stresses on the NanoLab structure, which pinpoints weak areas that may need improvement. The mesh on the payload structure is shown in Figure 10, and the applied boundary conditions are shown in Figure 11.

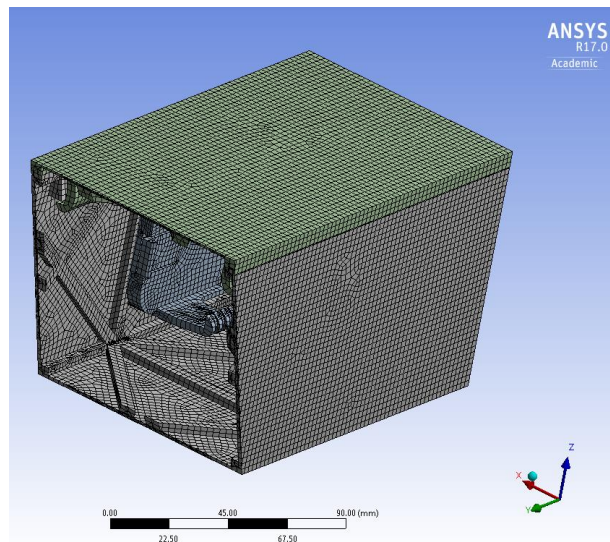


Figure 10: Structural mesh of CRExIM NanoLab

One of the main goals of performing this analysis is to test various 3D printing materials before printing the actual model. The different materials analyzed in this research are ABS, PLA, and CFRP. These materials are commonly used in 3D printing



applications and are readily available for purchase. The structural analysis can be performed for different materials using the same analysis setup in ANSYS. The material properties are obtained from the Material Data Sheet (MDS) found on the databases of the PLA, ABS [23] and CFRP-ABS [24] filament manufacturers. The collected material data is entered in the Engineering Data node inside the ANSYS structural module. Separate simulations are performed for each material and the material data for each material is shown in Table 3.

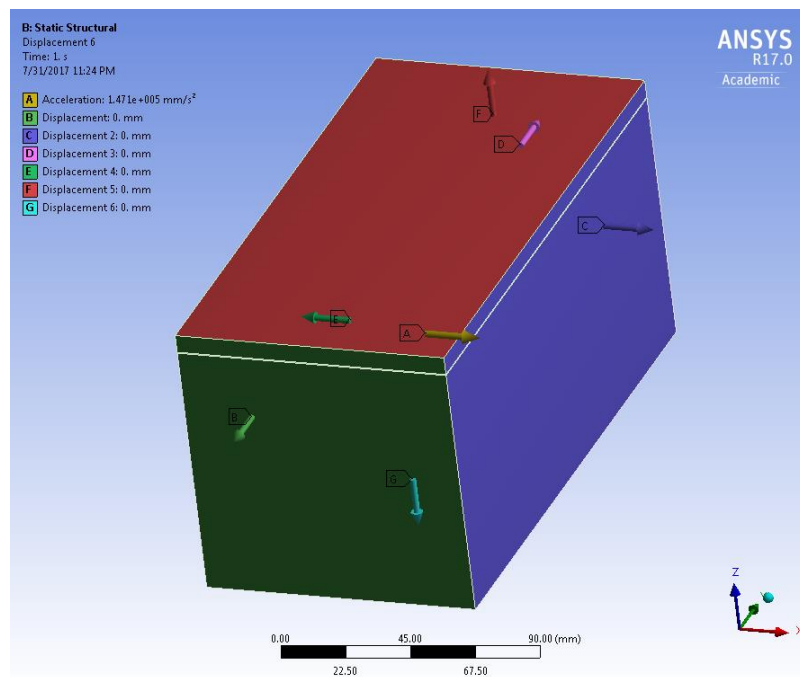


Figure 11: Boundary conditions

Table 3: Material properties

Material property	ABS	PLA	CFRP (ABS)
Density ( $\text{g/cm}^3$ )	1.04	1.3	1.11
Young's Modulus (Mpa)	2137.4	3500	4018
Poisson's Ratio	0.35	0.36	0.35
Tensile Yield Strength (Mpa)	34	46.8	44
Compressive Yield Strength (Mpa)	7.6	17.9	NA

### 3.3. Random Vibration Analysis

The vibration environment [9] specified by the flight provider is simulated on the payload structure using the “Random Vibration” module in ANSYS. A modal analysis is a prerequisite for random vibration analysis in ANSYS and is a powerful tool in predicting a system's natural frequencies and mode shapes. Therefore, the diagnostics in this section are vital in the survivability of the NanoLab in a vibration environment. ANSYS uses the data from the modal analysis to calculate the requested outputs in the random vibration analysis. Random vibration analysis is used to ensure that the stresses and deformations lie within permissible limits [25]. The applied random vibration profile is in the frequency domain. However, generating the same profile in a time domain is difficult which could be directly used to excite the structure. Therefore, ANSYS uses a statistical approach to predict how the structure would react to a random vibration excitation.

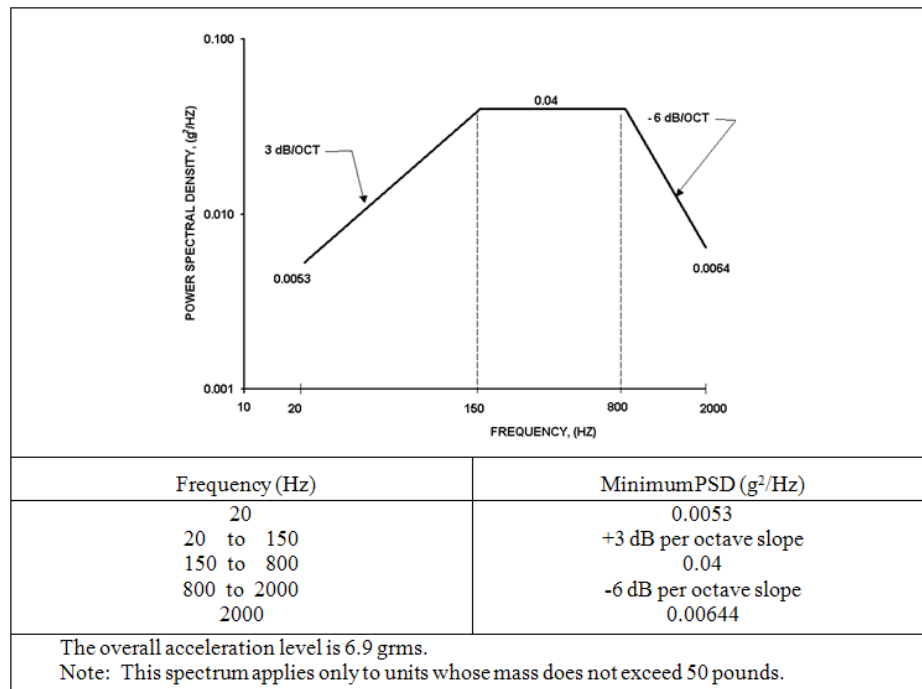


Figure 12: Simulated random vibration profile

The random vibration excitation is applied as a “PSD G Acceleration in ANSYS” in three separate cases (X, Y, or Z-Axis direction for each case). The simulated random vibration profile is shown in Figure 12.

### **3.4. Mass Optimization**

The maximum allowable mass of the payload is 0.499 kg. This critical requirement plays a significant role in the design of the NanoLab. Since the payload mass and the data logger are unalterable, the only room for a design change is in the payload housing structure. Reducing the structure's mass by incorporating material removal and structural redesign is the steps to accomplish the above goal. However, constraints that control the optimization process need to be identified and enforced to ensure that the design changes do not violate the safety envelopes of the system.

Direct optimization module in ANSYS is used to perform the mass optimization study in this research. Direct optimization works by comparing numerous designs that are governed by the geometric parameters of the structure. Direct optimization algorithm seeks for solution of the desired objective while enforcing the constraints specified by the user. In summary, this tool helps in reducing a user’s effort in running multiple simulations of different designs to obtain an optimal solution.

The CAD model of the NanoLab is constructed with design parameters that control the dimensions of critical geometries in the model. The parameters used here are the width of the horizontal and the vertical truss sections, the width of the diagonal truss sections, and the width of the outer skin or casing. These parameters are chosen based on their significance as crucial structural members making up the NanoLab assembly. These

parameters also affect the mass and stress distribution in the design more than other components.

The objective of the optimization is set to minimize the mass of the NanoLab structure. The same modules in ANSYS from the previous sections are used to derive results for the optimization. Maximum stress calculated in the G loading analysis and the X, Y and Z deformations calculated in the random vibration analysis is used as inputs for the constraints in the optimization. The parameters and constraints that are specified in this analysis are shown in Table 3.

Table 4: Mass optimization variables

Parameter name	Description	Parameter type	Value	Units
P1 - cube: DS Beam	Width of Horizontal and Vertical trusses	Design parameter	$3 < P1 < 10$	mm
P2 - cube: DS XFrame	Width of Diagonal trusses	Design parameter	$3 < P2 < 10$	mm
P3 - cube: DS Skin	Thickness of enclosure	Design parameter	$0.5 < P3 < 3$	mm
P4 – Maximum Equivalent Stress	Static structural analysis	Constraint	$P4 < 1$	MPa
P5 – Maximum X deformation	Random vibration analysis	Constraint	$P5 < 0.1$	mm
P6 - Maximum Y deformation	Random vibration analysis	Constraint	$P6 < 0.001$	mm
P7 - Maximum Z deformation	Random vibration analysis	Constraint	$P7 < 0.1$	mm
P8 - Geometry Mass	Total mass of the cube structure	Objective	Minimize	kg

A total of 120 design points is generated and analyzed. Five optimal design candidates are selected from the optimization study. Charts displaying trade-offs of various parameters, parameter sensitivities, and parameter histories are post-processed. An overall schematic of the ANSYS setup is shown in Appendix B.

### **3.5. Cell Vials Slosh Testing Using CFD**

Liquid slosh is an important phenomenon that affects any fluid in a vibration environment. The effects of liquid slosh forces on T cells will open new research pathways in future studies involving T cells in the space environment. Therefore, the results of this analysis could provide the groundwork for future payloads involving T cells. A CFD analysis is performed in STAR-CCM+ [26] to simulate the vibrations on the fluid inside the Eppendorf tubes to observe and track the slosh mechanics.

The 5.0 mL Eppendorf tube is modeled in CATIA V5 after carefully measuring its geometric dimensions. The CAD model is imported to the STAR-CCM+ environment, and the model surfaces are prepared and named appropriately to describe the domain of the fluid analysis. It is to be noted that the volume contained inside the Eppendorf tube is considered to be the fluid domain (liquid column and air volume), and therefore, only the fluid volume is extracted from the Eppendorf tube model and used in the analysis. The tube surfaces are specified as wall boundaries without any mass entering or leaving the system in conjunction with a sealed tube system.

A volume mesh is generated on the model using the “Part mesh” operation in STAR-CCM+. Various meshing models were tested, and the mesh was finalized based on solution convergence, solution time, and wall  $y^+$  values, which will be discussed further in future sections. The “Trimmer” mesh model is utilized for the volume mesh and

“Prism layer meshing,” used to resolve the fluid-wall boundary layer. Given the small scale of the model, a stringent mesh control and a high-resolution mesh is required to obtain accurate results. Higher mesh standards require more time in generating the mesh and solving the model. Therefore, to reduce mesh size while retaining good quality, a “volumetric control” is applied to areas of interest, and a low-resolution meshing is used elsewhere. After running simulations to convergence, multiple mesh cases were analyzed and compared, and a final mesh was selected with 7.5 million cells. The final mesh is shown in Figure 6, along with the CAD model and the CFD domain. The tube walls are divided into multiple sections to apply focused mesh refinement criteria.

Eulerian Multiphase and Volume of Fraction models simulate the liquid and the gas phases in this analysis. The non-homogeneous nature of the cell medium makes it difficult to estimate its liquid properties. Therefore, the liquid properties of water are utilized in the liquid phase of the analysis. The properties of air at standard atmospheric conditions are specified in the gas phase of this analysis. Phase interaction between air and water is specified in surface tension as 71.99 mN/m. The CAD model is designed in a specific orientation to ensure that the initial location of the two phases is distinguishable by the XY plane [27] at the 5.0 mL mark of the Eppendorf tube. This distinction is specified in the CFD environment as an initial condition by specifying the volume inside the tube below the XY plane as water and above the XY plane as air.

The fluid turbulence is solved using the k-epsilon turbulence model, and the flow is solved using the Reynolds-Averaged Navier-Stokes model. The G values are specified in the gravity node to simulate 1 G and microgravity scenarios. A Simple Harmonic Motion (SHM) is applied to the body instead of a random vibration profile. SHM is used instead

of a random vibration excitation due to the complications of generating a random vibration excitation. An "Implicit Unsteady" time scheme is used with a time step of 0.001 s, and each simulation is executed for a total time of 1 s. Six sub-iterations are solved under each step to reach convergence between time steps. The required reports, plots, and scenes are set up to display the liquid slosh and track the fluid force on the walls of the tube.

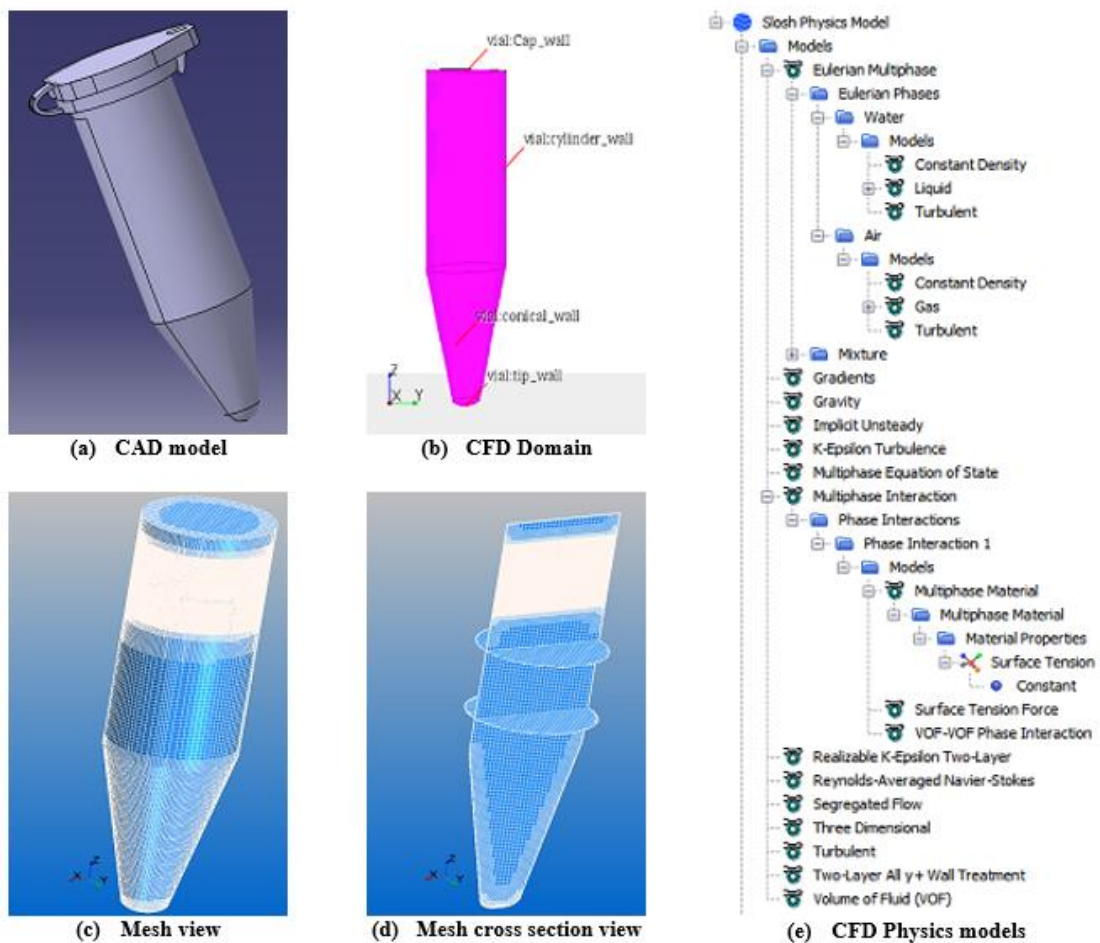


Figure 13: CFD setup

The initial conditions and the boundary conditions applied in the CFD simulation are listed below:

- Eulerian Multiphase model with 2 phases: water as liquid and air as gas

- The surface tension of water is 0.074 N/m
- Location of fluid phases: fluid volume above 5 mL mark (XY plane) is gas, and fluid volume below 5 mL mark is liquid
- A no-slip wall boundary condition is applied to all the fluid boundaries
- Acceleration due to gravity is applied in the negative Z-direction (1 G or 0.005 G depending on the simulated scenario)
- Velocity profile of the SHM motion is applied as a translation motion to the whole domain

### **3.6. 3D Printing**

There are multiple advantages of 3D printing a structure rather than fabricating one. One such advantage is that the design can be more readily customized. 3D printing enables the use of CAD software to have any additional pieces built directly into the print. This property reduces the need for assembly of parts post prototyping. Another significant advantage obtained from this technology is replicating the same part using alternate 3D printing materials. This facilitates rapid testing and comparison between these standard 3D printing filaments. The materials are usually light and possess structural characteristics that could be used beneficially in various applications. The payload housing NanoLab is 3D printed using the MakerBot Replicator 2X printer. MakerBot Replicator 2X printer uses the Fused Filament Fabrication (FFF) method, where a plastic 3D printer filament is heated and extruded through a nozzle, layer by layer, on a heated surface. The printer's filament spools are mounted on the 3D printer frame through an attachment on the backside of the printer. Initially, the filament is manually fed into the extruder until the winding motor in the extruder takes over, and the



filament is automatically fed according to the print requirement. The print bed is leveled before the print job is initiated, and the print surface is cleaned and prepared as per the instructions in the user manual [28].

MakerBot MakerWare software is utilized to process the CAD into a recognizable format for the 3D printer. MakerWare has also been used to set up the specifications of the print job. Before importing the CAD file to the 3D printer software, it is converted to STL Rapid Prototyping format in CATIA V5. The 3D printer software enables visualization, location adjustment, and prototype orientation printed on the print bed.

One of the main parameters in 3D printing is infill density, which defines the amount of material inside the print. An infill density of 100% means the printed object is completely solid, and any lesser value means only that a certain percentage is filled with material. A hexagon-shaped infill pattern was used for its higher structural strength and higher print speed characteristics. These honeycomb-shaped infill members provide beneficial structural characteristics. A high percentage of infill is not recommended as it increases the mass of the printed object, and it requires large amounts of printer filament. The FFF method prints layer upon layer, and therefore it requires a base layer to print on. So, in the case of overhanging or inclined geometry such as the X frames in our model, support structures are needed to print the layers at these locations. The MakerBot software can apply support structures, and bridges easily removed from the 3D printed NanoLabs.

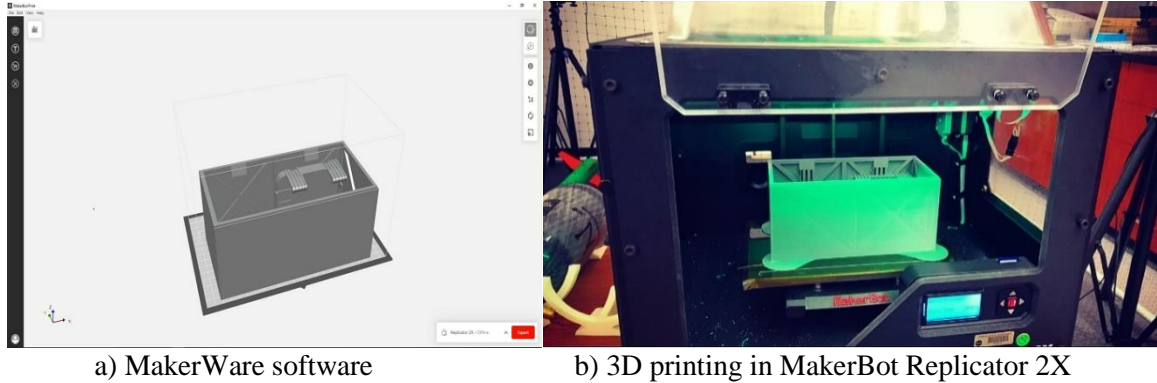


Figure 14: 3D printing the NanoLab structure

### 3.7. Results

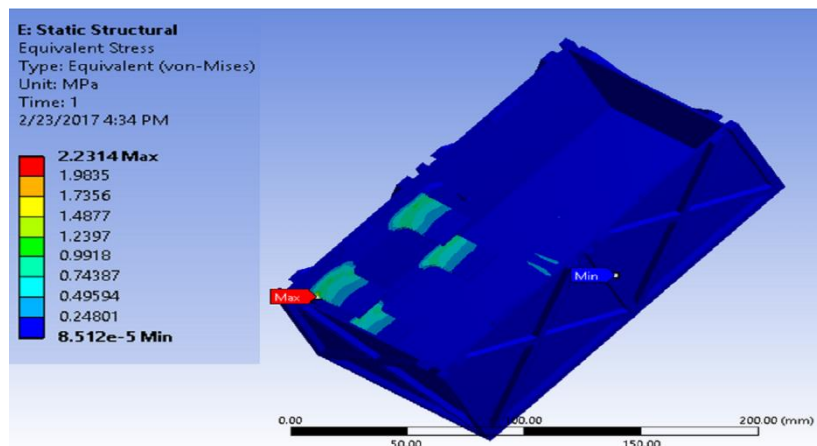
The results of the CRExIM payload development, testing, and flight are furnished in the following sections. The result subsections are organized in the same sequence as the previous methodology section.

#### 3.7.1 Structural Analysis with Acceleration Loads

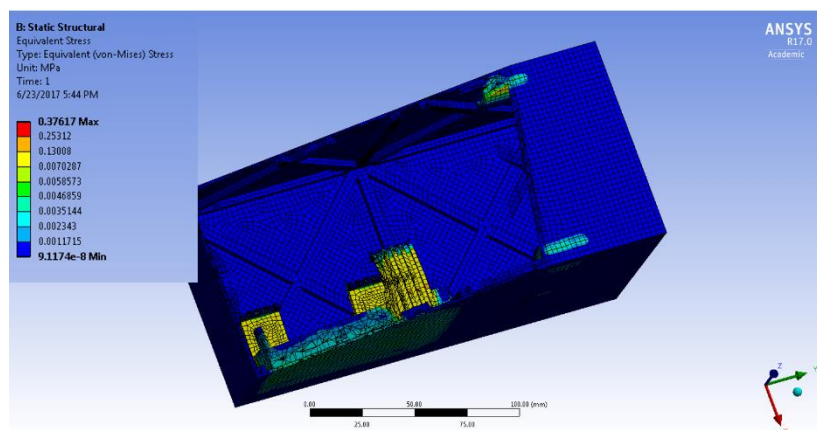
The results obtained in the FEA structural analysis are shown in Figure 15. A detailed representation of the FEA results is shown in

Table 5. The results are used to alter the design of the NanoLab and reinforce the structure on the identified critical areas of higher stress distribution.

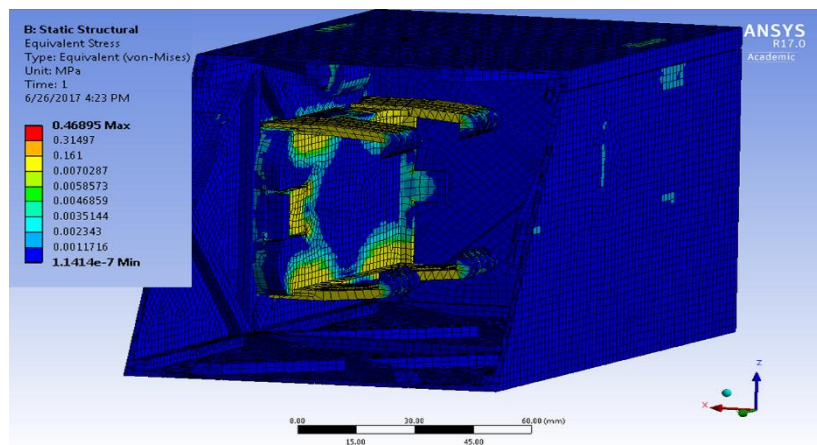
It is observed that the highest deformations in the NanoLab are on the device holder flaps and the lid lock flaps. The lid is secured to the bottom section of the NanoLab using a strong adhesive tape, and the experienced stresses at this location are therefore not an issue. However, the design of the device holder area is improved by reinforcing the holder flaps with additional material.



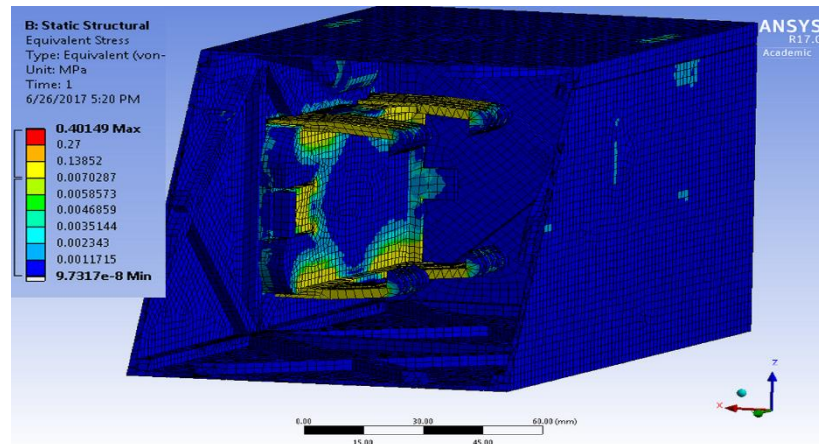
a) Initial model (ABS)



b) Updated model (ABS)



c) Updated model (PLA)



d) Updated model (CFRP)

Figure 15: Equivalent stress distribution with acceleration load applied in the positive Z direction.

Table 5: FEA results of the NanoLab structure

Direction of applied acceleration	Simulated material and model	Maximum equivalent stress (MPa)	Maximum total deformation (e-5 mm)
Positive X direction	ABS (Initial model)	0.5503	8.61
	ABS (Updated model)	0.0865	594.31
	PLA (Updated model)	0.1078	451.94
	CFRP (Updated model)	0.0923	337.42
Positive Y direction	ABS (Initial model)	1.1143	71.97
	ABS (Updated model)	0.1253	60.96
	PLA (Updated model)	0.1554	46.70
	CFRP (Updated model)	0.1337	34.61
Positive Z direction	ABS (Initial model)	2.2314	184.70
	ABS (Updated model)	0.3762	963.76
	PLA (Updated model)	0.4690	733.51
	CFRP (Updated model)	0.4015	547.18

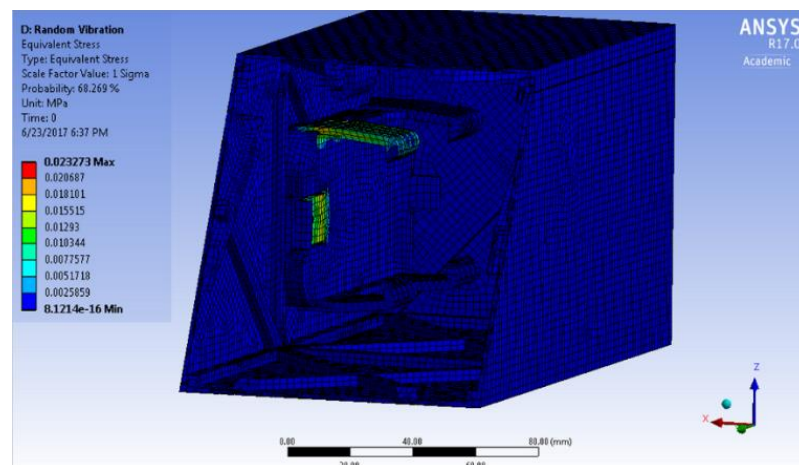
### 3.7.2 Modal and Random Vibration Analysis

The modal analysis results for the different materials and models used in this research are summarized in Table 6.

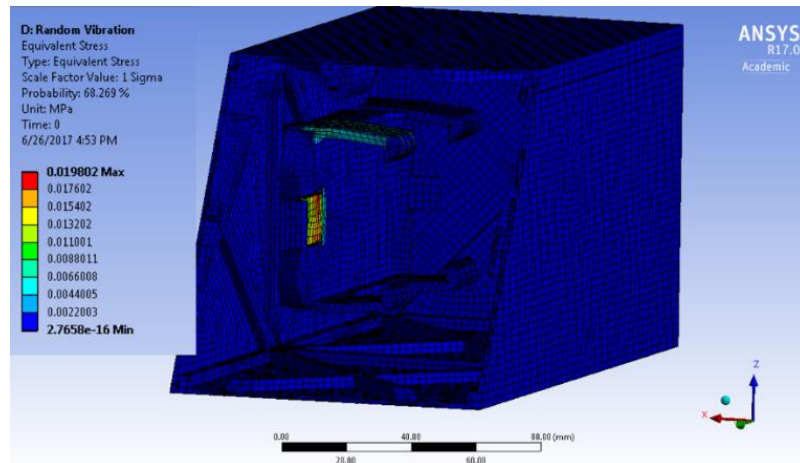
Table 6: Modal analysis of the NanoLab structure

Simulated material and model	Mode 1 (Hz)	Mode 2 (Hz)	Mode 3 (Hz)	Mode 4 (Hz)	Mode 5 (Hz)	Mode 6 (Hz)
ABS (Initial model)	2217.1	2234.7	2258.3	2284.5	2806.6	6518.4
ABS (Updated model)	754.5	757.4	765.9	766.8	943.9	1897.0
PLA (Updated model)	864.7	868.0	877.5	878.5	1082.5	2166.3
CFRP (Updated model)	1001.2	1005.1	1016.4	1017.5	1252.7	2517.5

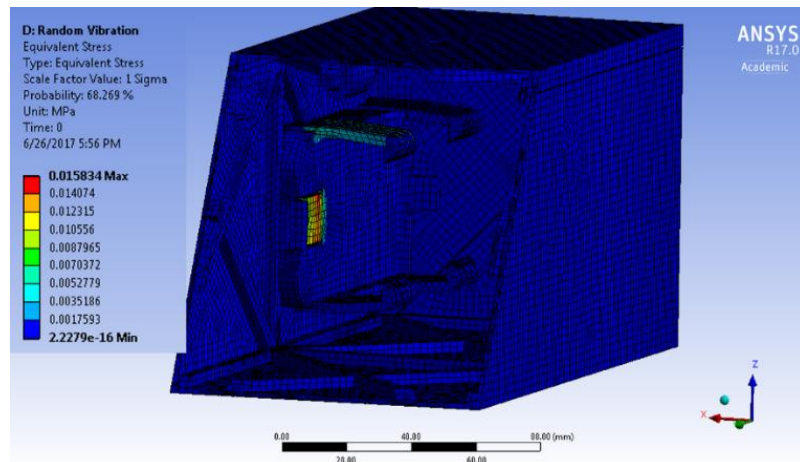
The random vibration analysis results are shown in Figure 9 and summarized in Table 7.



a) ABS case



b) PLA case



c) CRPF case

Figure 16: Equivalent stress results with random vibration spectrum applied in the Y direction

The modal analysis is a crucial tool in payload design to compare the natural frequencies of the system with the vibration frequencies of the flight environment. The obtained results show that the natural frequencies of the payload structure do not match with the vibration frequencies experienced in flight. Therefore, it is concluded that the NanoLab is safe from damage due to resonance. Random Vibration analysis shows that the maximum stress is in the device holder location. It is to be noted that the random vibration analysis performed is a statistical approximation, and no actual excitation is applied.

Table 7: Random vibration analysis results of the NanoLab structure

Direction of applied random vibration excitation	Simulated material and model	Maximum equivalent stress (MPa)	Maximum total deformation		
			X (e-5mm)	Y (e-5mm)	Z (e-5mm)
Positive X direction	ABS (Initial model)	0.5349	3.81	1.04	4.00
	ABS (Updated model)	0.2491	1823.80	492.87	347.48
	PLA (Updated model)	0.2907	1299.30	351.33	263.07
	CFRP (Updated model)	0.2326	905.93	244.82	183.33
Positive Y direction	ABS (Initial model)	0.0021	1.46	401	4.50
	ABS (Updated model)	0.0233	124.18	70.12	103.10
	PLA (Updated model)	0.0198	88.51	23.93	25.59
	CFRP (Updated model)	0.0158	61.68	16.67	15.67
Positive Z direction	ABS (Initial model)	2.1279	2.30	1.42	7.73
	ABS (Updated model)	1.1584	1203.70	46.87	3133.50
	PLA (Updated model)	1.4165	911.96	35.97	2372.90
	CFRP (Updated model)	1.1322	635.24	24.73	1653.70

### 3.7.3 Structural Design Optimization

One hundred design points were created and analyzed in the ANSYS Direct Optimization module. Out of the 100 optimization runs, 97 runs ran successfully, and 3 runs failed due to a mesh generation failure. Design parameters were changed at each design point, and the values for the outputs were computed under the Static Structural and Random Vibration modules.

The tradeoff charts in Figure 10 show the feasible design space. The green-colored points fall within feasible design space. These design points are further compared to obtain the optimal design candidates. The infeasible points fall out of the design space and violate the constraints, and thus are disregarded.

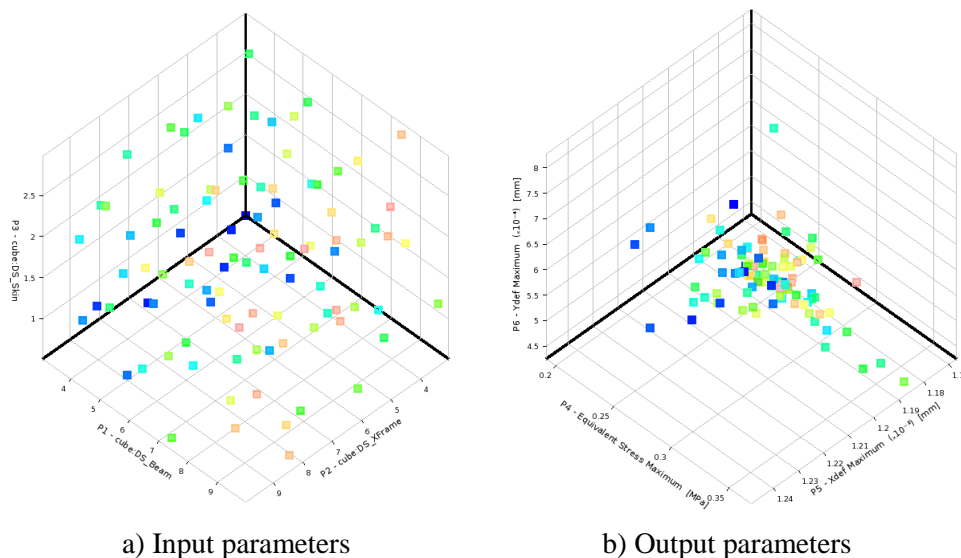


Figure 17: Optimization parameter tradeoff charts

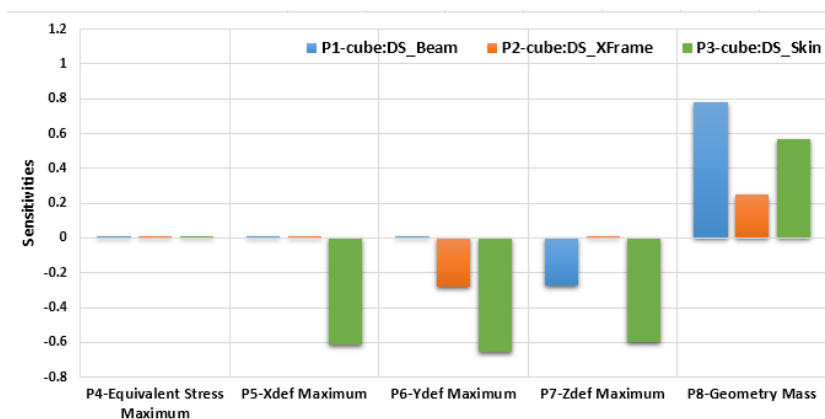


Figure 18: Parameter sensitivities

The parameter sensitivity chart in Figure 18 depicts the significance of each design parameter on the calculated outputs. This plot is used to identify the significance of each parameter in the design of a system, and it is observed that the width of the horizontal and vertical bars has the most influence on the NanoLab total mass.



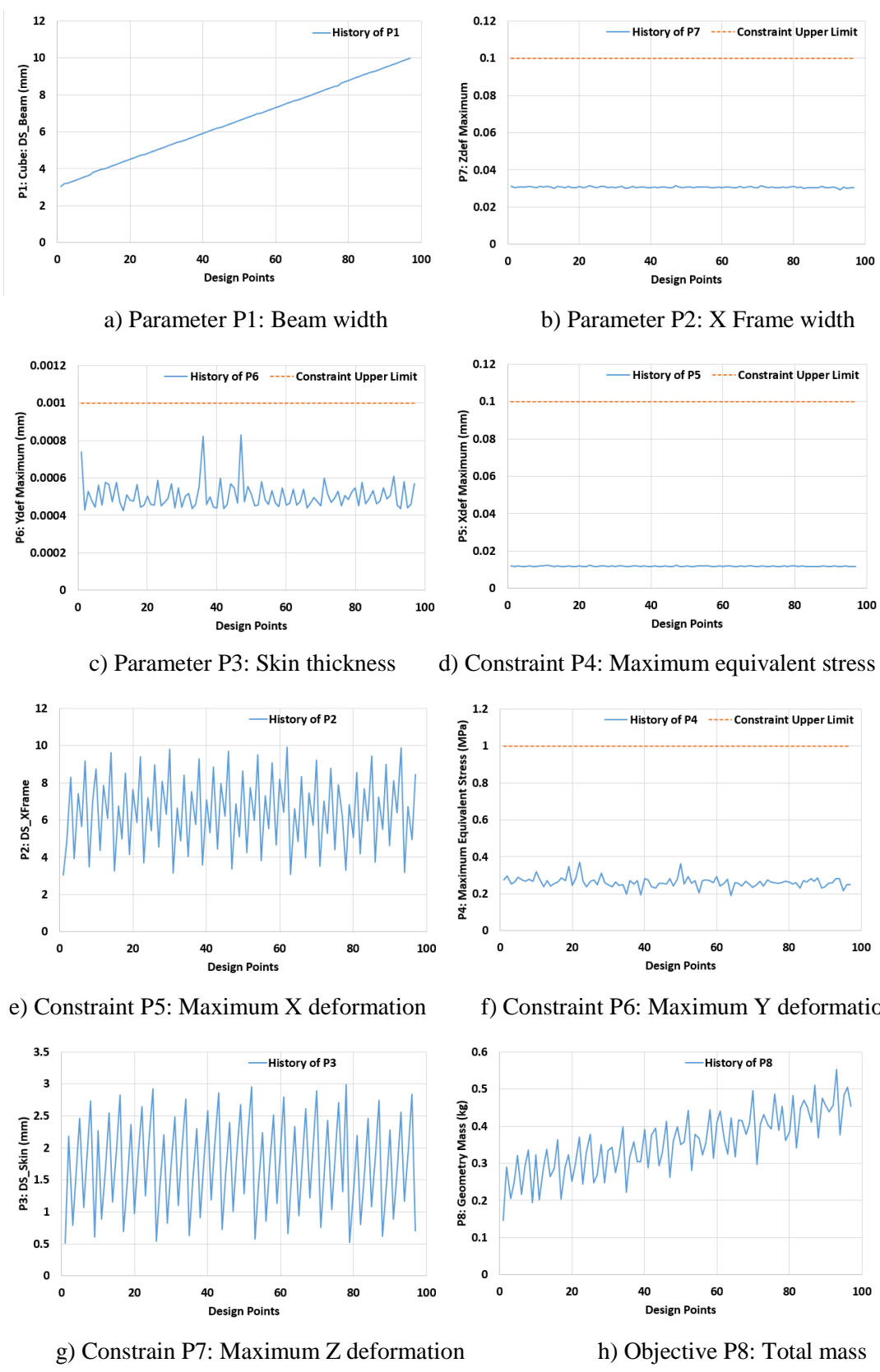


Figure 19: Recorded optimization parameter histories

Table 8: Optimization results

Parameter name	Candidate	Candidate	Candidate	Candidate	Candidate
	point 1	point 2	point 3	point 4	point 5
Number of optimization rank stars	1	1	2	3	2
P1 - cube:DS Beam (mm)	3.035	3.665	3.875	4.295	3.245
P2 - cube:DS XFrame (mm)	3.035	6.973	4.348	5.004	8.285
P3 - cube:DS Skin (mm)	0.513	0.605	0.883	0.698	0.790
P4 - Equivalent Stress Maximum (MPa)	0.276	0.268	0.278	0.287	0.254
P5 - Xdef Maximum (e-5mm)	1210	1200	1230	1200	1190
P6 - Ydef Maximum (e-5mm)	73.88	56.49	57.55	56.35	52.99
P7 - Zdef Maximum (e-5mm)	3110	3110	3131	3130	3076
P8 - Geometry Mass (kg)	0.1467	0.1951	0.2023	0.2030	0.2049

The parameter history charts in Figure 19 show the variation of each parameter throughout the optimization analysis. The change in the value of each parameter at each design point is governed by the optimizer algorithm and is usually directed to reach the optimum output as quickly as possible. Finally, five candidate points are computed as listed in Table 8. The candidate point with the greatest number of optimization rank stars is the most optimum design. Therefore, it is observed that Candidate point 4 is the most optimal design for this optimization study. The mass of the baseline design was 0.3277 kg, and the mass of the optimum design candidate is 0.2030 kg. Therefore, a mass reduction of 38% is achieved using the optimization tools in ANSYS.

### 3.7.4 Cell Vials Slosh Analysis

The final mesh with the required refinement of 7.5 million cells is obtained after reviewing the wall  $y^+$  values. A wall  $y^+$  value of 0 to 5 is highly recommended for a CFD simulation involving a complicated flow phenomenon. In our case, the wall  $y^+$  values (Figure 20) are observed to be well within the tolerable limits.

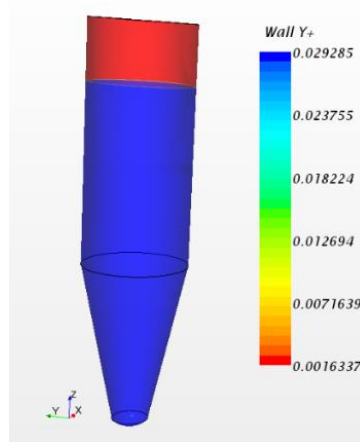


Figure 20: Wall  $y^+$  values

A scalar scene is displayed at each time step for a total simulation time of 1 s. The sloshing of the liquid inside the Eppendorf tube at various time intervals is shown in Figure 21. Irregular intervals of simulations are displayed to highlight the sloshing behavior. It is observed that after one cycle of oscillation, the liquid remains adhered to the top surface (near the cap of the tube), which is expected because of the surface tension of the fluid. The details of the forces on the tube walls for different scenarios are shown in Figure 22.

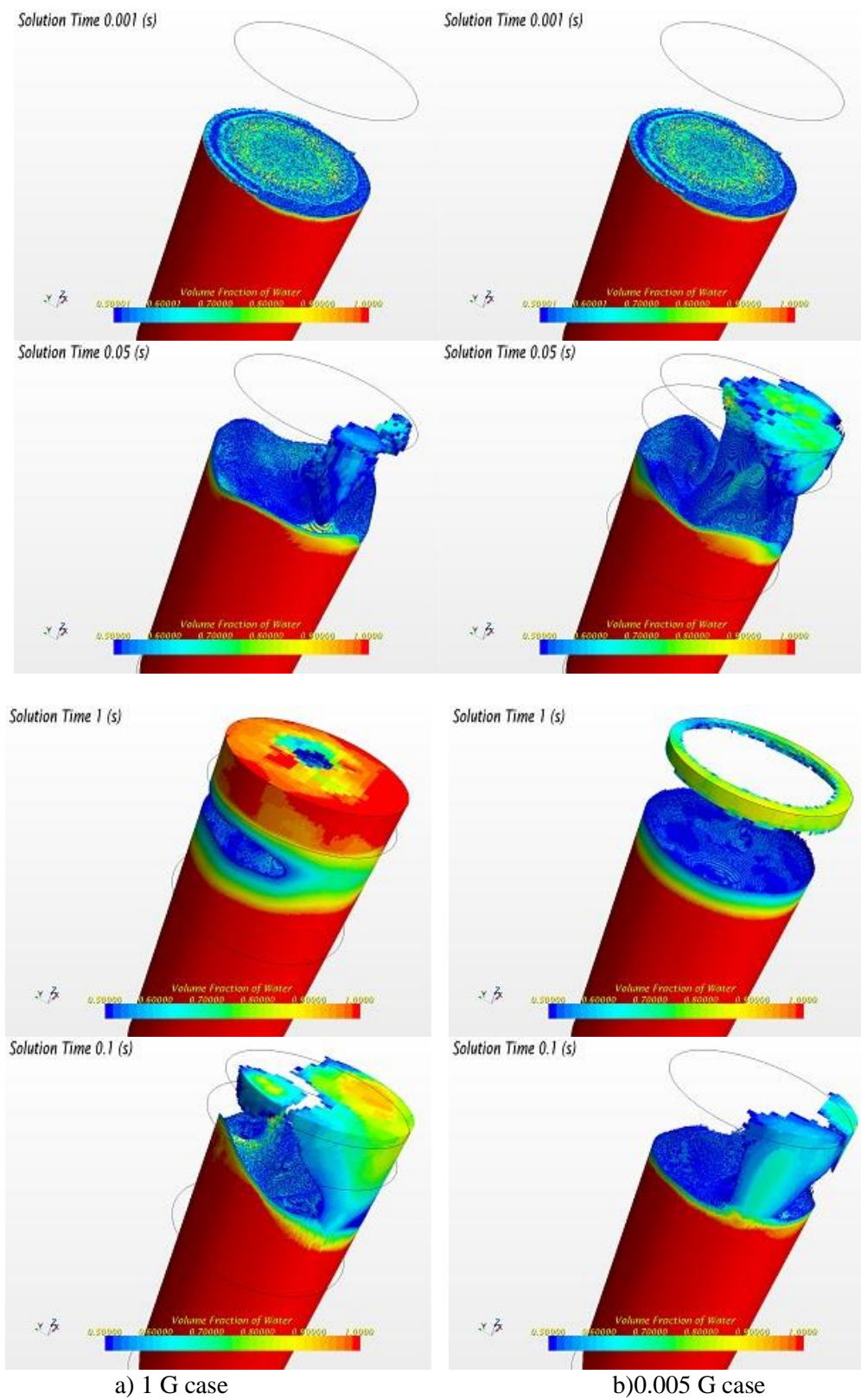
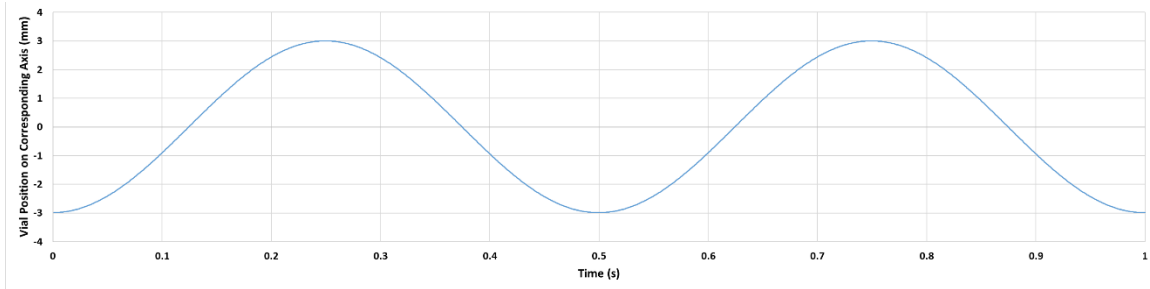
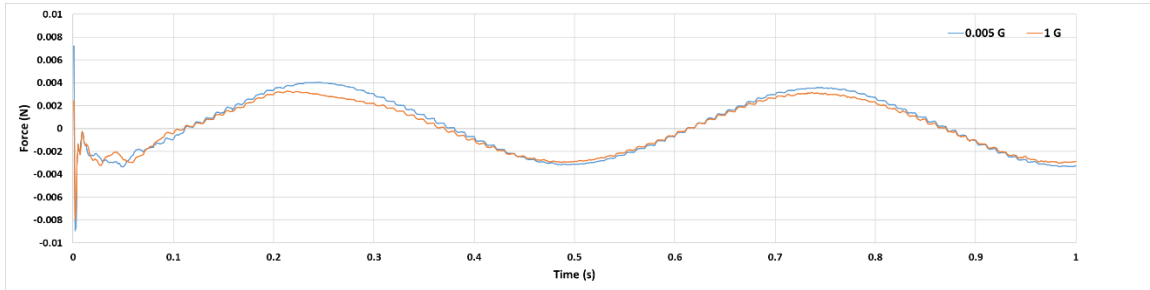


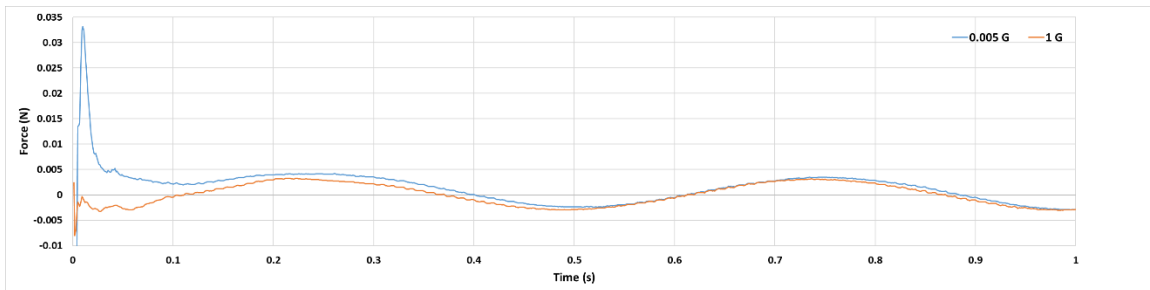
Figure 21: Scalar scenes showing the time history of liquid slosh inside 5.0 mL Eppendorf tube with lateral actuation and gravity acting vertical direction



a) Tube position history



b) Fluid force with lateral actuation



c) Fluid force with actuation along the gravity vector in the vertical direction

Figure 22: Tube actuation and corresponding slosh response observed in the Eppendorf tube

The CFD analysis of the 5.0 mL Eppendorf tube shows a ten times magnitude increase of wall forces compared to the 1.5 mL Eppendorf tube. It is to be noted that an SHM excitation is applied instead of a random vibration profile for the ease of simulation setup. It is impossible to synthesize and replicate a random vibration excitation in Star-CCM+, so the launch environment is not realistically applied.

### 3.7.5 Prototyping using 3D Printer and Final Assembly

Several challenges were overcome during the 3D printing process, involving filament jams, extruder issues, and warping. MakerBot Replicator 2X is an experimental printer,

and therefore some of the aspects of printing involve trial and error. Filament jams would occur when filament material crosses over itself on its roll or when the nozzle was wrongly calibrated to be too close to the print bed. Once the issue was identified, it was concluded that the material had been mishandled, which allows the printer filament to loosen itself and then entwine itself in a new pattern. Re-calibration of the printer bed height also aided in solving the jamming issues. This information saved a great deal of material wasted simply by ensuring that the filament roll is kept tightly wound. Another issue was the extruder not correctly latching onto the material, resulting in no material being used while the extruder continues to move around. This extruder issue was caused due to the amount of tension required to feed the filament being inadequate. Upgraded extruders were purchased, which were equipped to prevent the filament tension issue.

Warping is a significant problem since it would alter the shape of the final print and is caused by the uneven cooling and settling of the printed part. As a result, the bottom surface of the printed part detaches itself from the print bed, and thermal variations cause the whole part to distort. Rafts are printed on the bottom surface, which acts as a pseudo surface and prevents the distortion from the bottom from propagating into the central part. Although rafts improved the print quality, a small amount of warping still existed. One of the solutions was to increase the temperature of the heat bed, which allowed the printed part to stick to the print bed. In addition, a heat gun was used to target specific areas as soon as they began to warp, which also nullified the warping.

The quality of a 3D printed part dramatically depends on the resolution offered by a 3D printer. Initially, the payload structure was 3D printed with the geometric specification of the optimal candidate obtained in mass optimization. However, the

obtained prints were not structurally stable with those geometric specifications. Some support mass had to be added to take into account the resolution and 3D printing inconsistencies. These limits and tolerances were considered in the final 3D print of the NanoLab.

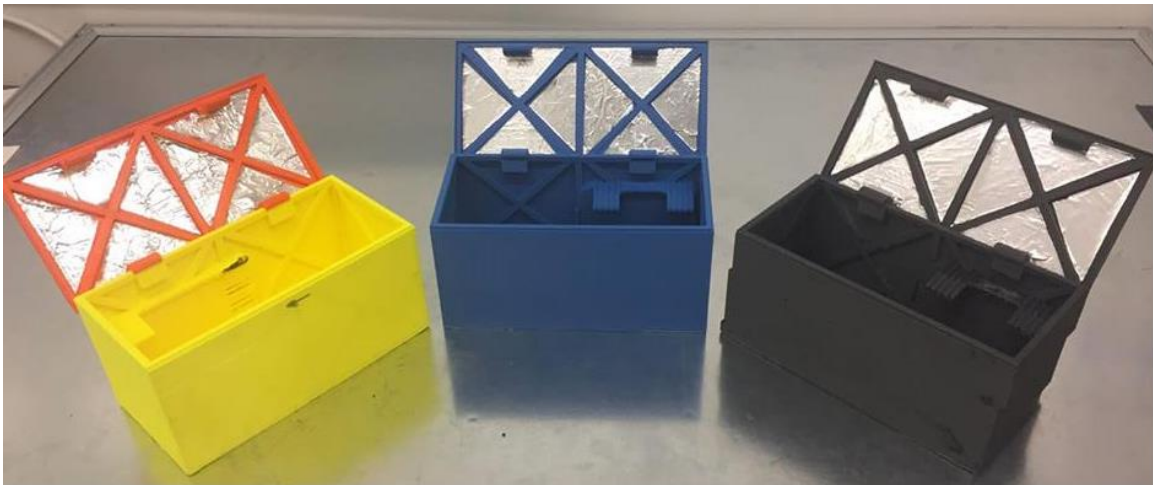


Figure 23: 3D Printed NanoLab structures. ABS with initial design holder (left) ABS with improved device holder (middle) and CFRP ABS (right)

Common 3D printing materials such as ABS, PLA, and CFRP infused ABS were analyzed. ABS and CFRP are used more for professional applications. PLA has storage issues and is prone to damages due to environmental factors as it is made up of organic compounds. The results from the structural analysis show that the CFRP-infused ABS material is more robust compared to ABS. However, the prints with CFRP failed due to extruder jams because of their hardness. The cost of CFRP is more than double that of the ABS printer material. The mass of the CFRP-printed part is approximately 25% higher than the part printed with ABS. Therefore, ABS plastic is chosen to be the candidate for the final payload structure due to its cost, availability, ease of 3D printing, and the mass constraint of the payload.

A fire-retardant foam is packed inside the NanoLab and is used to house the Eppendorf tubes and dampen the vibrations experienced by the payload. The payload is assembled and sealed with water-resistant tape. The Eppendorf tubes are enclosed in a vacuum-sealed plastic cove. The tube cap, plastic cover, foam, and water-resistant tape serve as four layers of containment for the payload. The components of the CRExIM NanoLab assembly are shown in Figure 24.



Figure 24: CRExIM payload final assembly [29]

### 3.8. Flight Operations and Post-flight Analysis

The payload engineering development was tailored to meet the requirements of the flight provider (Blue Origin), flight integrator (NanoRacks), and the payload science team (UTHSCSA). Payload operations are an integral part of the payload development process, and plans and operation manuals are required to complete all the payload mission goals.



### 3.8.1 Deliverables and Payload Review

In order to streamline the process of payload development, the flight providers and integrators set forth the submission of multiple deliverables and reviews. The definition of these processes was communicated to the flight customers/researchers through Payload User Guides (PUG). PUG is a document that contains detailed information on the flight, payload design, deliverables, testing requirements, timeline, and flight operations. The flight integrator carried out the intermediate and final certification of the payload based on the submitted deliverables and subsequent reviews. The deliverables and the corresponding timeline are shown in Table 9.

Table 9: Payload deliverables timeline

Deliverable	Typical timeline (months before launch)	Submission/Review Date
Payload Data Package (PDP)	5	14th January, 2017
PDP review	4.5	3rd February, 2017
Payload Safety Package (PSP)	3	26th February, 2017
PSP review	2.5	8th March, 2017
Launch Site Integration Package (LSIP)	1	1st October, 2017

Payload Data Package (PDP) is the initial proposal furnished by the payload research team, which details the planned experiments, expected scientific goals, preliminary payload design, test plans, and introduction of collaborators. PDP offers the primary investigators a tool to communicate their intent and the reviewers to confirm the compatibility of the proposed experiment with the available interfaces. The engineers reviewed the PDP at NanoRacks, and the first review meeting was conducted with all the

collaborators. The first review meeting involved the introduction of all key personnel, roles, and responsibilities. The review offered an opportunity for the science and engineering teams to understand the payload development requirements further. The review committee suggested that the engineering team review and update the containment of liquids inside the NanoLab. Based on the recommendations, the vacuum-sealed bags and underwater tape were utilized to provide two layers of containment.

Payload Safety Package (PSP) is a questionnaire to assess the hazards and ensure the safety of the payloads in the expected operational environment. The bill of materials (BOM) and safety data sheets of all the materials used in the payload are affixed to the document. Details on electrical schematics, electromagnetic sources, chemicals, and fire safety are specified. Mechanical safety tests are recommended, and graphic video evidence is sent to the review committee. The load test involves placing 15 lb weight in the axial direction and 10 lb weight in lateral directions for 2 minutes in each direction. The conducted tests on the NanoLab are shown in Figure 25. PSP review was conducted, and necessary modifications were recommended. The X frame truss structure outside the NanoLabs was moved inside to accommodate standoffs between the NanoLab and the payload locker walls. The PSP was approved, and the final assembly of the payload assembly was performed.

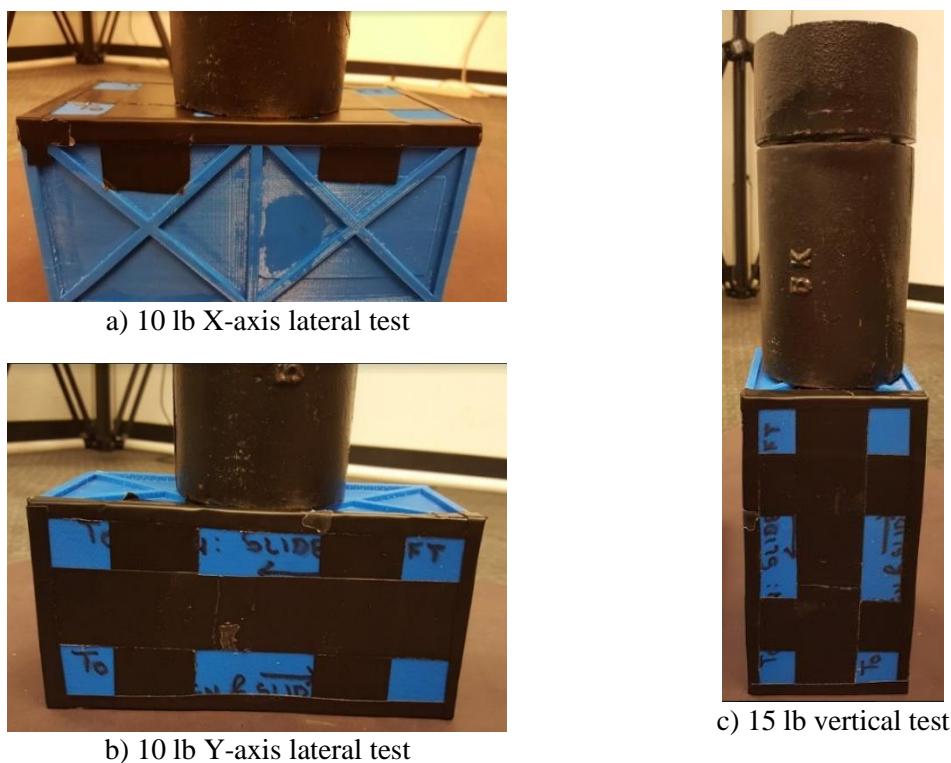


Figure 25: Safety load test

Launch site integration Package (LSIP) contains the questionnaire requiring the researchers to furnish details on the logistics of the payload before and after the flight. Blue Origin's New Shepard launches from their West Texas launch facility in Van Horn, Texas. The researchers are provided options to directly ship the payload components to the Payload Processing Facility (PPF) at the launch site. PPF is a controlled on-site facility for processing payloads pre and post-flight. Details of personnel visiting the site are provided in LSIP and any special requests for handling payloads.

### 3.8.2 Pre-flight and Post-flight Operations

Tasks and plans were devised for the different teams to assemble and configure flight hardware, prepare and maintain viable conditions for T-cell science experiments, and recover and collect data from the payload. The processing of the cells and the survival of the biomaterials were monitored during transportation, and the science team at

UTHSCSA handled post-recovery operations. Proper protocols in handling the biomaterials were prepared in advance and followed.

The engineering team was responsible for assembling all the hardware components, developing contingency plans, and ensuring safety. CRExIM payload consisted of passive components, and the only operational component was the EDL-XYZ data logger inside the NanoLab. Operational procedures for setting up the device and collecting data were produced as a procedure manual followed at the PPF. The operational timeline is shown in Figure 26.

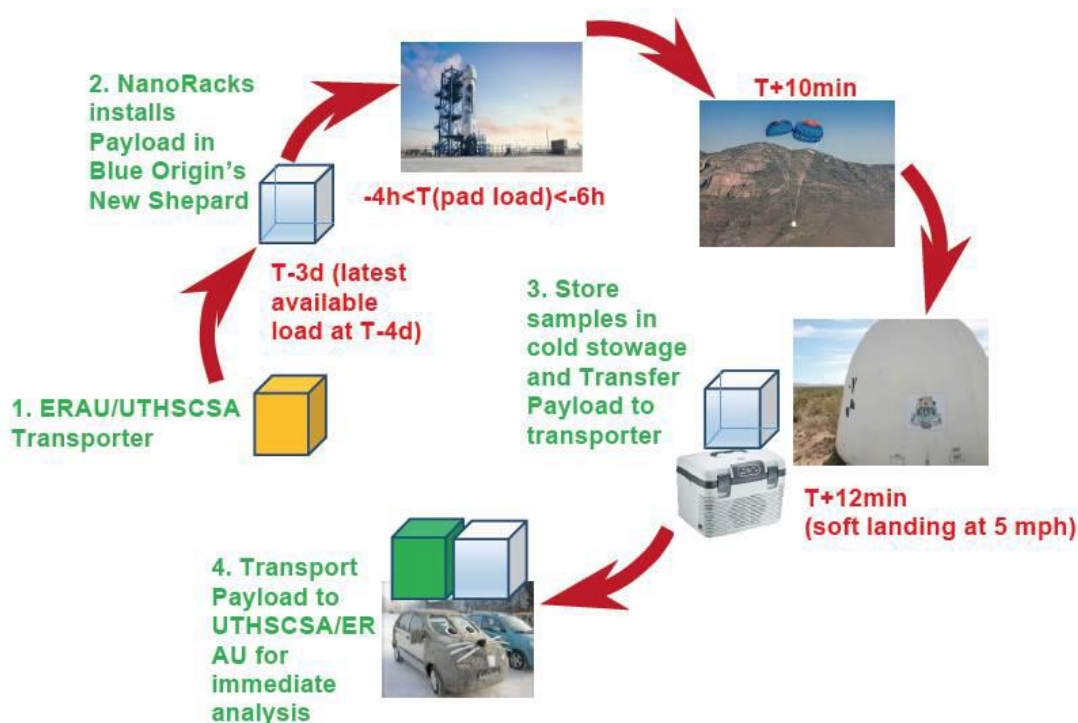


Figure 26: CRExIM operational timeline [30]

CRExIM was launched to suborbital space onboard the first flight of the new version of Blue Origin's New Shepard 3 capsule, and the launch mission's name was designated as "M7". The intended launch date was December 11<sup>th</sup>, 2017, and the launch was scrubbed until the next day. The next launch opportunity was set for the next day. The

payload was handed off to NanoRacks at 04:45 on December 12<sup>th</sup>, 2017. The launch happened at 10:59, and the launch vehicle reached an apogee of 98.269 km with an approximate microgravity time of 4 minutes. The capsule landed under parachutes after a 10-minute suborbital flight. The payloads were recovered and delivered to the researchers at 15:45 in PPF. The post-recovery operations included downloading the flight data from EDL-XYZ and securing the cells for future analysis. NanoRacks also provided supplemental flight data from sensors on the payload locker to the researchers.

### **3.8.3 Flight Data Analysis**

The first flight experience onboard Blue Origin's New Shepard capsule offered the researchers many lessons and insights into a suborbital launch's operational and technical environment. The launch scrub and the uncertainty towards a next flight opportunity offered some challenges to the survivability of the cells. Biological payloads are highly sensitive to stresses due to the handling and transportation of specimens. The temperatures at the launch site were lower than anticipated during that season, and the remote location of the launch site proved it impossible to transport back the cells to a more controlled environment before the next launch opportunity.

The cells underwent large thermal gradients on the launch scrub day. The science team came up with quick solutions to nourish the cells and improve their survivability. The engineering team employed Little Hotties 8-hour hand warmers procured locally as a temporary solution to keep the cells warm. The temperature of the cells was constantly monitored, and the warmers were used until before delivery of the payload to launch personnel. Blue Origin personnel wrapped the payloads in a thermal blanket to save the cells during transportation. Had the launch been scrubbed one more time, the cells

survival rate would have dropped significantly, rendering the science mission a failure. These critical lessons learned at the launch facility were documented and helped the researchers in developing future payloads.

The EDL-XYZ was preprogrammed at the PPF, and it collected data from 03:35 to 13:45 on the launch date. The device was retrieved, and the data was processed using EDL-XYZ MaxiThermal software. The datalogger started recording data after a 5-hour preset start delay to save memory and recorded for about 9 hours at a sampling rate of 4s. The acceleration data recorded during the flight (the recording during only flight phases) is shown in Figure 27. The critical flight events are highlighted to show their time occurred during the flight. The recording axes orientations of the data recorder are shown in Figure 28 a). The payload was oriented inside the NanoRacks locker so that the Y-axis of the datalogger pointed in the thrust direction of the launch vehicle.

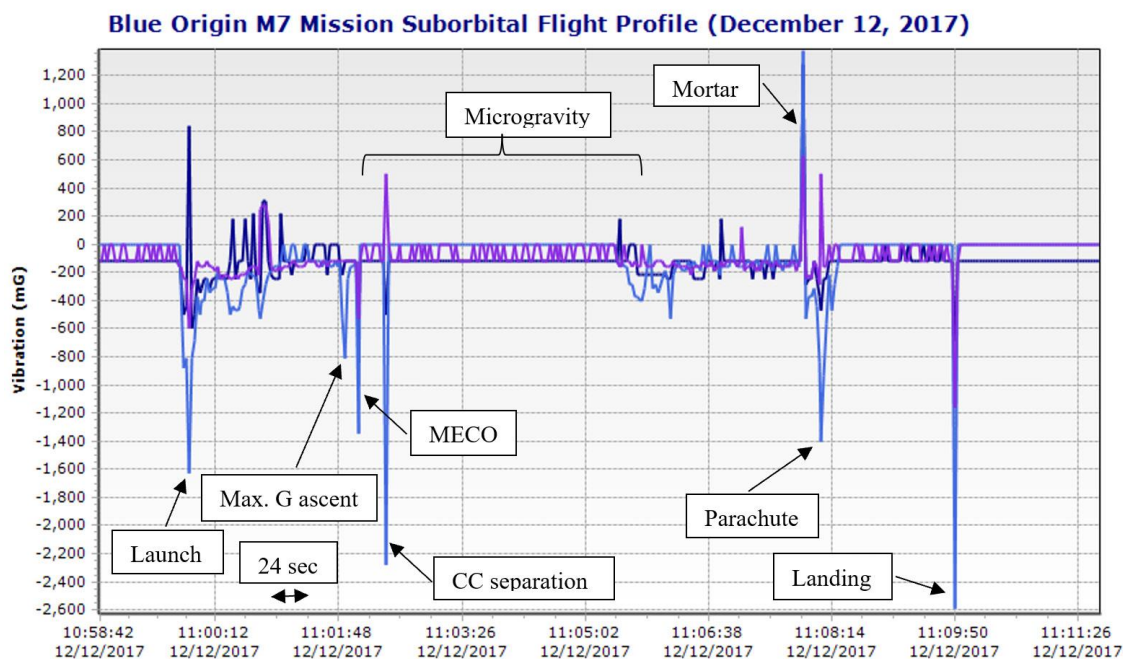
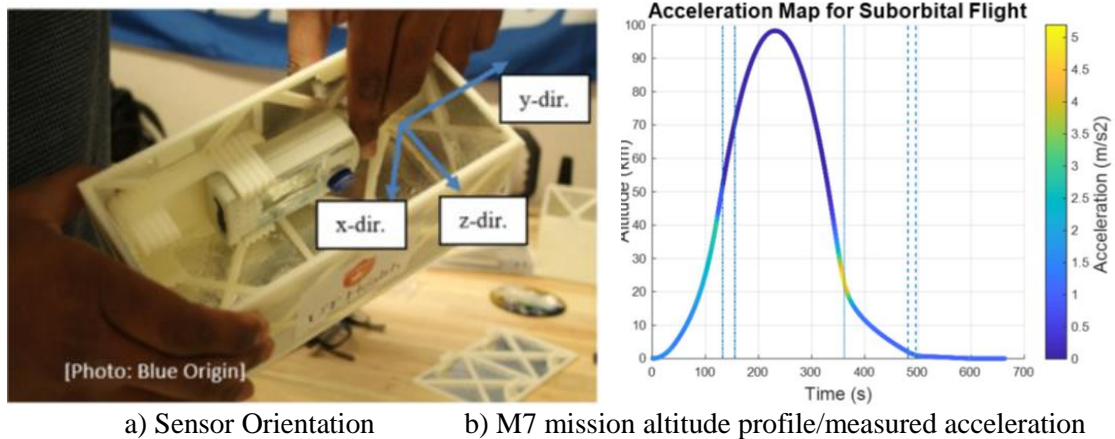


Figure 27: Acceleration data recorded by EDL-XYZ during the suborbital flight. X-axis (dark blue), Y-axis (light blue) and Z-axis (purple) [31]



a) Sensor Orientation      b) M7 mission altitude profile/measured acceleration

Figure 28: Flight profile showing acceleration experienced at different altitudes [31]

Summary of key observations from the data logger data are:

- The total flight time was a little over 10 minutes.
- EDL-XYZ measured 1.61 G acceleration during launch.
- The acceleration experienced at MECO was about 1.38 G.
- At crew capsule (CC) separation, the payloads experienced 2.3 G.
- A continuous microgravity time of about 3.2 minutes was recorded, and the microgravity levels were in the range of 120 mG.
- Brief moments of microgravity periods were experienced before CC separation and after 3.2 minutes. The minor changes to the levels could be attributed to RCS firings, as was suggested by Blue Origin.
- The drogue chute deployment event imparted 2 G on the payloads, and the main parachute deployments were measured at 1.55 G.
- 3 G was experienced due to the landing impact.

Figure 28b shows the altitude profile of the flight capsule, and the axis in the right highlights the acceleration experienced during flight at various altitudes while also comparing these parameters with the time progression of the flight. This flight data was

provided by Blue Origin and showed good accordance with the acceleration and altitude data suggested in PUG.

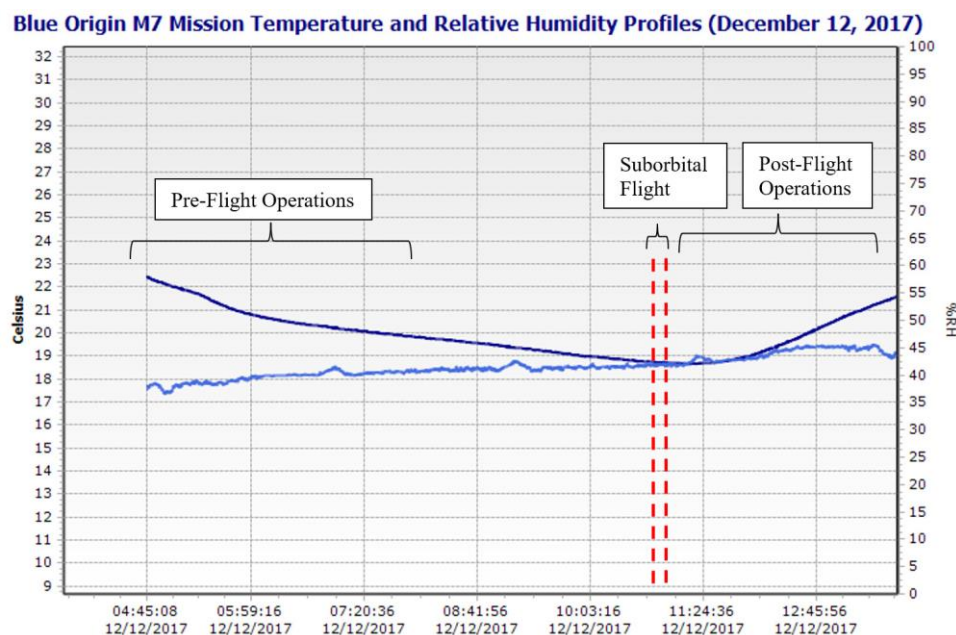


Figure 29: Temperature and relative humidity measured inside the NanoLab [31]

EDL-XYZ also measured temperature and relative humidity levels inside the NanoLab, which was an essential stressor in characterizing the behavior of T cells. On the day the launch was scrubbed, the ambient temperature was 4 °C, and the payloads were exposed to this environment inside the capsule for 6-8 hours. The average temperature recorded by the data logger was 14.6 °C, which is below the acceptable temperature levels for the cells. The thermal tape and the foam around the cell vials provided adequate insulation and ensured the survival of the cells.

During the launch day (12<sup>th</sup> December 2017), the external conditions were better than the previous day, and the average recorded temperature was 19.94 °C, and the lowest being 18.66 °C. Post recovery, the cells were immediately moved to UTHSCA, and the science team conducted post-flight cell analysis.



#### 4. MESSI McXIMUS Payload

After completing the first suborbital payload mission: CRExIM, onboard Blue Origin's New Shepard vehicle, researchers at ERAU were given a second opportunity to fly a NanoLab research payload. Blue Origin had flown and recovered three successful New Shepard missions since the M7 launch on the exact launch vehicle. The mission was designated NS-11 and carried 38 payload experiments, including nine experiments from NASA. With this opportunity and lessons learned from challenges faced in the CRExIM mission, researchers at ERAU planned to work on a more ambitious payload containing two biological science experiments. Each experiment was designated a mission name, and the objectives of the payload are as follows:

**Muscle characterization eXperiment In Microgravity Universal Spacelab** (McXIMUS) payload contained an experiment to study the effect of the space environment on zebrafish embryos (Figure 30a). The experiment was a research collaboration between UTHSCSA and ERAU. Zebrafish are chosen as study specimens as their genetic makeup is very similar to humans. Space travel induces many adverse effects on human physiology. The musculoskeletal system is altered by microgravity environment [32]. During space missions, astronauts are subject to many stressful conditions, such as cosmic radiation, microgravity, and stressors, that can have a negative impact on their health. This experiment aimed to evaluate the expression of stress genes during the suborbital flight and define which genes are altered by microgravity. Another severe adverse effect of space travel is abnormalities in vascularization, which could lead to muscle degeneration.

Scientific Objective 1 is to analyze stress markers in zebrafish. After the suborbital flight, embryos will be imaged, and gene analysis will be conducted. This objective will lead to the identification of the stress genes altered by the suborbital flight parameters.

Scientific Objective 2 determines the effects of microgravity on vascular formation in zebrafish embryos. Zebrafish cellular development is extremely fast within the first few days compared to humans (9 months). Thus, a few minutes (in microgravity) is considered a significant amount of time of their growth process [33]. Therefore, using the fluorescently labeled vascular system, we expect to see changes in their vascular formation.

Two 1 oz bottles containing fish water and zebrafish embryos were used for this experiment. In addition, several types of ground controls were studied. After the suborbital flight, all embryos will be brought to the UT Health Science Center for further analysis.

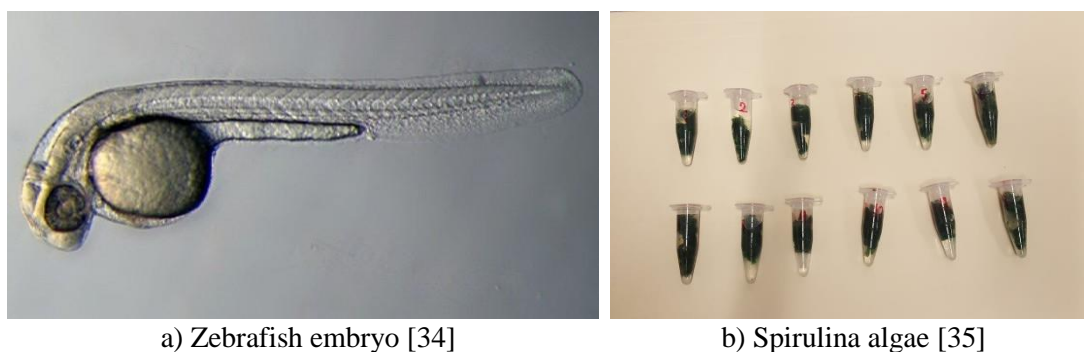


Figure 30: Bio organisms used in MESS/McXIMUS payload experiments

**Microgravity Experiment Spirulina Superfood In-vitro (MESSI)** is a payload that project seeks to see the effects (beneficial or otherwise) of suborbital spaceflight on the growth of *Cyanobacteria Arthrospira Platensis*, otherwise known as spirulina algae (Figure 30b). Furthermore, this will be done with spirulina in nine different conditions: three different lights sources (white, red, and blue lights) and three different food sources

(magnesium sulfate  $\text{MgSO}_4$ , potassium nitrate  $\text{KNO}_3$ , and citric acid  $\text{C}_6\text{H}_8\text{O}_7$ ). The reason spirulina is was tested is that it is an approved consumable by NASA for astronauts. Its health benefits include anti-inflammatory and antioxidant properties [36], increases in cornea and retina health, as spirulina is a source of vitamin A [37], 20%-30% higher muscle performance [38], controlling of allergies and allergic reactions [39], reduction of nasal congestion and blood pressure [40], increased activity of natural killer cells in the immune system [41], increased endurance [42], reduction of the size of cancer tumors [43], and mild antidepressant properties. It also has the ability to act as an air revitalization system restoring oxygen naturally [43].

The scientific objective of the MESSI experiment is to analyze the growth of spirulina in suborbital flight conditions and understand the effects of microgravity by measuring spirulina growth preflight and postflight. Data on various environmental parameters such as temperature, relative humidity, luminosity, and acceleration will be recorded inside the NanoLab using custom payload electronics. The spirulina flight samples, ground, and the mother colony at ERAU are compared.

The NanoLab chassis will be 3D printed with ABS plastic, and the NanoLab will be very similar to the NanoLab used for the CRExIM payload. The internal layout will be modified to suit the requirements of the McXIMUS and MESSI experiments.

#### **4.1. Payload Requirements**

The primary engineering objective of the MESSI/McXIMUS payload is to ensure the survival of the biological components in the science experiments. The first task for developing a payload is to collect the requirements of the experiment and understand launch vehicle provisions and the operational environment. This includes understanding

the conditions that affect the biological specimens, such as temperature, microgravity, vibrations, radiation, etc. The payload was more ambitious than CRExIM as the current mission consisted of two separate experiments and the goal was to maximize the usage of the payload capacity to achieve as much science as possible. The strict mass and size constraints, as shown in Table 2, were a challenge to accommodate two experiments. Another design goal was to make minimal changes to the NanoLab design used in CRExIM, which was already and flight-proven. Design improvements and simplifications increase the efficiency of the 3D printing process of the NanoLabs by lowering print times and reducing used filaments while ensuring fewer failed prints.

MESSI experiment consisted of live algae, which had to be contained in 1.5 mL centrifuge tubes. Multiple combinations of living conditions had to be tested by altering food sources and light levels. Therefore, the clear tubes had to be contained in different compartments illuminated with different color lights. Environmental parameters such as light levels, temperature, relative humidity, and accelerations had to be measured inside the payload compartments.

McXIMUS payload consisted of about 100 zebrafish embryos in fresh water placed inside a breathable bottle. The bottles had to be securely contained inside the NanoLab and did not require any special storage considerations.

Custom payload electronics were required to monitor the conditions inside the NanoLab. The electronics design required more sophistication in comparison to the CRExIM experiment, which used a commercial-off-the-shelf (COTS) datalogger EDL-XYZ. The NanoRacks Feather Frame (NFF) offered the payload customers to stream flight information from the Blue Origin capsule to each payload through a USB interface.

The research team believed that this data and data from onboard sensors would be instrumental in correlating and validate flight data with flight events. So, the electronics would have to receive the flight data packets from the USB interface and log it along with sensor data.

#### 4.2. Payload Design

The initial payload design iteration was performed with the considerations from the payload requirements in section 4.1. The initial CAD design was derived from the CRExIM NanoLab design with the same X frame truss structure. A divider was added inside the payload housing to make compartments for each separate experiment. The detailed design of the internal components was not considered in the initial model. The electronics and experiment components were still being determined at this point. The initial CAD design of MESSI/McXIMUS NanoLab is shown in

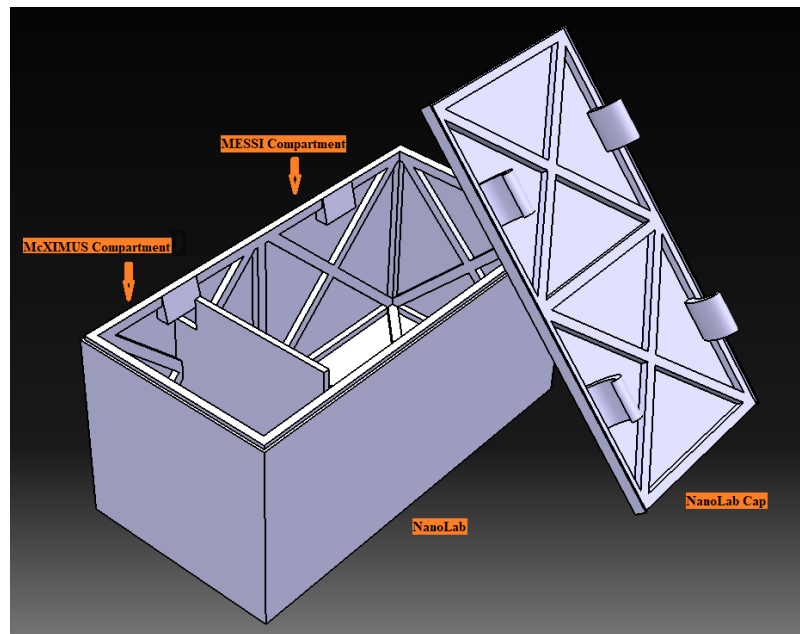


Figure 31: Initial MESSI/McXIMUS NanoLab CAD model

Several modifications were made to the initial model in several design iterations to improve and accommodate new payload components into the model. The necessary

electronics architecture was conceptualized, and the required parts were identified. The details on the electronics architecture, parts, and circuit diagrams are discussed in the future sections.

The main NanoLab structure was slightly modified from the original design. The multiple X frame structures were combined into a single X frame truss running through the whole length of each side wall. The sharp corners in the old design were changed to more smooth and filleted corners. A central circular junction was created where the X beams would meet. The goal was to reduce the flow of flight stresses on the walls of the NanoLab structure. The X frames were designed with chamfers in the vertical direction to avoid 3D printing support structures below the overhanging flat surfaces as seen in the old design.

The whole NanoLab was divided into 3 bays or compartments using dividers. The larger compartment will house the MESSI experiment with tube racks, sensors, and LED lights. The second compartment would be used to contain the McXIMUS experiment placed inside a foam housing. The third compartment will serve as the avionics bay with a microcontroller that powers and records all the sensors, a USB interface to transmit flight data, and battery packs to power the LED lights. The updated CAD model is shown in Figure 32.

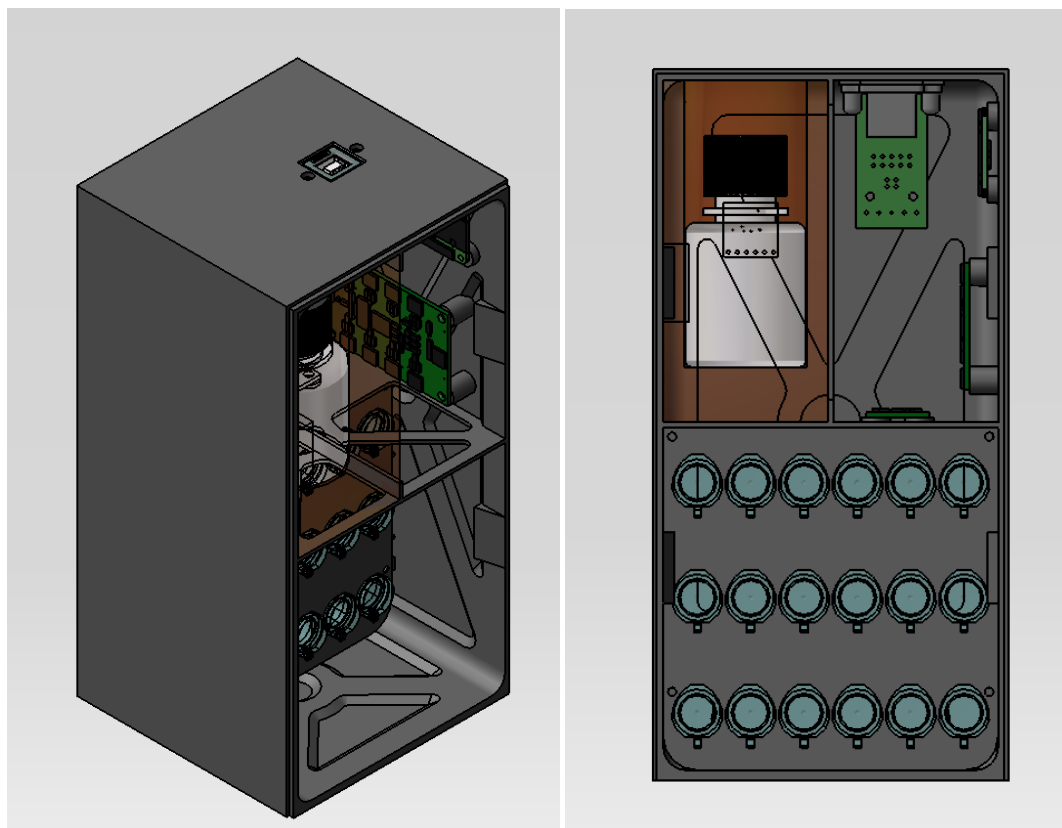


Figure 32: MESSI/McXIMUS updated CAD model

After clear deliberation and discussion with the science teams, the experiment components were determined, and the teams shared design ideas. Based on the inputs, the MESSI payload would contain 18-1.5 mL tubes containing spirulina. A tube rack model was suggested and designed. The NanoLab design this time involved modular components where parts of the NanoLab could be dismantled and reassembled. The modular design would increase the efficiency of the payload assembly process and reduce 3D printing issues. The tube rack would require a large number of supports while 3D printing as there are overhangs below the tube support rack. Issues such as support material falling off and support not being printed were experienced in CRExIM 3D prints. Modular parts also have the advantage of testing sub-components and performing fit checks separately without having to 3D print the whole NanoLab. This technique

significantly improved the speed and success rate of the 3D prints. The tube racks were designed with 18 holes with 3 rows having 6 evenly spaced holes each. The centrifuge tubes had a circular bevel around their diameter near the cap. The levels were used as click lock mechanisms to secure the tubes inside the holes of the tube rack. The hole diameters were optimized and reprinted to ensure a tight fit of tubes in the holes on the tube rack. Three sub-compartments were made inside the tube placement area with dividers to create three different lighting conditions for each set of 6 tubes. LEDs and sensors would be mounted on the other side of each divider, as shown in Figure 33.

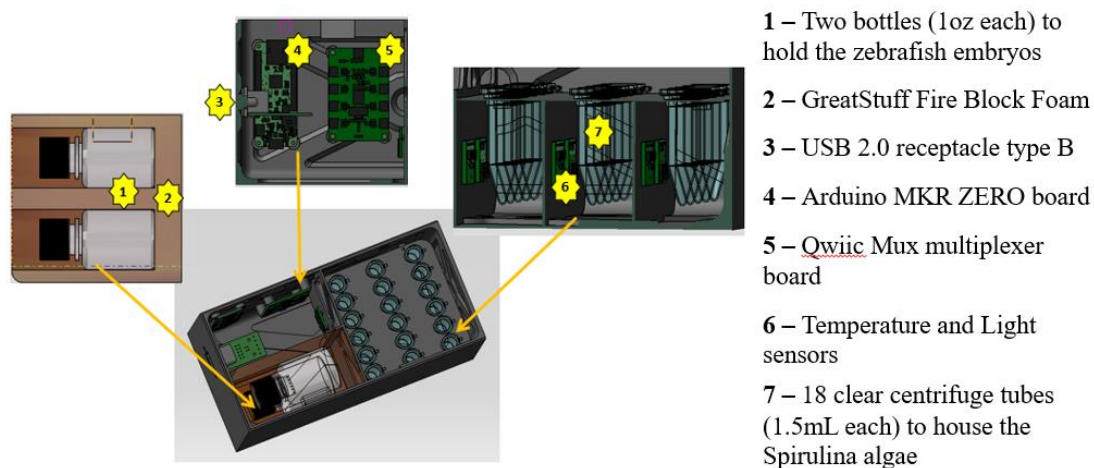


Figure 33: MESSI/McXIMUS updated CAD model design components

The lid of the NanoLab was redesigned and modified based on the lessons learned in the CRExIM mission. The push from top and click mechanism in the previous versions was removed. The small protrusions on the old lid served as the snap points were susceptible to breaking after multiple uses. The structural protrusions were also harder to 3D print requiring support structure and resulted in print failures. Furthermore, the old design required multiple test prints to lock the lid to the main housing properly. The new design utilized a slide and rail mechanism, with a thin sliding protrusion on the lid side and a matching slide cutout on the main housing. One side of the cutout had stops to limit



the movement of the lid from sliding over the other side. The underwater tape was still used to secure the lid to the NanoLab housing.

Table 10: MESSI/McXIMUS Payload mass

Component	Mass (g)
USB Connector	16
Humidity and Temperature Sensor	1
Accelerometer	2.4
Light Sensor (x3)	3
Arduino	7.5
Multiplexer	7.8
Wires	24
Housing (V4) without Lid	130
Lid (V4)	30
Partition (V3)	20
Velcro	3
Zebra Fish (Including Container)	100
Tube Housing	12
Test Tubes (x18)	36
1.5 ml of water (x18)	27
Battery Housing	12
Battery (AA) (x2)	30
LED Lights	1
Total:	462.7 g

Payload total mass was one of the key design considerations in the development of the payload. The goal was to maximize payload capacity while keeping the total payload mass within limits set by the flight integrator. The final mass of the components and total

mass of MESSI/McXIMUS payload after multiple iterations of design and 3D printing is shown in Table 10.

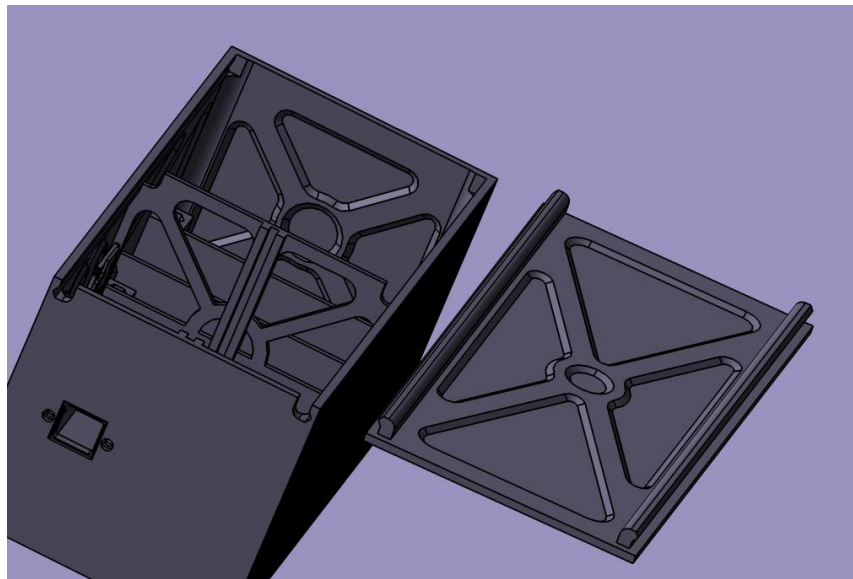


Figure 34: Updated NanoLab lid design

### **4.3. Payload Electronics**

Two different electronic systems were designed and developed for the MESSI/McXIMUS payload. The first system consisted of an Arduino-based custom data logger with multiple sensors and data communication with the NFF locker, and the second system consisted of the LED lighting system.

#### **4.3.1 Custom Data Logger with Flight Data Interface**

The datalogger would serve as a motherboard that powers and collects data from various sensors and stores the collected data in a microSD card. Arduino MKR zero was chosen as the microcontroller to perform the tasks mentioned above [44]. Various criteria were considered for the selection of Arduino MKR zero:

- Small form factor which is more suitable for placement inside the small volume of the avionics bay
- In-built microSD card slot which discounts the need for a separate microSD

card module and thereby saves space and consumes less power

- SAMD21 microcontroller chip has a higher processing speed compared to other conventional Arduino boards
- 3.3V sensor logic support which allows interfacing new generation, low power consumption sensors
- Simple programming options through the same Arduino IDE software environment [45] with plenty of online support forums
- Serial data communication capability through a USB interface, enabling the collection of flight data
- Flash memory of 256 kB offers plenty more code storage space for running long and complex programs

The Arduino MKR Zero served as the brain of the data collection system and was powered through the 5V USB connection from the NFF USB interface. The data logger would turn on when the power becomes available in the flight capsule before the flight and a few minutes after the flight totaling 21 minutes.

The sensors were selected to measure the temperature, light levels, and accelerations experienced by the payload. All the sensors were chosen from SparkFun's "Qwiic connect system" line of products for their modular and easy interface capabilities. The sensors used I<sup>2</sup>C serial bus protocol for signal communication [46]. I<sup>2</sup>C serial bus consists of only four wires for power, ground, data, and clock, respectively. The bus protocol enables the connection of multiple sensor connections to the same bus and saves the number of wires/connections needed in the circuits. The details of the sensors used and their electronic specifications, along with the power draw, are shown in Table 11.

Each I<sup>2</sup>C sensor has a unique address associated with it, and the sensor is called using this address. However, the data logger would have multiple instances of the same sensor; for instance, the light and temperature sensors consisted of more than one of the same sensors. This was an issue to call the sensors uniquely using the I<sup>2</sup>C bus protocol. Therefore, an 8-channel multiplexer is utilized to split the repetitive sensors into separate channels. The multiplexer will automatically allocate unique addresses to each channel, and thereby, up to 8 sensors with the same addresses can be used. The circuit diagram of the custom data logger is shown in Appendix B.

Table 11: Custom Datalogger components and power requirements

Component	Voltage (V)	Current (mA)	Power draw (W)
Arduino MKR ZERO	5	600	3
Qwiic Mux breakout	3.3	20	0.066
4 x Temperature Sensor (TMP 102)	3.3	1e-3	3.3e-6
Accelerometer MPU 9250	3.3	3.7	0.012
3 x Luminosity Sensor APDS-9301	3.3	0.6	0.002
	3.3 V sensors		3.080 W
Total:	5 V Power Supply	624.3 mA	1.08 Wh (21 minutes)

The NFF provided an option of transmitting flight event data to the customers through their serial USB interface. Payload customers can use this capability to automate payloads and trigger selective components inside the payload based on the current phase of the suborbital flight. In our case, the data logger would record the flight events along with the sensor's data. NanoRacks provided a software toolbox to simulate the

transmission of data packets through the USB ports in a local computer. This toolbox was utilized to program and test the Arduino for the collection of flight data.

The Arduino programs were developed in the Arduino IDE software, which is a C++-based programming environment. Arduino IDE provided options to use pre-built libraries, making the code very simple and easy for the users to carry out complex tasks. Each sensor had libraries available on their purchase website, and with the help of libraries, the sensors could be called, and data could be directly derived without performing complex parsing efforts. The communication and parsing of data are taken care of inside the pre-coded libraries. The custom data logger had to collect and store data from the sensors while also collecting flight data from the serial USB interface at the same time. Arduino compiler uses line by line compiler, and therefore to run multiple processes simultaneously, multithreading was used. The data collection from sensors, collection of data from the USB interface, and all the data storage take place simultaneously. The Arduino program that was used in the MESSI/McXIMUS payload is documented in Appendix A.



Figure 35: Electronics test dry run

The circuits were assembled by soldering Dupont connectors to the Arduino MKR Zero board. The I<sup>2</sup>C master bus line was connected to the main line on the multiplexer, and the sensors were connected using JST connectors to the 8 channels in the multiplexer. The LED lighting system consisted of a set of 6 same-colored SMD LEDs connected in parallel. Three sets of the colored LEDs were then connected in series and powered by a battery pack consisting of 2xAA batteries, with each battery operating at 1.5 V. Due to their sensitive nature, the batteries were reviewed and approved by Blue Origin before the flight. Power calculations showed that the lighting system could function for 12 hours, and multiple table tests were conducted. The circuit diagram for the LED lighting system is shown in Appendix B, and the electronics testing on a dry NanoLab is shown in Figure 36.

#### 4.4. Suborbital Flight Test

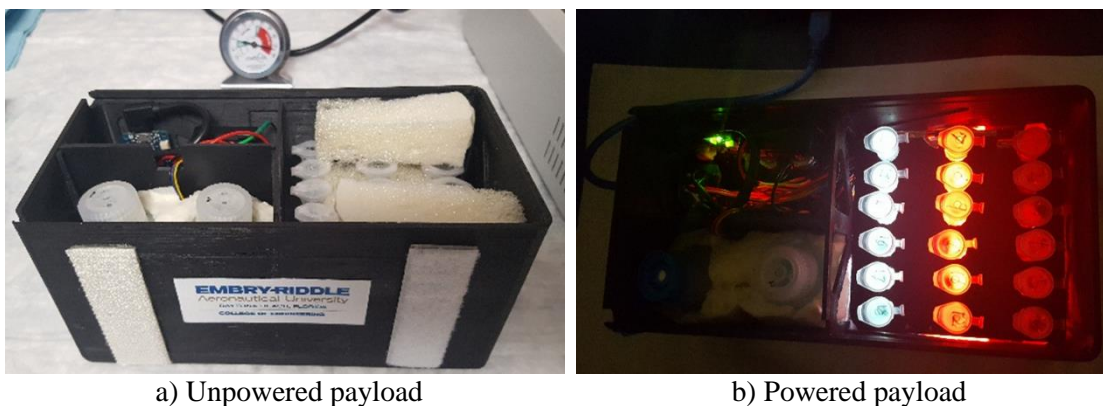


Figure 36: Fully assembled MESSI/McXIMUs payload preflight [47]

MESII/McXIMUS payload was flown onboard the New Shepard NS-11 mission, the fifth flight of that capsule, and the fourth flight since the CRExIM mission. The launch took place on 2<sup>nd</sup> May 2019, and liftoff was at 08:35 AM. The capsule reached an altitude of 105.5 km and, after a flight of about 10 minutes, landed under parachutes near the WTLS. The fully assembled payload at the PPF is shown in Figure 36. The flight

included a total of 38 different payloads, out of which NASA flew 9. After the successful flight, the payload was recovered, and the data from the data logger was analyzed.

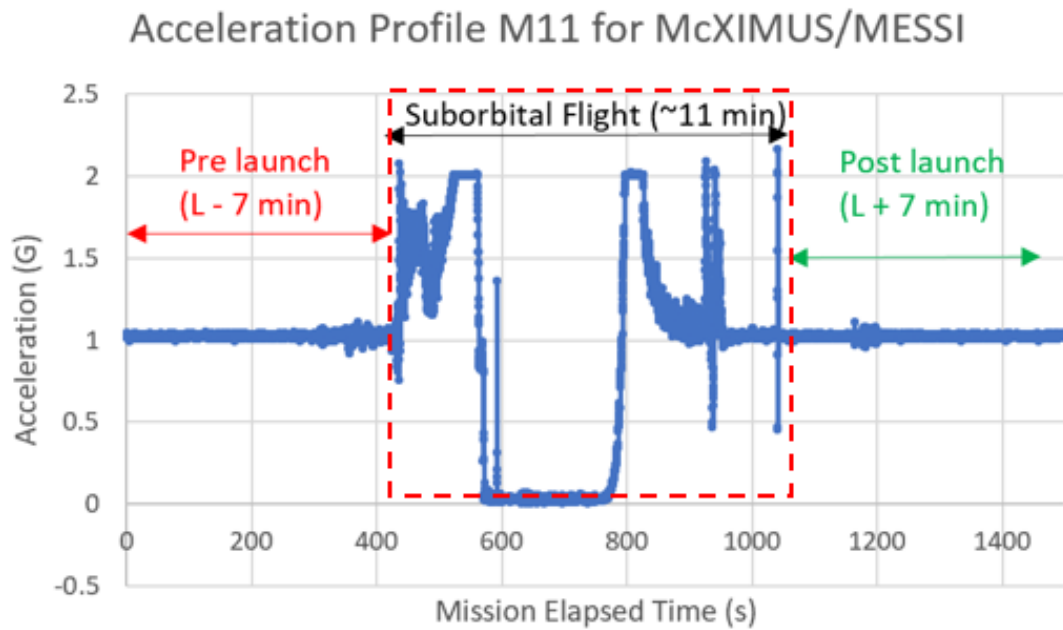


Figure 37: MESSI/McXIMUS flight acceleration profile [47]

## 5. PLD Payloads

The researchers at Embry-Riddle have been awarded a suborbital flight opportunity to fly payloads onboard PLD's MIURA 1 sounding rocket. PLD is a European space company based in Spain, and the payloads are stated to be launched on the first flight of the MIURA 1 rocket, projected to be at the end of 2021. MIURA 1 is a single-stage liquid propellant-sounding rocket that can lift a nominal payload mass of 100 kg. The flight vehicle, flight parameters, and details on the launch vehicle are shown in Figure 38.

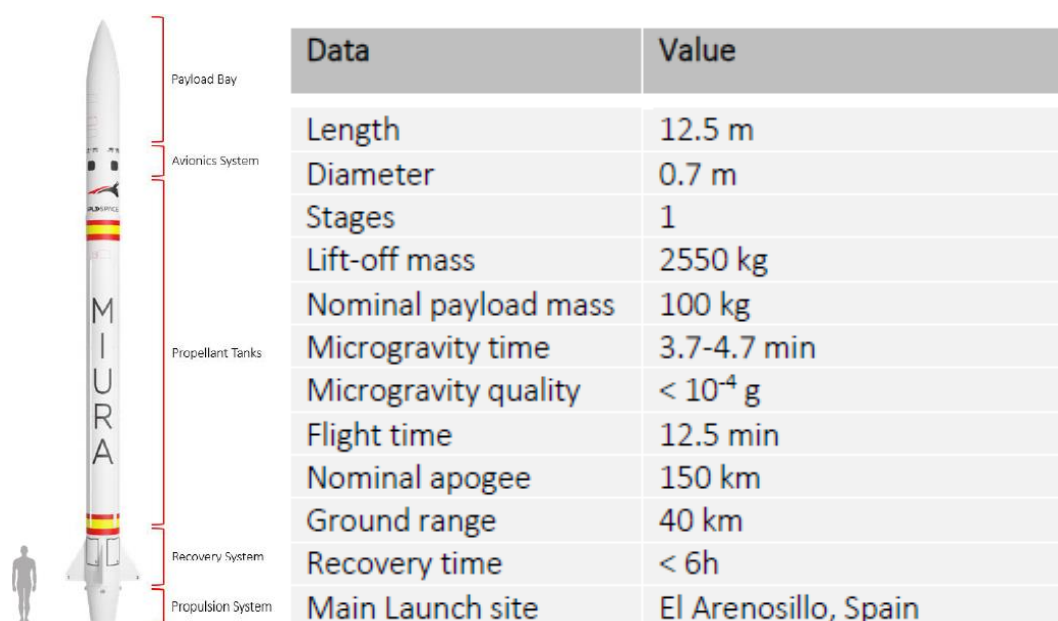


Figure 38: PLD Space's MIURA 1 launch vehicle and flight parameters [12]

ERAU has secured a single payload compartment on MIURA 1 to fly its proposed payloads. The higher payload volume available in the single compartment has allowed the development of multiple experiments as sub payloads. A higher science output is expected in this launch through the completion of multiple objectives simultaneously. By flying multiple experiments, the utilization of available microgravity time is maximized.



### 5.1. PLD ERAU Payload Design

The payload bay volume is shown in Figure 39a. The payloads will be mounted on a payload baseplate illustrated in Figure 39b. The actual flight hardware of the payload baseplate was shipped to ERAU by PLD Space to inspect the mounting of payloads and perform vibration acceptance tests of the payload assembly.

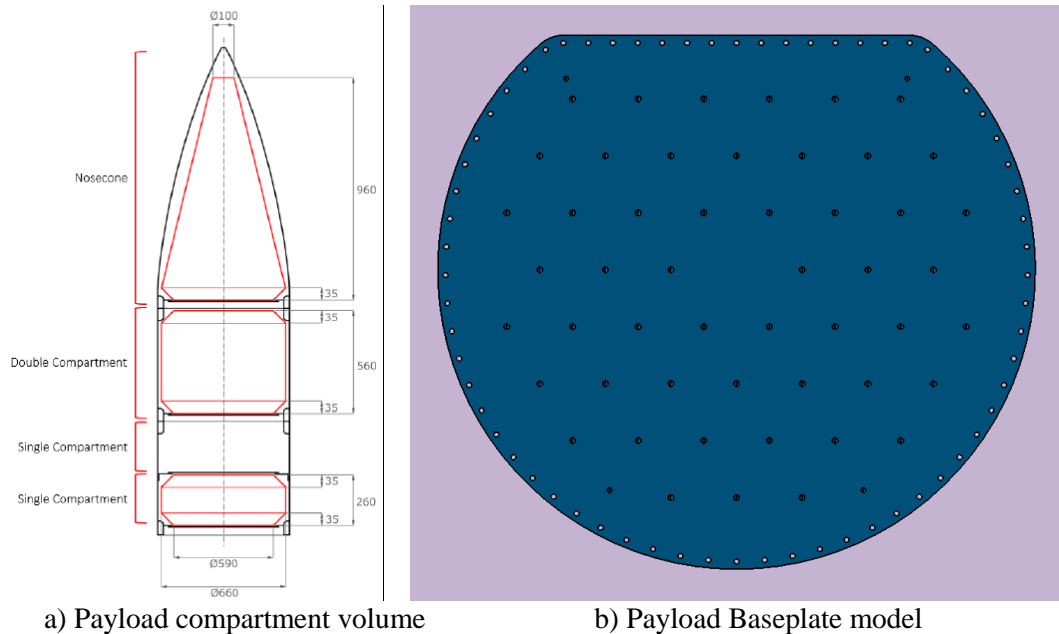


Figure 39: MIURA 1 payload specifications [12] . All units are in mm

Multiple payload research teams have worked on developing four different sub-payloads for the PLD launch. The four sub-payloads are MAPMD, avionics/telemetry, shunt, and in-vitro payloads. An initial CAD model of the proposed sub-payloads assembled on the baseplate is shown in Figure 40. The detailed description of each sub-payload is discussed in the following sections. The sub-payloads were designed to maximize the payload volume available in the single compartment of the MIURA 1 rocket. MAPMD payload will be mounted using M6 mounting points, and the NanoLab payloads are mounted using dual lock adhesive Velcro tapes.

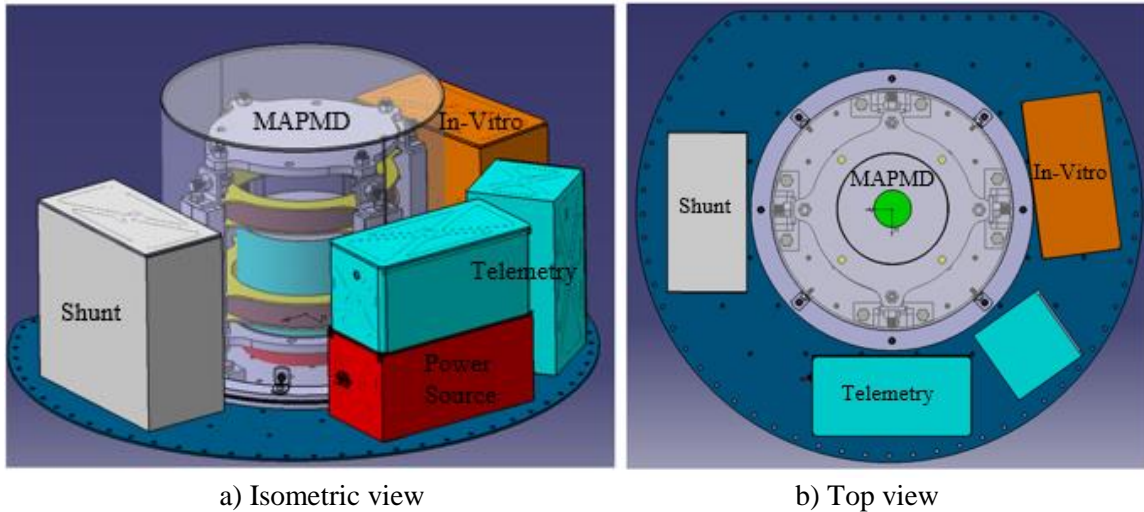


Figure 40: PLD ERAU payload experiments – Initial CAD model

The initial MAPMD payload design consisted of a suspended water tank mounted on four arms. This mounting scheme was initially conceptualized to utilize load sensors to measure liquid forces on the tank walls. Based on initial estimations, the load cells were removed from the payload design by the MAPMD research team. In the next design iteration, the Helmholtz coil assembly (shown in yellow and brown in Figure 41a) was used to electromagnetically control the floating membrane. The coil assembly was replaced with permanent magnets in subsequent designs (Figure 41b) as initial testing revealed the inadequacy of magnetic strength produced by the Helmholtz coil system for the MAPMD application.

The power source NanoLab, which consisted of the payload electronics and power supply for the MAPMD payload, was not required without using the Helmholtz coil system and removed from the payload design. The assembly and disassembly of the initial MAPMD payload were challenging due to the multitude of components and fastening joints. Vibration testing of the MAPMD payloads (vibration test campaign detailed in Section 5.5) also showed concerns in the initial structure, and the assembly

failed the High-G load tests. A comprehensive design overhaul of the MAPMD sub payload was carried out to accommodate the necessary changes. The updated MAPMD sub payload is shown in Figure 41b.

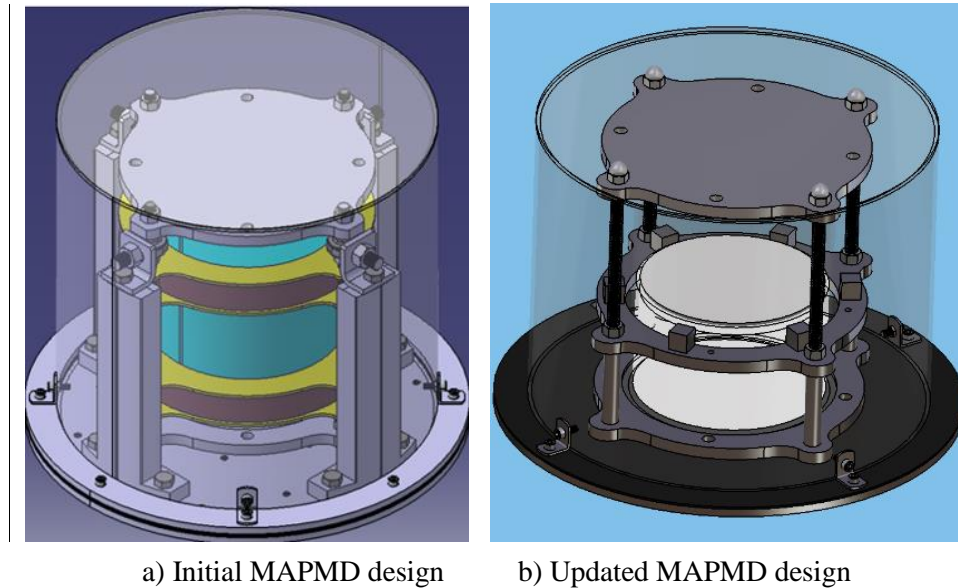


Figure 41: MAPMD design modification

In the updated MAPMD payload, the vertical support arms are removed, and the tanks are directly mounted to the MAPMD base plate using threaded rods. The Helmholtz coil system was replaced with 6 Neodymium permanent magnets. An aluminum support ring is added to mount the magnets using vertical spacers. The initial MAPMD design's external casing was taller than 260 mm. The external casing is modified to a height of 241.4 mm, thereby conforming to the maximum allowed height of 260 mm of the single compartment shown in Figure 39a. Rubber sheets are used to provide a water-tight seal and vibration dampening between the baseplate/external casing, top and bottom of the MAPMD tank. The updated CAD model of the PLD ERAU payload assembly is shown in Figure 42.

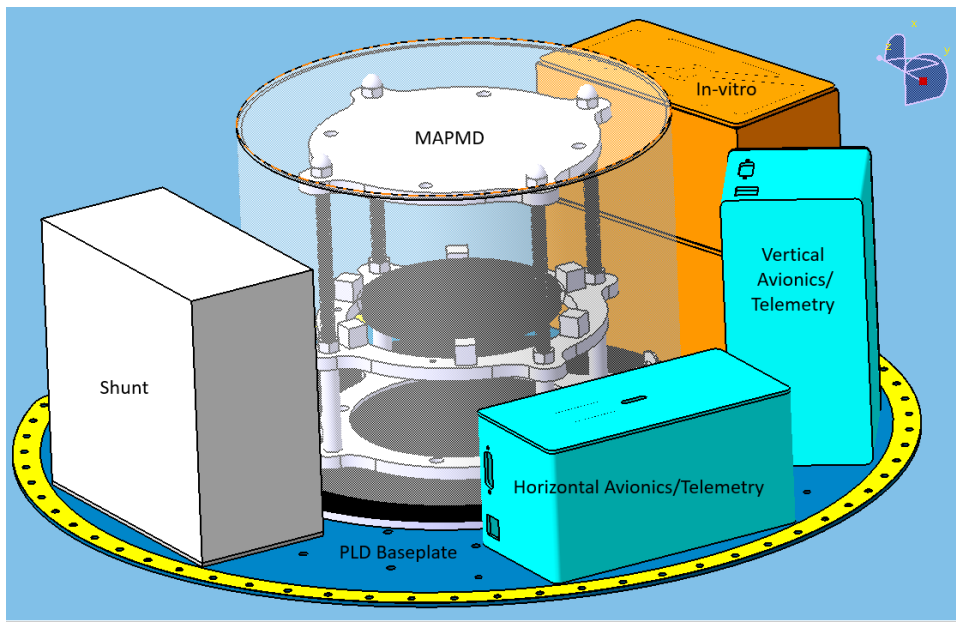


Figure 42: Updated CAD model of the PLD ERAU payload assembly

The maximum allowed payload mass is 25 kg for a single compartment. The maximum allowed center of gravity region is a cylindrical section on the top center of the PLD baseplate with 140 mm (Diameter) and 130 mm (Height). The coordinate system of the MIURA 1 rocket is shown in Figure 43, and the X-axis corresponds to the thrust direction.

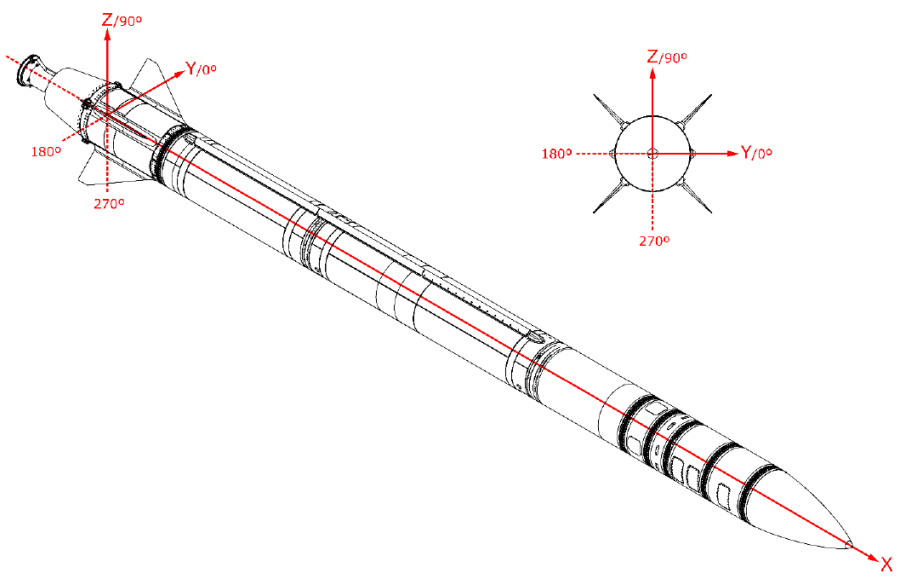


Figure 43: PLD Space MIURA 1 vehicle coordinate system

The CAD model was created with the same coordinate convention, and all the components were designed with the same material properties as in the final prototype. The calculated mass and center of gravity parameters are shown in Table 12. Table 12 also shows the calculated mass, size, and center of gravity compliance with PLD Space's requirements.

Maximum allowed payload physical characteristics:

Mass: 25 kg

Size: 590 mm (Diameter) and 260 mm (Height)

CG: Cylindrical section above baseplate 140 mm (Diameter) and 130 mm (Height)

Table 12: Calculated payload physical parameters for the PLD ERAU payload assembly

Parameter	Value
Mass (kg)	9.35
Payload assembly maximum dimensions (mm)	355.6 (Diameter) x 241.4 (Height)
Center of Gravity (mm)	CG <sub>x</sub> : 81.15
	CG <sub>y</sub> : 7.65
	CG <sub>z</sub> : -10.99
Moment of Inertia Tensor (kg.m <sup>2</sup> )	$\begin{bmatrix} 0.2028 & -0.0014 & -0.0023 \\ -0.0014 & 0.1273 & 0.0011 \\ -0.0023 & 0.0011 & 0.1846 \end{bmatrix}$

### 5.1.1 Scope of Study

The scope of study in this research with regards to PLD payloads will encompass the following topics: Development of the avionics/elementary payload structure, electronics design and assembly, benchmarking analysis of MAPMD performance in microgravity using CFD, vibration acceptance testing of all the PLD ERAU payloads on a shaker table. These topics will be discussed in detail in the following sections.

The Shunt and in-vitro sub payloads consist of biological experiments developed by other research teams. The shunt experiment investigates the effects of microgravity and space flight on the performance of a cerebrospinal fluid shunt device (technology demonstration). The invitro experiments study the effects of microgravity on the ability of certain anti-cancer drugs on cancerous tumor growth.

## **5.2. Avionics Payload Development**

This suborbital mission will be the first flight of PLD Space's MIURA 1 launch vehicle. Flying an avionics payload onboard the rocket aims to measure critical environmental parameters inside the launch vehicle throughout its flight envelope. Therefore, the researchers hope to characterize the flight environment, which will eventually serve as a pathfinder mission for future payload customers and researchers flying on the space vehicle. The data from the avionics package supports the research goals of other sub payloads in the ERAU payload package by providing additional data validation.

Characterizing the environment inside a suborbital flight vehicle involves understanding the applications and customers that can benefit from these launches. Some common research areas include space biology, manufacturing, technology demonstration, and life support systems. Based on these applications and dominant stressors experienced in space travel, the following parameters were chosen to be recorded by the avionics package:

- Accelerations, gyrations, magnetic headings, and quaternions
- Temperature
- Relative humidity

- Pressure
- Radiation
- Magnetic fields
- Air quality
- Infrared radiation

Acceleration data could aid in the characterization of the microgravity levels and durations and vibrations experienced in the flight envelope. Temperature, humidity, radiation, and air quality are essential for sensitive payloads, especially microbiology experiments. Evaluating pressure is critical for components that are pressurized or contain pressure vessels. Magnetic fields can influence payload electronics and components with higher magnetic permeability. The payloads bay will not be illuminated, and therefore infrared imaging of the payload bay is prescribed.

The avionics/telemetry payload is a new technology developed at ERAU to characterize the environment of the first suborbital flight of the MIURA 1 rocket. The electronics architecture and the NanoLab structural design are legacy systems of the previously flown suborbital missions and in-house model payload rocketry platforms. The project development of the avionics/telemetry payload has been rated using the TRL system, and the ultimate aim is to develop a commercial-off-the-shelf unit or a system kit that can aid users in evaluating flight parameters or support their flight experiments. This system will reduce the effort of other payload developers in developing their own avionics systems. Through previous experiences, design, fabrication, and breadboard validation in a laboratory environment, the avionics system technology has been improved to TRL 4. The system was flown along with the MAPMD payload on parabolic

flights, and through the validation of the components and breadboard in a relevant environment, the current rating of the technology is at TRL 5. The final prototype and all the payload systems will be validated in a space environment through the MIURA 1 suborbital spaceflight, and the new product will progress to TRL 7.

### **5.2.1 Payload Design**

Two avionics packages consist of two redundant sensor units, each contained in a separate NanoLab. Redundancy was one of the critical factors when making design considerations as this was the first flight for the launch vehicle, and it is useful to have multiple sets of data to characterize the flight. The payloads will be placed at different locations and orientations to capture the entire environment of the payload bay. The large payload capacity and higher electrical power features facilitated the inclusion of two avionics payloads simultaneously. These payload housings' design was derived from previous flight missions, and the NanoLabs are 3D printed using ABS plastic material. The design was slightly modified to accommodate the electronic components that were planned to go inside these NanoLab. The details on the electronics will be discussed in the next section. A sliding partition was designed to serve as the lid of the containers. The partitions walls house the circuit boards containing various sensors. Slots on the payload structure were designed to accommodate electrical interfaces, external electrical components, and a port for air quality and pressure sensors to sense the payload bay environment. The avionics package designs are shown in Figure 44.



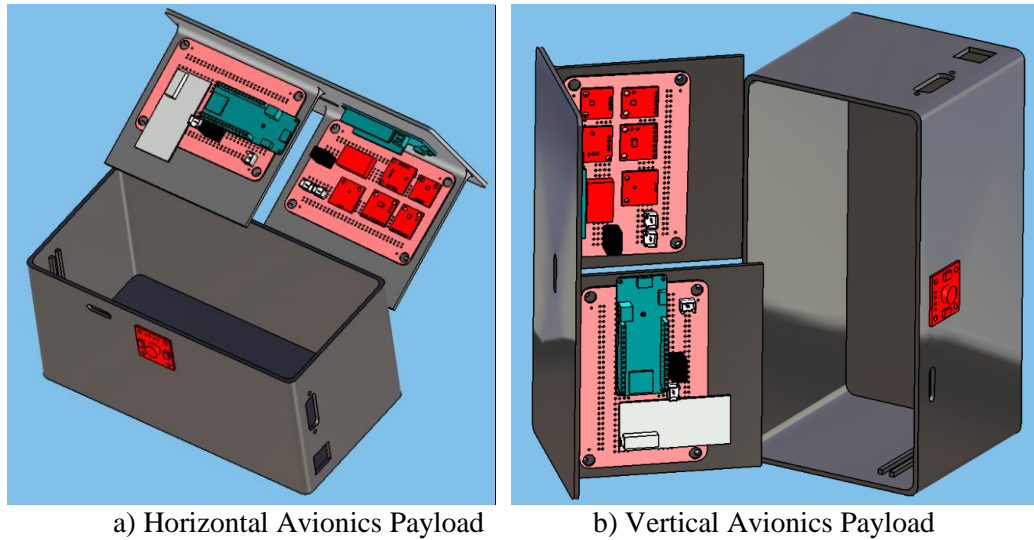


Figure 44: PLD ERAU Avionics payload design

### 5.2.2 Payload Electronics

The avionics payload primarily contains electronics and will measure various flight parameters using an array of sensors. The sensors were selected based on the parameters that were stated to be evaluated in the previous sections. Previous experiences with I<sup>2</sup>C sensors and the Arduino environment influenced the decision-making for sensors and microcontrollers used in the avionics package. PLD Space discusses the electrical interface and power capacities available in the launch vehicle in their Payload User Guide (PUG). The payload power supply will provide a voltage of 28 V with maximum current draw per connector at 10 A. These voltages are incompatible with Arduino and sensor voltages, and therefore a 28 V to 5 V voltage regulator is utilized to step down the voltage and distributes to the electronic circuits. A variance in the power levels can be expected as the payloads draw power from the vehicle batteries. Therefore, the voltage regulator is chosen to operate at a range of input voltages and provide a constant 5 V output to the circuits. A Command Data and Handling (CD & H) connection are also

available through the payload interface, stream live vehicle telemetry data over an Ethernet connection.

Four different electronic circuits are conceived to carry out the data collection tasks inside the payload. These circuits will be designed on four different circuit boards: Circuit Board 1 carries most of the sensors (air quality, temperature & humidity, pressure, inertial measurement unit (IMU), accelerometer, and magnetometer). Circuit Board 2 contains the radiation sensor. Circuit Board 3 contains the infrared imaging unit. Circuit Board 4 will contain the circuitry to collect the CD & H flight data. Running all the same board and controller unit tasks requires complex programming and is more susceptible to errors and failure risks. The researchers aim to improve data collection confidence levels and reduce data losses by having independent circuits spanning two redundant payload packages.

Circuit Board 1 will utilize the I<sup>2</sup>C bus architecture similar to MESSI/McXIMUS payload. All the I<sup>2</sup>C sensors have been paired in a single circuit board, and a multiplexer is not required this time since each sensor is unique and has a unique address. The four-wire bus line is passed in series through all the sensors, and the circuit diagram is shown in Appendix B.

A primary power connector is attached to the payload housing, receiving a 28 V power supply from the launch vehicle. The power from the connector is split and connected to Circuit Boards 1 and 2. Each board will have its voltage regulator step down the operating voltage to 5 V, and redundancy reduces the risk of power failure. The 5V regulated power will then supply to boards 3 and 4. JST connectors are used to provide

connections between all the boards and the internal power supply. Arduino MKR Zero is used as the microcontroller in both boards 1 and 2.

Circuit Board 2 will house the pocket Geiger radiation sensor. A separate circuit is used for this sensor due to the nature of the data signal from the sensor. Pocket Geiger does not support I<sup>2</sup>C [46], and the data is output in pulses when radioactive particles strike on the sensor. Therefore, a separate circuit is designed and shown in Appendix B to simplify and achieve uninterrupted data collection without using multi-threading programs. The corresponding Arduino programs (see Appendix A) and an example output file stored in the microSD card are shown in Appendix B.

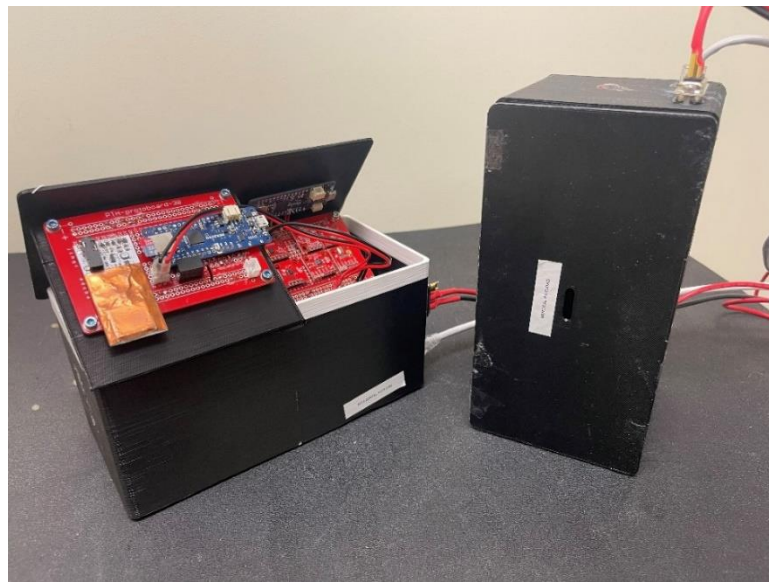


Figure 45: Assembled avionics payload NanoLabs

Circuit Board 3 houses the infrared thermal imaging sensor. Due to the higher processing requirements for the infrared sensor, a Teensy 4.1 microcontroller is utilized to collect and process data. Circuit Board 4 will contain the CD & H data collection system. The detailed design and communication protocols expected from the flight vehicle are being updated by PLD Space to payload customers as the launch vehicle is still under development. This board will be designed and developed based on further

inputs from PLD Space’s engineers and left as future research. The support and interfacing hardware have already been incorporated in the design and assembled in the hardware. An RJ45 8-pin connector has been attached, and the wiring has been completed to be incorporated into future circuit designs. The list of components in each avionics/telemetry NanoLab is shown in Table 13. The assembled and wired NanoLabs are shown in Figure 45.

Table 13: List of electronic components in each avionics/telemetry payload

Hardware Component	Description
Circuit Board 1	
Arduino MKR Zero	Microcontroller
TSR 1-2450	Voltage regulator (6.5-36 V IN; 5 V OUT)
Power connector (male)	Vehicle/payload power supply interface
Si7021 breakout	Temperature and relative humidity sensor
MPL3115A2 breakout	Pressure sensor
CCS811 breakout	Air quality sensor (CO <sub>2</sub> and TVOC)
MPU 9250 breakout	Inertial Measurement Unit (IMU)
HMC5883 breakout	Magnetometer
LIS331 breakout	Triple-axis accelerometer
Circuit Board 2	
Arduino MKR Zero	Microcontroller
Pocket Geiger-Type 5	Radiation sensor
Circuit Board 3	
Teensy 4.1	Microcontroller
MLX90640 breakout	Infrared sensor array
Circuit Board 4	
RJ45 8-pin connector	Ethernet data connection
Datalogging system	Future Work

### 5.3. MAPMD CFD Analysis

#### 5.3.1 Payload Background

The behavior of liquid propellants is highly unpredictable and chaotic in the microgravity environment experienced by launch vehicles and spacecraft that utilize liquid propellants. Sloshing occurs inside the propellant tanks due to the motion of the vehicle and in microgravity. Sloshing is the motion of a liquid with a free surface inside a container. The sloshing phenomenon can damage the structural parts of the rocket tanks and affect the vehicle's guidance and control trajectory by imparting undesirable forces on the tank walls.

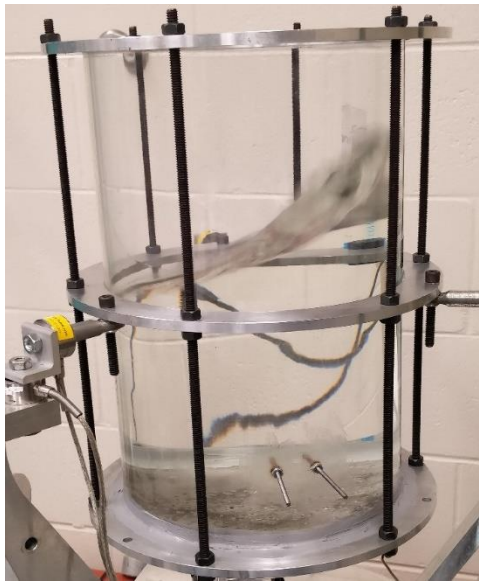


Figure 46: Liquid slosh in a cylindrical tank [27]

The slosh mitigation is vital in ensuring mission success in various space and terrestrial applications such as oil tankers and hazardous material trucks. Propellant Management Devices (PMD) performs the control of slosh, specifically in space applications. PMDs can be divided into three types: 1) Passive damping: This method involves structural modifications on the tank's structure employing partitions, vanes, and baffles or free-floating diaphragms or membranes, which break the slosh waves on the

free surface. These structures are bulky and are incapable of adapting to different slosh levels and intensities. 2) Active damping: This method involves measuring slosh wave frequencies and actively creating waves of opposing frequencies to cancel out the sloshing on the free surface. 3) Hybrid damping: This method employs active and passive methods by using actively controlled PMDs.

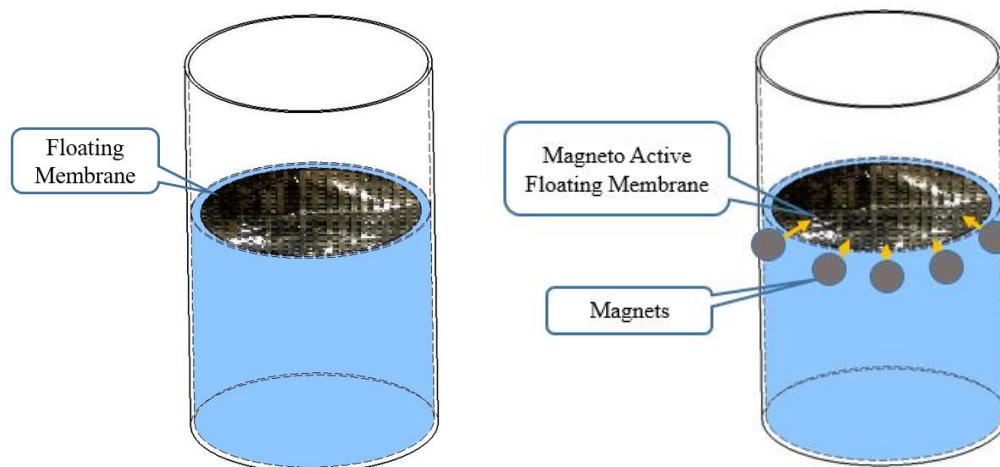


Figure 47: Slosh mitigation using PMD. Passive damping (left). Hybrid Damping (right)

Magneto Active Propellant Management Device (MAPMD) experiment is the primary payload investigated in the proposed PLD payload package. MAPMD payload is a technology demonstration in a natural spaceflight environment and will experience a microgravity time of about 3-4 minutes on board the PLD MIURA1 rocket at the end of 2022 or 2023. MAPMD is a slosh mitigation device that employs a hybrid slosh damping technique. The experiment consists of a floating membrane at the free surface of the sloshing fluid. A magnetic force from an electromagnet is used to control the magnetic membrane's orientation and motion. The membrane absorbs the kinetic energy from the liquid's free surface motion, thereby dissipating the slosh energy on the tanks.

A technology demonstration of MAPMD was carried out onboard NASA's Zero-G parabolic flight aircraft by ERAU in collaboration with Carthage College [15]. This flight

experiment served as a precursor to the suborbital test flight onboard the MIURA1 rocket, and the parabolic flight-testing and the lessons learned were applied to the design and development of the suborbital flight payload. The Zero-G aircraft executes a sequence of maneuvers following several parabolic flight trajectories to simulate microgravity and offers the investigators a gateway to weightlessness. The payload flown consisted of two experiments: the propellant mass gauging experiment and the MAPMD experiment. The MAPMD experiment consists of a transparent polycarbonate cylindrical tank internally measuring 3 in (7.62 cm) diameter and 17.7 in (44.76 cm) length with a fluid volume of 2 gallons (7.57 L). The liquid propellant was simulated using water as a safe alternative to hazardous propellants, and multiple levels of containments were employed to ensure protection from leaks or tank rupture.

The MAPMD system has been studied and developed through many years of research at ERAU. The previous research work to understand slosh behavior and experimental ground testing of the MAPMD system has improved the technology to TRL 4. The proof of concept testing on the parabolic flights has increased MAPMD to TRL 5 through component verification in a relevant environment. The goal of the MAPMD payload on the PLD mission is to demonstrate the technology in space and evaluate the effectiveness of the MAPMD system. The MAPMD development progress will be increased to TRL 6 through a prototype demonstration in space through this suborbital flight test.

The active slosh damping setup consists of a floating magnetic membrane made of Metglas and a series of permanent Neodymium magnets outside the tanks. Metglas 2714A is a nickel-iron amorphous metal alloy with a very high magnetic permeability of 1,000,000 m. This material was selected for its electromagnetic properties, along with its

high hardness and strength characteristics. Twenty-two layers of Metglas were wound around a 3D printed baffle made of ABS plastic [16]. Cameras were used to record the behavior of the liquid inside the tanks and capture the performance of MAPMD in both passive damping (floating membrane without magnetic field) and hybrid damping (floating membrane with magnetic field) scenarios.

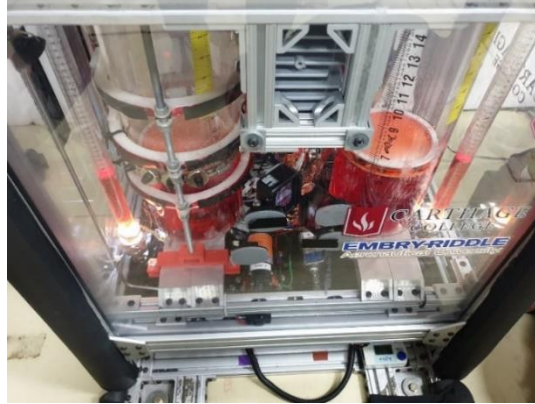


Figure 48: MAPMD Zero-G flight experiment rig [15]

Various sensors were flown with MAPMD in the parabolic flights. The experimental avionics payload unit collected flight data, also a sub payload for the upcoming PLD mission. The parabolic flight provided an excellent opportunity to test this future payload, while collecting flight environment data for MAPMD using its array of sensors. The PLD avionics payload was modified by adding a battery pack to power the payload and a LED to display sensors and data collection activation.



Figure 49: Modified avionics payload flown onboard parabolic Zero-G flight



The critical parameter that affects the fluid motion is the acceleration due to the motion of the flight vehicle, which was measured. The parabolic aircraft on which the payload was flown is shown in Figure 50, along with the corresponding Z direction. The flight trajectory consisted of 32 parabola maneuvers, and the acceleration profile is shown in Figure 51.



Figure 50: Zero-G parabolic flight aircraft [48]

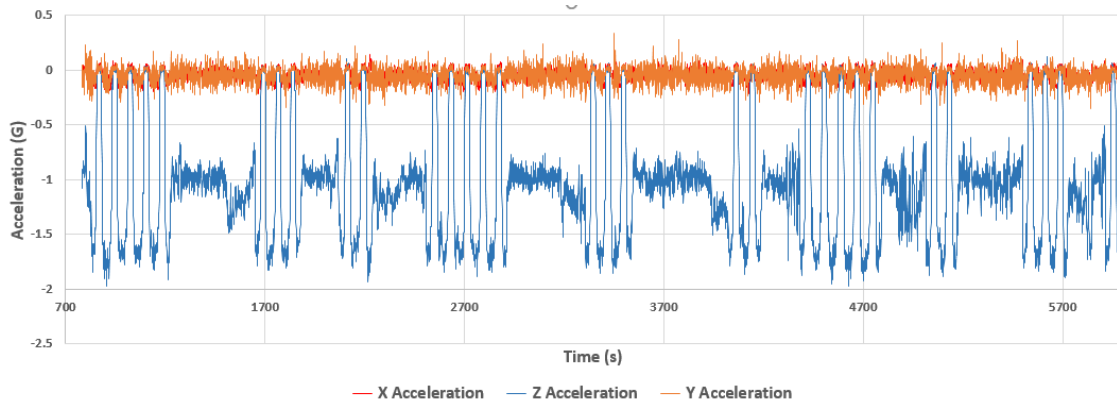


Figure 51: Acceleration profile. Zero-G parabolic flight conducted on November 19, 2020

The liquid slosh behavior inside tanks can be modeled using numerical analysis and CFD simulations. Therefore, a CFD analysis is carried out to evaluate the performance of MAPMD. The parabolic flight data (acceleration profile) and the geometry of the experimental tanks are utilized in performing the CFD analysis. The videography data of the liquid levels from the parabolic flights are used to validate the CFD models. The overall goal of the CFD analysis is to benchmark a methodology to analyze liquid behavior on payloads containing liquids and optimize the payload design based on the

results. The benchmarking could be applied to analyze trajectories on other suborbital flights using the data from parabolic flights and valid CFD models. These flight tests are costly and limited in the available microgravity time, thereby minimizing the opportunities to test various experiment scenarios and configurations. CFD benchmarking could help simulate numerous other scenarios vital in improving a new technology at faster turnaround times and lower costs.

### 5.3.2 Fluid Domain

Star-CCM+ is a commercial CFD program used by several users in the industry and academics. Star-CCM+ is utilized in performing this CFD analysis. The analysis domain is modeled in the CAD environment in Star-CCM+. The internal volume of the tank is modeled as the fluid domain. An overset region containing the floating membrane is modeled separately. This overset region is designed to move within the fluid domain using overset mesh topology, explained in later sections. The boundaries are named appropriately based on their function inside the domain. A surface repair tool is utilized to check for any gaps or problems in the model's surfaces.

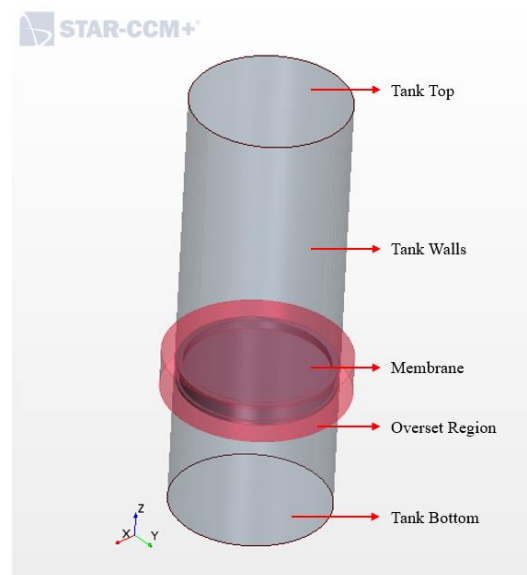


Figure 52: MAPMD CFD domain showing distinct background (Tank) and overset regions

### 5.3.3 Fluid Mesh

Meshing is the process of discretizing the computational domain to solve the governing equations of the fluid flow using an iterative process. The properties of the fluid mesh are vital in the simulation's accuracy and affect the computational solving time. A well-defined and appropriate mesh type is necessary for the domain where critical flow phenomenon occurs, such as where motion is expected. Star-CCM+ offers various options for generating surface and volume meshes on the model. The parts-based meshing technique is used for flexibility and adaptability in making the fluid mesh independent from the physics setup, so changes and edits could be performed easily. A surface mesher is used to mesh the boundary surfaces, and the trimmed cell mesher is utilized to extrude the volume mesh from the surfaces by cutting hexahedral patterns. The trimmed cell mesher offers a robust and fast method for creating aligned meshes on the domain and better free surface resolution characteristics.

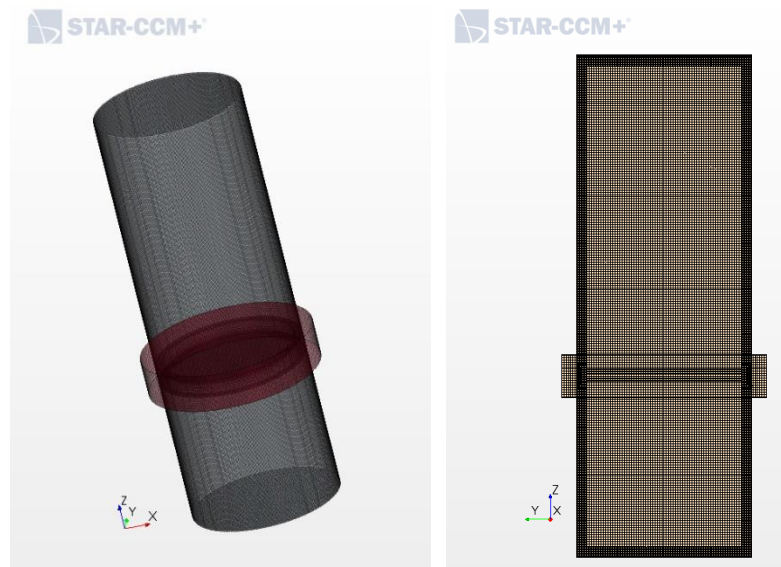


Figure 53: Volume Mesh. 3D Mesh view (left). Mesh cross-section (right)

Prism layer mesh is created on the boundaries where a boundary layer formation is expected. Prism layers produce a tight structural mesh around the boundaries and ensure proper resolution of the boundary layer.

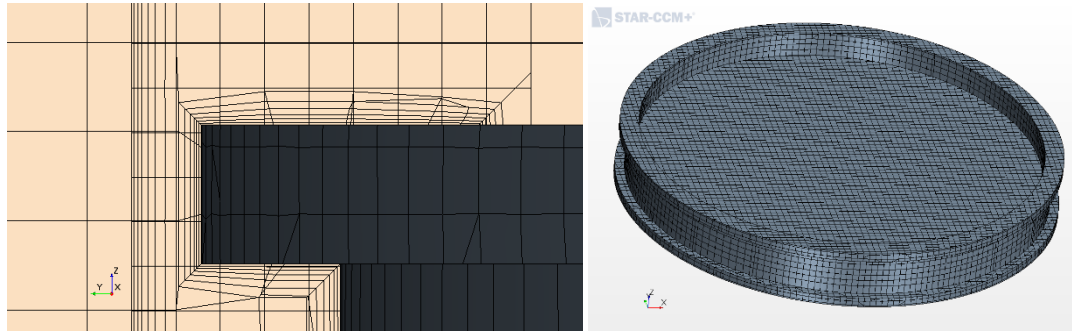


Figure 54: Mesh Details. Prism layer cells around the flow boundaries (left). Overset mesh on the floating membrane (right)

Volumetric control is utilized to refine the mesh in the areas of interest. In this simulation, distinct volumetric mesh regions are created on various areas in the domain. A more refined volume mesh is created along the walls of the tank. The gap between the membrane and the tank walls is small (2.54 mm), and proper refinement is required in this area. An essential requirement of overset meshes (explained in detail in the next section) is that at least 3-4 cells always exist between the boundaries of the moving overset region and background mesh region to ensure proper communication of parameters between the two regions. The combination of prism layers and volumetric refinements ensures that this criterion is met in all scenarios of membrane motion inside the tank. The other important criterion of overset mesh is that the mesh density or size in both regions should be of the same scale or close to the same scale to avoid overset interpolation losses. The second volumetric control on the inner areas of the tanks and overset region enforce the two meshes to be of the same density. In a scenario where the membrane rotates  $90^\circ$  with respect to the tanks and in a vertical configuration, some cultured cells around the membrane edges will overlap the under refined regions of the

tank. The overset interpolation error is expected to be small as the same mesh densities were used in the overset and background meshes. The interpolation errors could be resolved entirely by refining the mesh on the entire domain matching the cell size of the boundaries. However, this is not feasible as the overall cell count increases exponentially, and the simulation becomes highly computationally expensive to solve. The inner volumetric control is set to 0.04 in (1.016mm), and the outer volume is set at 0.08 in (2.032 mm), resulting in a mesh containing about 4.3 million cells (4.1 million cells on the tank background region and 0.2 million overset region).

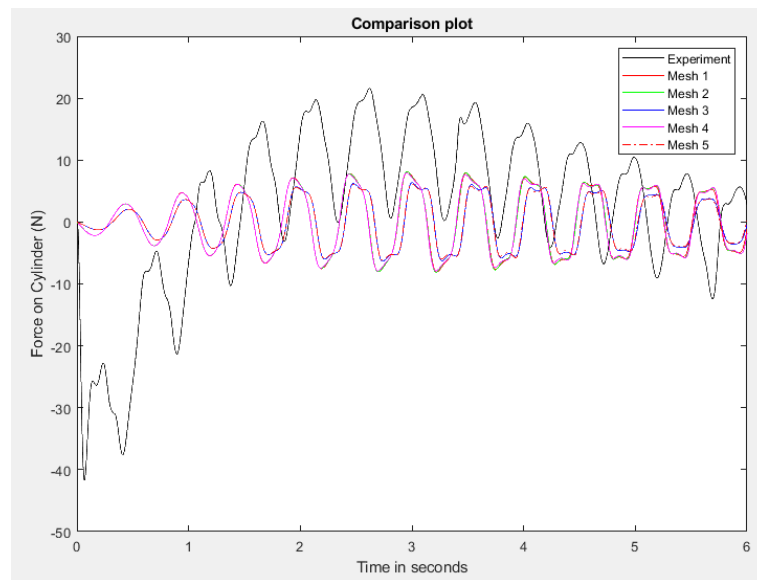


Figure 55: Free slosh comparison

A free slosh comparison is performed with the experimental ground test analysis in the MAPMD development process [27]. The slosh responses show a good correlation up to four seconds of excitation. The actuation in the original study was stopped after this time, and in the simulation, a continuous actuation was applied, which could be the difference observed in the last few seconds. A mesh independence study of the free slosh condition was performed with five different mesh sizes, and better convergence was

observed from Mesh case 3 onwards. The same mesh size parameters were employed in the passive damping cases in the scaled tank.

Table 14: Mesh independence study

Mesh designation	Base Size (mm)	Total cells count (million)	Processor solving time (hrs)
1	5.08	0.502	3.7
2	3.048	1.826	8.1
3	2.54	2.932	9.9
4	2.032	5.289	17.8
5	0.07	7.581	19.95

### 5.3.4 Overset Mesh

Overset meshing is a technique that involves the creation of overlapping independent meshes in distinct regions of the fluid domain. Overset mesh is a powerful tool when the analysis involves multiple bodies interacting or moving with respect to each other. The application of discrete meshes on independent regions offers a significant advantage by reducing the requirement to refine the mesh around moving bodies, thereby rendering a more computationally efficient solution. Furthermore, this technique avoids the mesh morphing process that is usually accompanied in simulations involving motion. In the morphing process, the overall mesh of the domain must adapt to the changes in the orientation of the moving object, and the mesh will become skewed; therefore, remesh is required if mesh quality drops below a specific value. The mesh morphing method is computationally expensive, and an overset mesh offers an efficient alternative where only the overset mesh moves with respect to the background mesh.

In this scenario, the floating membrane moves inside the tank boundaries due to the liquid forces imparted by the sloshing fluid on the membrane. In overset meshes, the cells

are grouped into inactive, active, and acceptor cells. The flow equations are solved in the active region, and the flow parameters are interpolated and exchanged between the overset and background regions at the interpolation boundary marked by the acceptor cells. The overset mesh topology performs a hole cutting process, where a hole is cut in the background mesh to accommodate the overset region cells. This process determines which cells in the domain become active, inactive, or acceptor cells. A linear interpolation method is utilized to interpolate flow parameters between the two regions. The linear interpolation method offers better accuracy but is computationally more expensive compared to other available approaches.

The overset region is modeled to extend outside the boundaries of the background region. This model maintains mesh consistency around the small gap between the membrane and the tank boundaries. As the membrane moves inside the tank, the membrane is expected to come in close proximity to the tank walls. The program is unable to interpret this behavior as the cells in the overset region exit out of the background region. A zero-gap overset interface option is available to deal with such scenarios where zero gaps are expected. It works by changing the cells in the zero-gap region to inactive cells as the two regions approach each other and the number of cells between the approaching boundaries reaches below a preset value. In this simulation, 3 cell layers are set as the zero-gap criteria, equal to a gap of 0.008 in (0.2032 mm).

The overset mesh is initialized before running the simulation to check the validity of the overset mesh. The interface was initialized without any interpolation errors or penetrations. A display scene showing overset cell status on the regions is shown in Figure 56 and Figure 57.

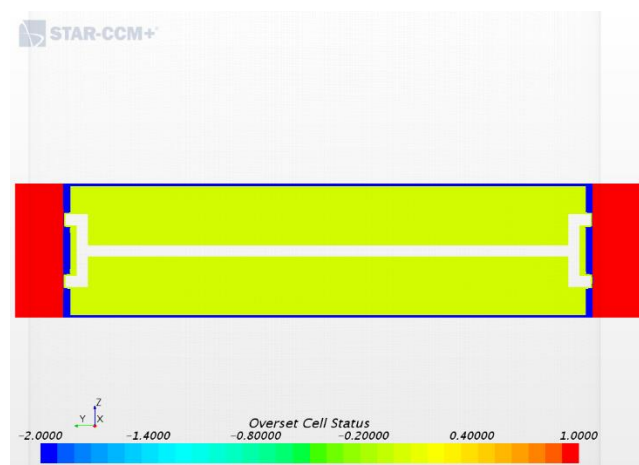


Figure 56: Overset cell status on the overset region

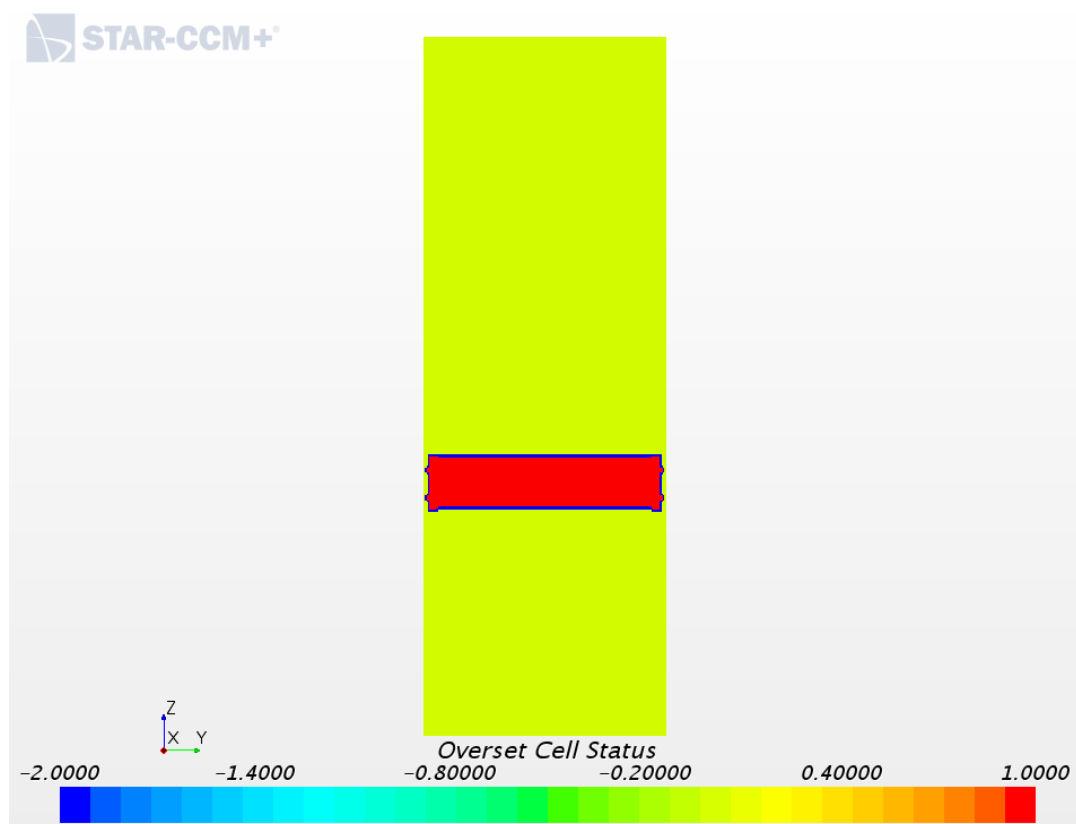


Figure 57: Overset cell status on the background (Tank) region

### 5.3.5 Simulation Physics, Governing Equations, and Boundary Conditions

The Eulerian Multi-Phase model is used to resolve the multiple fluid phases. Water is simulated as the liquid phase, and air as an ideal gas is simulated as the gas phase. The air phase follows the ideal gas equation of state. The Volume of Fluid (VOF) method is



utilized to resolve the gas and fluid phases interface. In this method, the spatial distribution of each phase at a given time [49] is defined in terms of a variable called volume fraction  $a_i$  and is given by:

$$a_i = \frac{V_i}{V} \quad (1)$$

where,  $V_i$  is the volume occupied by the corresponding phase inside a cell, and  $V$  is the total volume of the cell. The index  $i$  refers to the phase, and the parameters are solved for each phase separately (in this case, air, and water). Other flow parameters are calculated as follows:

$$\text{Density } \rho = \sum_i \rho_i a_i \quad (2)$$

$$\text{Dynamic viscosity } \mu = \sum_i \mu_i a_i \quad (3)$$

$$\text{Specific heat } C_p = \sum_i \frac{(c_p)_i \rho_i}{\rho} a_i \quad (4)$$

The governing equations of fluid flow for each distinct phase [50] are applied as follows:

Continuity equation:

$$\frac{\partial}{\partial t} \left( \int_V \rho dV \right) + \oint_A \rho v \cdot da = \int_V S dV \quad (5)$$

The continuity equation expresses the law of conservation of mass and the transport of the phases in the flow. The continuity equation has two terms on the left-hand side of the equation. The first term is the time rate of change of mass of the system, and the second term is the net rate of flow of mass through each control surface. The term on the right side of the equation is the net mass change from the mass sources.

Momentum equation:

$$\begin{aligned} \frac{\partial}{\partial t} (\int_V \rho v dV) + \oint_A \rho v \otimes v \cdot da = - \oint_A p l \cdot da + \oint_A T \cdot da + \\ \int_V \rho g dV + \int_V f_b dV - \sum_i \int_A a_i \rho_i v_{d,i} \otimes v_{d,i} \cdot da \end{aligned} \quad (6)$$

The momentum equation consists of two terms on the left-hand side. The first term is total momentum inside the control volume, and the second term is the momentum flux over the entire boundary. The terms on the right-hand side are the pressure gradient, viscous stress tensor, gravity force, body forces, and surface forces.

Energy equation:

$$\begin{aligned} \frac{\partial}{\partial t} (\int_V \rho E dV) + \oint_A [\rho H v + p + \sum_i a_i \rho_i H_i v_{d,i}] \cdot da = - \oint_A \dot{q}'' \cdot da + \\ \oint_A T \cdot v da + \int_V f_b \cdot v dV + \int_V S_E dV \end{aligned} \quad (7)$$

where  $E$  is the total energy,  $H$  is the total enthalpy,  $\dot{q}''$  is the heat flux vector,  $T$  is the viscous stress tensor,  $f_b$  is the body force vector, and  $S_E$  is the additional energy source term.

The momentum and the energy equations express the laws of conservation of momentum and energy, respectively. The momentum equation states that the time rate of momentum change in each direction equals the sum of surface forces and body forces acting on the fluid in that direction [51]. Therefore, the flow must satisfy the above equation, and generally, the solution is obtained by solving the momentum and energy equations in tandem to estimate important flow parameters.

All of the boundaries in the domain are modeled as the no-slip wall boundary condition. This boundary condition mimics the closed/contained fluid domain, as is the case in the MAPMD tank.

### 5.3.6 Simulation Cases

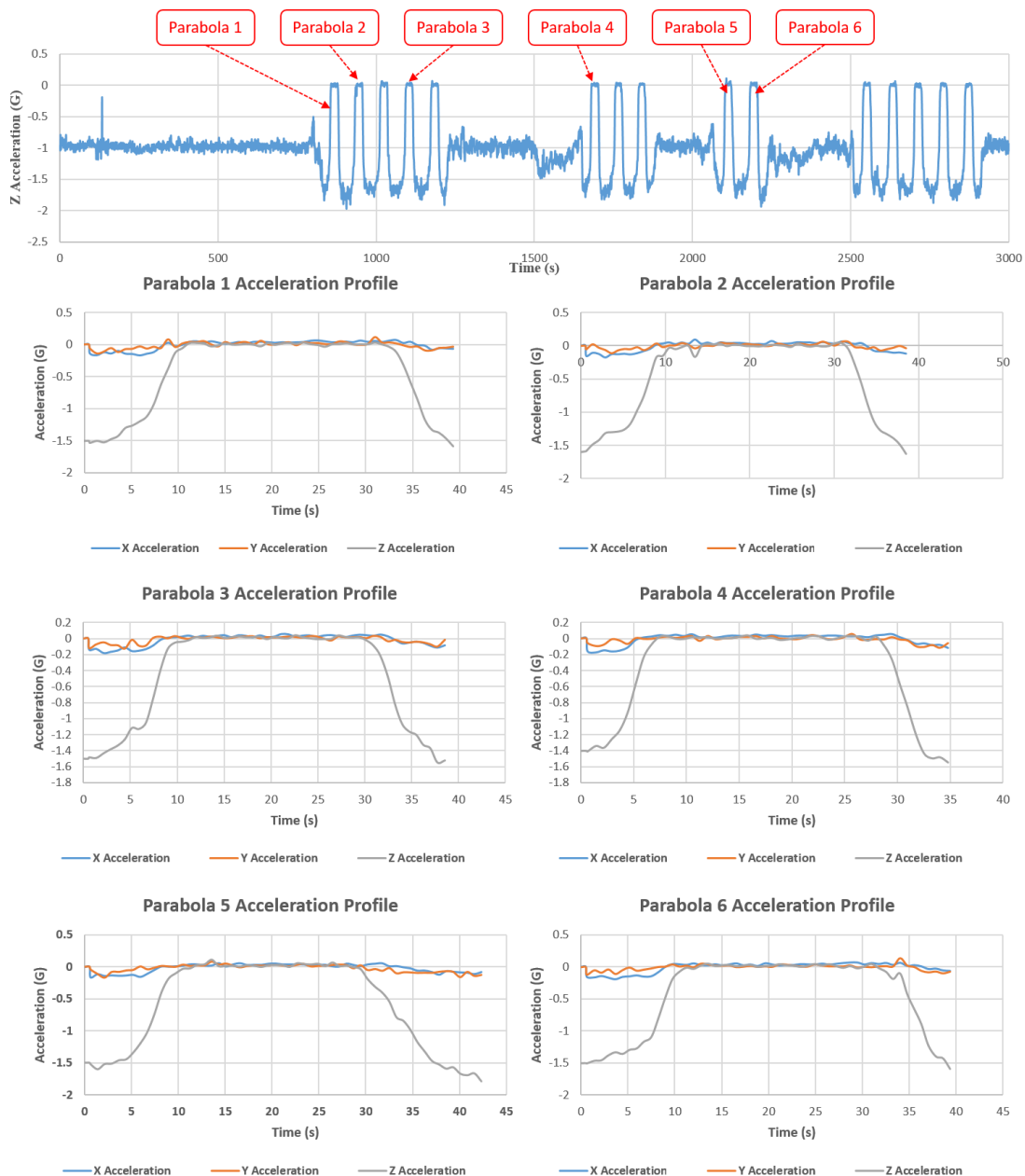


Figure 58: Parabolic acceleration profiles used in CFD simulation cases

The acceleration profile of the parabolic flights is reproduced from the experiment data by inputting these values in the “gravity reference values” entry fields of the physics continuum. The acceleration in X, Y, and Z directions are read from a table and

interpolated using a user-defined field function to apply the acceleration profile with respect to solution time.

Acceleration profile interpolation field function:  $(\text{interpolateTable}(@\text{Table}(\text{"Acce1\_1"}), \text{"Time"}, \text{LINEAR}, \text{"X"}, \$\text{Time})) * 9.80665$

Multiple parabolas were flown on a single flight, and the corresponding data were measured for each parabola. The maneuvers consisted of a continuous sequence of parabolas, followed by level flight and then repeated as a sequence. Four parabolas containing corresponding experimental results are chosen from each sequence arbitrarily and constituted four separate solution cases. The acceleration profiles are shown in Figure 58.

### **5.3.7 DFBI Motion**

The motion of the floating magneto active membrane is modeled using the Dynamic Fluid Body Interaction (DFBI) solver in Star-CCM+. The membrane is assumed to be a rigid body, and the DFBI module uses the governing equations of rigid body motion to estimate the forces and moments on the rigid body. The fluid flow inside the domain exerts pressure and shear forces on the DFBI body which are resolved into direct forces and moments on the body. The forces and moments are then used to evaluate the new position of the rigid body, and thus the new orientation and motion of the DFBI body are estimated. The governing equations of DFBI rigid body motion [52] are shown in Equations 8 to 17.

The primary source of the forces acting on the solid body from the interaction with the fluid flow is pressure and shear. The forces and moments acting on the DFBI body (floating membrane) are calculated as follows:

$$\text{Pressure forces } f_p = \sum_f p_f a_f \quad (8)$$

$$\text{Pressure moments } n_p = \sum_f [r_f \times (p_f a_f)] \quad (9)$$

$$\text{Shear forces } f_\tau = - \sum_f \tau_f a_f \quad (10)$$

$$\text{Shear moments } n_\tau = - \sum_f [r_f \times (\tau_f a_f)] \quad (11)$$

$$\text{Gravity force } f_g = mg \quad (12)$$

The total resultant force and moment on the DFBI rigid body are calculated by the summation of all the forces acting on the DFBI body:

$$\text{Resultant force } f = f_r \left( f_p + f_\tau + f_g + \sum f_{ext} \right) \quad (13)$$

$$\text{Resultant moment } n = f_r \left( n_p + n_\tau + \sum n_{ext} \right) \quad (14)$$

where  $f_r$  is the ramping factor that can be applied in the DFBI setup. The ramping factor is used to gradually increase the forces on the body after the DFBI body release time to improve the convergence of the simulation.  $f_{ext}$  and  $n_{ext}$  are all the external forces and moments applied to the DFBI body. Star-CCM+ offers various options to external input forces in the form of direct normal force, dampening coefficients, joints, or couplings.

In reaction to the forces and moment sources mentioned above, the rigid body translates and rotates about the inertial coordinate system. The translation of the body is given by Equation 15.

$$m \frac{dv}{dt} = f \quad (15)$$

where  $m$  is the body mass,  $v$  is the velocity of its center of mass and  $f$  is the resultant force acting on the body. The rotation of the body is given by Equation 16.

$$M \frac{d\vec{\omega}}{dt} + \vec{\omega} \times M\vec{\omega} = n \quad (16)$$

where  $\vec{\omega}$  is the angular velocity of the rigid body,  $n$  is the resultant moment, and  $M$  is the tensor of the moment of inertia given by Equation 17.

$$M = \begin{bmatrix} M_{xx} & M_{xy} & M_{xz} \\ M_{xy} & M_{yy} & M_{yz} \\ M_{xz} & M_{yz} & M_{zz} \end{bmatrix} \quad (17)$$

The DFBI setup involves the input of structural properties of the rigid body. The mass, moment of inertia components, and the body's center of mass are specified initially. The degrees of freedom for the motion are set initially, and, in this case, the vertical translation (along the z-axis) and lateral rotation (rotation along x and y-axis) are unrestricted, while the other degrees of freedom are restricted. The x and y translations are restricted as the gap between the tank walls, and the membranes are small in those directions. Rigid body penetration between the membrane and tank walls is expected if motion is allowed in these directions. The release time and the ramp time to freeze the DFBI motion solver during the initial simulation stages can be specified to prevent simulation instabilities and avoid divergence of the solution.

As the membrane undergoes motion due to the forces acting on it, the membrane is expected to move to the extremities of the tank, and penetration between the membrane surface and tank wall surface is expected. This scenario is more common in the passive damping scenario, where the unrestricted floating membrane is expected to move freely

up to the tank extremities during the microgravity period. DFBI motion does not automatically predict and resolve the contact of the body with other boundaries. DFBI coupling provides an option to manage such scenarios through a method called contact body coupling.

Table 15. DFBI setup parameters

DFBI Body Property	Value
Mass	0.0667 kg
Moment of Inertia Diagonal Components ( $M_{xx}$ , $M_{yy}$ , $M_{zz}$ )	(1.1918e-4, 1.19179e-4, 2.3555e-4) kg/m <sup>2</sup>
Degrees of Freedom	Z translation, X, Y and Z rotation
Release time	0.1 s
Ramp time	0 s

The contact body coupling is utilized to resolve the impact of the DFBI body on the tank boundaries. This method applies an opposing force to the DFBI body, stopping the motion when the object reaches the boundaries. The contact coupling monitors the closest distance between the surfaces of the DFBI object and the surfaces of the outer boundaries. An effective range value of 0.2 in (5.08 mm) is used. An opposing ramp force is applied on the membrane as it moves closer to tank boundaries at a distance lesser than the effective range value. The ramp force stops the body's motion and rebounds it back in the direction of the approach.

The rebound force must be entered in the contact coupling module in the form of an elastic coefficient ' $k$ .' The input elastic coefficient value must be an appropriate value sufficient to stop the motion of the body entirely before it hits the boundaries and also ensure that the repulsive force is not too large. The contact force resulting from the elastic

coefficient should be analogous to the reaction force experienced by an impacting body.

The elastic coefficient is calculated as follows:

$$k = \frac{m}{A} \cdot \frac{v_{n,rel}^2}{(d_0 - d_{min})^2} \quad (18)$$

where  $k$  is the elastic coefficient,  $m$  is the mass of the DFBI body,  $A$  is the area of contact,  $v_{n,rel}$  is the normal relative impact velocity between the DFBI body and the contact surface,  $d_0$  is the effective range and  $d_{min}$  is the minimum gap distance the body should stop.

The objective of this simulation is to predict the motion of the membrane and to understand slosh behavior. The impact velocity is not constant as the membrane moves at different velocities and impacts the surface at unpredictable durations. It is, therefore, evident that the velocity of the membrane inside the tank is unknown initially. Evaluation of the elastic coefficient is impossible without the knowledge of the impact velocity. The velocity of the membrane is monitored inside the tank, and the impact velocity is supplied to Equation 18 when a close contact condition is expected. This process involves constantly monitoring the solution, stopping and applying the necessary changes to the contact coupling whenever necessary. This process is not feasible when running the jobs in a cluster.

The contact coupling method also requires more computational resources to solve and is therefore not feasible throughout the solution. The average solution time per time step for the DFBI active simulation without contact coupling running on five nodes (36 processors per node) is 15 s per time step. The time taken per time step with contact coupling enabled under the same job settings is about 35 s. This large jump in solution



time is shown in Figure 59. It is therefore not economical to enable the contact coupling model throughout the solution.

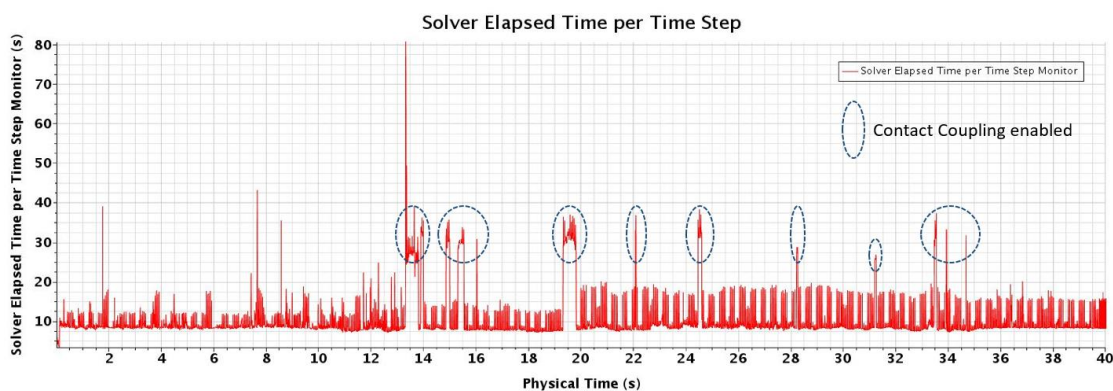


Figure 59: Time taken by the Star-CCM+ solver for each time step

A JAVA script is written to automate the switching of contact coupling when the impact is imminent and disable the coupling otherwise. The JAVA script accesses the minimum contact distance reports and the membrane velocity report from the simulation. The program then determines if contact is imminent and enables the contact coupling model with a preset effective range and a calculated elastic coefficient based on the current velocity of the membrane. The enabling/disabling of contact coupling is evident in Figure 59. This process efficiently solves the problem by saving time by not enabling the contact coupling throughout the run. The JAVA script utilized in the run is shown in Appendix A.

### 5.3.8 Simulation Execution

A time step of 0.001 s with a first-order implicit unsteady scheme is used to resolve the time progression of the simulation. The selected time step showed good convergence, and the courant number values are under the allowable limits. The time step is also chosen to ensure that the membrane motion does not exceed the distance of a single cell per time step. Based on the monitored velocity values, it is established that this condition

did not occur throughout the simulation. Eight inner iterations are solved for each time step, and it is sufficient to resolve the flow and motion within a time and showed converging residuals within time steps. The simulations are run for a total physical time averaging 40 s. Each case has different stop times as the flight parabola lengths are different.

The simulations are run on the Cray supercomputer, also called Vega, at ERAU. The simulations are computationally expensive due to the highly complex flow phenomena in this problem involving multiple phases, DFBI motion, and microgravity conditions. Vega cluster offers 84 nodes with 36-2.3 GHz cores in each node. The parallel computing option partitions the volume mesh in the simulation domain and solves each partition simultaneously. Therefore, it is more efficient to run complex CFD simulations on the supercomputer. A total of 6 nodes (36 processors in each node) is utilized in running the simulations for each case. The simulation file and the job run script are uploaded and submitted to the cluster's job queue. An example job submission script is shown in Appendix A. The simulations took approximately a week to solve for each case.

### **5.3.9 Post Processing**

The post-processing of the simulation and the acquisition of the results is done through the following reports and monitors.

*Water threshold derived part:* A threshold derived part isolates the cells containing only the water phase. This derived part is utilized to measure water only volume, mass and display water distribution inside the tank.

Water isosurface derived part: An isosurface derived part is utilized to remap the free surface of the water/air interface. This part is used in measuring the Courant number and the water surface height inside the tank.

Plane section: Custom plane sections are created to visualize the cross-section of the domain. This part is utilized in viewing the details in the mesh, interface interpolation status, and water distribution cross-sections.

Courant number report: Two reports measuring the average Courant number and the maximum Courant number on the liquid surface. These reports help in monitoring the accuracy of the interface resolution during the simulation and in validating the time step and mesh size necessary to model the multiphase flow problem

Acceleration report: The acceleration profile applied as tabular data in the simulation is monitored with respect to solution time is monitored using an expression report. Three reports will be used to track the acceleration in each coordinate direction as the simulation progresses.

Overset interpolation quality report: A new option called the overset interpolation quality report is automatically available when an overset interface is created. This report will be used to track the overset interpolation deviation between the background and overset region, and a value of zero deviation is ideal.

Water volume and mass reports: The volume of water contained in the tank is measured using a sum report. The sum report calculates the total volume of all the cells containing water in the water threshold derived part. An expression report is used to calculate the mass of water by multiplying water volume with the density of water ( $997.561 \text{ kg/m}^3$ ). The mass report is utilized to track the change in the total mass of water

contained within the CFD domain and evaluate the solution's continuity divergence. Disparities in continuity are expected when the Multiphase VOF model and overset mesh technique are used.

Water surface height report: A maximum report on the water isosurface-derived part estimates the highest point of the water surface inside the tank. This report is used for validation with graphic video evidence from parabolic flights.

Solution time reports: Two reports are created to monitor the solution progress and the actual time taken to solve and render the simulation: Total Solver Elapsed Time report measures the total time taken to solve the simulation. Solver Elapsed Time per Timestep report measures the time taken by the solver in each timestep. These reports are beneficial for monitoring simulation progress and setting the computational resources required (number of cores in the cluster) for the efficient and faster running of cases.

Force reports: Three force reports, each in corresponding coordinate directions, are created to measure the forces of the fluids on all the walls of the tank. The force measured is sourced from the pressure and shear forces of fluids impinging on the tank walls.

DFBI membrane reports: Multiple reports on the DFBI body are specifically available when a DFBI body is used in the simulation. The Membrane translation and rotation reports were created to evaluate the orientation of the membrane as it moved inside the tank. The Membrane force reports are created to evaluate the forces on the membrane. Separate reports are created for different sources of force on the membrane. The three sources are fluid force, gravity force, and contact coupling force.

Contact distance report with surface data mapper: Surface data mappers are used to map a particular parameter on the surface of an object used in the simulation. The centroid of the cells in the moving membrane body is mapped for each time step. A custom field function then calculates the distance between the mapped centroid and the centroid of another surface on the tank walls. A minimum report is used to evaluate the minimum distance between the tank walls and the membrane surface. This report is used to monitor the clearance between the membranes and the tank walls.

#### 5.4. MAPMD CFD Results

Six different parabolas from the parabolic test were simulated on the passive and active damping cases. Each parabola imparted about 20 seconds of microgravity to the payloads. The input parabolic acceleration profiles are shown in Figure 59. Only the vertical Z-axis acceleration is shown; however, all the measured accelerations in the corresponding axes were simultaneously applied.

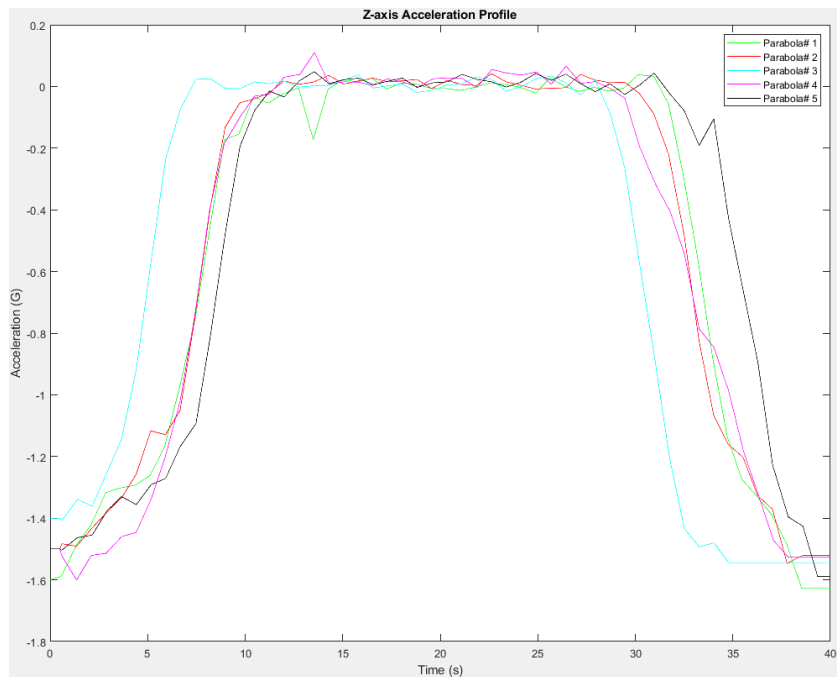


Figure 60: Acceleration profile for each simulation case

The simulation progress was monitored using the residuals and the Courant number at the water surface (air/water interface). Courant number is the ratio of the flow velocity to the size of a grid cell and measures how much information passes through a cell in a unit of time. Therefore, it measures the validity of the grid and the time step size set by the user. In general, a maximum Courant number value of less than 1.0 is preferred [53]. The average Courant number of the water surface for all six runs is shown in Figure 61. It is observed that the Courant number values are below 1 in most cases. A few spikes are encountered during critical flow interactions between the DFBI body and the flow.

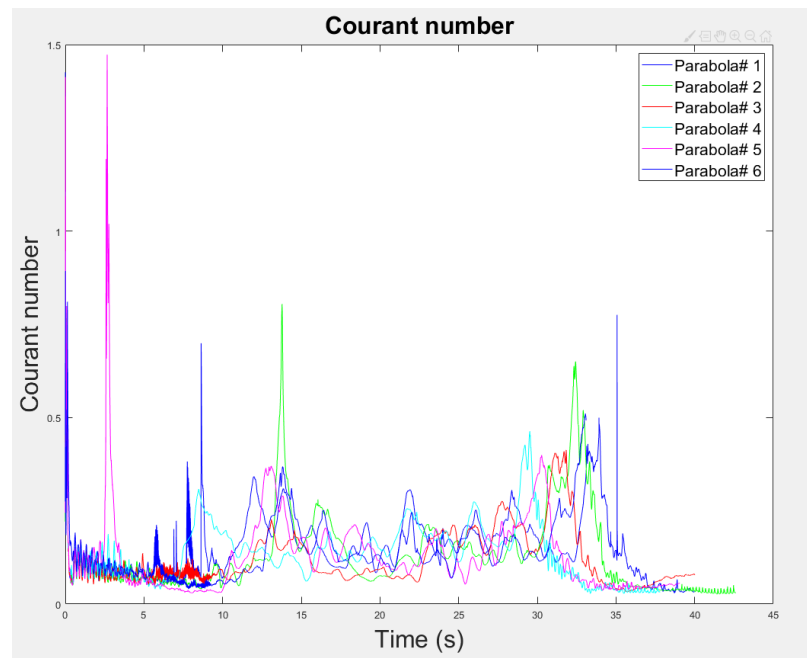


Figure 61: Average Courant number on the water surface

The maximum water level mark is estimated inside the tank throughout the simulation. As the acceleration  $G$  levels decrease, the water volume starts migrating towards the top of the tank. The water first wets one side of the tank, and bulk motion happens due to surface tension and wetting between the liquid and the solid walls of the tank. By comparing Figure 62 and Figure 60, it can be noted that the water motion begins around 10 s in simulation time which corresponds to 0.2  $G$  in acceleration level for all the

cases. Sloshing is observed in microgravity periods, and it is inferred that these disturbances could result from accelerations changes in the lateral directions. Equilibrium settling of the water volume is not observed during the short microgravity periods.

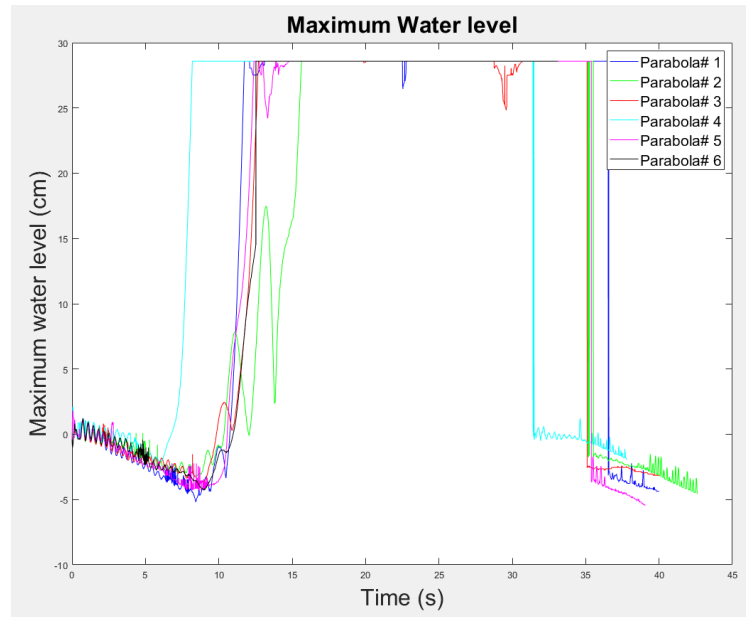


Figure 62: Maximum water level; Passive damping cases

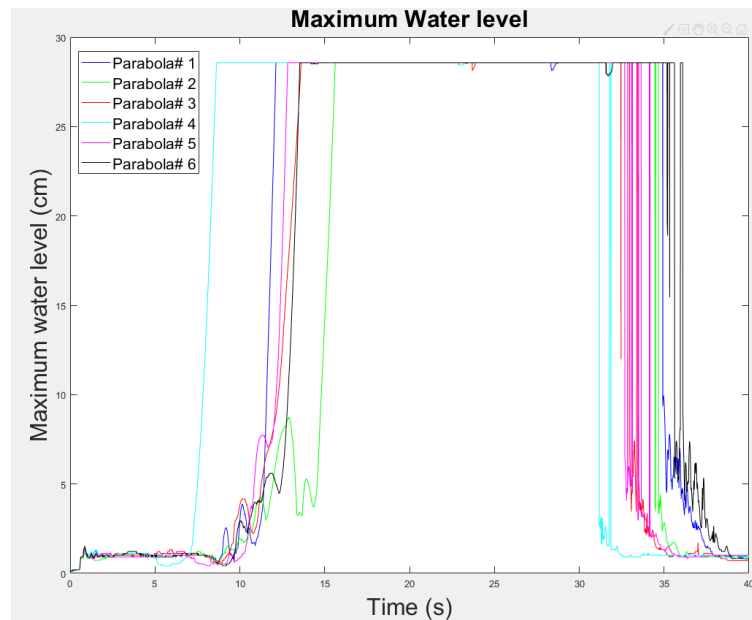


Figure 63: Maximum water level; Active damping cases

The active damping cases were simulated, assuming that the membrane body was fixed at the initial water surface. A similar trend as passive damping is observed in the

active damping cases for the maximum water levels. Since the motion of the membrane was entirely restricted, the water flowed through the gaps between the membrane and the tank walls.

The force on the tank wall due to the liquid motion is estimated and shown in Figure 64 for the passive damping parabola 1 case. These forces are due to the pressure and shear that the liquid imparts on the tank walls. Sloshing is observed during the microgravity periods. The force peaks on the graph are due to the liquid motion as the membrane impacts the tank boundaries. The evaluated force is an important parameter for estimating the slosh of the liquids inside the tank.

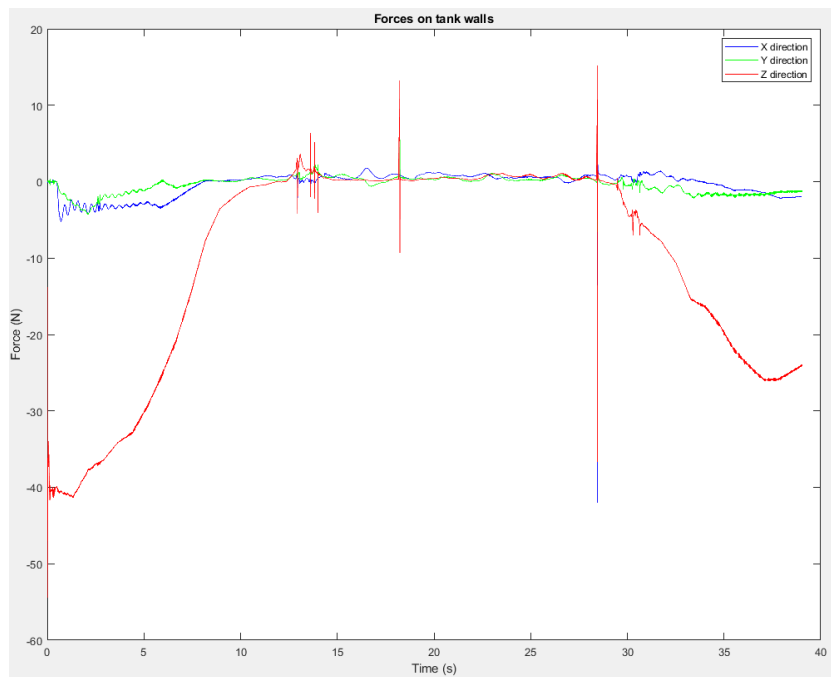
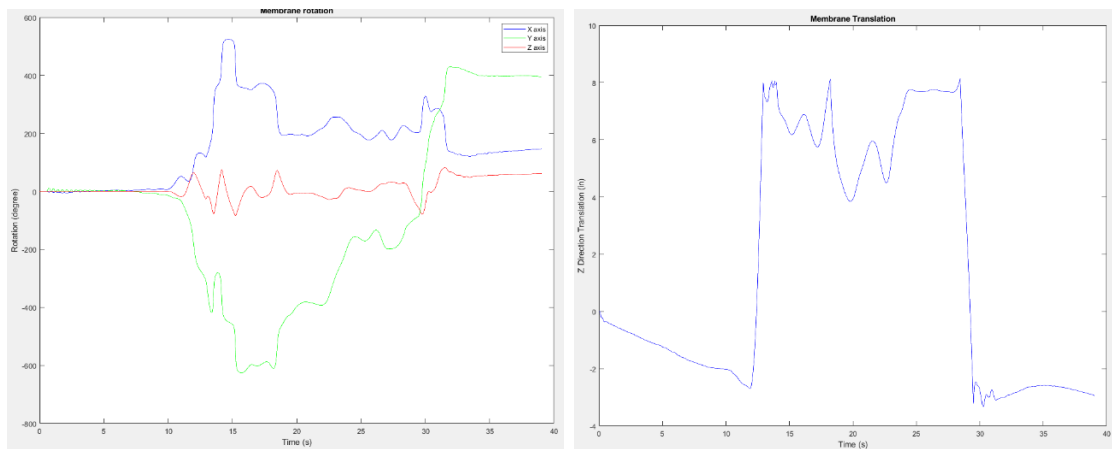


Figure 64: Liquid forces on tank walls

The membrane spatial parameters are estimated using the membrane rotation and translation monitors. The membrane translation and rotation plots are shown in Figure 65. It is to be noted that the membrane translation in X and Y (lateral) direction is restricted.



The orientation of the membrane could be compared in the upcoming suborbital flight using motion capture cameras and is recommended as a part of the MAPMD payload.



a) Membrane rotation

b) Membrane translation

Figure 65: Membrane spatial parameters

The VOF distribution of the multiphase fluid: air and water, is recorded at every time step, and the images are stitched together to form a time history. The time history animation shows the solution's progression, membrane motion, and liquid behavior subjected to the parabolic flight acceleration profile.

The water distribution and membrane orientation at different time steps are shown sequentially in Figure 66. The water initially settled in the bottom of the tank, and the membrane floats on the water surface. As the acceleration drops to around 0.2 G, the membrane flips, and the water mass begins traveling towards the top of the tank. The membrane flips and moves independently of the water location. This phenomenon was not observed in the actual parabolic flight. The membrane slid along the tank walls in the actual flight and was locked in one orientation due to friction with the tank walls. The translation was restricted in X and Y directions in the CFD simulation, and the real impact was not modeled between the tank walls and the membrane. Therefore, the membrane is moved freely in the vertical direction, causing it to flip multiple times.

Fluid-structure interaction with impact modeling is recommended to capture better and replicate the membrane behavior in microgravity. These models are computationally intensive and not conducted in this preliminary benchmarking study.

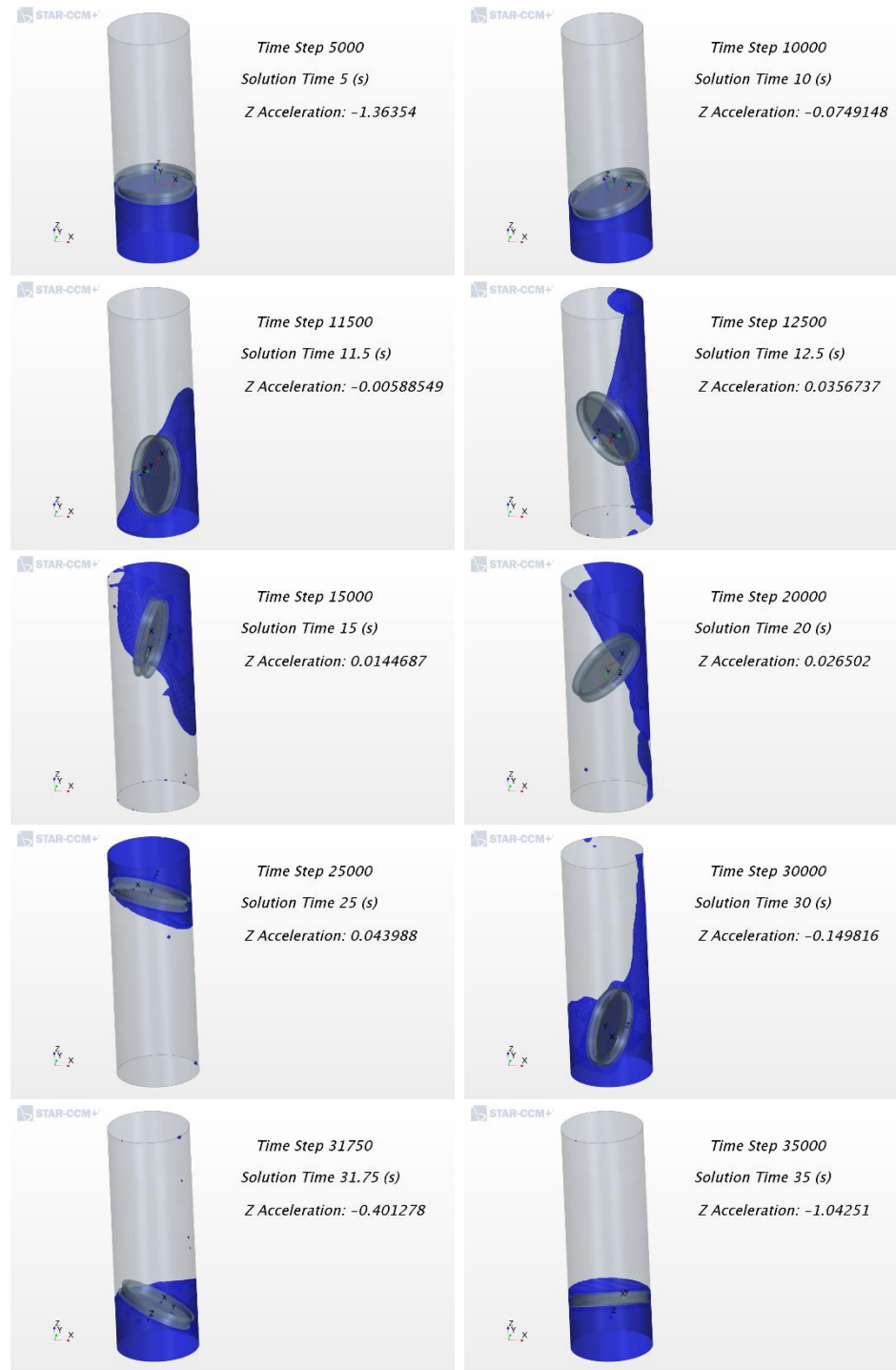


Figure 66: Passive damping case visualized at various time steps

## **5.5. PLD Payloads Vibration Test Campaign**

Payloads launched on the suborbital flight platforms experience a high-level acceleration and vibration environment. This high-stress environment influences the performance of the payload. The ability of the payload components and the structures to survive these forces is key to the success of a suborbital payload mission. The launch provider evaluates the vibration and acceleration levels experienced during the flight and provides feedback to each payload customer. The parameters are defined as Maximum Predicted Environment (MPE) in the PUG [12]. The launch provider requires each payload to be subjected to the MPE to test the survivability and to demonstrate the functioning of the experiments precisely as proposed by the payload researcher. The tests are conducted for the flight provider's requirement and improve the researcher's confidence of mission success while enabling the entire understanding of the design life and expected behavior of the experiments in flight. These physical experiments involving exact replication of the flight environment offer a unique opportunity for the engineers to make necessary modifications and better predict failure scenarios before the actual flight.

### **5.5.1 Test Objectives**

A vibration test campaign was devised to test the PLD ERAU payloads on a vibration shaker table as per the requirements of the flight provider. The baseplate, where all the payloads will be mounted in flight, was shipped to ERAU to run these tests, and the part is the actual flight hardware used in the mission. SMC standard SMC-S-016 [54] was suggested as the test standard to be followed during this test campaign. The test standard specifies test methods, key test definitions, test level durations, test criteria, and common

practices. It encompasses various environmental parameters, but this test campaign will cover only modal testing, random vibration testing, and static load testing.

Vibration acceptance tests are conducted on the flight hardware systems, and subsystems suggested in the test methodology on SMC standards. The MPE levels provided by PLD Space will be employed in the tests. This campaign aims to demonstrate that the flight hardware is free of workmanship defects, meets specified performance requirements [12], and is acceptable for delivery to the launch provider.

### **5.5.2 Test Equipment**

The test campaign was conducted on the Dynamic Solutions DS-1300VH-9 electrodynamic shaker with a GT600 M slip table at the Structures lab in Micaplex. The specifications of the shaker are shown in Appendix B. This shaker was selected based on these specifications within the test levels' margins and the test articles' mass limitations. The test campaign was part of the first-time operation of this shaker machine at ERAU. Through this test campaign and the experiences gained, it is hoped to improve the access and enable the operations of this new shaker for future researchers and payload tests.

An electrodynamic shaker system primarily consists of five components: electrodynamic shaker, amplifier, blower, slip table, and a vibration controller. The electrodynamic shaker uses field coils to generate magnetic flux, and an AC field passing through this flux imparts electrodynamic forces on the armature where the test subject is attached. The amplifier is the power supply unit for the shaker, and it converts the signals from a vibration controller to the necessary drive voltages for the field coils. The blower supplies the airflow over the field coils, which prevents them from overheating during operation. The shaker equipment and its components are shown in Figure 67.

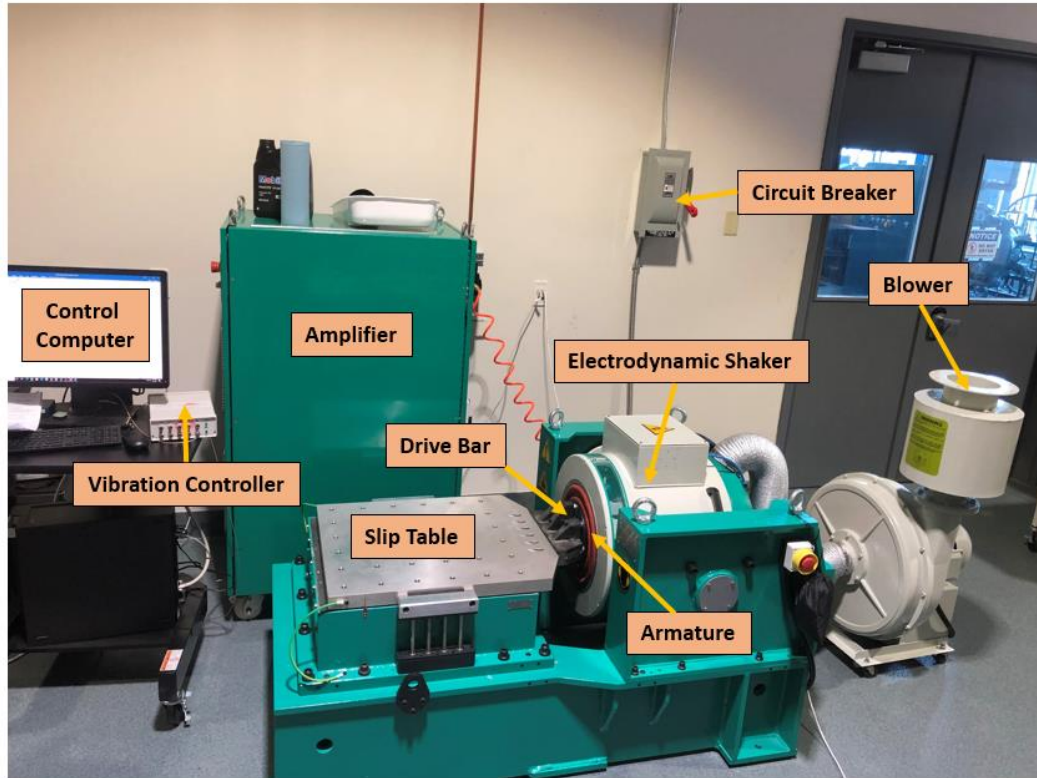


Figure 67: Electrodynamic shaker used in the vibration test campaign

The shaker table consists of two test configurations: vertical and lateral. The original setup of the shaker is designed to operate in the vertical configuration. The test article is attached to the armature on top of the shaker, and the vibrations are applied in the vertical direction. For lateral testing, a slip table is used. The slip table consists of a granite slab that slides freely over an oil film. A hydraulic pump oil is passed through V grooves under the slip table by a pump operating at  $1.0 \pm 0.2$  MPa. At a flow rate of 2L/min. A reservoir with an oil capacity of 9 L supplies the pump. The shaker can be entirely tilted using pivots and attached to the slip table using a drive bar.

A DVC-8 controller from Dynamic Solutions is used in this test campaign. The vibration controller synthesizes the user input profiles to control signals. The controller is connected to a computer, and users can input vibration profiles using the associated software provided by the controller manufacturer. The controller has a drive channel that

supplies control signals to the amplifier. Along with the drive channel, the controller also offers 8 input channels that can read acceleration data. The controller requires at least one control channel input to drive the shaker. The control channel works as a feedback loop that ensures that the controller output signals produce desired drive levels on the shaker conforming to the user input profile. The controller also functions as a data acquisition device through the other input channels. The controller processes the acceleration data from sensors mounted on the test article, and a Frequency Response Function (FRF) is generated on the computer screen. FRF shows the structural response of the test article in the frequency domain and is normalized by the magnitude of excitation. This feature of the DVC-8 controller is ideal for post-processing results as the process of synthesizing raw acceleration waveform data to FRF using Fast Fourier Transforms (FFTs) is cumbersome. The vibration controller and the associated DVC-8 control software can handle sine sweep, random vibration, and classical shock models.

Piezoelectric single-axis acceleration transducers are used as measurements devices that provide inputs to the vibration controller. The sensors are calibrated, and the manufacturer supplies the measurement sensitivities. The sensitivities are entered in the controller software application for each channel, respectively. The matching sensitivities must be accurately entered to convert voltage levels measured by the sensor to appropriate acceleration values. The mounting scheme for the accelerometer is shown in Figure 68.

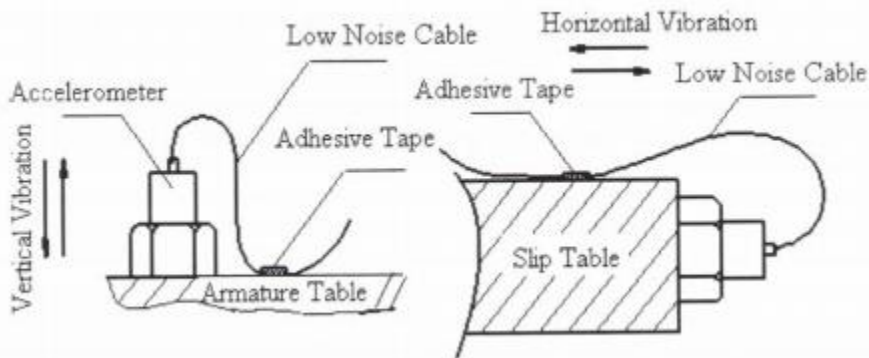


Figure 68: Acceleration sensor mounting scheme

### 5.5.3 Test Fixture

The test article mounting fixture was designed based on the baseplate design provided by PLD Space and the shaker schematics in the shaker manual [55]. The fixture serves as interfacing hardware between the shaker armature or slip table and the baseplate. The design criteria were to ensure a rigid and secure attachment of the baseplate to the shaker and symmetrically transfer the shaker motion to the baseplate. Essentially, the fixture should not cause any off-axis loading and avoid unexpected resonance to the test articles. Therefore, a low-profile design with an interfacing plate for the attachment screws and raised rectangular fixtures are designed as shown in Figure 69. PLD space recommended handling and mounting the baseplate only using the holes on the outer radius (5.5 mm holes at 66 places). The screw patterns on the attachment plate were designed to interface with the shaker armature in vertical test configuration (using 17x5/16-18 size screws in a circular pattern) and the slip table in the lateral test configuration (using 16x3/8-16 size screws in a grid pattern). The detailed mounting scheme is shown in Appendix B. PLD Space shipped the payload base plate to ERAU to perform fit checks and conduct the vibration test campaign. The original flight hardware is used in this vibration test campaign.

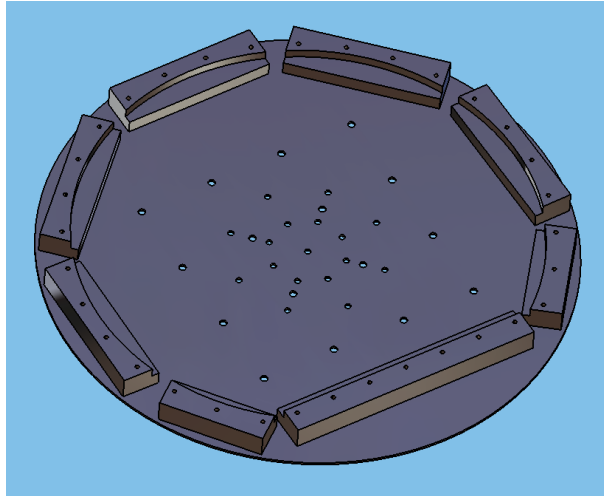


Figure 69: Test fixture design

#### 5.5.4 Test Plan and Test criteria

A test plan was developed with reference to the standards, shaker user manual, and PLD Space’s payload testing requirements and review. The acceptance test plan involves random vibration testing, modal survey, and sine burst tests performed sequentially in each corresponding axis for prescribed levels and durations. The test sequence in each axis is listed below.

- Test 1: Crosstalk test
- Test 2: Low-level Sine sweep #1
- Test 3: Random Vibration
- Test 4: Low-level Sine sweep #2
- Test 5: Sine Burst #1 low-level acceleration
- Test 6: Low-level Sine sweep #3
- Test 7: Sine Burst #2 high-level acceleration
- Test 8: Low-level Sine sweep #4

It is to be noted that the X-axis corresponds to the vertical direction or the launch vehicle thrust direction (Figure 43). Y and Z axis correspond to the lateral directions.



This is based on the convention used by PLD Space, and their axis system is marked on the attachment plate for reference and illustrated in Figure 70 and Figure 74 near the bottom of the attachment plate. A technical report of the test plan, procedures, and test criteria was furnished and submitted to PLD Space for approval [56]. The report was reviewed, and technical suggestions and recommendations were provided as feedback by PLD Space. The recommendations were incorporated into this vibration test campaign.

The sequence of tests was chosen based on standard practices recommended in vibration testing of small satellites [17]. Using a low-level sine sweep technique, the modal survey test is performed before and after each significant test to retrieve and compare the structure's FRF, which will serve as a basis for each vibration test's pass/fail criteria. Any changes in the FRF between the tests can indicate changes in the structure in local yielding or fastener failure. The variance in low-frequency modes is the primary concern as they indicate changes in the main payload structure. Higher frequency mode changes indicate issues in the fasteners or joints of the structures. PLD space requirements suggest that an FRF change of 5-10% in the frequency is acceptable.

SMC standard recommends testing all electronics systems in the intended mission operation to test for failures. Since all the sub payloads contain electronics, all the circuits were assembled and operated during the testing. All the cables, connectors, and harnesses were replicated in the test as in the actual flight configuration. The following pass/fail criteria were formalized based on these recommendations:

- The test profile and the input excitations should match the recommended MPE.
- The difference between the FRF frequencies of the first and second significant modes between two subsequent FRFs shall not exceed 10%.

- The difference between the FRF response levels of the first and second significant mode between two subsequent FRFs shall not exceed 30%.
- Payload electronics should be fully operational during the tests and function nominally throughout the test.
- Visual inspections should ensure no structural damage to any of the payload components.
- Fasteners, joints, and attachment points should not become loose.

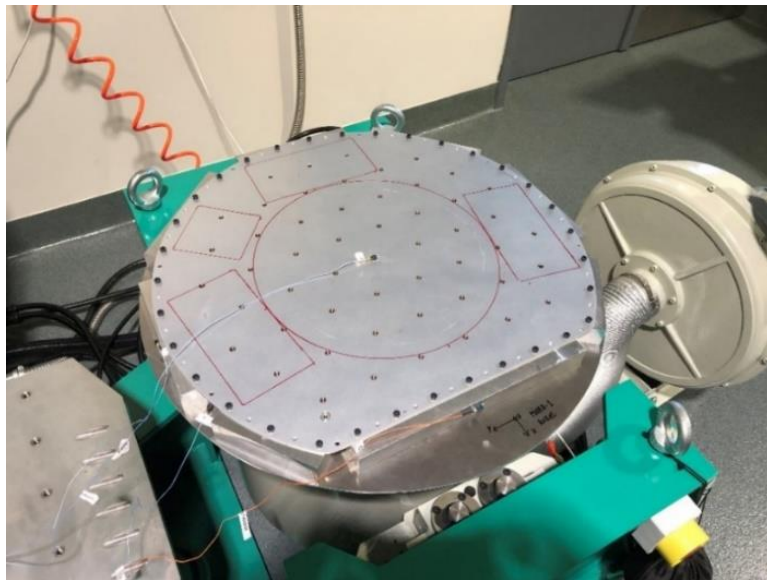


Figure 70: Crosstalk test setup

Crosstalk test is a method to verify the proper leveling of test fixtures and ensure uniform distribution of input excitation on the test article. The crosstalk must be conducted when running new tests on each axis before mounting the payloads on the baseplate. The test involves attaching a single accelerometer pointing to the fixture in each native axis direction (X, Y, and Z). The control accelerometer is attached to the shaker armature. As per the SMC standards [54], the crosstalk levels shall not exceed the input levels for the respective axes. The crosstalk test setup in vertical test configuration is shown in Figure 70.

Table 16: Low-level sine sweep test parameters

Setup parameter	Value
Frequency range	5-2000 Hz
Constant acceleration level	0.5 G
Sweep type	Logarithmic
Sweep rate	1.5 octave/min
Sweep direction	Ascending

Low-level sine sweep test is performed between each vibration test to estimate the natural frequencies of the structure. The result is an FRF that compares each payload's structural response between each major vibration test. In a sine sweep test, the shaker imparts sinusoidal accelerations at gradually increasing or decreasing frequencies. The test is usually performed at a constant acceleration level between a range of frequencies. The acceleration levels are kept very low as the response acceleration of the structure at resonance can be significantly higher than the excitation acceleration. This test does not involve subjecting the test articles to MPE vibration levels and does not assess the structure's survival in the flight environment. It is instead a test probing the structure's FRF. Therefore, low acceleration levels are used in order not to damage any of the flight hardware components. The following parameters are used in the low-level sine sweep tests.

The parameters shown in Table 16 are based on PLD Space's test recommendations. The frequency range is the range between which the frequencies are varied. Acceleration level is the sinusoidal peak amplitude of the input waveform. A logarithmic sweep type updates the frequency values in logarithmic steps. The sweep rate is the speed at which the frequency is swept between the lower and upper-frequency ranges. The value of 1.5 octave/min takes about 4 minutes and 50 seconds to sweep through the entire frequency

range and is sufficient to capture all modes. The frequency will be swept in only one direction from lowest to highest frequency. The sine sweep profile setup in sine controller software of the DVC-8 controller is shown in Figure 71.

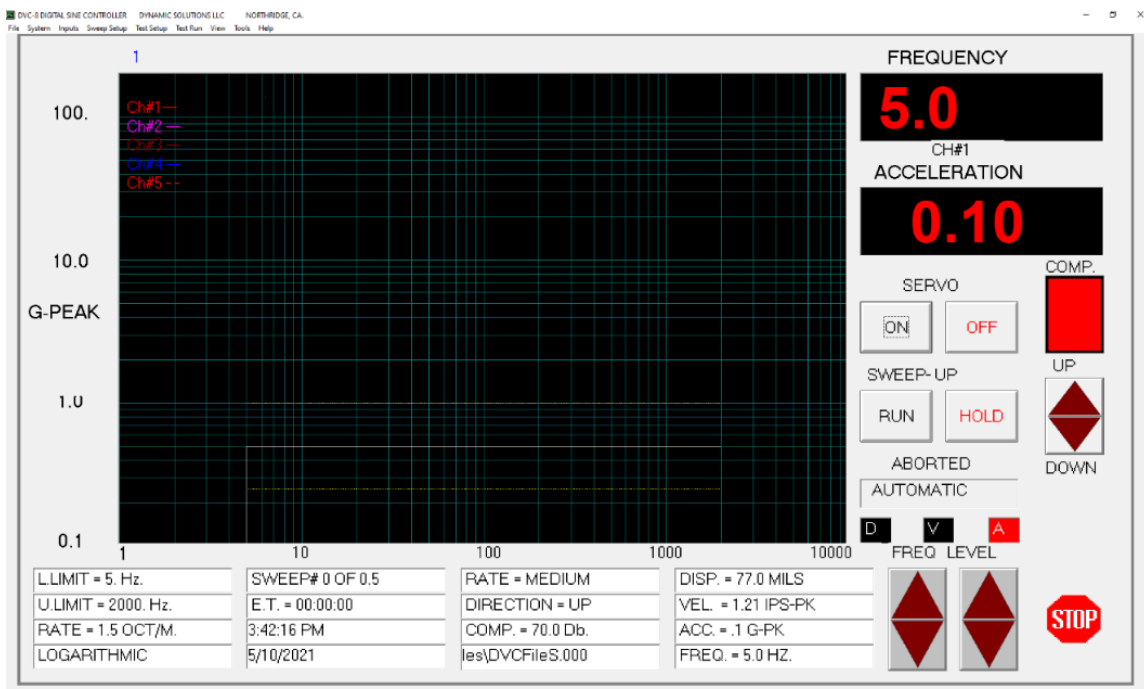


Figure 71: Sine sweep profile setup on the DVC-8 sine controller software

Random vibration test is one of the primary vibration tests conducted in the test article. Therefore, a random vibration environment is expected during the launch and powered flight of the suborbital launch vehicle and is one of the primary satellites and payload test requirements. In a random vibration test, the test article is simultaneously subjected to multiple frequencies, and acceleration levels are varied at each frequency randomly. The name “random vibration” is hence derived from the randomness of the excitation parameters. The input levels are specified in terms of Acceleration Spectral Densities (ASD) with respect to frequencies. The parameters used for acceptance testing of payloads with mass less than 23 kg are given in Table 17.

Table 17: Random vibration profile breakpoints

Frequency (Hz)	ASD ( $G^2/Hz$ )
20	0.002
100	0.01
1000	0.01
2000	0.0025

Overall acceleration level is 3.8 GRMS

The random vibration acceptance level test is conducted for a duration of 60 seconds on each corresponding axis. The acceptance testing involves subjecting the flight hardware to MPE and. A pretest of the assemblies is conducted at 3dB below the whole excitation level for a few seconds and ensuring all assemblies are safe before the whole vibration level is applied. The random vibration profile setup in random controller software of the DVC-8 controller is shown in Figure 72

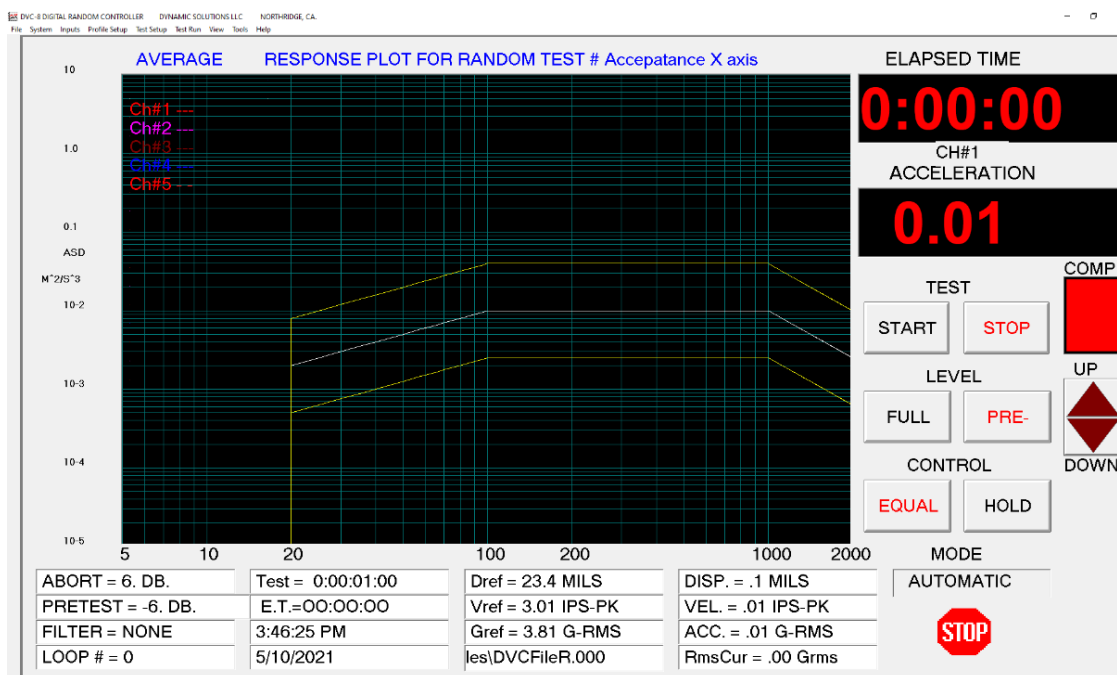


Figure 72: Random vibration profile setup on the DVC-8 sine controller software

Sine-burst test is performed to subject the payloads to maximum acceleration loads expected during flight. The maximum loads are usually experienced during launch and parachute deployment events flight phases. A sinusoidal acceleration is applied to test the article by the shaker at a constant low frequency. The acceleration levels are gradually increased, maintained at the expected load levels, and then decreased. A low frequency is selected to avoid exciting the structure at resonant frequencies. This test is also called a quasi-static load test, as a constant load is not applied for a continuous duration. Sine-burst testing is an efficient method that allows complete envelope acceptance testing of payloads under a single test platform. The prescribed load levels are shown in Table 18.

Table 18: Sine-burst test specifications

Test name	Axial static load (G)	Lateral Static load (G)
Low level sine-burst (Ascent)	+6.0	±1.0
High level sine-burst (re-entry)	-15.0	±3.0

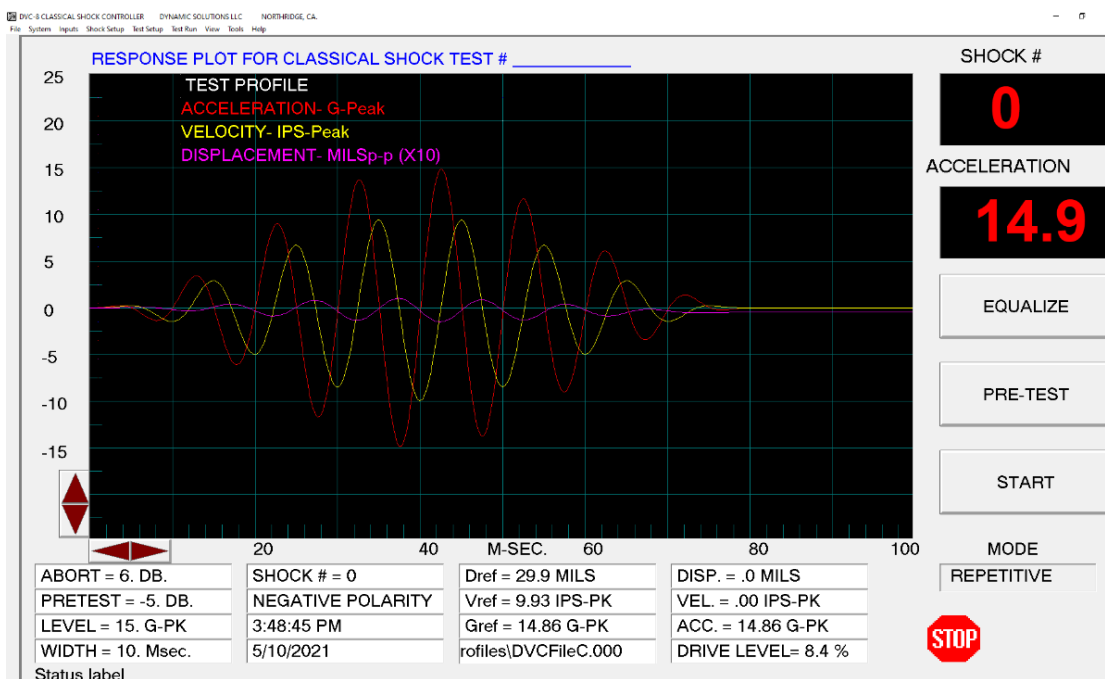


Figure 73: Sine burst profile setup on the DVC-8 sine controller software

Thirty sine-burst waveforms are applied continuously at a rate of 1 sine-burst/s. Each wavelet is administered for 10 ms, and the acceleration level is switched between 1 G and 3 G for lateral tests and 6 G and 15 G for axial tests. The sine-burst test profile setup in classical shock controller software of DVC-8 controller for a 15 G load is shown in Figure 73.

### **5.5.5 Test Setup Procedures**

The test setup assembly procedures shown in Appendix B are carried out to assemble the payloads on the shaker table. The procedures are carried out in the following order:

1. The shaker test section is leveled by adjusting the airbags, and a height level indicator is used to inspect the leveling. While running tests on the slip table, the hydraulic pump oil is filled in the reservoir, and the pump is operated for at least 15 minutes before testing or reorienting the shaker.
2. The attachment plate is fastened to the shaker armature or the slip table using appropriate screws.
3. The fixtures are mounted and aligned on the attachment plate.
4. The baseplate is placed over the fixtures, and appropriate screws are used to fasten the test assembly.
5. All the sub payloads are assembled to resemble their flight configurations. Cable wiring and harnesses are connected and secured.
6. MAPMD sub payload is mounted on the base plate using M5 screws, and the NanoLab payloads are attached to the base plate using dual lock Velcro strips.
7. The accelerometers are attached to each sub payload using wax (Figure 74).

A separate accelerometer is connected to record the response from each sub payload: MAPMD, Shunt, and one on each avionics/telemetry payload. A control accelerometer is mounted on the fixture plate or slip table depending on the test configuration being performed. The controller uses the control accelerometer data to evaluate the necessary drive voltages for the shaker to match the vibration profile set by the user. The accelerometers are connected to channels with unique identifiers on the DVC-8 controller. Table 19 shows the accelerometer placement locations, connected channel, and corresponding sensor sensitivity.

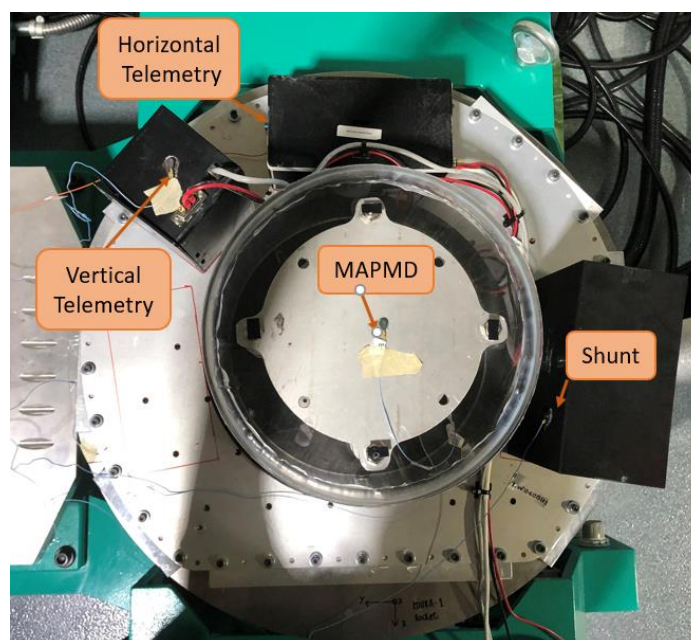


Figure 74: Acceleration sensor locations on the sub payloads

Table 19: Accelerometer placement locations

Channel Number	Location	Sensitivity (mV/G)
1	Fixture plate or slip table	98.6
2	Shunt payload	101.6
3	MAPMD payload	101.6
4	Horizontal avionics/telemetry payload	9.81
5	Vertical avionics/telemetry payload	101.4



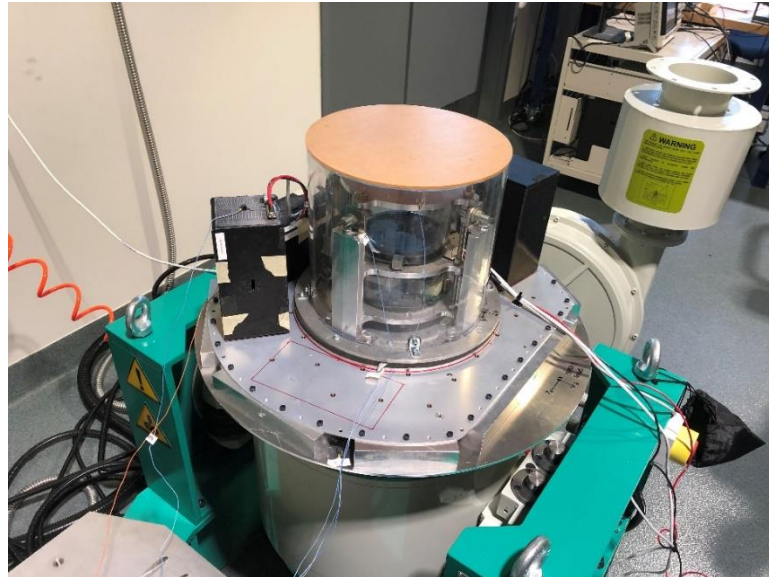


Figure 75: PLD ERAU payloads mounted in the vertical configuration (old design)

The first done is performed in the vertical/axial configuration, and the assembled payloads are shown in Figure 75. After the test, all the sub payloads are removed, and the test fixtures are dismantled. The shaker is tilted and locked in the horizontal position. The shaker armature is connected to the slip table using a drive bar, and the entire test assembly is mounted on the slip table (Figure 76) following the same steps as above.

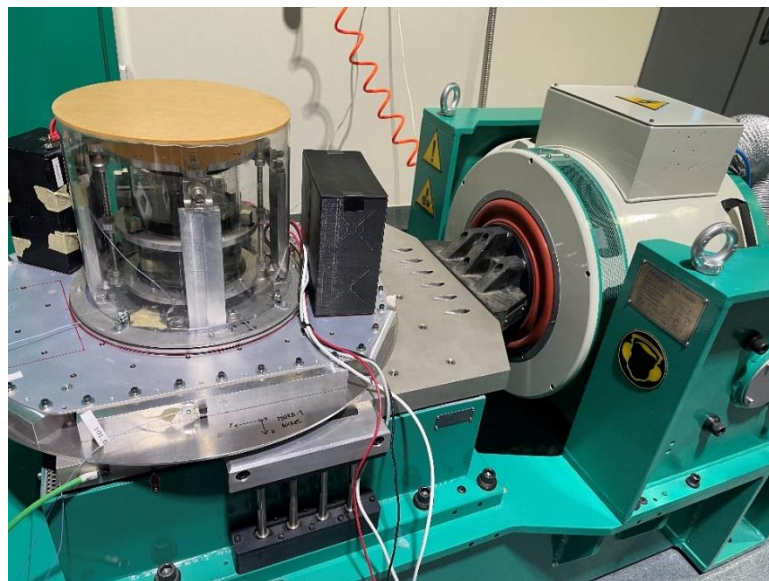


Figure 76: Lateral testing configuration on the horizontal slip table

### 5.5.6 Vibration Test Results

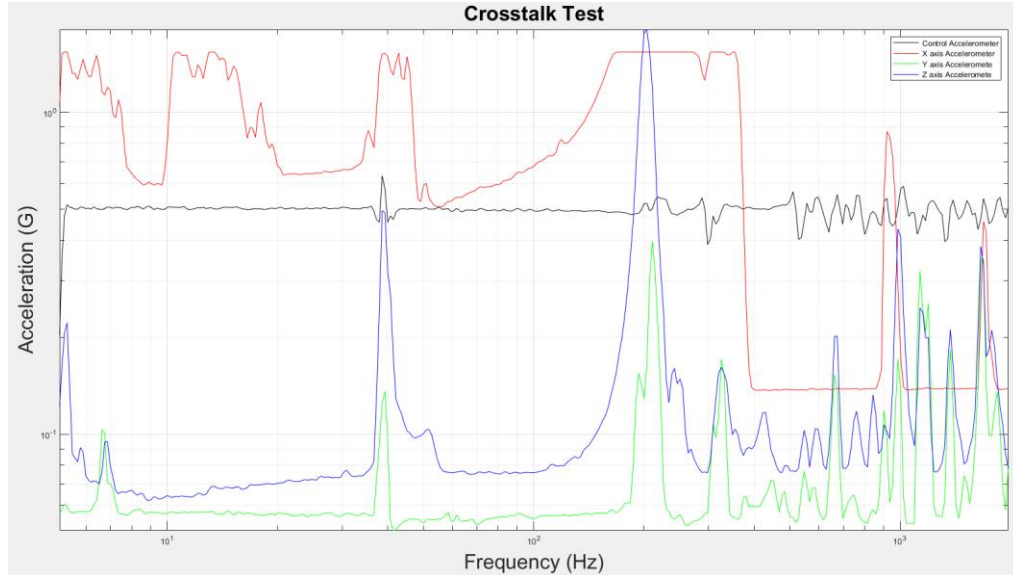


Figure 77: Crosstalk test in vertical configuration (X-axis excitation)

The vibration test campaign was conducted at the Micaplex Structures lab with the actual flight hardware on the shaker table between May and June 2021. The first test was the crosstalk test in the vertical test configuration with excitation along X-axis. The later test configurations correspond to Y and Z axes.

A low-level sine sweep was performed to evaluate crosstalk levels. From Figure 77, it can be observed that an excitation response is only present along the X-axis (direction of excitation). The acceleration response in the Y and Z directions is well below the control accelerometer response, thus confirming the pass criteria for the crosstalk test. The fixture also undergoes resonance, and the natural frequency peaks must be ignored in this test as they are periods of resonance. Similar responses were observed in the lateral configuration crosstalk tests, and the fixture assembly passed the test criteria in all the instances.

It is to be noted that there were two successive test campaigns conducted. The main difference between the two campaigns is the modification of the MAPMD payload

design. The first test campaign showed irregularities in the MAPMD structure, specifically after 15 G, high-level sine burst testing in a vertical configuration. The discrepancies can be noticed in Figure 78, and the significant difference in post sine burst FRF frequencies failed test criteria. The fasteners lost their tension, and the payload design also had to be changed to meet PLD Space’s size requirements. The modes are the particular frequencies at which significant acceleration peaks are observed.

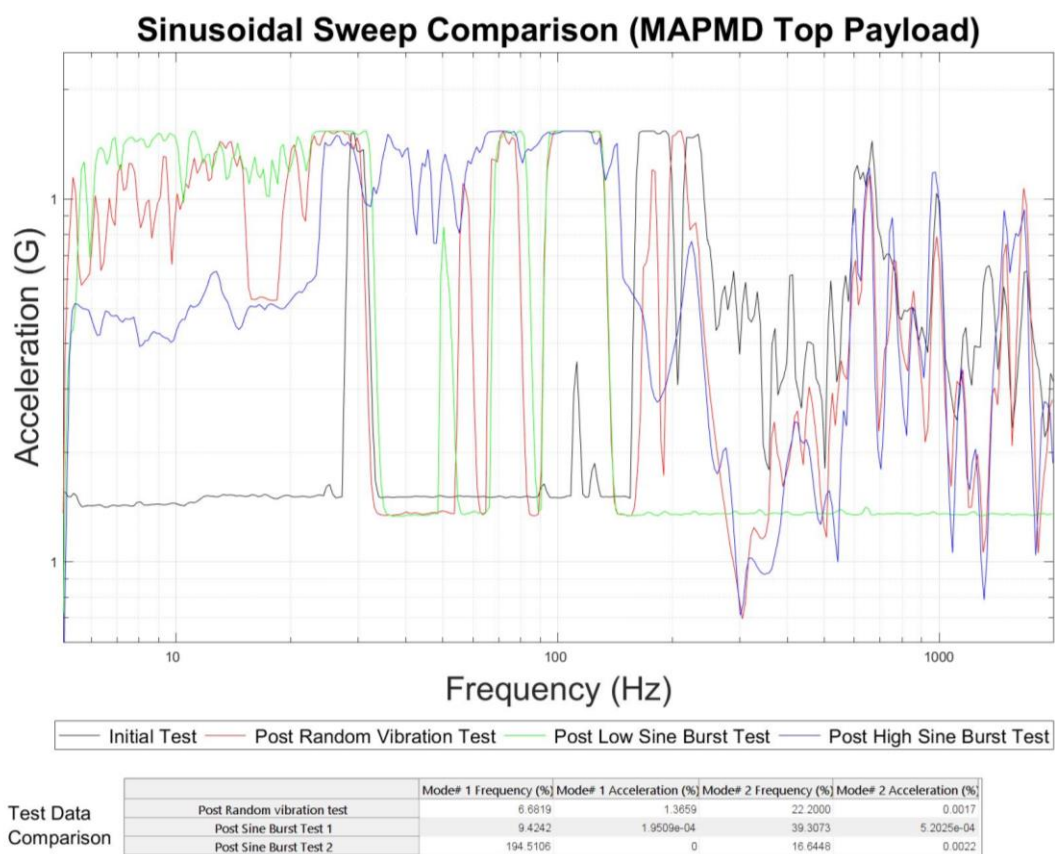


Figure 78: Preliminary MAPMD hardware FRF

The modified MAPMD design discussed in Section 5.1 and shown in Figure 41 was fabricated, and the modified structure of the MAPMD payload is shown in Figure 79. The Shunt payload electronics were turned ON during final tests. All results furnished in the following sections are from the vibration testing of the modified payload assembly flight hardware.

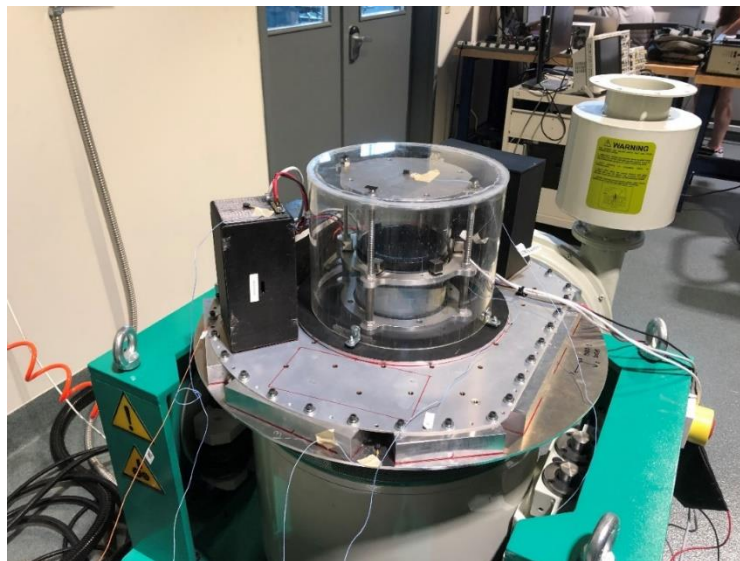


Figure 79: Modified and final flight hardware version mounted on the shaker table

The random vibration test response shown in Figure 80 does not characterize the structure's test criteria but rather validates that the control (blue line) accelerometer response matches the input random vibration spectrum (black line). The random vibration method applies acceleration levels at random frequencies, and the spectrum is synthesized statistically. Longer duration runs produce better synthesis results.

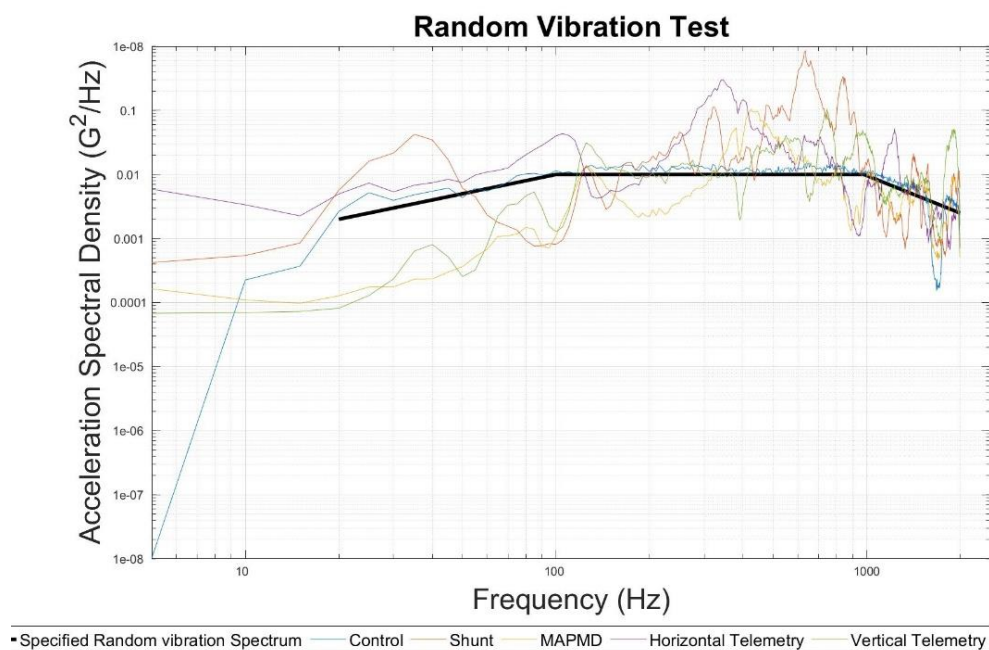


Figure 80: Random vibration test ASD response of the Lateral Y test

The high level 3 G sine burst test response in lateral test configuration is shown in Figure 81. The peak control frequencies show the levels specified as an input in the controller software. The same pulse waveform is repeated 30 times in each test.

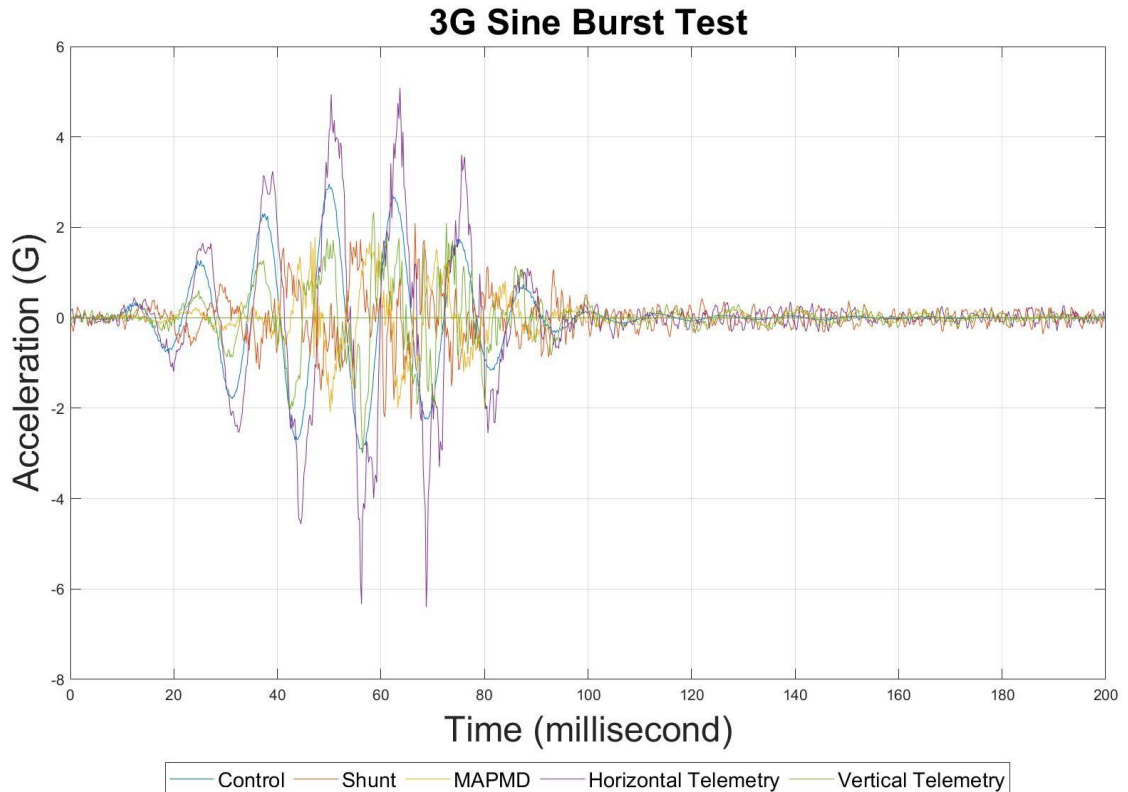


Figure 81: Lateral test of high-level sine burst with 3 G quasi-static load condition

The following plots will show the low-level comparisons between each major vibration test: Random vibration, low-level sine-burst, and high-level sine burst. The sinusoidal sweep comparisons will highlight any changes in the structure between each test. The first two significant modes will be compared to determine the health of each sub payload between every test. Additional test criteria involved visual inspection, total electronics system runs and checks, and fastener inspections.

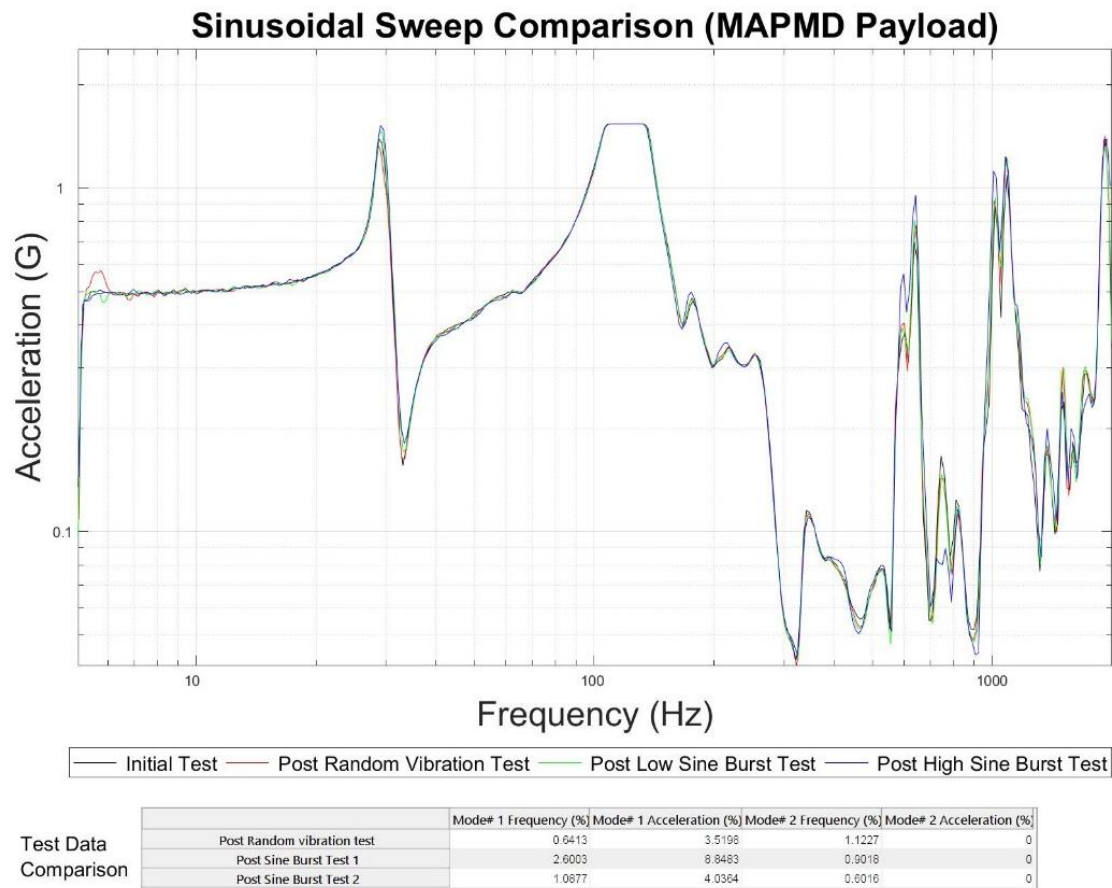


Figure 82: FRF comparison: Vertical test configuration, MAPMD sub payload

The vertical configuration test with vibration excitation applied in the X direction was conducted after the crosstalk test. The same random frequency spectrum (Table 17) is used in all the random vibration tests. However, the sine burst test levels are varied depending on test configuration. In this case, a low-level sine burst of 6G and a high-level sine-burst of 15G was applied. A peak-to-peak difference analysis was performed in MATLAB to evaluate the difference in modal frequencies and acceleration response levels. FRF comparison (Figure 82) between each sine test for MAPMD payload shows the excellent correlation between the peaks' modal frequencies and acceleration levels. A maximum frequency difference of 2.6% is observed after the low-level sine burst test,

and an acceleration response difference of 4% is observed after the high-level sine burst test. Both the test results are well within the test pass/fail criteria.

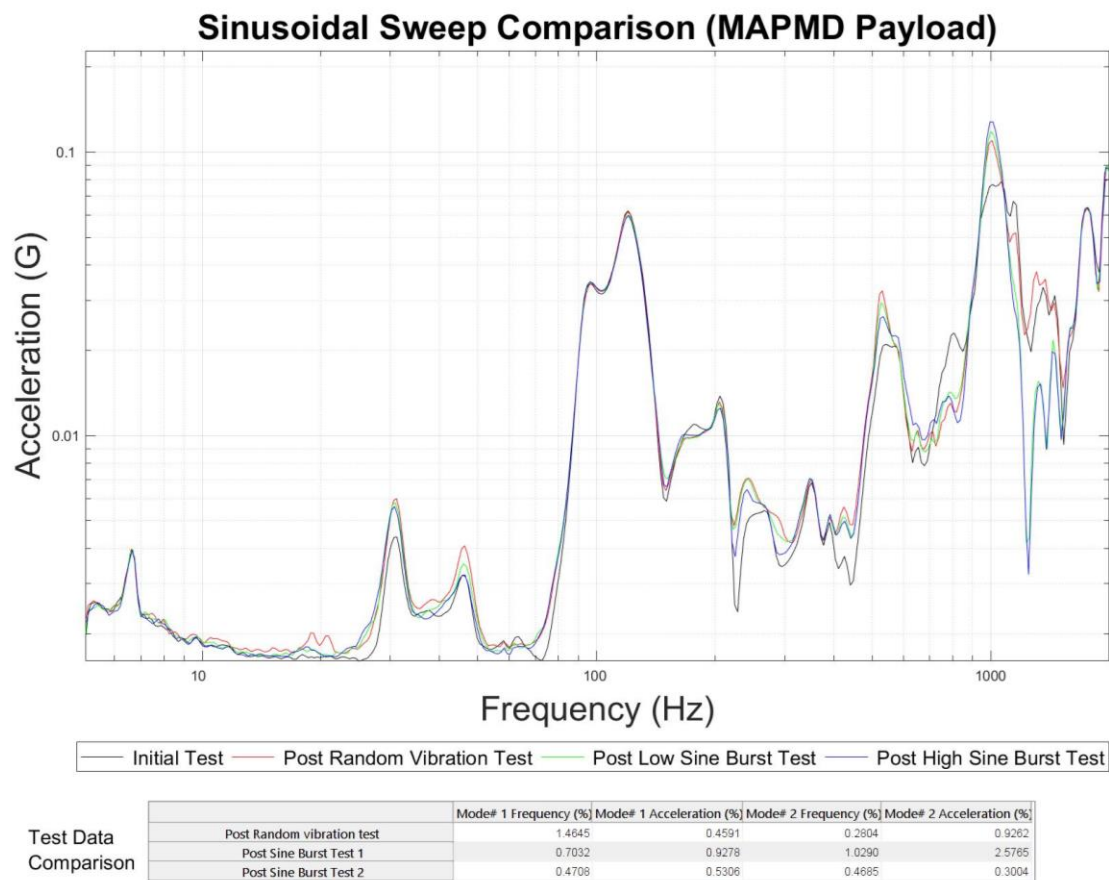


Figure 83: FRF comparison: Lateral test configuration (Y direction), MAPMD sub payload

The lateral test configuration was set up on the slip table, and the vibration excitation was applied in the Y direction. Compared to a vertical configuration, the difference in vibration test levels is low-level, and high-level sin-burst levels were run 1 G and 3 G, respectively. FRF comparison for this test case shows a good correlation between the MAPMD payload and the structure that passed the test criteria. A maximum frequency difference of 1.45% and acceleration response difference of 2.5% was recorded.

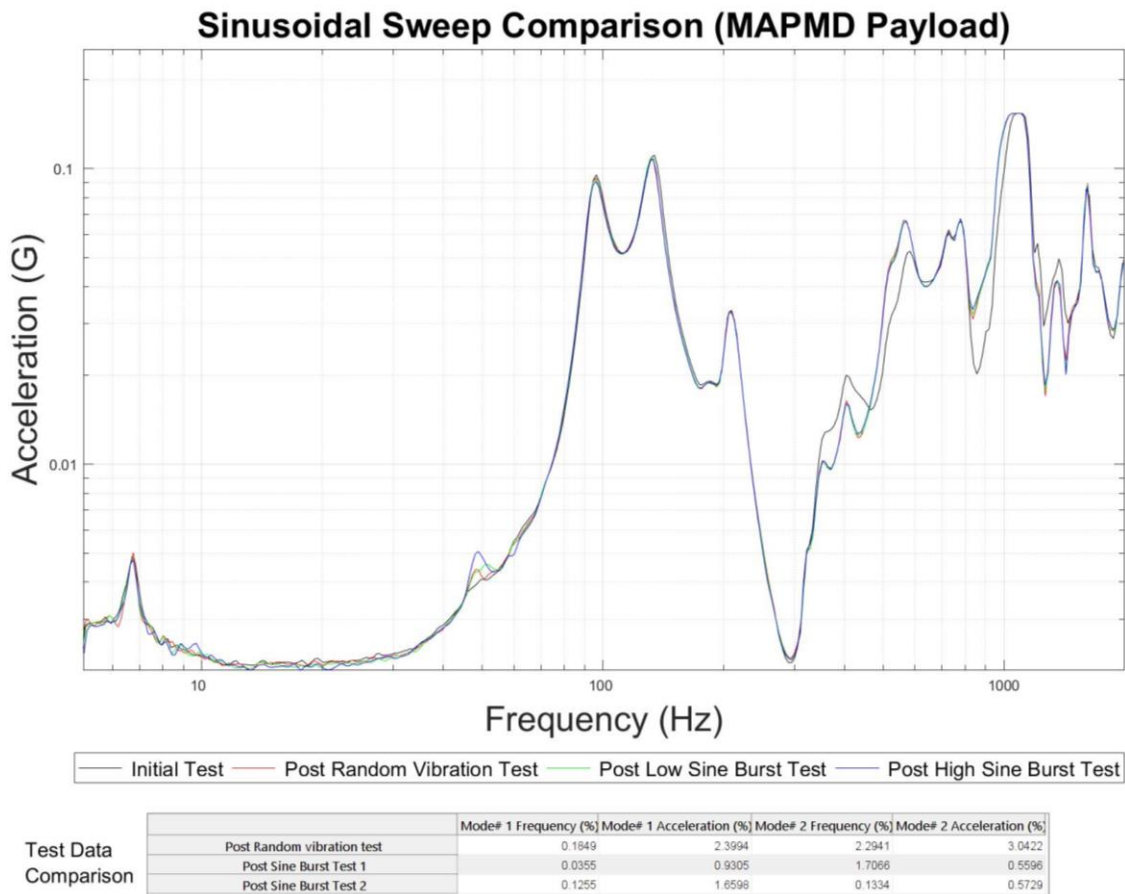


Figure 84: FRF comparison: Lateral test configuration (Z direction), MAPMD sub payload

The same lateral test levels were replicated in the Z direction test after removing the baseplate and reoriented on the slip table. The results show a good correlation between modal frequencies after each test. A maximum frequency difference of 2.3% and acceleration response difference of 3% is measured on the first two significant modes. MAPMD payload structure passed all the tests in each axis direction.



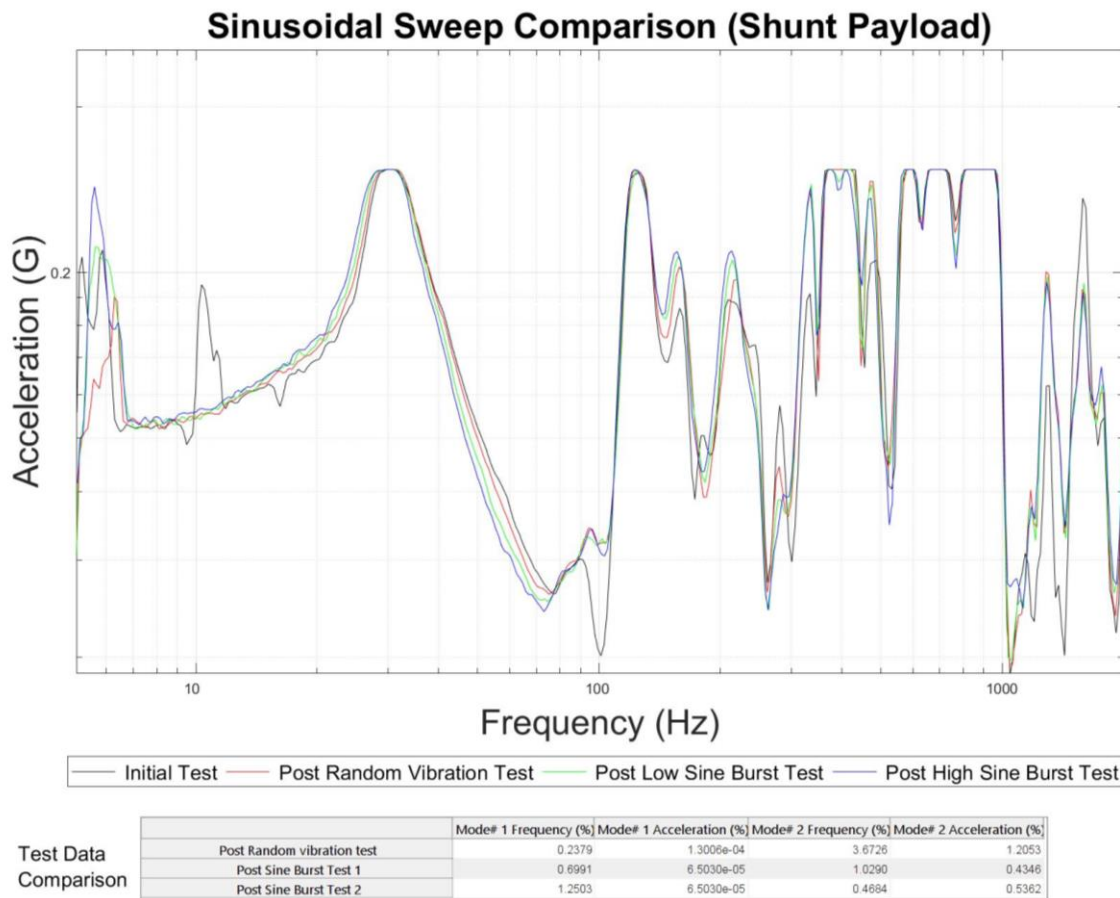


Figure 85: FRF comparison: Vertical test configuration (X direction), Shunt sub payload

The shunt payload consisted of a 4U NanoLab which was attached to the baseplate using the dual lock. The FRF shows a low-level rocking mode that appears at 10 Hz during the initial test. The exact model did not appear after the subsequent tests. Based on the similar FRF trend observed in the subsequent tests, it can be considered that the first anomaly was an isolated event. The variation could be due to the dual lock attachment, which is not as tight as a fastened joint. However, the comparison of significant modes shows the excellent correlation of the FRF frequencies and acceleration levels. A maximum of 3.7% frequency difference and 1.2% acceleration difference was observed. The shunt payload passed the health check in all the test configurations, and all the payload electronics worked as designed.

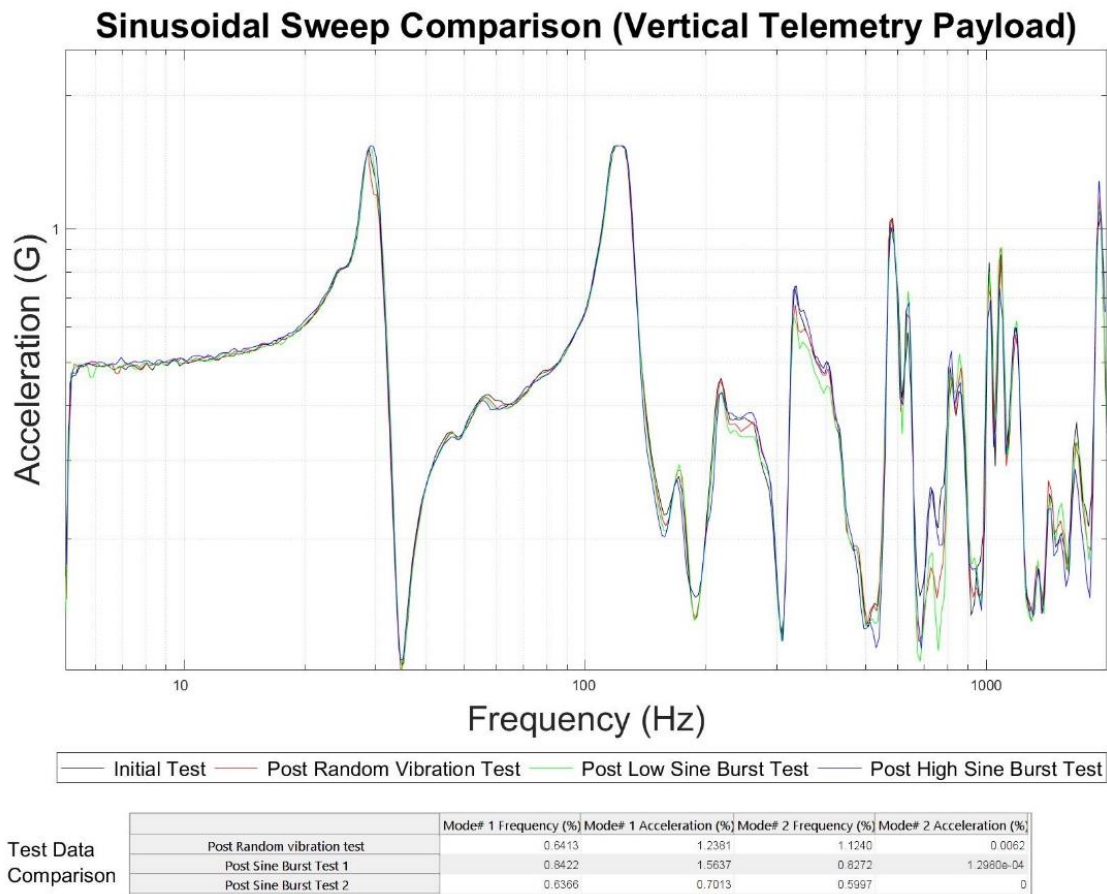


Figure 86: FRF comparison: Vertical test configuration, Vertical avionics sub payload

The avionics payloads included two redundant NanoLabs attached using dual lock in different orientations. The vertical avionics NanoLab showed a good correlation of FRF frequencies and acceleration levels in all the tests. A maximum of 1.1 frequency difference and 1.2% acceleration difference was observed in the vertical configuration tests. The avionics and the radiation data logger units collected data without any interruption throughout the tests. The shaker tests offered a unique opportunity to test the electronics and subject them to flight loads. The vibration tests are crucial to ensure the survival of electronic components, solder joints, connectors, and mounts.

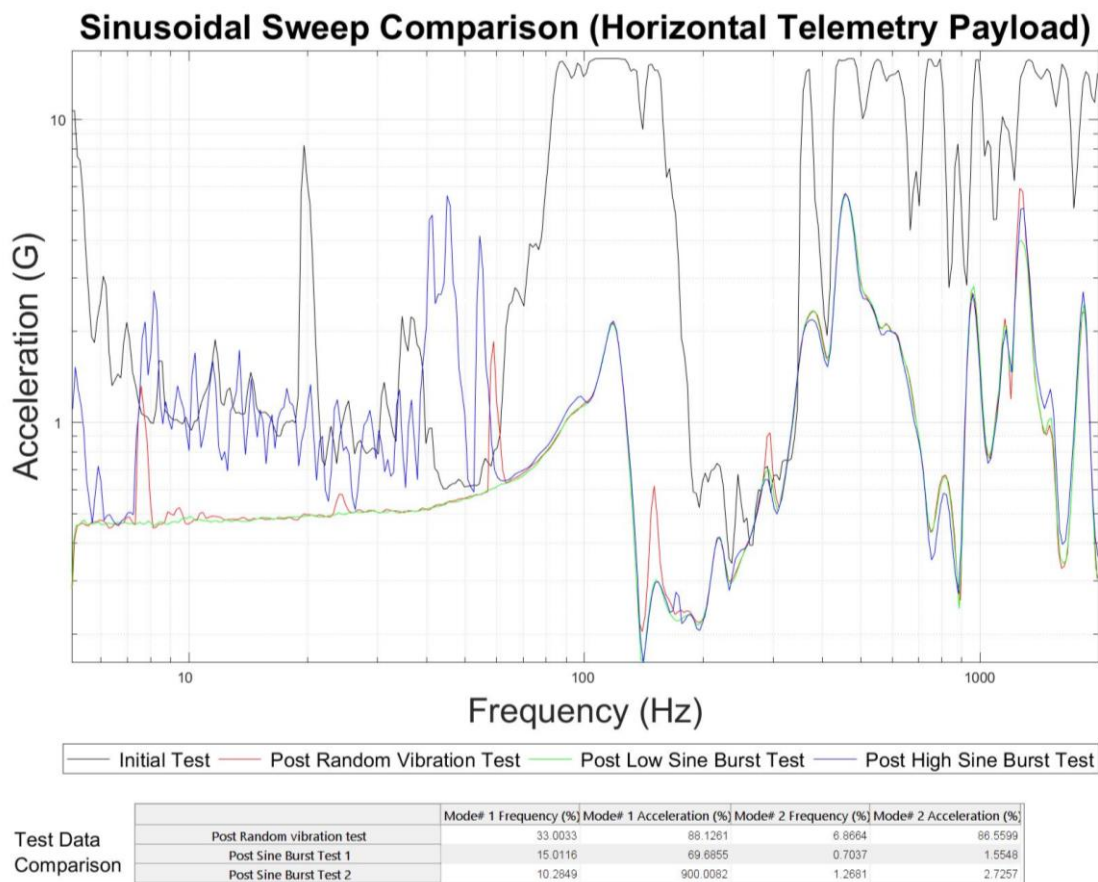


Figure 87: FRF comparison: Vertical test configuration, Horizontal avionics sub payload

The horizontal avionics payload did not show a good correlation between FRF after each test. This difference was significant in the first fundamental mode. The post random test comparison showed a significant deviation from the initial structure's FRF. The NanoLab was visually inspected, and no anomalies were observed in the structure. The electronics worked without any flaws, and the data logger performed without any flaws. The possible causes of this discrepancy could be attributed to the dual lock attachment becoming loose during the tests or to a faulty accelerometer sensor. Retesting of the horizontal payload is recommended. PLD Space's review and feedback on these results are awaited, and recommendations from PLD Space are to be considered in future retests.

Based on the FRF responses of each sub payload to vibration excitation in each corresponding direct, the test matrix results are shown in Table 20. The MAPMD and the vertical avionics/telemetry payload passed all the test criteria outlined in Section 5.5.4. The FRF response of the horizontal avionics/telemetry sub payload shows significant deviations between each test. The Shunt sub payload failed the vertical configuration tests.

Table 20: Vibration test campaign results

Sub Payload	Vertical X-axis	Lateral Y-axis	Lateral Z-axis
MAPMD	Pass	Pass	Pass
Vertical Avionics/Telemetry	Pass	Pass	Pass
Horizontal Avionics/Telemetry	Fail	Fail	Fail
Shunt	Fail	Pass	Pass

The discrepancies noticed in the horizontal NanoLab require retesting the sub payload separately in qualification test levels. Once the structure passes the qualification test, the payloads must be tested at acceptance test levels on the baseplate. Initially, the test accelerometer sensor used in previous tests has to be verified for accuracy, and if the sensor is not found to be ambiguous, ensuring a secure fit of the dual lock attachment is recommended.

## **6. Suborbital Payload Rocket Research Platforms**

The commercial suborbital launch market is a new capability being made available for students and the aerospace industry. Suborbital payload projects go through various levels of development and design review processes. The launch provider and flight integrators require multiple levels of testing for many scenarios that the payload will go through during a suborbital flight.

Proper planning of operational procedures pre-flight and post-recovery is vital in achieving the mission goals of the payload experiment. Usually, these procedures cannot be planned without prior experiences of going through a launch process. For a payload customer, it will be beneficial to understand a launch vehicle development process and launch operations to tailor the requirements of their payloads.

The scaled-down rocket research platforms will serve as a test facility for future suborbital payloads. The payloads will undergo flight loads and the different stresses that are expected in a launch. An in-house launch capability and experience gained in launching payloads will aid the researchers in better understanding the associated challenges with suborbital launches. The payload research team can also develop and practice the launch procedures before the actual suborbital flight. Although the flight envelopes are vastly different, the lessons learned in the smaller launches can be applied, and contingency scenarios can be identified and planned through these research platforms. The development of different rocket research platforms is discussed in the following sections.

## **6.1. Level 1 Rocket**

Model rockets were used as a tool in developing the payload research platform, and the first rocket launch mission was named Marea Roja. The National Association of Rocketry (NAR) classifies model rockets as Level 1, 2, or 3 based on the type of rocket motor used. NAR also provides licenses and guidelines for new members while also providing resources [57] needed for building and flying these rockets. A level 1 EZI-65 rocket kit from Apogee Rockets was utilized in this research. The rocket kit featured a simple design and assembly process, and it was a popular choice for many new hobby rocket enthusiasts.

### **6.1.1 Rocket and Payload Development**

The rocket kit consists of cardboard body tubes, a coupler tube, a motor mount tube, a plastic nosecone, plywood fins, a nylon cloth parachute, and all other necessary hardware. High power rocket motors have their own classifications similarly, and the compatible motors for this kit are H through J. The rocket motors also carry a delay charge that goes off on the top side of the rocket motor. The delay charge is used to deploy the parachutes stuffed inside the rocket body above the motor bay.

The flight phases of the rocket are as follows:

1. Motor ignition and lift-off
2. Powered climb
3. Engine cutoff and coasting period
4. Apogee
5. Depending on levels of deployment, a drogue chute or main chute is deployed at the apogee

6. Rocket descent under a parachute

7. Touchdown

The deployment phases can widely vary depending on flight profile requirements. A dual deployment method is used on high-powered rockets, where a drogue chute is deployed at apogee. The drogue chute slows the descent just enough so that the rocket does not drift too far downrange (which is a possibility under main chutes). A second deployment of the main chutes happens at a lower altitude. The deployment in this method is usually triggered by electronically controlled charges which use altimeter data to time the deployment. Marea Roja used a single deployment method which used a preset delay charge on the motor to deploy the main parachute.

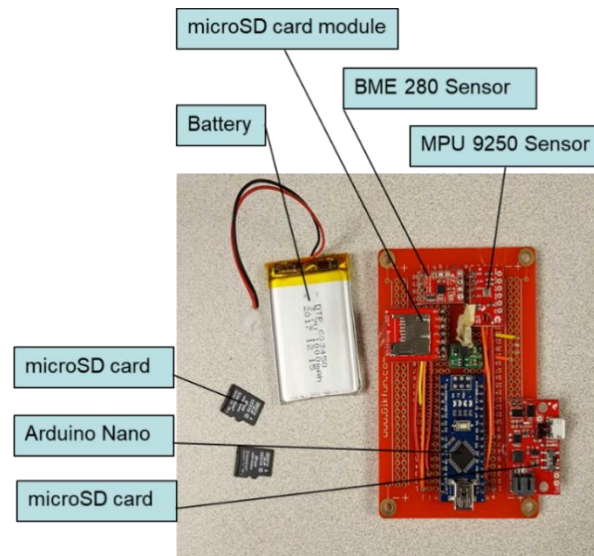


Figure 88: Level 1 rocket data logger

A customized payload was designed and built for payload testing onboard the level 1 rocket research platform. A payload bay was 3D printed and integrated into the design of the rocket kit. One of the body coupler tubes was replaced with this payload bay, and a custom data logger and a Pixhawk 2.4.8 were flown onboard. The custom data logger was a precursor to the payload electronics used in MESSI/McXIMUS and PLD payloads.

The data logger used the same electronics architecture as previous sections and was powered by a 3.7 V LiPo battery. The data logger (Figure 88) could autonomously measure acceleration, gyration, magnetic heading, temperature, relative humidity, pressure, and altitude in a microSD card. The Pixhawk was primarily used for its GPS capabilities. The payloads were placed inside foam containment before being placed inside the payload bay.

The rocket assembly was carried out in the Payload lab, and the first part assembled was the thrust/motor section. The 54 mm motor tube was attached with centering rings using epoxy. The centering rings act as a guide for the motor tube inside the rocket body tube. The assembly had to be accurately centered on avoiding an asymmetric thrust condition.

The three rocket fins were assembled symmetrically around the body and epoxied to the motor and body tubes. Glue fileting techniques were employed to ensure a rigid attachment of fins to the rocket body. The rocket assembly comprises two separate body tube sections designed to come apart during deployment. The top side with the nose assembly, and the bottom side with motor tube and parachutes. The coupler tube is friction fitted between the two parts and expected to slide out during deployment.

A nylon shock cord is used to connect the nose section and the motor tube section so that all the rocket bodies descend together under the parachute. A 36 in (91.44 cm) diameter parachute is folded, and the parachute rope is tied to the eyebolt in the motor tube assembly.

The design modifications to accommodate payloads required the evaluation of new flight parameters, which would vary from the manufacturer's specifications. RockSim



software [58] is model rocket simulation software used to evaluate key flight parameters before the flight. The modified rocket design was modeled in the software, and each part used in the assembly was programmed.

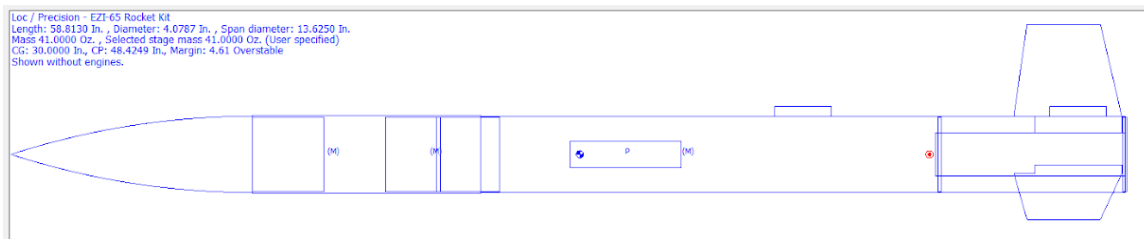


Figure 89: RockSim level 1 rocket simulation

RockSim evaluated the key flight parameters such as the center of gravity, the center of pressure, expected flight profile, stability, and thrust data using Barrowman equations [59]. The expected flight profile simulated using RockSim is shown in Figure 90. The simulated apogee was 2250 ft (685.8 m) using a Cessaroni I75 motor.

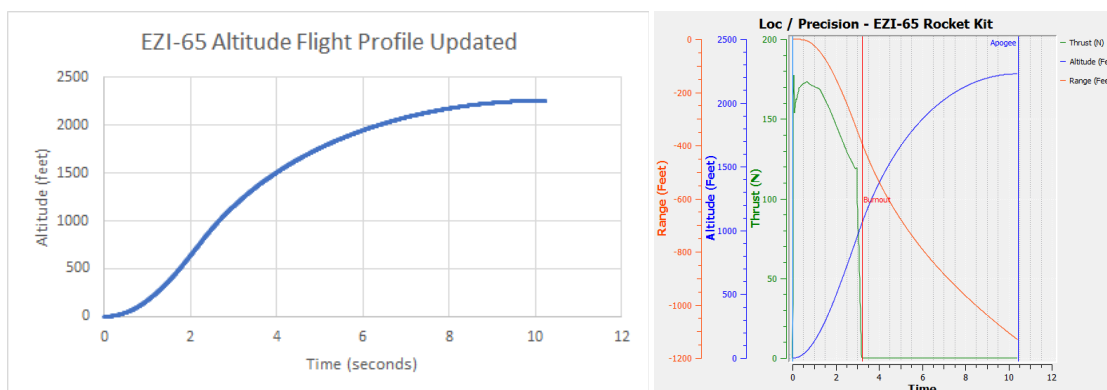


Figure 90. Simulated flight profile and flight parameters using RockSim [31]

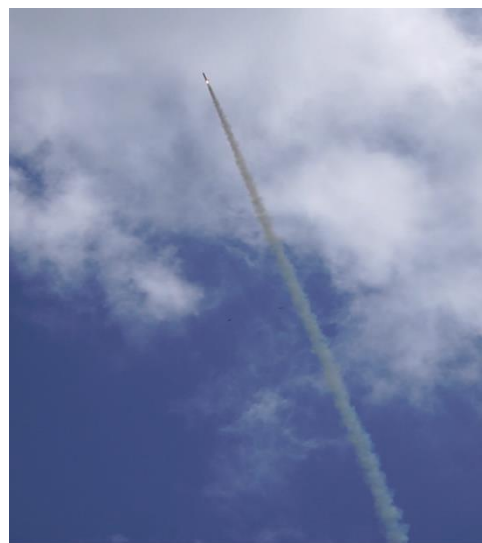
Pre-flight and post-flight operational procedures were created to prepare the payload and the rocket at the launch site. This process helped the research team understand the nuances of rocket launches, and the experiences gained aided in future payloads research projects such as MESSI/McXIMUS and PLD ERAU payload.

### 6.1.2 Level 1 Rocket Launch and Flight Analysis

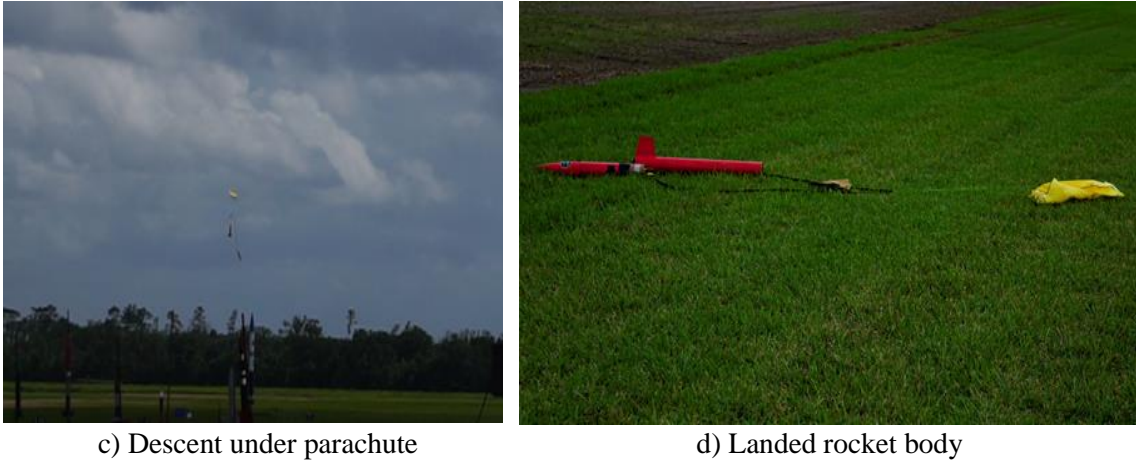
With the help of the Northeast Florida Association of Rocketry (NEFAR), the level 1 rocket was launched at the launch site in Bunnell, Florida. The rocket launched without incident. However, the descent was faster than had been anticipated, and as a result, the parachute suffered damage from the high-tension force that it experienced. The parachute deployment should have been right after apogee was reached, and the delay is assumed to be due to the faster descent from the higher mass. From the post-flight assessment of the rocket, it was determined that the use of a motor that had a longer delay in parachute deployment and exceeding the parachutes weight limit with the additional payload tube were the main factors that caused the fracturing of the parachute. The longer delay meant that the rocket was coming down too fast when the parachutes deployed, and the higher speed resulted in higher loads on the parachute chords. It was also found that the Pixhawk data collection device had corrupted data and could not be read. Therefore, most of the data were obtained from the Arduino data logger and used in the post-flight assessment. The various phases of the rocket flight are shown in Figure 91.



a) Rocket launch



b) Powered climb



c) Descent under parachute

d) Landed rocket body

Figure 91: Marea Roja level 1 rocket flight phases [31]

The flight profile with the maximum apogee height at 1845 ft (562.4 m) is shown below in Figure 92. It is observed that RockSim over-predicted the apogee altitude. This could be due to various factors such as wind conditions on the day of the launch, uneven mass distribution inside the payload (RockSim assumes uniform mass distribution), assembly errors, and irregularities in the motor.

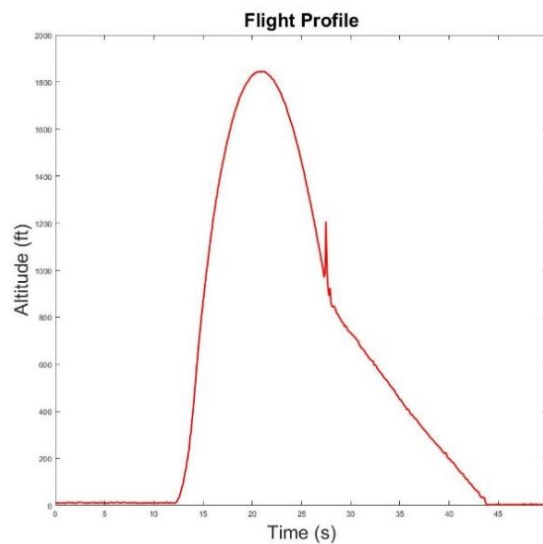


Figure 92: Actual flight profile of the level 1 rocket

The acceleration data showed the critical phases of the flight, such as the launch, ascent, coasting, deployment, and landing. The Y-axis direction of the data logger

corresponds to the thrust direction of the rocket. The profile showed that the payloads experienced about 4 seconds of microgravity during the coasting period. A maximum of 14 G was measured at parachute deployment, followed by 12 G due to the landing impact. This shows evidence that the rocket bodies came down faster than anticipated. The temperature and humidity sensors measured the expected profiles in a rocket launch.

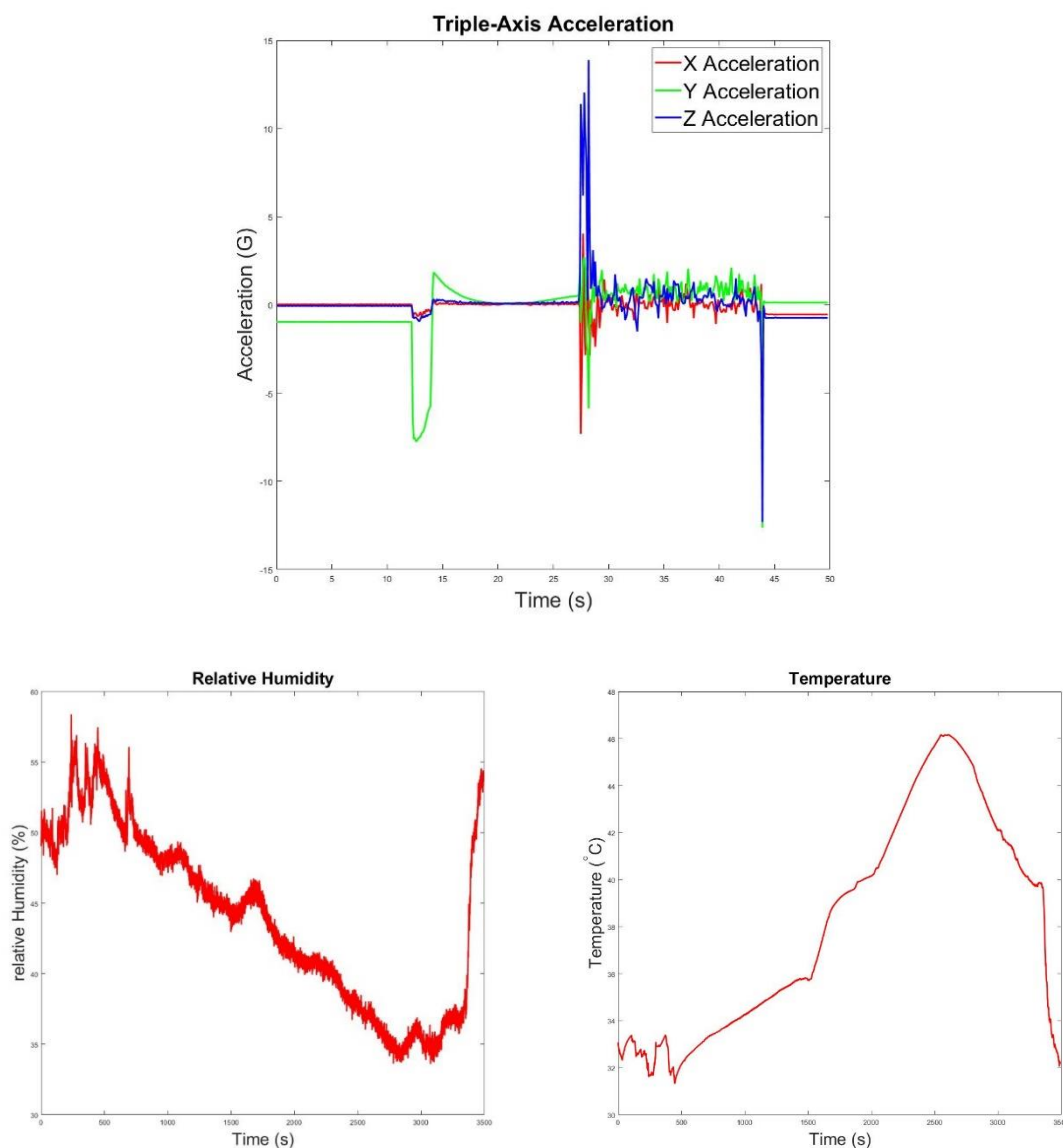


Figure 93: Level 1 rocket data logger payload data

Both the rocket and the data logger performed as expected. Valuable lessons were learned through hands-on rocket development, payload integration, and flight operation.

## **6.2. Level 3 Rocket**

The objective of this research endeavor is to design and build a Level 3 Rocket that can serve as a research platform for launching, testing, and recovering payloads to be flown in commercial suborbital platforms such as Blue Origin's New Shepard, Exos Aerospace's SARGE, Interorbital Systems' Neptune, and PLD space's Miura 1 rockets. The rocket will initially be launched to measure humidity, temperature, and radiation in the atmosphere. However, other electronics and educational experiments will be launched in the future. The rocket is being constructed at the Payload Applied Technology Operations (PATO) laboratory using state-of-the-art materials and manufacturing techniques, such as 3D printing and CNC machining, with multiple levels of redundancy which maximizes the payload capabilities and the safety and reliability [60] of the launch vehicle.

### **6.2.1 Preliminary Rocket Design and Fabrication**

The Suborbital Technology Experimental Vehicle for Exploration (STEVE) project is the vehicle name of the prospective Level 3 Rocket that will serve as a scaled-down model of a rocket in which future researchers can flight test payloads. The rocket is expected to be 4.877 meters in length and 0.278 meters in diameter. The rocket has a cylindrical payload bay with a maximum capacity of 0.0716 cubic meters and can carry a payload up to 13.607 kilograms. STEVE will utilize a dual deployment technique using custom-built rocket avionics systems. A drogue chute will deploy at apogee and slow the rocket down, and the main chutes will deploy at an altitude of 1000 ft (304.8 m).

The initial rocket design has been completed using CAD software. The various parts were conceptualized based on previous experiences in model rocketry and the availability of commercial-off-the-shelf rocketry hardware. The primary component of the rocket is the body tubes which constitute the most significant part of the rocket. Three 10.75 in (273.05 mm) inner diameter 0.1 in (2.54 mm) thickness and 48 in (1219.2 mm) long twill carbon fiber weave tubes were purchased. The twill pattern was chosen due to its higher tensile strength and better load distribution characteristics in all fiber directions.

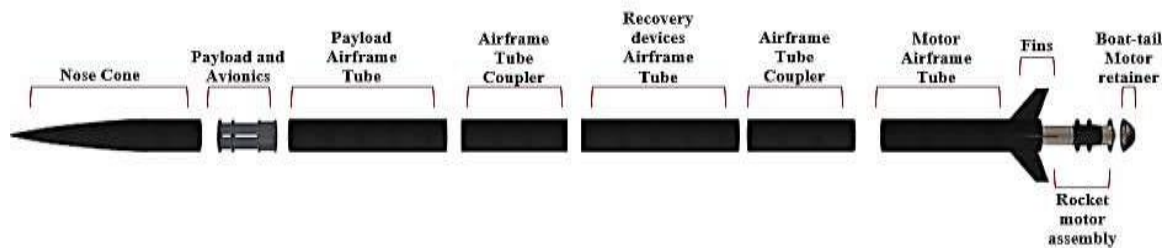


Figure 94: STEVE level 3 rocket design

The three body sections are labeled as the motor airframe, recovery airframe, and payload airframe. As their names suggest, the motor airframe will contain the motor tube, centering rings, and rocket motor hardware. The recovery motor tube will contain the main parachute, shock cord, and deployment electronics. The payload frame tube will serve as the payload bay volume for test payloads. Each section will be connected using coupler tubes using shear pins or rivets. Shear pins are used where separation of the rocket body is expected during deployment, and these pins break at a preset force. Rivets are used at the permanent attachment points, and the reason for building the rockets is to enable easier access to the internal rocket components while also aiding in handling and logistics. The nose cone will be 42 in (1066.8 mm) long. The shape parameters were derived from the Von Karman or Haack series nosecones with a shape parameter of zero, and the nose cone 2D coordinates are derived from Equations 19 and 20.

$$y = \frac{R}{\sqrt{\pi}} \sqrt{\theta - \frac{\sin(2\theta)}{2} + C \sin^3(\theta)} \quad (19)$$

where  $x$  and  $y$  are the corresponding coordinates in each respective axis,  $R$  is the radius of the nose cone base,  $L$  is the total length of the nose cone,  $C$  is the shape parameter equal to  $\theta$  for the Von Karman nose cone. The value of  $\theta$  is given by

$$\theta = \arccos\left(1 - \frac{2x}{L}\right) \quad (20)$$

The Von Karman nose cone was chosen for its excellent drag reduction characteristics [61]. Multiple iterations on simulation software with different nose cone types showed the best performance results for this type of nosecone.

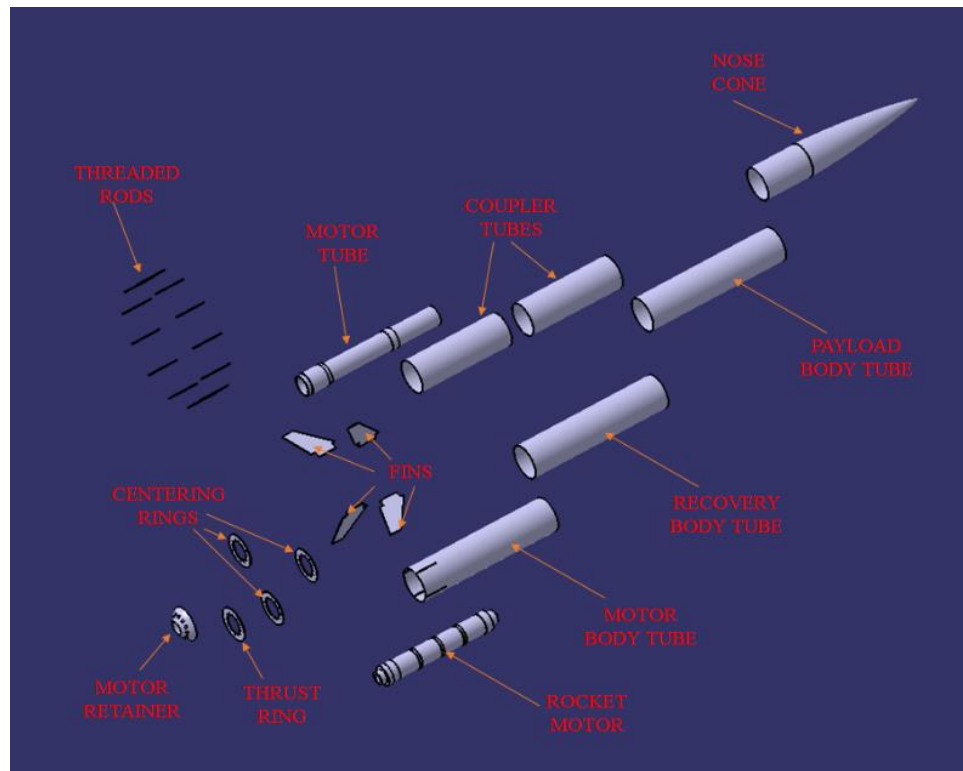


Figure 95: STEVE design exploded view with all rocket parts labeled

Figure 95 shows the detailed view of all the rocket hardware design components. The motor tube will serve as the casing for the rocket motor and transfer the rocket's thrust to the rocket body. The motor tube is centered using three centering rings which are held

together by threaded rods. The four fins assembled on the motor tube as shown in Figure 96. A thrust ring is designed at the extremity of the motor tube, which overlaps the rocket body tube's outer diameter and transfers the thrust to the rocket body. A metallic motor retainer is designed with a bow tail shape to hold the motor and reduce drag by avoiding airflow separation downstream of the rocket.

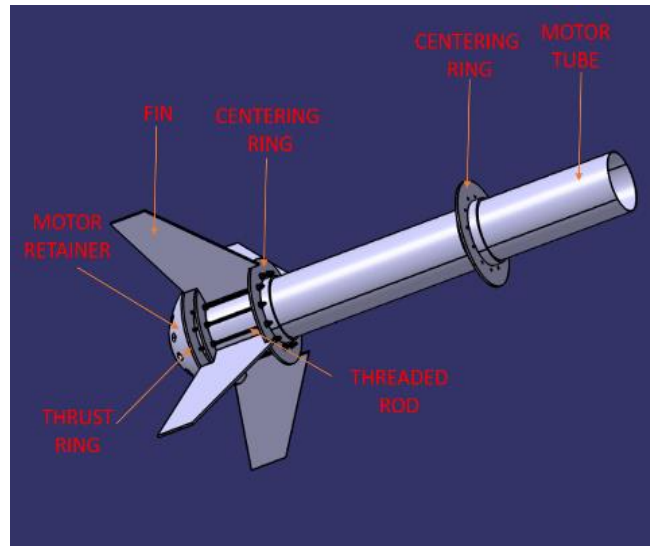


Figure 96: Motor tube assembly

Due to the motor tube's extreme structural and environmental requirements, a custom part was fabricated by layup of carbon fiber sheets over a phenolic tube. The phenolic tube has been considered to show excellent thermal characteristics in the model rocket community. Layers of carbon fiber weave were added to the outer diameter of the phenolic tube to obtain the correct size for mating with the centering rings. After curing, the motor tube was sanded for an accurate outer diameter and roundness. However, it was realized that the layer of carbon fiber was too thick because it expanded due to not being adequately cured within a vacuum bag. Thus, the centering rings did not properly fit onto the motor tube, and therefore post-fabrication adjustments were necessary. The post-processing of the motor tubes was carried out at the structures and material lab in the



department of Aviation Maintenance Sciences. The completed motor tube is shown in Figure 97, and the rocket motor is designed to fly 150 mm and 98 mm motors.

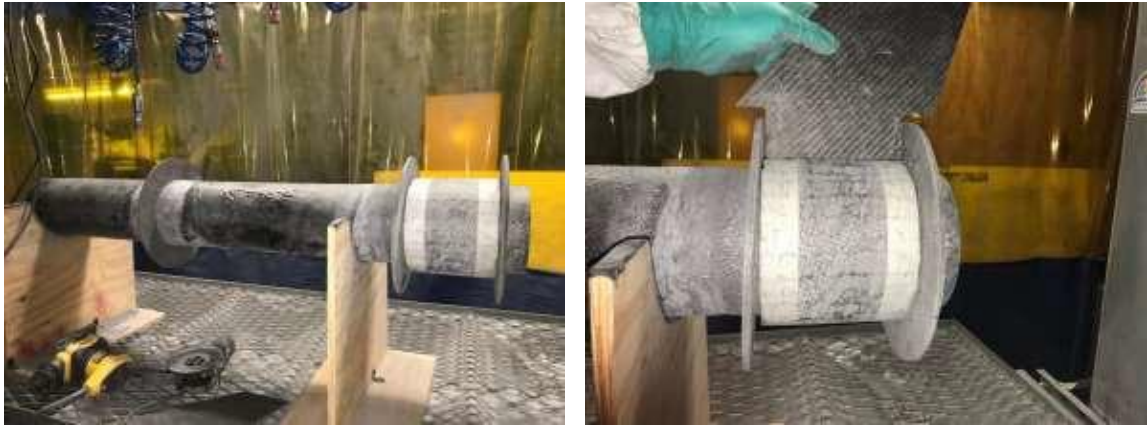


Figure 97: Fabricated motor tube after completion of the sanding and grinding processes [62]

A fin alignment box was designed and fabricated to enable the proper alignment of fins to the motor tube and the rocket bodies. Symmetric attachment of the fins is paramount to avoid any dynamic instabilities to the rocket's flight. The fin box design is shown in Figure 98.

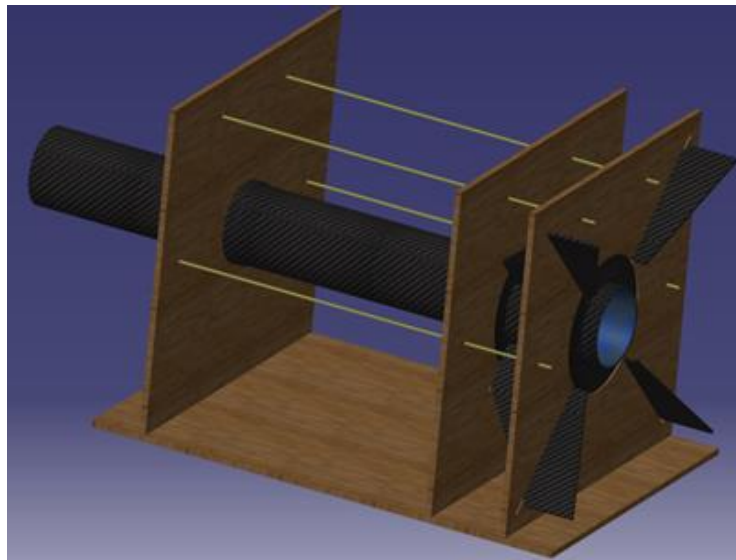


Figure 98: Fin alignment box

## 6.2.2 Level 3 Rocket Simulations

Preliminary rocket simulations show that the level 3 rocket is expected to reach a maximum altitude of 4.25 km (class B airspace) with a payload of 30 kg. The rocket simulations were carried out in OpenRocket and Cambridge rocketry simulators.

OpenRocket software environment and the level 3 rocket setup is shown in Appendix B.

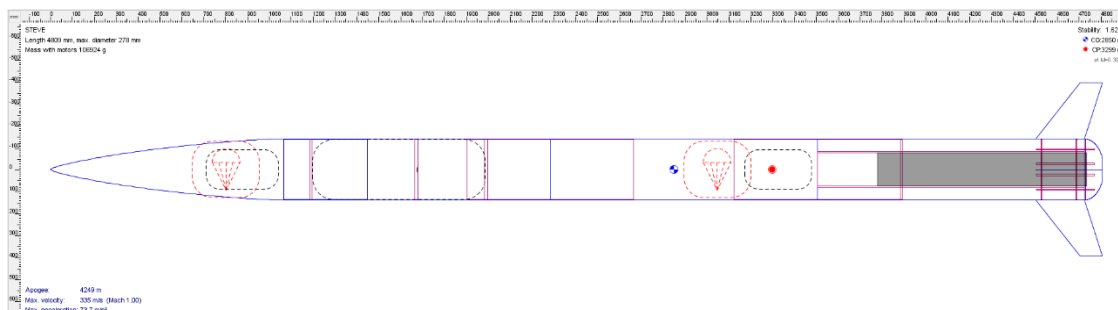
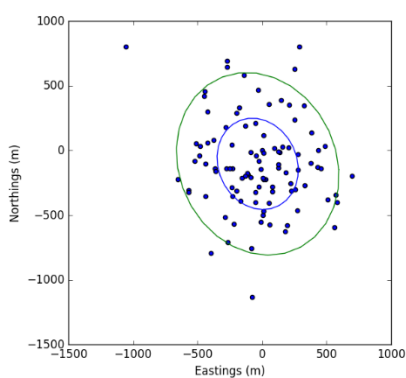
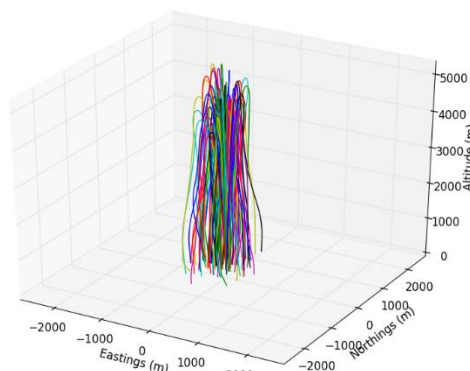


Figure 99: OpenRocket Level 3 rocket simulation results

Cambridge Rocketry software was used to generate a splashdown plot, a vital parameter in high-power rocket launches. The splashdown range is critical in getting approval for launching and ensuring the rocket does not fly too downrange and land beyond the boundaries of the launch site. The software uses Monte Carlo simulation techniques to generate the plots. The splashdown plots show that the landing locations are within acceptable limits, as seen in Figure 100.



a) Splashdown plot



b) Trajectories plot

Figure 100: Cambridge rocketry Monte Carlo run results

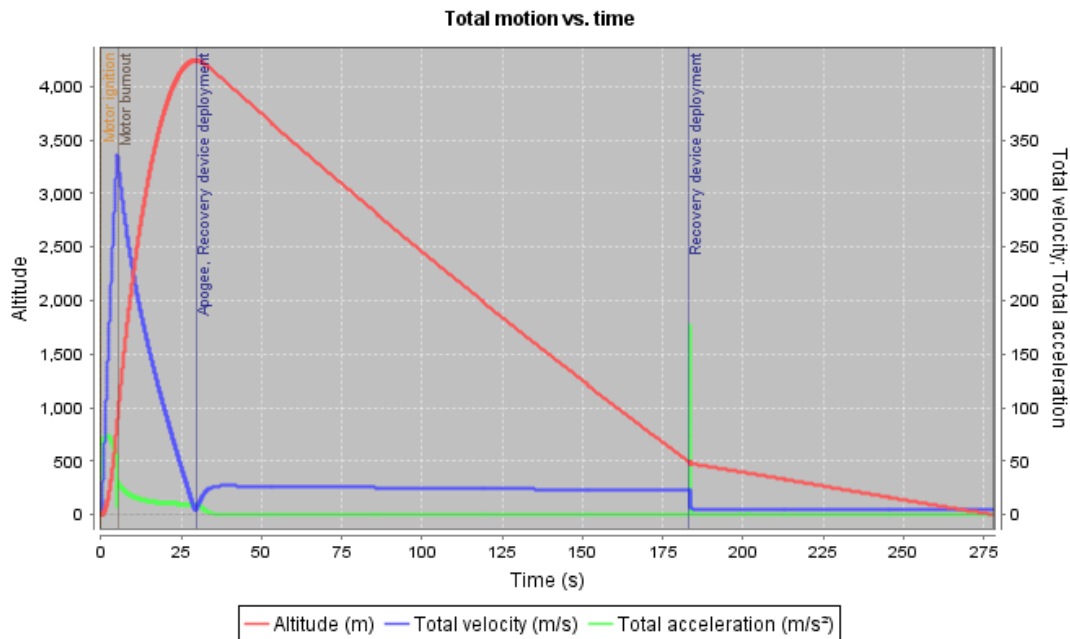


Figure 101: Simulated level 3 rocket motion parameters

The level 3 rocket was simulated with Cesaroni Technology's O8000 motor, with a total impulse of 40960 N.s. The simulated apogee altitude was 4245 m with a maximum velocity of 0.96 Mach and acceleration of 7.65 G, as seen in Figure 101. A fin flutter analysis was performed, and based on the fin shape and the material, the flutter Mach number was 2.17 Mach. Therefore, the fin assembly is deemed to operate within safe limits throughout the flight envelope.

Stability is a crucial parameter for rocket flight. Stability is estimated based on the centers of gravity and pressure locations along the length of the rocket. The rocket's stability varies through the flight due to the change in the total mass of the rocket as the solid propellant burns. As shown in Figure 102, the stability margin throughout the flight is within acceptable limits.

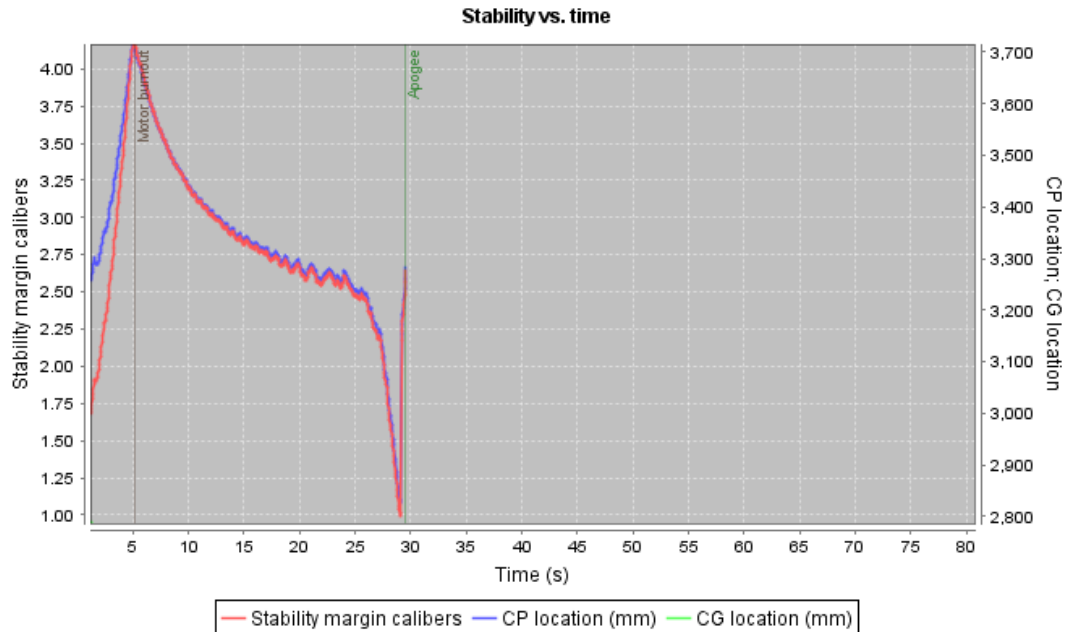


Figure 102: Simulated level 3 rocket stability parameters

Building the level 3 rocket of this scale involves substantial effort and planning to launch and recover the payloads successfully. The design phase and the fabrication of fins, centering ring and motor tube, and the acquisition of drogue parachute, shock cords, bulkheads, and structural hardware have been completed. The next phase would require acquiring main parachutes, motor hardware, nose cone, and flight avionics. The groundwork has been completed in availing the payload research platform, and the further integration of the level 3 rocket is left as future work in this research.

### 6.2.3 Analysis of Custom Payload Bay

A custom payload bay was designed and fabricated by student research teams from the CSO390 class to accommodate suborbital payloads inside the payload airframe motor tube of the Level 3 rocket. The design (Figure 103) consisted of a payload volume to accommodate 2-2U NanoLabs, 2-1U NanoLabs, and 4 Tubesats form factors along with flight avionics. These payload form factors are the commonly available payload volumes in commercial suborbital flight platforms.

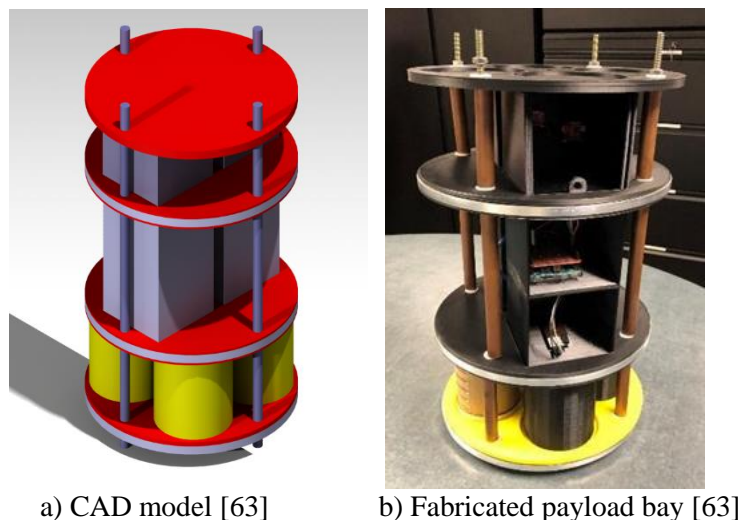


Figure 103: Custom payload bay

An FEA analysis is performed on the custom payload bay model in ANSYS. The acceleration loads from the rocket simulation were applied to the FEM. The maximum stresses are observed in the connecting rods of the payload structure, which were designed to take the flight loads. The connecting rods are the most robust design components, and the flight payloads were not subjected to high stresses. Further analysis involving launch vibrations and deployment events is required.

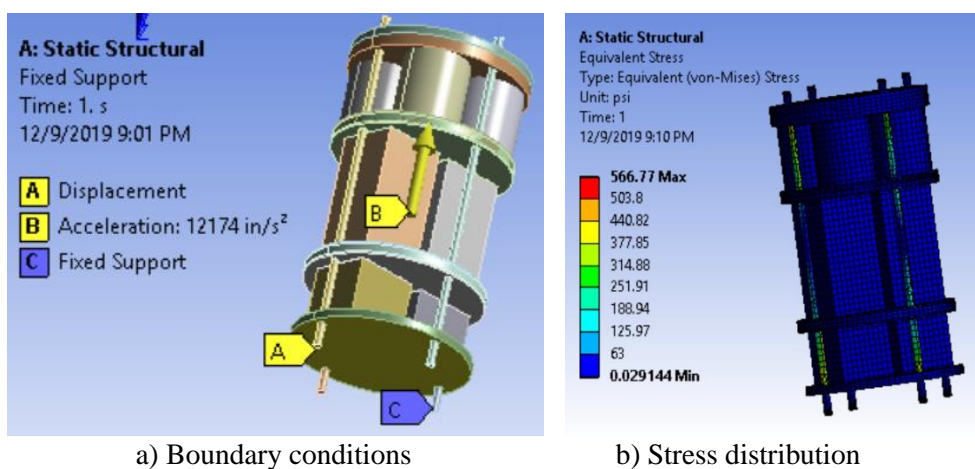


Figure 104: Custom payload bay structural analysis

### 6.3. Vacuum Chamber Test Capability

The payload thermal environment is an essential factor to consider in-flight experiment planning. Biological systems are highly susceptible to temperature changes and usually require a particular operating environment for survival. NanoLab experiments are constrained by tight capacity and weight requirements. The development of thermal control systems in challenging space environments requires innovative design and extensive testing. Post-flight analysis of the CRExIM mission highlighted the importance of a thermal control system for a biological payload. In 2017, the ERHASER payload developed by student research teams was flown on NASA's WB-57 aircraft up to 60,000 ft, and it was determined that the thermal system used could be refined. A vacuum thermal testbed has been developed to improve the test capabilities for future payloads. The testbed consists of a customized vacuum chamber with the hardware requirements shown in Figure 105.

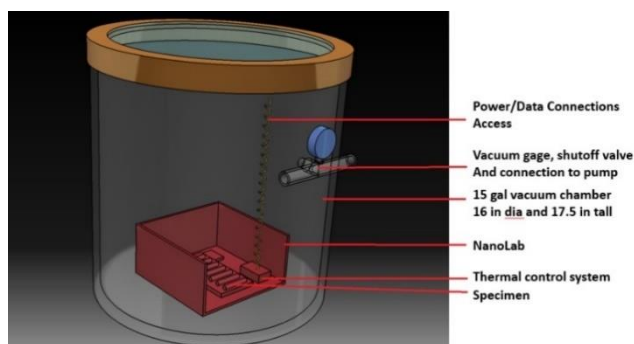


Figure 105: Vacuum chamber design considerations

A custom vacuum chamber was purchased with MIL-STD electrical connectors. The electrical connectors are utilized to connect electrical sensors and probes inside the vacuum chamber. A vacuum chamber environment monitoring electronics system (see Appendix B) was developed with two temperature monitoring probes and a pressure breakout to measure the vacuum pressure inside the chamber. A rotary vane vacuum

pump is used to maintain vacuum pressures inside the test chamber. The test assembly is shown in Figure 106.

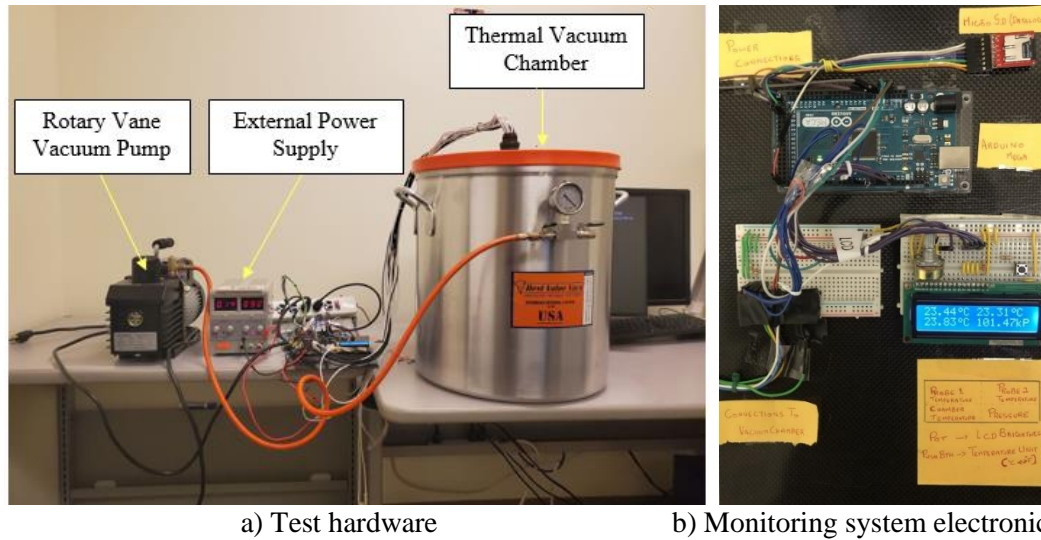


Figure 106: Assembled vacuum chamber testbed

## 7. Conclusions and Future Recommendations

CRExIM payload was successfully flown onboard Blue Origin's M7 mission and recovered. Various design challenges were overcome, and the final design was developed in accordance with the flight provider's requirements and the mission requirements of the payload. The final design incorporated four layers of containment to prevent any liquid from escaping the NanoLab. FEA analysis showed that our NanoLab design could endure the acceleration loads experienced in flight. The investigation on the natural frequencies and the stresses calculated on the structure using modal and random vibration analysis, respectively, demonstrated the safety of the payload in a vibration environment. The mass of the fully assembled NanoLab is 0.497 kg which is within the maximum allowed payload mass of 0.499 kg. Mass optimization, 3D printed light materials, and innovative design changes helped adhere to the mass constraint and maximize the payload carried inside the Nanolab.

CRExIM's mass Optimization using ANSYS resulted in a mass reduction of 38% from the initial baseline design. A CFD analysis was performed to analyze the sloshing behavior of the liquid contained in the Eppendorf tubes, and the forces experienced by the cells are estimated. The CFD analysis showed an interesting distinction between the 1 G and microgravity case, with the fluid forces being higher in the microgravity case. Common 3D printing materials such as ABS, PLA, and CFRP were compared, and ABS was chosen for this payload. In this research, many milestones set by the flight provider were completed, and the results obtained here were used to justify the safety of the payload. This study provided valuable data that passed the compliance reviews of PDP and the PSP. The utilized methodology and the information gathered in this research will



serve as a benchmark for improving future Nano payloads focused on space biology research.

CRExIM's post-flight analysis showed a good correlation of acceleration data as specified in PUG and revealed concerns about the temperatures inside the flight capsule. The research team did not anticipate the large temperature fluctuations that could affect the success criteria of the mission. Blue Origin has since added a cabin thermal control system in later missions, and the temperature fluctuations have not been an issue in recent payloads. However, appropriate thermal considerations are necessary for payloads containing biological components, and a thermal control system to maintain an acceptable temperature range throughout the mission is recommended.

MESSI/McXIMUS payload development was derived from findings in CRExIM's mission. Design modifications were made to improve NanoLab handling and payload capacity to accommodate two different payloads inside a single 2U NanoLab. The payload requirements offered insights for researchers to work with payload electronics. A custom data logger along with a LED lighting system for the spirulina algae growth chamber was devised. The payload was flown onboard Blue Origin's NS-11 mission and successfully recovered. The electronics systems worked as designed and collected data throughout the 10-minute flight. The flight data was analyzed post-recovery. The NanoLabs designed at ERAU has been successfully flight-proven and can potentially be used by future payload researchers who would utilize the NanoRacks Feather Frame locker facility or other payload applications.

The upcoming launch of PLD Space's MIURA 1's first mission has provided an opportunity for many research teams to develop sub payloads with the large payload

capacity available in its single payload bay compartment. An avionics payload has been designed, developed, and tested. The avionics/telemetry payload will serve as a pathfinder mission characterizing the payload bay environment on its maiden flight. Sophisticated electronics systems have been developed to measure acceleration, gyration, magnetic heading, temperature, relative humidity, air quality, magnetic field, radiation, infrared radiation, and pressure during flight. The payload electronics were tested on the ground and parabolic flight test and functioned without any problems. The groundwork for interfacing with the flight vehicle's CD & H (flight data communication) system has been performed. This system's detailed design and fabrication are left as future work, pending further inputs from PLD Space as they work to evolve their systems and provide more information to payload customers. The avionics system has been proposed as a COTS system for future suborbital payload, and the current development has improved the project progress to TRL 5. Through the suborbital flight test onboard MIURA 1 rocket, the technology will be improved to TRL 7.

The MAPMD payload is a technology demonstration mission, and the design and development of the payload in this research will increase the technology's TRL to 6 after the suborbital flight. The MAPMD CFD analysis showed that the multiphase fluids did not reach equilibrium during the short microgravity periods of the parabolic flight. The fluid membrane flipped multiple times, which was not observed in the actual flight. The assumptions involving DFBI degree of freedom to restrict the translation of the membrane in X and Y direction is observed as the reason for this behavior. This assumption was used to simplify the model and to reduce the computational expense of the solution. A high-fidelity fluid-structure interaction model with impact analysis is

recommended to resolve the motion of the membrane better. For the upcoming suborbital flight, evaluation of crucial flow parameters such as pressure, water level, membrane motion capture, and liquid forces on the tank during the flight mission is recommended. These parameters will help understand the performance of the MAPMD in a space environment and provide key validation points for future CFD models.

A vibration test campaign was performed to test all the flight hardware systems and subsystems of the PLD ERAU payloads. Test standards recommended by PLD Space were strictly adhered and at first, a test plan and objectives were proposed and reviewed by PLD engineers. Upon clearance, the vibration tests were conducted with all the payloads mounted on the base plate using the shaker table at Micaplex. The MPE vibration excitation levels were applied on the payload assembly for the prescribed duration. A random vibration test followed by a low-level and high-level sine-burst test was conducted in each corresponding axis. Low-level sine sweep tests were performed between each vibration test to probe the FRF, highlighting the natural frequencies of the structures. MAPMD payload design was modified based on the results from the initial tests, and the final hardware was tested again. FRF data comparison verifies the MAPMD, shunt, and vertical avionics sub payload's compliance to the test criteria. The test campaign initially involved a shock test which was not completed during this campaign. The shock spectrum supplied by PLD Space was not supported by the DVC-8 vibration controller equipment used in these tests. Attempts were made to synthesize the spectrum to a readable format by the controller software without success. The shock tests require a more sophisticated vibration controller, which was not acquired for this research.

The feasibility of using model rockets as payloads research platforms has been identified, and a level 1 rocket was fabricated with a custom payload bay. The goal was to test prospective suborbital payloads by launching the level 1 rocket from Bunnell, Florida, and completed. The rocket development using flight simulations and fabrication techniques performed in the level 1 rocket provided the path to developing a higher payload capacity level 3 rocket. Rocket design, mission planning, flight simulations with trajectory, flight loads, and splashdown analysis were performed. A custom payload bay along with the rocket motor tube assembly and fins were fabricated. The ambitious level 3 rocket project requires more research and support to supplement the development pipeline and test each subsystem. The framework developed in this research will aid future researchers in launching their payloads.

## References

- [1] M. Smith, C. Douglas, N. Herrmann, N. McIntyre and K. Goodliff, "The artemis program: An overview of nasa's activities to return humans to the moon," in *2020 IEEE Aerospace Conference (pp. 1-10)*, 2020.
- [2] D. Miranda, "2020 NASA technology taxonomy.," NASA, Washington DC, 2019.
- [3] J. S. Alwood, A. E. Ronca, R. C. Mains, M. J. Shelhamer, J. D. Smith and T. J. Goodwin, "From the bench to exploration medicine: NASA life sciences translational research for human exploration and habitation missions.," *npj Microgravity*, no. 3.1, 2017.
- [4] H. Jones, "The recent large reduction in space launch cost.," in *8th International Conference on Environmental Systems*, 2018.
- [5] R. Mains and L. Chu-Thielbar, "Commercial Reusable Suborbital Research (CRuSR): NASA Becoming a Collaborative Customer For a New Era.," in *AIAA SPACE 2010 Conference & Exposition*, 2010.
- [6] C. Carissa, E. Gresham, K. Maliga, S. Johnson, J. Hay, E. Hinds and P. Guthrie, "Ten-year forecast of markets and launches for suborbital vehicles.," in *AIAA SPACE 2012 Conference & Exposition*, 2012.
- [7] I. Tzinis, "Technology Readiness Level," NASA, 2021. [Online]. Available: [https://www.nasa.gov/directorates/heo/scan/engineering/technology/technology\\_readiness\\_level](https://www.nasa.gov/directorates/heo/scan/engineering/technology/technology_readiness_level). [Accessed 13 07 2021].

- [8] R. Moro-Aguilar, "The new commercial suborbital vehicles: an opportunity for scientific and microgravity research.," *Microgravity Science and Technology*, no. 26, 2014.
- [9] BLUE ORIGIN, "New Shepard Payload User's Guide for Research and Education Missions. NSPM-MA0002-B, REV B," 2016. [Online]. Available: <https://www.blueorigin.com/>. [Accessed 22 04 2017].
- [10] BLUE ORIGIN, "New Shepard Payload User's Guide For Research," 2017. [Online]. Available: <https://www.blueorigin.com/>. [Accessed 25 04 2019].
- [11] NanoRacks, "NanoRacks Feather Frame (NFF) Payload User's Guide (NFF PUG)," no. NR-BLUE-W0001, 2016.
- [12] PLD Space, "PLD Space MIURA 1=Payload User's guide," 13 11 2018. [Online]. Available: <https://www.pldspace.com/es/miura-1>. [Accessed 22 01 2021].
- [13] A. Kim, K. Hurlbert, A. Boone, T. Jon-michael and R. Williams, "Design and Implementation of an Instrumentation Package to Characterize Blue Origin's New Shepard Vehicle Cabin Environment.," in *ASCEND 2020*, 2020.
- [14] A. Toorian, K. Diaz and S. Lee, "The cubesat approach to space access.," in *2008 IEEE Aerospace Conference*, 2008.
- [15] T. Peterson, C. Bossong and B. Bartel, "Modal Propellant Gauging in Microgravity.," in *Proceedings of the Wisconsin Space Conference*, 2019.
- [16] M. Vairamani, K. Crosby, P. Llanos, S. Gangadharan and S. Nagendra, "Magneto-Active Slosh Control System Using Free Floating Membrane for Cylindrical Propellant Tanks.," in *AIAA Scitech 2019 Forum*, 2019.

- [17] T. Sarafin, P. Doukas, L. Demchak and M. Browning, "Vibration Testing of Small Satellites," Copyright 2017 Instar Engineering and Consulting, Inc., [Online]. Available:  
[https://www.instarengineering.com/vibration\\_testing\\_of\\_small\\_satellites.html](https://www.instarengineering.com/vibration_testing_of_small_satellites.html).  
[Accessed 04 05 2021].
- [18] T. Campbell, S. Seufert, R. Chavez, J. Brewer, R. Tomiozzo, C. Whelan and M. Okutsu, "Model rocket projects for aerospace engineering course: Simulation of flight trajectories.," in *54th AIAA Aerospace Sciences Meeting*, 2016.
- [19] NASA, "Yuri Gagarin: First Man in Space," [Online]. Available:  
[https://www.nasa.gov/mission\\_pages/shuttle/sts1/gagarin\\_anniversary.html](https://www.nasa.gov/mission_pages/shuttle/sts1/gagarin_anniversary.html).  
[Accessed 03 August 2021].
- [20] S. Hauschild, S. Tauber, B. Lauber, C. Thiel, L. Layer and O. Ullrich, "T cell regulation in microgravity–The current knowledge from in vitro experiments conducted in space, parabolic flights and ground-based facilities.," *Acta Astronautica 104*, vol. 1, 2014.
- [21] M. Krummel, F. Bartumeus and A. Gerard, "T cell migration, search strategies and mechanisms.," *Nature Reviews Immunology*, vol. 16, no. 3, 2016.
- [22] H. Lee, Finite element simulations with ANSYS Workbench 18, SDC publications, 2018.
- [23] MakerBot, *PLA and ABS Strength Data*.
- [24] 3DXTECH, *CarbonX Carbon Fiber Reinforced ABS 3D Filament Technical Data Sheet, Rev 2.1..*

- [25] S. Raviprasad and N. Nayak, "Dynamic analysis and verification of structurally optimized nano-satellite systems.," *Journal of Aerospace Science and Technology*, no. 1.2, 2015.
- [26] CD-Adapco, *STAR-CCM+ Version (10.02) User Guide*, 2015.
- [27] L. Paul, "Study of Hybrid Magneto-Active Propellant Management Device for Slosh Damping," *Dissertations and Theses*, no. 230, 2016.
- [28] MakerBot, *Replicator 2X user manual*.
- [29] V. V. Duraisamy, F. Pastrana, T. Collin, K. Andrijauskaite, S. Gangadharan and P. Llanos, "Design, Development and Testing of a Suborbital NanoLab Research Experiment in Microgravity.," in *AIAA SPACE and Astronautics Forum and Exposition*, 2017.
- [30] J. Vela, r. Lindquist, K. Andrijauskaite and P. Llanos, "Operations and Testing of a Suborbital Research Payload," in *AIAA SPACE and Astronautics Forum and Exposition*, 2017.
- [31] P. Llanos, K. Andrijauskaite, V. V. Duraisamy, F. Pastrana, E. Seedhouse, S. Gangadharan, L. Bunegin and M. Rico, "Challenges of ERAU's First Suborbital Flight Aboard Blue Origin's New Shepard M7 for the Cell Research Experiment In Microgravity (CRExIM)," *Gravitational & Space Biology*, no. 7.1, 2019.
- [32] P. Llanos and K. Andrijauskaite, "Examination of Molecular Mechanisms on Vascular Formation and Stress Response in Zebrafish by Different Microgravity Environments," in *International Astronautical Congress*, Washington DC, 2019.



- [33] P. Llanos, K. Andrijauskaite, M. Rubinstein and S. Chan, "Investigation of Zebrafish Larvae Behavior as Precursor for Suborbital Flights: Feasibility Study.," *Gravitational & Space Biology*, no. 6.1, 2018.
- [34] C. Kimmel, W. Ballard, S. Kimmel, B. Ullmann and T. Schilling, "Stages of embryonic development of the zebrafish.," *Developmental dynamics*, vol. 203, no. 3, 1995.
- [35] M. P. Team, "MESSI/McXIMUS Payload Data Packagae (PDP) submitted to NanoRacks," 2018.
- [36] W. Qinghua, L. Liu, A. Miron, B. Klimova, D. Wan and K. Kuca, "The antioxidant, immunomodulatory, and anti-inflammatory activities of Spirulina: an overview.," *Archives of toxicology*, vol. 90, no. 8, 2016.
- [37] A. Deosthale and M. Bamji, "Spirulina as a source of vitamin A.," *Plant foods for human nutrition*, vol. 41, no. 2, 1991.
- [38] B. D. Sandhu and S. Shweta, "Efficacy of Spirulina Supplementation on Isometric Strength and Isometric Endurance of Quadriceps in Trained and Untrained Individuals--a comparative study.," *Ibnosina Journal of Medicine & Biomedical Sciences*, no. 2.2, 2010.
- [39] C. Cingi, M. Conk-dalay, H. Cakli and C. Bal, "The effects of spirulina on allergic rhinitis," *European Archives of Oto-Rhino-Laryngology*, vol. 265, no. 10, 2008.
- [40] M. A. Juarez\_Oropeza, D. Mascher, T. Duran, J. M. Farias and M. Cristina, "Effects of dietary Spirulina on vascular reactivity.," *ournal of medicinal food*, vol. 12, no. 1, 2009.

- [41] C. H. Nielsen and et al, "Enhancement of natural killer cell activity in healthy subjects by Immulina®, a Spirulina extract enriched for Braun-type lipoproteins.," *Planta medica*, vol. 76, no. 16, 2010.
- [42] H.-K. Lu and et al, "Preventive effects of Spirulina platensis on skeletal muscle damage under exercise-induced oxidative stress.," *European journal of applied physiology*, vol. 98, no. 2, 2006.
- [43] Y. Akao and et al, "Enhancement of antitumor natural killer cell activation by orally administered Spirulina extract in mice.," *Cancer science*, vol. 100, no. 8, 2009.
- [44] Y. A. Badamasi, "The working principle of an Arduino.," in *11th international conference on electronics, computer and computation (ICECCO)* , 2014.
- [45] m. Fezari and A. A. Dahoud, "Integrated Development Environment “IDE” For Arduino.," in *WSN applications* , 2018.
- [46] J. Mankar, C. Darode, K. Trivedi, M. Kanoje and P. Shahare, "Review of I2C protocol," *International Journal of Research in Advent Technology*, vol. 2, no. 1, 2014.
- [47] P. Llanos, "MESSI/McXIMUS Post Flight Data Analsyis," 2019.
- [48] J. Foust, "Zero-G plans international expansion," SPACENEWS, [Online]. Available: <https://spacenews.com/zero-g-plans-international-expansion/>. [Accessed 13 07 2021].
- [49] CD-adapco, *STAR CCM+ user guide version 12.04.*, New York, 2017.

- [50] A. Teskeredzic, I. Demirdzic and S. Muzaferija, "Numerical method for heat transfer, fluid flow, and stress analysis in phase-change problems.," *Numerical Heat Transfer: Part B: Fundamentals*, vol. 42, no. 5, pp. 437-459, 2002.
- [51] S. H. Collicott, D. T. Valentine, E. L. Houghton and P. W. Carpenter, *Aerodynamics for Engineering Students*, Butterworth-Heinemann, 2016.
- [52] A. A. Shabana, *Computational Dynamics*, John Wiley & Sons., 2001.
- [53] S. Chang and X. Wang, "Courant number insensitive CE/SE Euler scheme.," in *38th AIAA/ASME/SAE/ASEE Joint Propulsion Conference & Exhibit*, 2002.
- [54] Command, Air Force Space, "Test Requirements for Launch, Upper-stage and Space Vehicles," Space and Missile System Standard SMC-S-016, 2014.
- [55] DYNAMICS SOLUTIONS LLC, "DS-1300VH-9 SPA602 ACU402 GT 600 M Electrodynamic Vibration System, Operation Manual," 2017.
- [56] P. Llanos, M. Vairamani and V. V. Duraisamy, "Investigation of Engineering and Scientific Experiments in Microgravity aboard PLD Space's MIURA 1 Suborbital Vehicle: Flight Acceptance Ground Testing," Technical Report, 2021.
- [57] G. H. Stine and B. Stine, *Handbook of model rocketry*, Wiley, 2004.
- [58] P. Fossey, *RockSim Program Guide*, Apogee components, 2003.
- [59] J. Barrowman, "The practical calculation of the aerodynamic characteristics of slender finned vehicles," NASA, 1967.
- [60] NAR, "National Association of Rocketry Level 3 High Power Certification Requirements," National Association," [Online]. Available:

<https://www.nar.org/wpcontent/uploads/2014/08/L3certreq.pdf>. [Accessed 02 2019].

- [61] S. Varma, S. Sathayanarayana and S. J, "CFD analysis of various nose profiles.," *International Journal of Aerospace and Mechanical Engineering*, no. 3.3, 2016.
- [62] N. Amberkar, V. V. Duraisamy, M. Mastroliberti, M. Munasinghe, G. Maupin, P. Llanos and S. Gangadharan, "Suborbital Payload Testing Aboard Level 3 Rocket Research Platform," in *AIAA Scitech 2020 Forum*, Orlando, 2020.
- [63] CSO 390 Class and P. Llanos, "Payload Experimental Design for Rocket Operations (P.E.D.R.O)," Project Report, 2019.
- [64] B. Dunbar and N. Pekar, "STMD: Flight Opportunities," NASA, 02 07 2021.  
[Online]. Available:  
<https://www.nasa.gov/directorates/spacetech/flightopportunities/flightproviders>.  
[Accessed 06 07 2021].

## Appendix A

### A. MESSI/McXIMUS NanoLab Arduino Code

Program created by Vijay Vishal Duraisamy and Morgan Shilling

```

#define SerialDebug false // Set to true
to get Serial output for debugging
#define ExtendedIMUcalc true
#include <Wire.h> //standard header
files
#include <SPI.h>
#include <SD.h>
#include
<Sparkfun_APDS9301_Library.h>
//header for Light sensors
#include
<SparkFun_Si7021_Breakout_Library.h
> //header for temp/humidity sensor
#include <SparkFunMPU9250-DMP.h>
//header files for Accelerometer/IMU
#include <Thread.h> //header files
for Multithreading library
#include <StaticThreadController.h>
//and controllor
#define heart LED_BUILTIN
Thread NFF_THREAD = Thread();
//declaration of Thread object for NFF
Thread MESSI_THREAD = Thread();
//declaration of Thread object for Messi
Thread TMP_THREAD = Thread();
Thread HEARTBEAT = Thread();
StaticThreadController<4> controller
(&NFF_THREAD,
&MESSI_THREAD, &TMP_THREAD,
&HEARTBEAT);
//declaration of Thread controller object
with two members
MPU9250_DMP IMU;
//accelerometer/mag/gyrometer
APDS9301 apds; //luminosity sensor
//Initialization of sensors
Weather weather; //temp/humidity
sensor
//counter variables
unsigned int count = 1;

uint32_t elapsedTime = 0; //amount of
time passed since program start
char Fl_state; //var to convert
nrdata.flight_state to Char
float data[40]; //array to hold all data
before output to file
float imuHeading = 0;
float q0 = 0;
float q1 = 0;
float q2 = 0;
float q3 = 0;
float imuYaw = 0;
float imuPitch = 0;
float imuRoll = 0;
typedef struct NRdata //struct used by
NFF to store flight data
{
char flight_state;
double exptime;
double altitude;
double velocity[3];
double acceleration[3];
double attitude[3];
double angular_velocity[3];
bool liftoff_warn;
bool rcs_warn;
bool escape_warn;
bool chute_warn;
bool landing_warn;
bool fault_warn;
} NRdata;
NRdata* flight_info; //declaration of
struct pointer
//declaration of Data Logging function
void LogData(float data[]);
//parse function used by NFF to get data
from serial.read and save it to the
appropriate struct member
int parse_serial_packet(const char* buf,
NRdata* flight_data);

```

```

void temp() {
  float tmp[4];
  float humidity[4];
  for (byte x = 4; x < 8; x++) {
    enableMuxPort(x);
    tmp[x - 4] = weather.readTemp();
  }
  //initialize weather sensor and set temp
  to local array
  humidity[x - 4] = weather.getRH();
  //initialize weather sensor and set hum to
  local array
  disableMuxPort(x); //Tell mux to
  disconnect from this port
}
data[13] = tmp[0];
data[14] = tmp[1];
data[15] = tmp[2];
data[16] = tmp[3];
data[17] = humidity[0];
data[18] = humidity[1];
data[19] = humidity[2];
data[20] = humidity[3];
}

void sensors() { //sensor polling
function
  float light[3] = {0}; //var for APDS
Light sensors
  float mpu[3][3] = {0}; //two
dimensional array var for MPU acc x, y,
then z, then gyr xyz, then mag xyz
  //float humidity[4] = {0}; //var for
Si7021 Humidity
  //float tmp[4] = {0}; //var for Si
Temperature
  //for cycles four iterations, enabling
each mux port 0-3, querying and saving
//the sensor data to local var, later sets
correllating data var to value
  for (byte x = 0 ; x < 4 ; x++)
  {
    enableMuxPort(x); //Tell mux to
connect to this port, and this port only
    if (x == 0) { //if MUX is connecting
to 0th port
      // Calibrate gyro and accelerometers,
load biases in bias registers
      IMU.update(UPDATE_ACCEL |
UPDATE_GYRO |
UPDATE_COMPASS); //get updated
figures from IMU Accelerometer, Gyro
and Mag
      mpu[0][0] =
IMU.calcAccel(IMU.ax);
//appoint values to local array
      mpu[0][1] = IMU.c
alcAccel(IMU.ay);
      mpu[0][2] =
IMU.calcAccel(IMU.az);
      mpu[1][0] =
IMU.calcGyro(IMU.gx);
      mpu[1][1] =
IMU.calcGyro(IMU.gy);
      mpu[1][2] =
IMU.calcGyro(IMU.gz);
      mpu[2][0] =
IMU.calcMag(IMU.mx);
      mpu[2][1] =
IMU.calcMag(IMU.my);
      mpu[2][2] =
IMU.calcMag(IMU.mz);
      if (ExtendedIMUcalc){
        if ( IMU.fifoAvailable() > 0 ){ //
Check for new data in the FIFO
          // Use dmpUpdateFifo to update
the ax, gx, qx, etc. values
          if ( IMU.dmpUpdateFifo() ==
INV_SUCCESS ){
            IMU.computeCompassHeading();
            imuHeading = IMU.heading;
            IMU.computeEulerAngles(1);
            q0 = IMU.calcQuat(IMU.qw);
            q1 = IMU.calcQuat(IMU.qx);
            q2 = IMU.calcQuat(IMU.qy);
            q3 = IMU.calcQuat(IMU.qz);
            imuYaw = IMU.yaw;
            imuPitch = IMU.pitch;
            imuRoll = IMU.roll;
          }
        }
      }
    } else { // (x == 1-3)

```

```

    apds.begin(0x39);    //initialize
light sensor
    light[x - 1] = apds.readLuxLevel();
//set lux value to local array
} //if (x == 0)
if (x == 4) //if MUX is connecting to
4th port
{
    tmp[0] = weather.readTemp();
//initialize weather sensor and set temp
to local array
    humidity[0] = weather.getRH();
//initialize weather sensor and set hum to
local array
}
if (x == 5) //if MUX is connecting to
5th port
{
    tmp[1] = weather.readTemp();
//initialize weather sensor and set temp
to local array
    humidity[1] = weather.getRH();
//initialize weather sensor and set hum to
local array
}
if (x == 6) //if MUX is connecting to
6th port
{
    tmp[2] = weather.readTemp();
//initialize weather sensor and set temp
to local array
    humidity[2] = weather.getRH();
//initialize weather sensor and set hum to
local array
}
if (x == 7) //if MUX is connecting to
7th port
{
    tmp[3] = weather.readTemp();
//initialize weather sensor and set temp
to local array
    humidity[3] = weather.getRH();
//initialize weather sensor and set hum to
local array
}

    disableMuxPort(x); //Tell mux to
disconnect from this port
}
data[1] = mpu[0][0]; //set all local
array values to global data array
data[2] = mpu[0][1];
data[3] = mpu[0][2];
data[4] = mpu[1][0];
data[5] = mpu[1][1];
data[6] = mpu[1][2];
data[7] = mpu[2][0];
data[8] = mpu[2][1];
data[9] = mpu[2][2];
data[10] = light[0];
data[11] = light[1];
data[12] = light[2];
/*data[13] = tmp[0];
data[14] = tmp[1];
data[15] = tmp[2];
data[16] = tmp[3];
data[17] = humidity[0];
data[18] = humidity[1];
data[19] = humidity[2];
data[20] = humidity[3];*/
return; //break sensor function
and return to main
}
void LogData(float data[]) { //data
logging function
    File Datalog = SD.open("datalog.txt",
FILE_WRITE); //declare file pointer
and create file for writing
    if (Datalog) //if file can be
created/modified
    {
        if (count == 1) //only on first iteration,
prints file header
        {
            Datalog.print(F("Sample
Number,Flight State,Nanolab elapsed
time (ms),NR exptime (s),X
Acceleration (G),Y Acceleration (G),Z
Acceleration (G),X Gyration (deg/s),Y
Gyration (deg/s),Z Gyration (deg/s),X
Magnetic field (mu*T),Y Magnetic field
(mu*T),Z Magnetic field

```

```

(mu*T),A_Light Intensity (lux),B_Light
Intensity (lux),C_Light Intensity
(lux),A_Temperature
(C),B_Temperature (C),C_Temperature
(C),D_Temperature (C),A_Humidity
(%),B_Humidity (%),C_Humidity
(%),D_Humidity (%),Flight Altitude
(ft),FV1,FV2,FV3,Facc1,Facc2,Facc3,F
att1,Fatt2,Fatt3,Fw1,Fw2,Fw3,Floff,Frcs
,Fesc,Fchu,Flan,Ffau));
    if (ExtendedIMUcalc){

Datalog.print(F("heading,q0,q1,q2,q3,ya
w,pitch,roll"));
    }
    Datalog.println();
}
elapsedTime = millis();
Datalog.print(count); //write count
and FL state to file
Datalog.write(',');
Datalog.print(FL_state);
Datalog.write(',');
Datalog.print(elapsedTime);
for (byte i = 0; i < 40; i++)
//increment through data[] and print to
file
{
    Datalog.write(',');
    Datalog.print(data[i]);
}
if (ExtendedIMUcalc){
    Datalog.write(',');
    Datalog.print(imuHeading);
    Datalog.write(',');
    Datalog.print(q0);
    Datalog.write(',');
    Datalog.print(q1);
    Datalog.write(',');
    Datalog.print(q2);
    Datalog.write(',');
    Datalog.print(q3);
    Datalog.write(',');
    Datalog.print(imuYaw);
    Datalog.write(',');
    Datalog.print(imuPitch);

    Datalog.write(',');
    Datalog.print(imuRoll);
}
Datalog.println();
}
Datalog.close(); //close file
}
else
{ //alternate to previous decision, if file
can't be created sends error message
    Serial.println(F("error opening
datalog.txt"));
}
count++; //increment count
return; //exit function
}
void DebugOutput(float data[] {
//output values to serial monitor to
ensure proper data logging
    int i;
    if (SerialDebug) {
        Serial.print(count);
        Serial.print(F("\t"));
        for (i = 0; i < 40; i++) { //increments
through data[i] and prints to serial
monitor
            Serial.print(data[i]);
            Serial.print(F("\t"));
        }
        if(ExtendedIMUcalc){
            Serial.print(imuHeading);
            Serial.print(F("\t"));
            Serial.print(q0);
            Serial.print(F("\t"));
            Serial.print(q1);
            Serial.print(F("\t"));
            Serial.print(q2);
            Serial.print(F("\t"));
            Serial.print(q3);
            Serial.print(F("\t"));
            Serial.print(imuYaw);
            Serial.print(F("\t"));
            Serial.print(imuPitch);
            Serial.print(F("\t"));
            Serial.print(imuRoll);
        }
        Serial.println();
}

```



```

    }
    return;
}
void checkNRdata() {
    if (Serial.available()) {
        getNRdata();
    }
}
void beatHeart(){
    int beat=digitalRead(heart);
    if(beat == LOW){
        digitalWrite(heart, HIGH);
        Serial.print("on");
    } else {
        digitalWrite(heart, LOW);
        Serial.print("off");
    }
}
void setup() { //setup function runs
when Arduino boots up
    delay(10); //wait for hardware
initialization
    Wire.begin(); //initiate i2c bus and
library
    Serial.begin(115200); // Set baud
rate to 115200 (Default serial
configuration is 8N1).
    if (SerialDebug) {
        while (!Serial) {
            //Wait for serial port connection to
establish for serial monitor use
        }
    }
    if (SerialDebug) {
        Serial.println(F("Initializing
IMU..."));
    }
    enableMuxPort(0); //connect to IMU
    IMU.begin(); //initialize IMU
    IMU.setSensors(INV_XYZ_GYRO |
INV_XYZ_ACCEL |
INV_XYZ_COMPASS); //sets modes
of IMU to be used
    Serial.println(F("IMU sensors
initialized"));
    Serial.println(F("IMU initialized.));

    disableMuxPort(0); //disconnect from
IMU
    Serial.println(F("Initializing SD
card..."));
    if (!SD.begin()) {
        Serial.println(F("Card failed, or not
present"));
        // don't do anything more:
        while (1);
    }
    Serial.println(F("SD card initialized.));
    weather.begin();
    // NFF timeout //
    Serial.setTimeout(20); // Set timeout
to 20ms (It may take up to 17ms for all
of the data to // transfer from the NFF,
this ensures that enough time has passed
// to allow for a complete transfer
before timing out).
    NFF_THREAD.onRun(checkNRdata);
//when NFF thread runs, trigger
getNRdata
    MESSI_THREAD.onRun(sensors);
//when Messi thread runs, trigger sensors
function
    TMP_THREAD.onRun(temp); //when
Messi thread runs, trigger sensors
function
    HEARTBEAT.onRun(beatHeart);
    controller[0].setInterval(5); //NFF
set interval to 5ms
    controller[1].setInterval(10); //MESSI
set interval to 100ms
    controller[2].setInterval(2500); //tmp
    controller[3].setInterval(625);
//heartbeat
    Serial.println(F("Threads initialized.));
    pinMode(LED_BUILTIN, OUTPUT);
}
void loop() { //actual loop program
runs after setup
    while (1) { //endless loop
        controller.run(); //begins static thread
controller

```

```

    if (NFF_THREAD.shouldRun()) {
//when NFF thread gets ran, LogData
and report to serial monitor
    LogData(data);
    DebugOutput(data);
    }
    if (MESSI_THREAD.shouldRun()) {
    LogData(data);
    }
    DebugOutput(data);
    }
    if (TMP_THREAD.shouldRun()) {
    LogData(data);
    DebugOutput(data);
    }
    }
    }
    }

```

## B. PLD ERAU Payload – Avionics Sub payload Circuit Board 1 Arduino Program

Program created by Vijay Vishal Duraisamy and Nikita Amberkar

```

#include <Wire.h> // library for I2c
Protocol
#include "SparkFunCCS811.h" //
Library for air quality
#include
"SparkFun_Si7021_Breakout_Library.h"
// Library for Temp and Humidity
#include "SparkFunMPL3115A2.h" //
Library for altitude and pressure
#include <SparkFunMPU9250-DMP.h>
// Library for aceperometer
#include <H3LIS331DL.h> // Library
for new sensor
#include <SPI.h> // libaray for spi
protocol
#include <SD.h> // SD card library
int LED = 8;
float DataFile[31]; // Initiazling the array
int SampleRate = 10; //delay/sampling
rate in milliseconds
float SampleCount = -1; //start sample
code
float Time = 0.000; // current time
float Time1= 0.000; // time for code has
been running
#define CCS811_ADDR 0x5B //
Memory address
CCS811 AirQuality(CCS811_ADDR);
Weather TempHum;
MPL3115A2 PressAlt;
#define ExtendedIMUcalc true
MPU9250_DMP IMU;
#define HMCAddr 0x1E //0011110b,
I2C 7bit address of HMC5883,
#define VAL_X_AXIS 203 //please get
these value by running
H3LIS331DL_AdjVal Sketch
#define VAL_Y_AXIS 165
#define VAL_Z_AXIS 371
H3LIS331DL h3lis;
float CO2 = 0;
float TVOC = 0;
float Humidity = 0;
float TempF = 0;
float Pressure = 0;
float BaroTemp = 0;
float Altitude = 0;
float accelX = 0;
float accelY = 0;
float accelZ = 0;
float gyroX = 0;
float gyroY = 0;
float gyroZ = 0;
float magX = 0;
float magY = 0;
float magZ = 0;
float IMUHeading = 0;
float q0 = 0;
float q1 = 0;
float q2 = 0;
float q3 = 0;
float IMUYaw = 0;

```

```

float IMUPitch = 0;
float IMURoll = 0;
int magXHMC =0;
int magYHMC =0;
int magZHMC =0;

float accelXLIS =0;
float accelYLIS =0;
float accelZLIS =0;
void setup() // This loop will run once
when arduino is turned on
{
Serial.begin(115200); // 115200 baud
rate for serial communication between
USB computer - Arduino
Wire.begin(); // I2C communication
begin
pinMode(LED, OUTPUT);
digitalWrite(LED, LOW);
Serial.println(F("Initializing SD
card..."));
  if (!SD.begin())
  {
    Serial.println(F("Card failed, or not
present")); //if SD card cannot be
accessed, waits indefinitely. No point in
performing any operations without
ability to log data
    while (1); // the remainder of the code
will not execute
  }
Serial.println(F("SD card initialized.));
AirQuality.begin();
delay (1000); // giving extra time for air
quailty sensor to boot up
TempHum.begin();

PressAlt.begin();
PressAlt.setModeBarometer();
// Measure pressure in Pascals from 20
to 110 kPa
PressAlt.setOversampleRate(7);
// Set Oversample to the recommended
128

PressAlt.enableEventFlags();
// Enable all three pressure and temp
event flags
IMU.begin();
IMU.setSensors(INV_XYZ_GYRO |
INV_XYZ_ACCEL |
INV_XYZ_COMPASS);
IMU.dmpBegin(DMP_FEATURE_6X_
LP_QUAT | // Enable 6-axis
quat

DMP_FEATURE_GYRO_CAL,
// Use gyro calibration
10);
Wire.beginTransmission(HMCAddr);
Wire.write(0x02);
//select mode register
Wire.write(0x00);
//continuous measurement mode
Wire.endTransmission();
h3lis.init();
h3lis.importPara(VAL_X_AXIS,VAL_
Y_AXIS,VAL_Z_AXIS); //Import the
data for 3 axis
}
void loop() // will start the main code
and this code runs continously
{

if (SampleCount == 1)
{
  Time1 = millis(); // current program
execution time
}
Time = millis();
Time = (Time-Time1)/1000.000;
//Correct the recorded time and reset to
zero when
AirQuality.readAlgorithmResults();
CO2 = AirQuality.getCO2();
//Collect Carbon dioxide data
TVOC = AirQuality.getTVOC();
//Collect Metal oxide data
Humidity = TempHum.getRH();
//Collect humidity data

```

```

TempF = TempHum.getTempF();
//Collect temperature data
Pressure = PressAlt.readPressure();
//Collect pressure data
BaroTemp = PressAlt.readTempF();
//Collect altitude data
IMU.update(UPDATE_ACCEL |
UPDATE_GYRO |
UPDATE_COMPASS); //Update
acceleration, gyration, and magnetic
field
accelX = IMU.calcAccel(IMU.ax);
//Collect acceleration data in the x
direction
accelY = IMU.calcAccel(IMU.ay);
//Collect acceleration data in the y
direction
accelZ = IMU.calcAccel(IMU.az);
//Collect acceleration data in the z
direction
gyroX = IMU.calcGyro(IMU.gx);
//Collect gyration data in the x direction
gyroY = IMU.calcGyro(IMU.gy);
//Collect gyration data in the y direction
gyroZ = IMU.calcGyro(IMU.gz);
//Collect gyration data in the z direction
magX = IMU.calcMag(IMU.mx);
//Collect magnetic field data in the x
direction
magY = IMU.calcMag(IMU.my);
//Collect magnetic field data in the y
direction
magZ = IMU.calcMag(IMU.mz);
//Collect magnetic field data in the z
direction
if (ExtendedIMUcalc)
{
  if ( IMU.fifoAvailable() )
  { // Check for new data in the FIFO //
    Use dmpUpdateFifo to update the ax, gx,
    qx, etc. values
    if ( IMU.dmpUpdateFifo() ==
    INV_SUCCESS )
    {
      IMU.computeCompassHeading();
//Calculate the rocket headings
      IMUHeading = IMU.heading;
      IMU.computeEulerAngles();
//Calculate the Euler angles
      q0 = IMU.calcQuat(IMU.qw);
//Calculate initial quaternion (q0)
      q1 = IMU.calcQuat(IMU.qx);
//Calculate first quaternion (q1)
      q2 = IMU.calcQuat(IMU.qy);
//Calculate second quaternion (q2)
      q3 = IMU.calcQuat(IMU.qz);
//Calculate third quaternion (q3)
      IMUYaw = IMU.yaw;
//Calculate yaw
      IMUPitch = IMU.pitch;
//Calculate pitch
      IMURoll = IMU.roll;
//Calculate roll
    }
  }
}
Wire.beginTransmission(HMCAddr);
Wire.write(0x03);
//select register 3, X MSB register
Wire.endTransmission();
Wire.requestFrom(HMCAddr, 6);
if(6<=Wire.available())
{
  magXHMC = Wire.read()<<8;
//X msb
  magXHMC |= Wire.read();
//X lsb
  magZHMC = Wire.read()<<8;
//Z msb
  magZHMC |= Wire.read();
//Z lsb
  magYHMC = Wire.read()<<8;
//Y msb
  magYHMC |= Wire.read();
//Y lsb
  double xyz[3];
  h3lis.getAcceleration(xyz);
  accelXLIS = xyz[0];
  accelYLIS = xyz[1];
  accelZLIS = xyz[2];
}
DataFile[1] = SampleCount;

```

```

DataFile[2] = Time;
DataFile[3] = CO2;
DataFile[4] = TVOC;
DataFile[5] = TempF;
DataFile[6] = Humidity;
DataFile[7] = Pressure;
DataFile[8] = BaroTemp;
DataFile[9] = accelX;
DataFile[10] = accelY;
DataFile[11] = accelZ;
DataFile[12] = gyroX;
DataFile[13] = gyroY;
DataFile[14] = gyroZ;
DataFile[15] = magX;
DataFile[16] = magY;
DataFile[17] = magZ;
DataFile[18] = q0;
DataFile[19] = q1;
DataFile[20] = q2;
DataFile[21] = q3;
DataFile[22] = IMUHeading;
DataFile[23] = IMUPitch;
DataFile[24] = IMURoll;
DataFile[25] = IMUYaw;
DataFile[26] = magXHMC;
DataFile[27] = magYHMC;
DataFile[28] = magZHMC;
DataFile[29] = accelXLIS;
DataFile[30] = accelYLIS;
DataFile[31] = accelZLIS;
File Datalog = SD.open("DataLog.txt",
FILE_WRITE); // access SD card
if (Datalog)
//if file can be created/modified
{
  if (SampleCount == -1.0)
  {
    Datalog.print(F("Sampling Delay
Time (millis), Air Quality, Barometer,
Temp/Humidity, IMU"));
    Datalog.println();
    Datalog.print(SampleRate);
  }
  if (SampleCount == 0.0)
//only on first iteration, prints file header
  {
    Datalog.print(F("Sample
Number,Time (millis),CO2
(ppm),TVOC (ppb), Temperature
(F),Humidity (%), Pressure(Pa), Pressure
Sensor Temperature (F), X Acceleration
(g), Y Acceleration (g), Z Acceleration
(g), X Gyration (g), Y Gyration (g), Z
Gyration (g), X Magnetic field
(mu*T),Y Magnetic field (mu*T),Z
Magnetic field (mu*T), Quartenion q0,
Quartenion q1, Quartenion q2,
Quartenion q3, Heading (Deg), Pitch
(Deg), Roll (Deg), Yaw (Deg), X
Mag_HMC5883L, Y Mag_HMC5883L,
Z Mag_HMC5883L, X
Acceleration_LIS331 (g), Y
Acceleration_LIS331 (g), Z
Acceleration_LIS331 (g)"));
    }
    if (SampleCount >= 1.0)
    {
      for (int i = 1; i < 32; i++)
//increment through data[] and print to
file
      {
        Datalog.print(DataFile[i],3);
        Datalog.write(',');
      }
    }
    Datalog.println(); // print a new line
    digitalWrite(LED, HIGH);
    Datalog.close(); // close your file
  }
  else
  {
    //alternate to previous
decision, if file can't be created sends
error message
    Serial.println(F("error opening
datalog.txt"));
  }
  SampleCount= SampleCount+1; //
Updating the sample count
delay(SampleRate); //set the sampling
rate (millisecond)
  digitalWrite(LED, LOW);
  } // the continous loop ends here

```

### C. PLD ERAU Payload – Avionics Sub payload Circuit Board 1 Arduino Program

Program created by Vijay Vishal Duraisamy and Nikita Amberkar

```

int signPin = 2; //Radiation Pulse
(Yellow)
int noisePin = 5; //Vibration Noise Pulse
(White)
#include <SPI.h> // libaray for spi
protocol
#include <SD.h> // SD card library
float DataFile[8]; // Initiaizling the array
float SampleCount = -1; //start sample
code
int LED = 12;
#include <avr/dtostrf.h>
const double alpha = 53.032; // cpm =
uSv x alpha
int index1 = 0; //Number of loops
char msg[256] = ""; //Message buffer for
serial output
int signCount = 0; //Counter for
Radiation Pulse
int noiseCount = 0; //Counter for Noise
Pulse
int sON = 0; //Lock flag for Radiation
Pulse
int nON = 0; //Lock flag for Noise Puls
double cpm = 0; //Count rate [cpm] of
current
double cpmHistory[200]; //History of
count rates
int cpmIndex = 0; //Position of current
count rate on cpmHistory[]
int cpmIndexPrev = 0; //Flag to prevent
duplicative counting
int prevTime = 0;
int currTime = 0;
int totalSec = 0; //Elapsed time of
measurement [sec]
int totalHour = 0; //Elapsed time of
measurement [hour]
int cpmTimeMSec = 0;
int cpmTimeSec = 0;
int cpmTimeMin = 0;
char cpmBuff[20];

char uSvBuff[20];
char uSvdBuff[20];
void setup()
{
  Serial.begin(9600);
  pinMode(LED, OUTPUT);
  digitalWrite(LED, LOW);
  pinMode(signPin, INPUT);
  digitalWrite(signPin, HIGH);
  pinMode(noisePin, INPUT);
  digitalWrite(noisePin, HIGH);

  Serial.println("hour[h]_sec[s]_count_cp
m_uSv/h_uSv/hError");
  for (int i = 0; i < 200; i++ )
  {
    cpmHistory[i] = 0;
  }
  prevTime = millis();
  Serial.println(F("Initializing SD
card..."));
  if (!SD.begin())
  {
    Serial.println(F("Card failed, or not
present"));
    while (1); // the remainder of the code
will not execute
  }
  Serial.println(F("SD card initialized."));
}
void loop()
{
  int sign = digitalRead(signPin);
  int noise = digitalRead(noisePin);
  if (sign == 0 && sON == 0)
  { //Deactivate Radiation Pulse counting
for a while
    sON = 1;
    signCount++;
  } else if (sign == 1 && sON == 1) {
    sON = 0;
  }
}

```

```

//Noise Pulse normally keeps high for
about 100[usec]
if (noise == 1 && nON == 0)
{ //Deactivate Noise Pulse counting for
a while
  nON = 1;
  noiseCount++;
} else if (noise == 0 && nON == 1) {
  nON = 0;
}
digitalWrite(LED, LOW);
if (index1 == 10000) //About 160-170
msec in Arduino Nano(ATmega328)
{
  currTime = millis();
  if (noiseCount == 0)
  {
    if ( totalSec % 6 == 0 &&
cpmIndexPrev != totalSec)
    {
      cpmIndexPrev = totalSec;
      cpmIndex++;
      if (cpmIndex >= 200)
      {
        cpmIndex = 0;
      }
      if (cpmHistory[cpmIndex] > 0)
      {
        cpm -= cpmHistory[cpmIndex];
      }
      cpmHistory[cpmIndex] = 0;
    }
    cpmHistory[cpmIndex] +=
signCount;
    cpm += signCount;
    cpmTimeMSec += abs(currTime -
prevTime);
    //Transform from msec. to sec. (to
prevent overflow)
    if (cpmTimeMSec >= 1000)
    {
      cpmTimeMSec -= 1000;
      if ( cpmTimeSec >= 20 * 60 )
      {
        cpmTimeSec = 20 * 60;
      } else {
        cpmTimeSec++;
      }
      totalSec++;
      if (totalSec >= 3600)
      {
        totalSec -= 3600;
        totalHour++;
      }
    }
    double min = cpmTimeSec / 60.0;
    if (min != 0)
    {
      dtostrf(cpm / min, -1, 3, cpmBuff);
      dtostrf(cpm / min / alpha, -1, 3,
uSvBuff);
      dtostrf(sqrt(cpm) / min / alpha, -1,
3, uSvdBuff);
    } else {
      dtostrf(0, -1, 3, cpmBuff);
      dtostrf(0, -1, 3, uSvBuff);
      dtostrf(0, -1, 3, uSvdBuff);
    }
    sprintf(msg,
"%d,%d,%03d,%d,%s,%s,%s",
totalHour, totalSec,
cpmTimeMSec,
signCount,
cpmBuff,
uSvBuff,
uSvdBuff
);
    Serial.println(msg);
    DataFile[1] = SampleCount;
    DataFile[2] = totalHour;
    DataFile[3] = totalSec;
    DataFile[4] = cpmTimeMSec;
    DataFile[5] = signCount;
    DataFile[6] = atof(cpmBuff);
    DataFile[7] = atof(uSvBuff);
    DataFile[8] = atof(uSvdBuff);
    File Datalog = SD.open("DataLog.txt",
FILE_WRITE); // access SD card
    if (Datalog)
    //if file can be created/modified
    {

```

```

        if (SampleCount == 0.0)
//only on first iteration, prints file header
    {
        Datalog.print(F("Sample ID, Total
Hour, Total Seconds, cpmTimeMsec,
signCount, cpmBuff, uSvBuff,
uS3vdBuff"));
    }
    if (SampleCount >= 1.0)
    {
        for (int i = 1; i < 9; i++)
//increment through data[] and print to
file
        {
            Datalog.print(DataFile[i],3);
            Datalog.write(',');
        }
    }
    Datalog.println(); // print a new line
    digitalWrite(LED, HIGH);
    Datalog.close(); // close your file
}
SampleCount= SampleCount+1;
}
prevTime = currTime;
signCount = 0;
noiseCount = 0;
index1 = 0;
}
index1 = index1+1;
}

```

#### D. MAPMD CFD Simulation: Job Execution Script

```

#!/bin/bash
#PBS -q normalq
#PBS -l walltime=23:58:00
#PBS -l nodes=5:ppn=36
#PBS -e star_pbs_errors.out
#PBS -o star_pbs_stdout.out
module load openmpi/gcc/64/1.10.3
module load star-ccm/12.02.011
cd $PBS_O_WORKDIR
# set case name here
case=MAPMD
rm DONE -f
rm ABORT -f
date >> $case.log
echo -n "=====  
$case.log
echo ----- RUN ON PROCESSORS --  
----- >> $case.log
cat $PBS_NODEFILE >> $case.log
echo "=====  
Processors" >> $case.log
echo $PBS_NP >> $case.log
# if necessary, add java file after batch  
tag, and before case name.  
starccm+ -v -rsh ssh -licpath  
2000@DBLicman3 -machinefile  
$PBS_NODEFILE -np $PBS_NP -time  
-cpubind off -batch automate.java  
$case.sim >> $case.log
# Note finish wall time  
echo -n "=====  
$case.log
date >> $case.log
# create a "DONE" file to indicate  
completion  
touch DONE

```

#### E. MAPMD CFD Simulation: Contact Modeling Automation JAVA script

```

// STAR-CCM+ macro: automate.java
// Written by STAR-CCM+ 12.02.011
package macro;
import java.util.*;
import star.common.*;
import star.base.neo.*;
import star.base.report.*;
import star.sixdof.*;

```



```

import star.mapping.*;
public class automate extends StarMacro
{
public void execute() {
    execute0();
}
private void execute0() {
Simulation simulation_0 =
getActiveSimulation();
double currentPhysicalTime=0;
double gap1=0.000000;
double gap2=0.000000;
double vel=0.000000;
double k=0.000000;
MinReport minReport_0 =
((MinReport)
simulation_0.getReportManager().getRe
port("TopContact"));
MinReport minReport_1 =
((MinReport)
simulation_0.getReportManager().getRe
port("BotContact"));
LinearVelocityReport
linearVelocityReport_0 =
((LinearVelocityReport)
simulation_0.getReportManager().getRe
port("Membrane Velocity Z"));
ContactCoupling contactCoupling_0
=
((ContactCoupling)
simulation_0.get(SixDofBodyCoupling
Manager.class).getObject("Contact
1"));
NormalContactForce
normalContactForce_0 =
contactCoupling_0.getNormalForce();
while (currentPhysicalTime < 40){

simulation_0.getReportManager().getRe
port("TopContact");
gap1=minReport_0.getValue();
simulation_0.println("");
simulation_0.println("Top Contact
gap distance (in): " +
String.format("%.6f", gap1));
simulation_0.println("");

simulation_0.getReportManager().getRe
port("BotContact");
gap2=minReport_1.getValue();
simulation_0.println("");
simulation_0.println("Bottom Contact
gap distance (in): " +
String.format("%.6f", gap2));
simulation_0.println("");

simulation_0.getReportManager().getRe
port("Membrane Velocity Z");

vel=Math.abs(linearVelocityReport_0.ge
tValue());
k=vel*vel*70311182.32417;
simulation_0.println("");
simulation_0.println("Z Velocity
(m/s): " + String.format("%.6f", vel));
simulation_0.println("");
if (gap1<0.21 || gap2<0.21) {

simulation_0.get(SixDofBodyCoupling
Manager.class).getObject("Contact 1");
contactCoupling_0.setEnabled(true);
contactCoupling_0.getNormalForce();

normalContactForce_0.getElasticCoeffic
ient().setValue(k);

simulation_0.getSimulationIterator().ste
p(500);
}
else {

simulation_0.get(SixDofBodyCoupling
Manager.class).getObject("Contact 1");
contactCoupling_0.setEnabled(false);

simulation_0.getSimulationIterator().ste
p(5);
}
currentPhysicalTime =
simulation_0.getSolution().getPhysicalTi
me();
}}}

```

## Appendix B

### A. Research facility

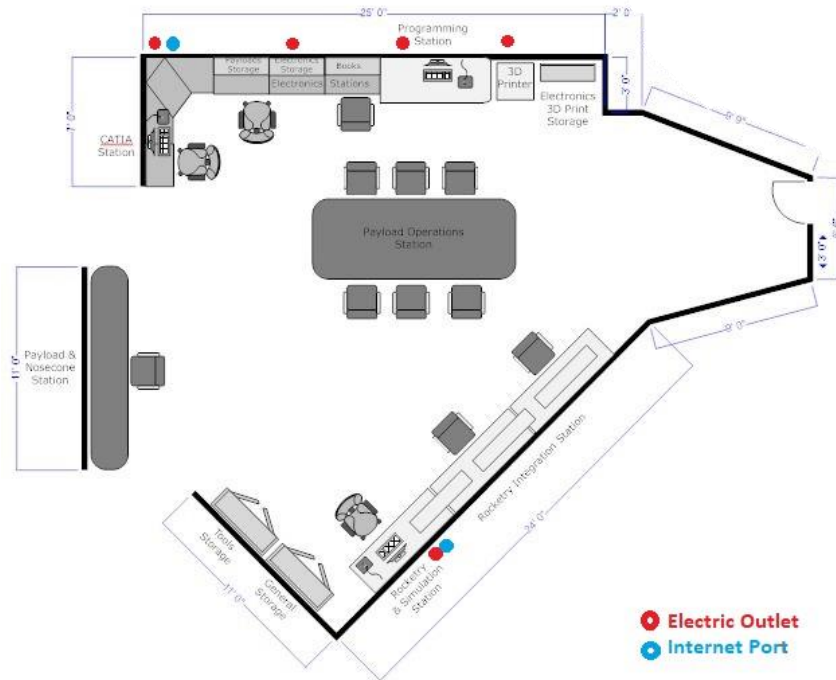


Figure B.1: PATO lab floorplan

### B. CRExIM Analysis

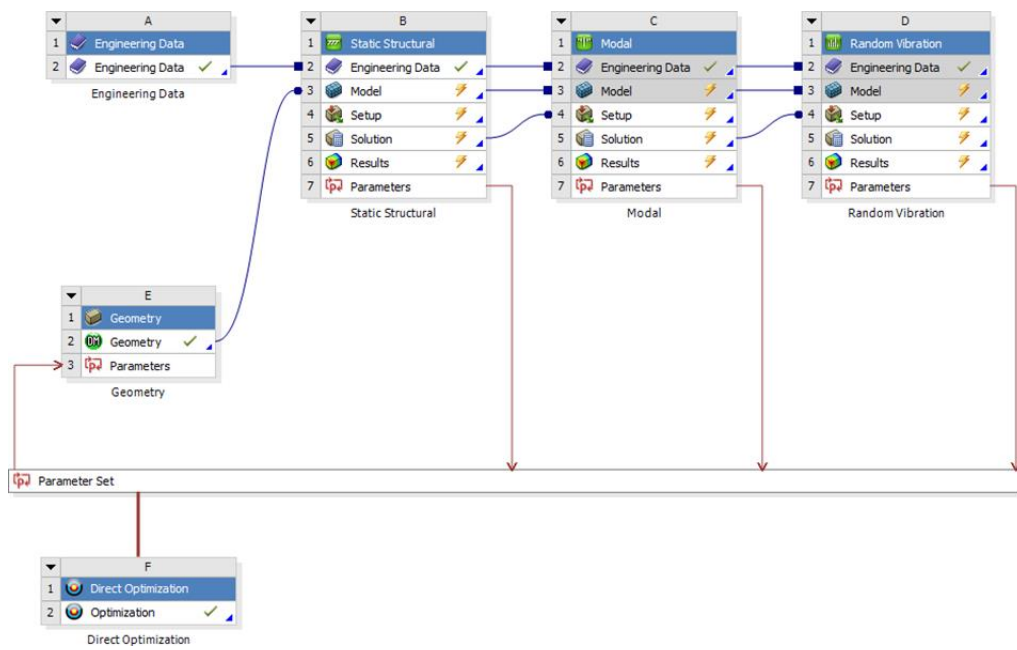


Figure B.2: ANSYS optimization project view

C. MESSI/McXIMUS Electronics

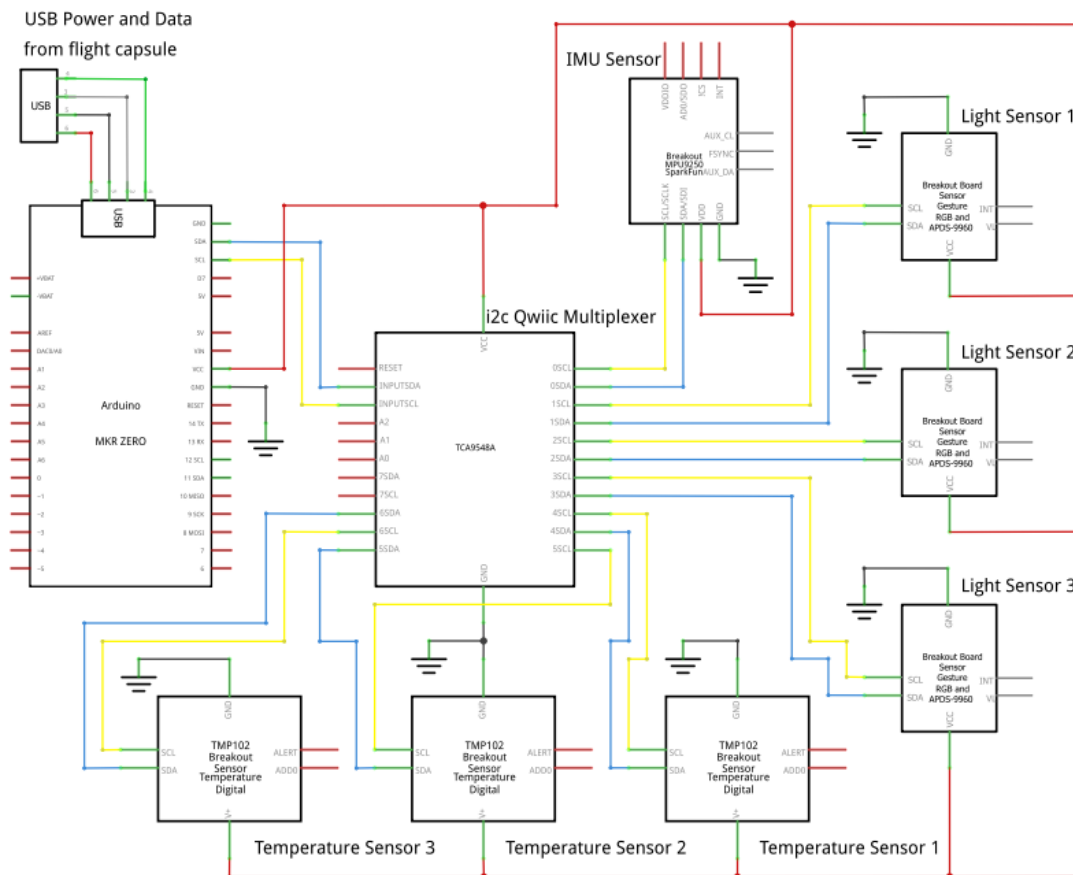


Figure B.3: Custom data logger circuit schematic

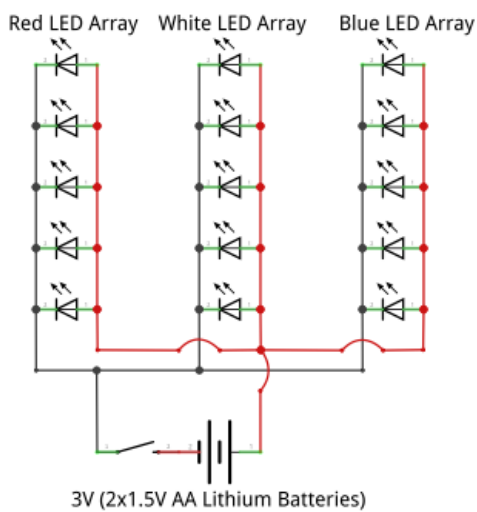


Figure B.4: LED lighting system circuit schematic

D. PLD ERAU Payload Electronics

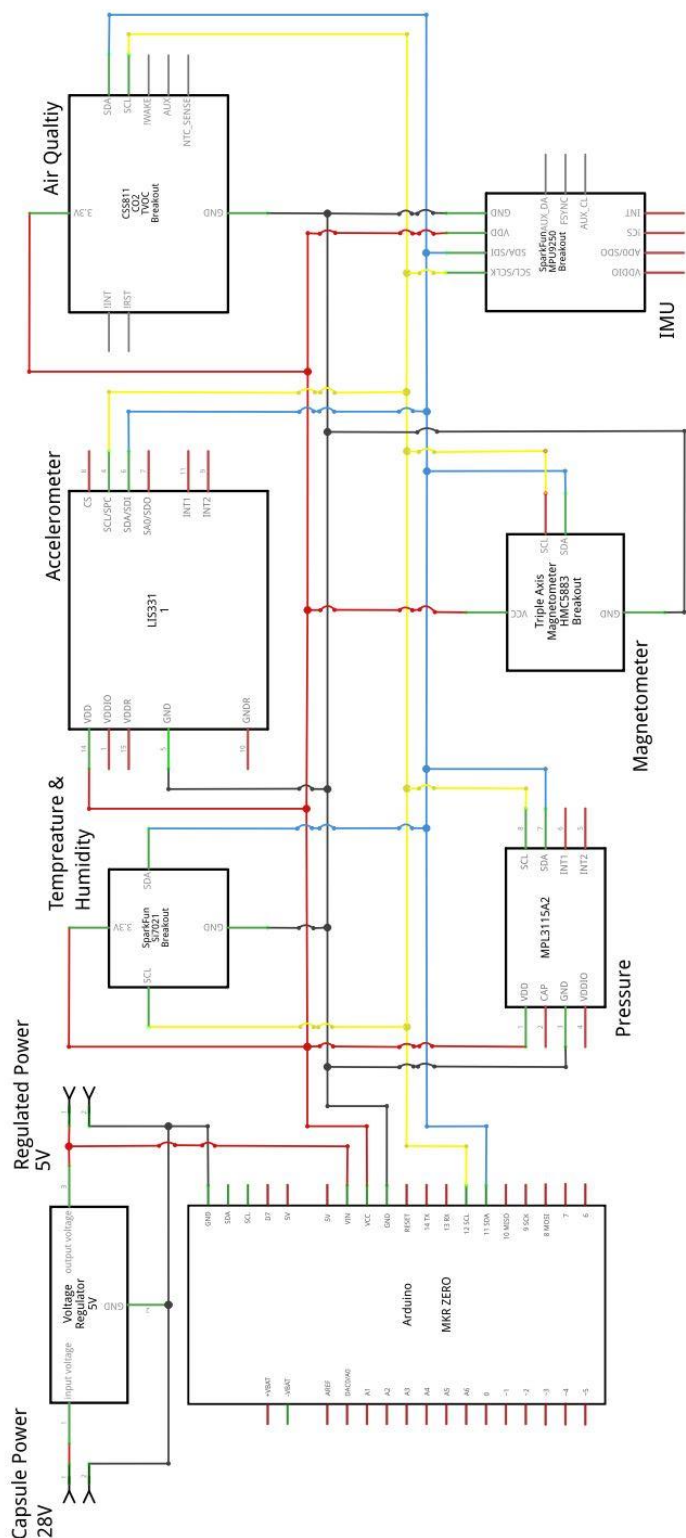


Figure B.5 Avionics sub payload Circuit board 1 schematic

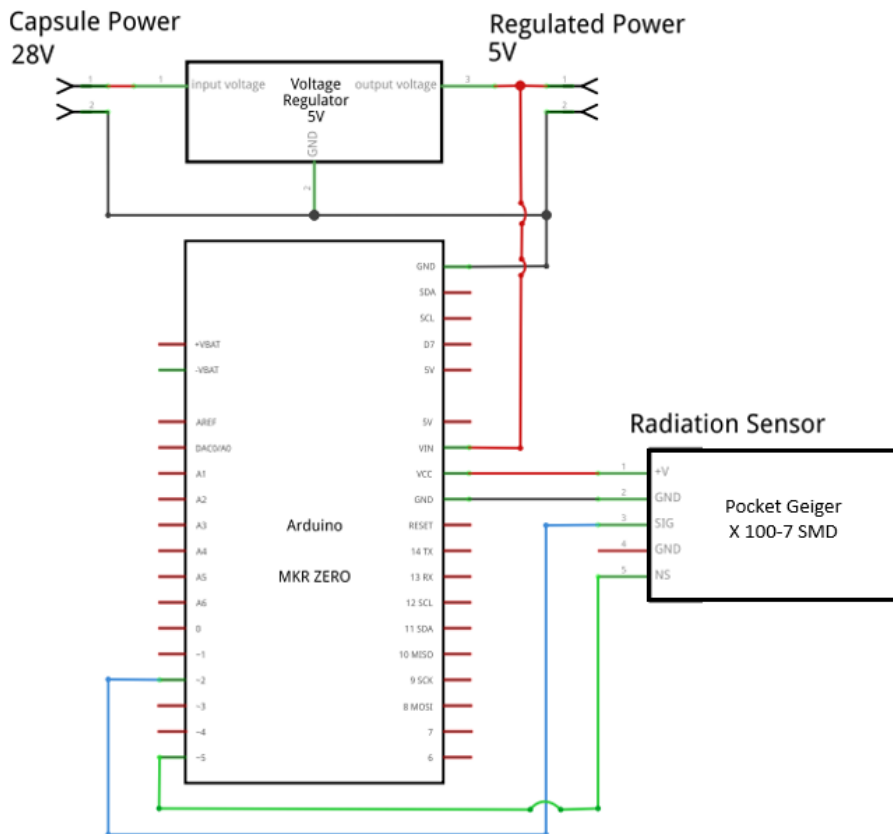


Figure B.6: Avionics sub payload Circuit board 2 schematic

```

Sampling Delay Time (millis), Air Quality, Barometer, Temp/Humidity, IMU
500
Sample Number,Time (millis),CO2 (ppm),TVOC (ppb), Temperature (F),Humidity (%), Pressure(Pa), Pressure Sensor Temperature (F), X Acceleration (g), Y Acceleration (g), Z Acceleration (g), X Gyration (g), Y Gyration (g), Z Gyration (g), X Magnetic field (mu*T),Y Magnetic field (mu*T),Z Magnetic field (mu*T), Quaternion q0, Quaternion q1, Quaternion q2, Quaternion q3, Heading (Deg), Pitch (Deg), Roll (Deg), Yaw (Deg), X Mag_RMC5682, Y Mag_RMC5682, Z Mag_RMC5682, X Acceleration_LIS331 (g), Y Acceleration_LIS331 (g), Z Acceleration_LIS331 (g)
1.000,0.000,500.000,0.000,76.474,51.144,101818.000,74.750,0.021,-0.989,0.008,0.305,0.915,-0.061,72.618,47.412,-6.452,0.995,-0.100,0.000,-0.001,56.860,359.877,11.527,0.060,6536
7.000,64756.000,87.000,-16.257,-0.399,-1.113
2.000,0.749,400.000,0.000,76.474,51.144,101820.500,74.750,0.019,-0.989,0.010,0.183,0.915,-0.122,74.869,47.412,-7.502,0.991,-0.136,0.000,-0.001,57.655,359.890,15.632,0.094,6536
7.000,64757.000,86.000,-16.257,-0.207,-1.401
3.000,1.500,400.000,0.000,76.474,51.144,101817.500,74.750,0.031,-0.977,0.016,0.122,0.854,-0.122,73.369,47.412,-7.052,0.985,-0.171,0.000,-0.001,57.129,359.904,19.656,0.139,6536
7.000,64758.000,78.000,-16.257,-0.303,-1.065
4.000,2.250,400.000,0.000,76.456,51.137,101817.250,74.750,0.024,-0.985,0.025,0.183,0.976,-0.183,74.569,46.812,-6.902,0.979,-0.204,0.000,-0.002,57.881,359.902,23.576,0.184,6536
8.000,64759.000,89.000,-16.162,-0.399,-1.113
5.000,3.000,400.000,0.000,76.474,51.159,101819.500,74.750,0.036,-0.981,0.017,0.244,0.854,-0.244,74.119,46.962,-8.102,0.972,-0.237,0.000,-0.002,57.642,359.863,27.384,0.230,6536
6.000,64763.000,76.000,-16.353,-0.063,-1.065
6.000,3.751,400.000,0.000,76.474,51.144,101818.500,74.750,0.026,-0.975,0.020,0.183,0.915,0.000,74.419,46.212,-8.102,0.964,-0.268,0.000,-0.003,58.161,359.815,31.052,0.281,6536
7.000,64756.000,87.000,-16.353,-0.399,-1.209
7.000,4.501,400.000,0.000,76.455,51.144,101817.250,74.750,0.022,-0.976,0.000,0.244,0.793,-0.183,74.869,46.662,-6.752,0.964,-0.268,0.000,-0.003,58.161,359.815,31.052,0.281,6536
8.000,64760.000,77.000,-16.401,-0.399,-1.113
8.000,5.250,400.000,0.000,76.455,51.144,101813.250,74.750,0.019,-0.979,0.003,0.183,1.037,-0.061,74.119,46.962,-6.002,0.716,-0.697,0.020,-0.040,57.642,350.300,88.360,1.650,6536
4.000,64770.000,78.000,-16.785,-0.303,-0.873
0.000,2.000,400.000,0.000,76.452,51.144,101818.750,74.750,0.008,0.000,0.000,0.183,0.915,0.000,74.419,46.212,-8.102,0.964,-0.268,0.000,-0.003,58.161,359.815,31.052,0.281,6536
Sample ID, Total Hour, Total Seconds, cpmTimeMsec, signCount, cpmBuff, uSvBuff, uS3vdBuff
1.000,0.000,0.000,369.000,0.000,0.000,0.000,0.000,0.000
2.000,0.000,0.000,447.000,0.000,0.000,0.000,0.000,0.000
3.000,0.000,0.000,525.000,0.000,0.000,0.000,0.000,0.000
4.000,0.000,0.000,603.000,0.000,0.000,0.000,0.000,0.000
5.000,0.000,0.000,681.000,0.000,0.000,0.000,0.000,0.000
6.000,0.000,0.000,759.000,0.000,0.000,0.000,0.000,0.000
7.000,0.000,0.000,838.000,0.000,0.000,0.000,0.000,0.000
8.000,0.000,0.000,916.000,0.000,0.000,0.000,0.000,0.000
9.000,0.000,0.000,994.000,0.000,0.000,0.000,0.000,0.000
10.000,0.000,1.000,75.000,0.000,0.000,0.000,0.000,0.000
11.000,0.000,1.000,153.000,0.000,0.000,0.000,0.000,0.000
12.000,0.000,1.000,231.000,0.000,0.000,0.000,0.000,0.000
13.000,0.000,1.000,310.000,0.000,0.000,0.000,0.000,0.000
14.000,0.000,1.000,388.000,0.000,0.000,0.000,0.000,0.000
15.000,0.000,1.000,466.000,0.000,0.000,0.000,0.000,0.000
16.000,0.000,1.000,545.000,0.000,0.000,0.000,0.000,0.000
17.000,0.000,1.000,623.000,0.000,0.000,0.000,0.000,0.000
18.000,0.000,1.000,704.000,0.000,0.000,0.000,0.000,0.000
19.000,0.000,1.000,786.000,0.000,0.000,0.000,0.000,0.000
20.000,0.000,1.000,864.000,0.000,0.000,0.000,0.000,0.000
21.000,0.000,1.000,942.000,0.000,0.000,0.000,0.000,0.000
22.000,0.000,2.000,21.000,0.000,0.000,0.000,0.000,0.000
23.000,0.000,2.000,99.000,0.000,0.000,0.000,0.000,0.000
24.000,0.000,2.000,177.000,0.000,0.000,0.000,0.000,0.000
25.000,0.000,2.000,256.000,0.000,0.000,0.000,0.000,0.000
26.000,0.000,2.000,334.000,0.000,0.000,0.000,0.000,0.000
    
```

Figure B.7: Avionics payload data output (Circuit board 1 on top and Circuit board 2 on bottom)

## E. Vibration Test Campaign

DS-1300VH-9 SPA602 ACU402 Electrodynamic Shaker		
Generated Force	Sine (Pk)	690 kgf (1500 lbf)
	Random (Rms)	600 kgf (1320 lbf)
	Shock (Pk)	1,380kgf (3,000lbf) @6ms
Useable Frequency		5-4,000Hz
Maximum displacement (Peak-Peak):		
Continuous duty		51 mm (2 in.)
Shock		51 mm (2 in.)
Between mechanical stops		58 mm (2.3 in.)
Maximum Velocity		2 m/s (78.7in/s)
Maximum Acceleration		100g
Fundamental Resonance Frequency (Nominal, Bare Table)		3513Hz
Body Suspension Natural Frequency (Thrust Axis)		Lower than 3 Hz
Power Supply Requirement		480V/60Hz 3 Phrase
Armature Rated Current		75 Arms
Armature Rated Voltage		110 Vrms
Armature Coil Resistance		0.28 $\Omega$
Effective Nominal Armature Mass		6.9kg (15.2 lbs)
Armature Diameter		230 mm (9 in.)
Vertical Load Support		300 kg (660 lbs)
Load Attachment Points (Standard)		16 stainless steel 5/16-18 UNC inserts
Field Rated Current (DC) cold		24.7 ADC
Field Rated Voltage (DC) cold		251.6 VDC
Field Coil Resistance R20		2X7.5=15 $\Omega$
Drive Coil Isolation Resistance to Armature		>10M $\Omega$
Drive Coil Isolation Resistance to Shaker Body		>10M $\Omega$
Stray Flux Density with degauss coil		10 gauss @ 152 mm above table
The height between shaker body to the armature table surface after remove the top cover		118mm
The maximum noise of the system		110dB
SPA602 Power Amplifier		
Rated Output Capacity		6 kVA
Amplifier Frequency response (Sine mode, resistive load)		Full power from 5 Hz to 3000Hz rolling off to 3 dB at 4000 Hz with 6 dB/Octave slope
Distortion (at rated output)		From 5 Hz to 3000Hz less than 1%
Signal-Noise-Ratio		Greater than 65 dB
DC stability		Less than 0.05% of full output voltage with 10% change in line voltage.
Input Drive		1.5 Vrms into 10 K Ohms for full output
Input Power		480V, 60 Hz, 3 Phase 17.5kVA
160 Hz Sine Trial Testing		70Arms/60.2Vrms @100 g

Figure B.8: Electrodynamic shaker specifications



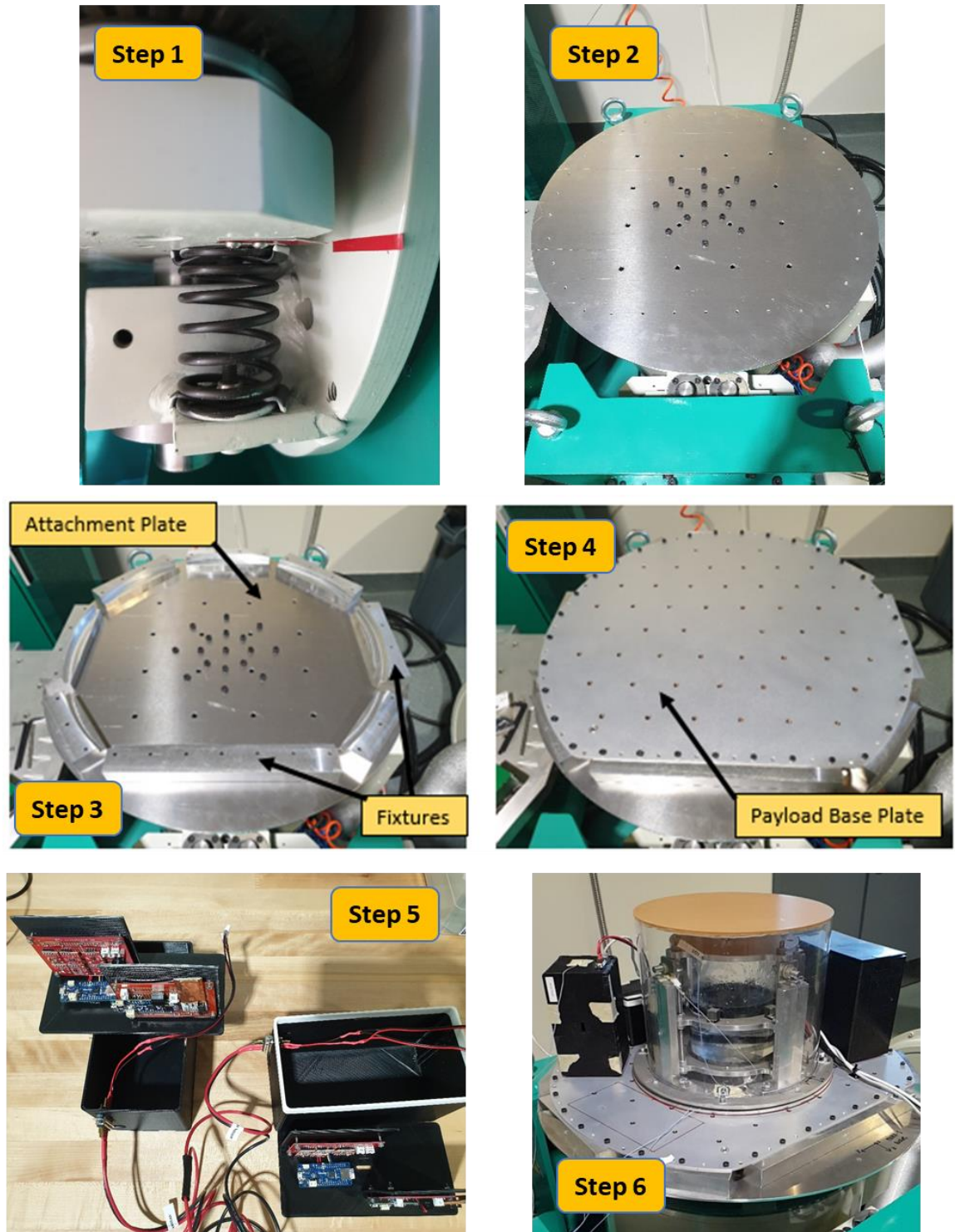


Figure B.10: Shaker test setup procedures





G. Level 3 Rocket

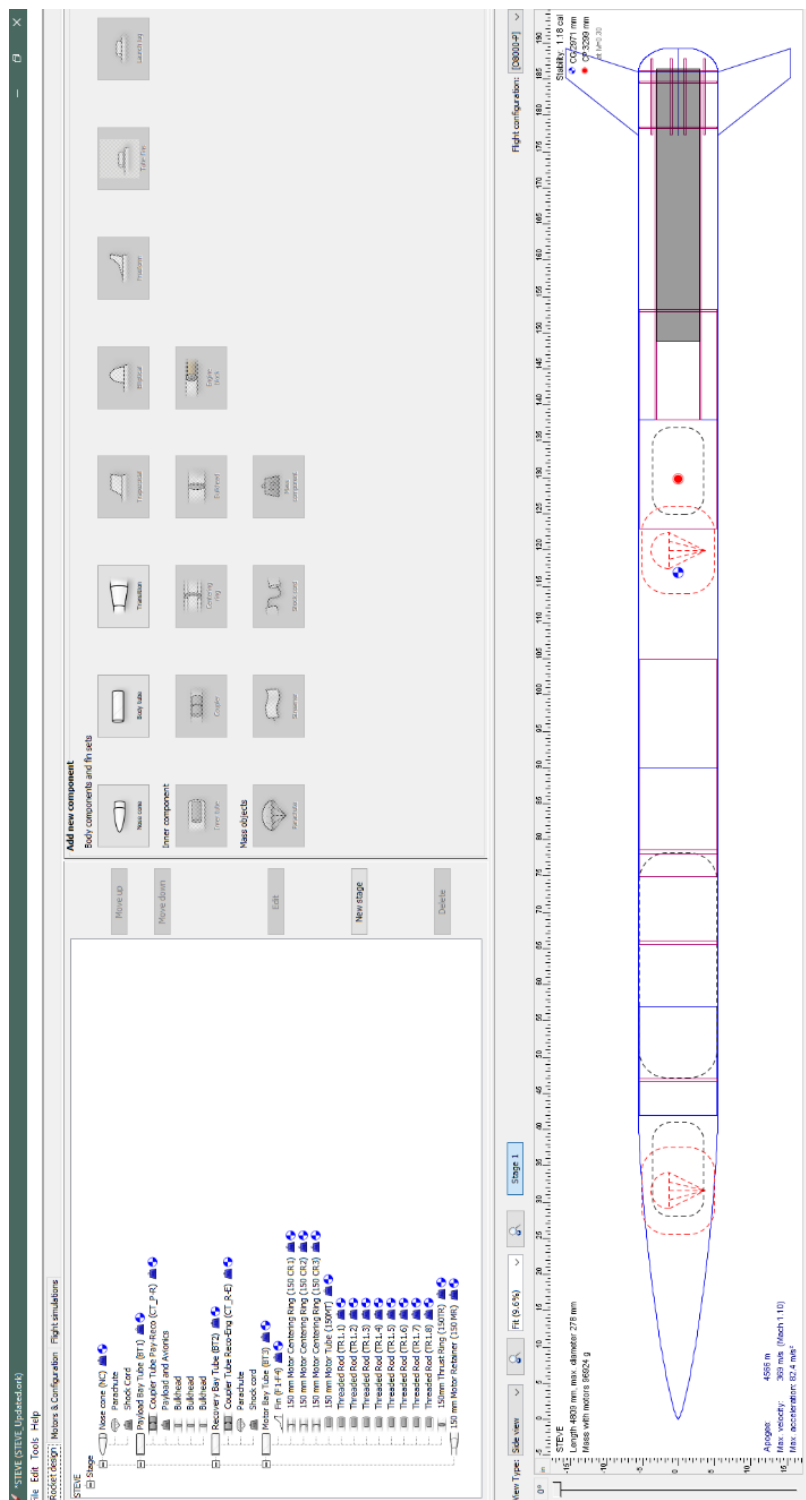


Figure B.13: OpenRocket simulation

### H. Vacuum Chamber Test Setup

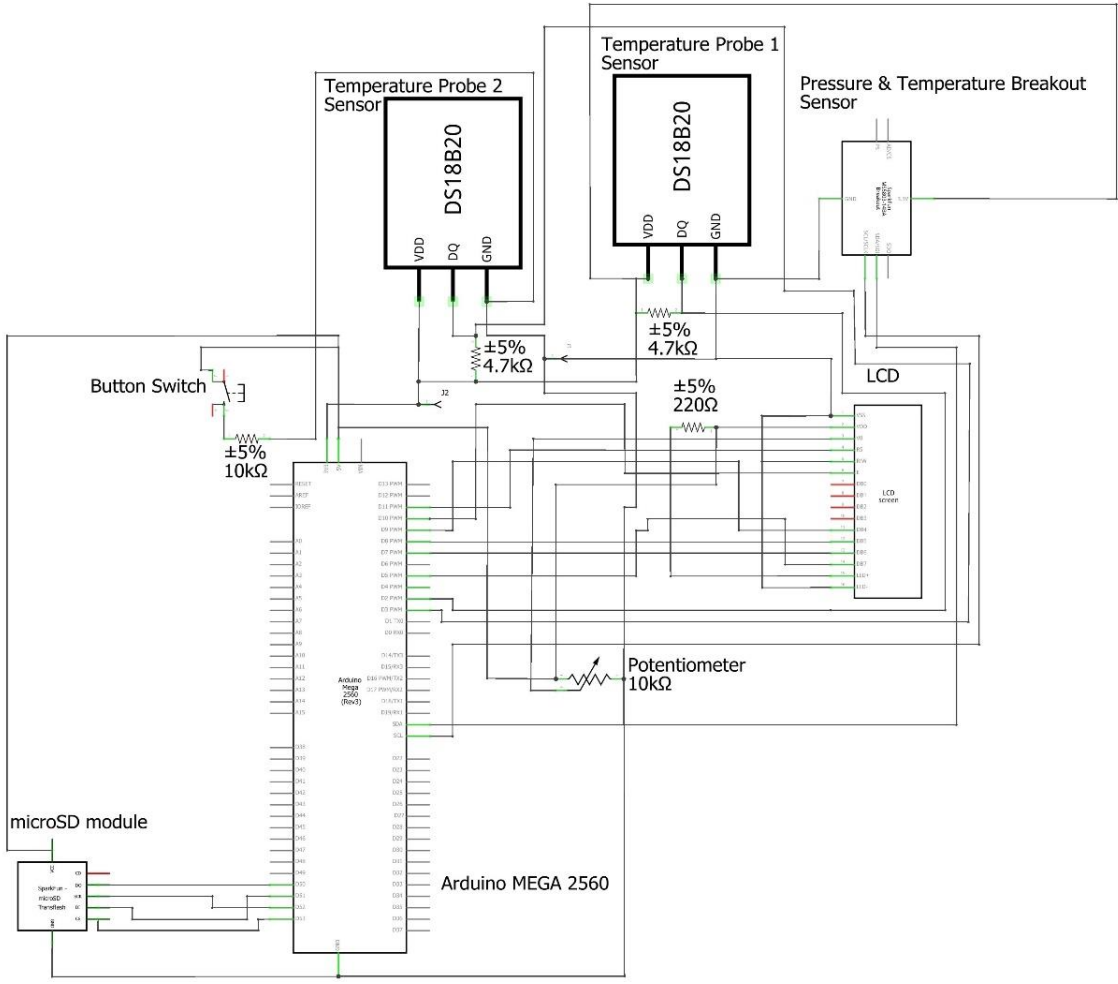


Figure B.14: Vacuum chamber environment monitoring system circuit schematic